

Synthesis and characterization of CVD graphene on copper: Towards the fabrication of synthetic graphene suspensions

Bernat Sempere Nomen

<http://hdl.handle.net/10803/401494>

ADVERTIMENT. L'accés als continguts d'aquesta tesi doctoral i la seva utilització ha de respectar els drets de la persona autora. Pot ser utilitzada per a consulta o estudi personal, així com en activitats o materials d'investigació i docència en els termes establerts a l'art. 32 del Text Refós de la Llei de Propietat Intel·lectual (RDL 1/1996). Per altres utilitzacions es requereix l'autorització prèvia i expressa de la persona autora. En qualsevol cas, en la utilització dels seus continguts caldrà indicar de forma clara el nom i cognoms de la persona autora i el títol de la tesi doctoral. No s'autoritza la seva reproducció o altres formes d'explotació efectuades amb finalitats de lucre ni la seva comunicació pública des d'un lloc aliè al servei TDX. Tampoc s'autoritza la presentació del seu contingut en una finestra o marc aliè a TDX (framing). Aquesta reserva de drets afecta tant als continguts de la tesi com als seus resums i índexs.

ADVERTENCIA. El acceso a los contenidos de esta tesis doctoral y su utilización debe respetar los derechos de la persona autora. Puede ser utilizada para consulta o estudio personal, así como en actividades o materiales de investigación y docencia en los términos establecidos en el art. 32 del Texto Refundido de la Ley de Propiedad Intelectual (RDL 1/1996). Para otros usos se requiere la autorización previa y expresa de la persona autora. En cualquier caso, en la utilización de sus contenidos se deberá indicar de forma clara el nombre y apellidos de la persona autora y el título de la tesis doctoral. No se autoriza su reproducción u otras formas de explotación efectuadas con fines lucrativos ni su comunicación pública desde un sitio ajeno al servicio TDR. Tampoco se autoriza la presentación de su contenido en una ventana o marco ajeno a TDR (framing). Esta reserva de derechos afecta tanto al contenido de la tesis como a sus resúmenes e índices.

WARNING. The access to the contents of this doctoral thesis and its use must respect the rights of the author. It can be used for reference or private study, as well as research and learning activities or materials in the terms established by the 32nd article of the Spanish Consolidated Copyright Act (RDL 1/1996). Express and

DOCTORAL THESIS

Title	Synthesis and characterization of CVD graphene on copper: Towards the fabrication of synthetic graphene suspensions.
Presented by	Bernat Sempere Nomen
Centre	IQS School of Engineering
Department	Chemical Engineering and Materials Science
Directed by	Dr. Carles Colominas i Guardia

Als meus pares

“Los imposibles de hoy serán posibles mañana”

Konstantin Tsiolkovsky

Acknowledgements

El desenvolupament d'aquesta tesi no hagués estat possible sense la inestimable ajuda i suport de tota la gent que m'ha envoltat en el camí recorregut. Sense voler oblidar-me a ningú hi ha persones que es mereixen una menció especial.

Aquesta tesi ha estat possible gràcies al suport i guiatge ofert per part del Dr. Carles Colominas. Així com de la inestimable col·laboració de Javier Herrero i Tomàs Baldi amb els seus TFM, de Pepe Bermúdez amb el seu PFC i Boris Agea i Ariadna Chueca amb els seus TFG. A tots ells agrair els esforços posats en ajudar a avançar punts concrets de la tesi. També a Anna Ramos per oferir grans dosis de coneixement i visió crítica.

Agrair també la col·laboració dels grups de la Dra. Núria Ferrer del departament de Física Aplicada de la UPC, al Dr. Joan Josep Roa de la UPC per la seva gran ajuda en els nostres inicis tortuosos en AFM i a la Dra. Gemma Rius del CNM de Bellaterra.

A tots els meus amics per a haver-me acompanyat en aquesta llarga travessia fent-a molt més divertida i assumible. En especial al Guillem i al David per haver-me iniciat en el hobby de fabricar cervesa artesanalment entre altres "frikades".

Finalment, a la meua família i, en especial, als meus pares que han hagut de viure tant els moments feliços com d'aguantar els moments més difícils quan la desesperació i la frustració marcaven el meu estat d'ànim. El suport, ajuda i motivació que he rebut de part seva ha estat, és i serà, impagable.

Aquesta tesi ha estat possible amb el suport de Fons Socials Europeus i de la Secretaria d'Universitats i Recerca del Departament d'Economia i Coneixement de la Generalitat de Catalunya mitjançant l'ajut FI-DGR [2013FI-B 00401, 2014FI-B1 00204, 2015FI-B2 00197], així com a Flubetech S.L. i a la IQS School of Engineering de la Universitat Ramon Llull.

Abstract

Graphene is a one-atom thick layer of carbon, tightly packed in a hexagonal lattice. It can be seen as each one of the layers that form graphite. It has been called the wonder material of the XXI century, because it has amazing properties that opens the possibility for many applications. Presently, it can be found in the market as both films deposited on different substrates, mainly by Chemical Vapor Deposition (CVD), and particles or suspensions consisting of graphene platelets produced by exfoliation of graphite. CVD graphene results in polycrystalline films commonly of high quality, in relation to monolayer structure, purity and low density of defects. On the other hand, exfoliated materials show almost no control over the size nor the number of layers, which results in suspensions of multilayer graphene or even thin graphite flakes, often with high oxygen content.

This thesis is aimed at synthesizing a new kind of graphene product, consisting of a suspension of synthetic graphene flakes of high quality, monolayer structured with narrow and controllable particle size distributions. To achieve this goal, different developments on graphene synthesis and transfer methods have been combined. First, a CVD reactor was built, able to produce monolayer graphene and experimental conditions to tailor graphene grain size were studied using gas flow restrictions inside the reactor. Second, a simple, robust and repetitive method based on photocatalytic oxidization of copper through graphene's grain boundaries was developed in order to measure graphene grain size. Finally, graphene was deposited onto high area copper substrates and subsequently transferred to suspension using an electrochemical approach with and without surfactants.

Graphene samples are characterized throughout the work by optical microscopy, SEM, AFM and Raman Spectroscopy. To evaluate the quality of produced graphene samples, THz Time Domain Spectroscopy (THz-TDS) was also used and the influence of grain size on the THz conductivity was explored. Moreover, electrical contacts were microfabricated to allow the measurement of graphene conductivity across several lengths as well as across single grain boundaries and monolayer and bilayer islands.

Characterization using Tyndall effect and Raman spectroscopy after filtration of synthetic graphene suspensions, confirms that monolayer graphene flakes can be found on aqueous suspension containing minimal amounts of surfactant.

Resum

El grafè està compost per una capa de carboni de només un àtom de gruix, agrupats en una matriu hexagonal. Es pot entendre com una de les làmines que formen el grafit. Se l'ha anomenat el material meravellós del segle XXI degut a les seves excepcionals propietats i les aplicacions potencials que se'n desprenen. Actualment, es pot trobar dipositat sobre diferents substrats, principalment per "Chemical Vapor Deposition" (CVD), i partícules o suspensions formades per plaquetes de grafè obtingudes per exfoliació de grafit. La producció de grafè per CVD resulta en capes policristal·lines de gran qualitat, en relació a la seva estructura monocapa, la baixa densitat de defectes i la seva puresa. Per contra, en els materials exfoliats pràcticament no hi ha control sobre la mida o el nombre de capes resultant en suspensions de grafè multicapa o grafit molt prim i, molts cops, amb elevat contingut d'oxigen.

Aquesta tesi s'enfoca a la síntesi d'un nou tipus de producte de grafè, en concret, una suspensió de partícules de grafè sintètic de gran qualitat amb una estructura monocapa i una distribució de mida de partícula estreta i controlable. Per assolir aquest objectiu, s'han de combinar diversos avenços en la síntesi i transferència de grafè sintètic. En primer lloc, s'ha dissenyat i construït un reactor CVD capaç de produir grafè monocapa i s'han estudiat les condicions que, en conjunció amb restriccions de cabal dins el reactor, permeten controlar la mida dels grans del grafè. En segon lloc, s'ha desenvolupat un mètode simple, robust i repetible basat en l'oxidació foto-catalítica del coure a través dels límits de gra del grafè per tal de calcular la mida dels grans. Finalment, s'ha sintetitzat grafè sobre substrats amb elevades àrees superficials i s'ha transferit directament a suspensions amb i sense tensioactius mitjançant processos electroquímics.

Les mostres de grafè al llarg del treball s'han caracteritzat mitjançant tècniques de microscòpia òptica, SEM, AFM i espectroscòpia Raman. THz-TDS s'ha emprat tant per a determinar i estudiar la qualitat del grafè, com per avaluar la influència de la mida de gra en la conductivitat en els THz. A més, la conductivitat del grafè s'ha mesurat mitjançant contactes metàl·lics micro-fabricats. Aquests han permès mesurar grafè a través de varies distàncies i, també, a través d'un únic límit de gra i dins d'illes de grafè monocapa i bicapa.

La caracterització de les suspensions de grafè sintètic mitjançant efecte Tyndall i espectroscòpia Raman, després de filtrar-les, confirma la presència de partícules de grafè monocapa en les suspensions aquoses que contenen quantitats mínimes de tensioactiu.

Resumen

El grafeno está compuesto por una capa de carbono solamente de un átomo de grosor, agrupados en una matriz hexagonal. Se puede entender como una de las láminas que forman el grafito. Se lo ha llamado el material maravilloso del siglo XXI debido a sus excepcionales propiedades y las aplicaciones potenciales que se derivan de ellas. Actualmente, se puede comprar depositado sobre distintos sustratos, principalmente por “Chemical Vapour Deposition” (CVD), y partículas o suspensiones formadas por plaquitas de grafeno obtenidas por exfoliación de grafito. La producción de grafeno por CVD resulta en capas poli-cristalinas de gran calidad, en relación a su estructura monocapa, la baja densidad de defectos y su pureza. Por contra, en los materiales exfoliados prácticamente no hay control sobre la medida o el número de capas lo que se traduce en suspensiones de grafeno multicapa o grafito muy delgado y, en muchos casos, con un elevado contenido de oxígeno.

Esta tesis se enfoca a la síntesis de un nuevo tipo de producto de grafeno, en concreto, una suspensión de partículas de grafeno sintético de gran calidad con una estructura monocapa y una distribución de medida de partícula muy estrecha y controlable. Para conseguir este objetivo, se tienen que combinar varios avances en la síntesis y transferencia de grafeno sintético. En primer lugar, se ha diseñado y construido un reactor CVD capaz de producir grafeno monocapa y se han estudiado las condiciones que, en conjunción con restricciones de caudal dentro el reactor, permiten controlar la medida de los granos del grafeno. En segundo lugar, se ha desarrollado un método simple, robusto y repetible basado en la oxidación foto-catalítica del cobre a través de los límites de grano del grafeno con el fin de calcular la medida de los granos. Finalmente, se ha sintetizado grafeno sobre sustratos con grandes áreas superficiales y se ha transferido directamente a suspensiones con y sin tensoactivo mediante procesos electroquímicos.

Las muestras de grafeno a lo largo del trabajo se han caracterizado mediante técnicas de microscopia óptica, SEM, AFM y espectroscopía Raman. THz-TDS se ha utilizado tanto para determinar y estudiar la calidad del grafeno, así como, para evaluar la influencia de la medida de grano en la conductividad en los THz. Además, la conductividad del grafeno se ha medido mediante contactos metálicos micro-fabricados. Estos han permitido medir grafeno a través de varias distancias y, también, a través de un único límite de grano y dentro de islas de grafeno monocapa y bicapa.

La caracterización de las suspensiones de grafeno sintético mediante efecto Tyndall y espectroscopia Raman, después de filtrarlas, confirma la presencia de partículas de grafeno monocapa en las suspensiones acuosas que contienen cantidades mínimas de tensoactivo.

Index

1	Introduction	1
1.1	Brief history of Graphene.....	1
1.2	Structure.....	4
1.2.1	Defects.....	5
1.3	Fabrication methods	8
1.3.1	Top down approach	8
1.3.2	Bottom up approach	10
1.3.2.1	Chemical Vapor Deposition (CVD).....	11
1.3.2.2	Transfer	18
1.3.2.3	Large scale CVD	20
1.4	Structural and morphological characterization	21
1.4.1	Number of layers.....	22
1.4.2	Grain size	24
1.5	Properties	29
1.5.1	Mechanical properties	29
1.5.2	Thermal properties.....	30
1.5.3	Electrical properties	31
1.6	Optoelectronic properties.....	33
1.6.1	Influence of grain size	34
1.7	Forms of graphene and applications.....	37
1.7.1	Forms of graphene	37
1.7.2	Potential applications.....	39
1.7.2.1	Additives.....	41
1.7.2.2	Conductive inks	41
1.7.2.3	Anticorrosion and impermeable coatings.....	42
1.7.2.4	Energy storage.....	42

1.7.2.5	Electronics	43
1.7.3	Products on the market.....	45
2	Objectives.....	49
3	Monolayer graphene synthesis.....	51
3.1	Reactor design.....	51
3.1.1	Fixed furnace.....	51
3.1.2	Sliding furnace.....	53
3.2	Graphene transfer.....	56
3.3	Monolayer growth.....	58
3.4	Determining conditions for monolayer graphene growth.....	61
3.4.1	Electropolishing.....	63
3.4.2	Growth on electropolished copper	66
4	Graphene grain size.....	71
4.1	Photocatalytic oxidation of copper: preliminary results.....	71
4.2	Photocatalytic oxidation of copper: method development.....	75
5	Grain size control	85
6	Graphene characterization.....	97
6.1	Terahertz-time-domain-spectroscopy (THz-TDS).....	97
6.1.1	Comparison with other CVD graphenes and substrates	99
6.1.2	Influence of grain size on THz conductivity.....	102
6.2	Physical electrical measurements	106
7	Synthetic graphene suspensions.....	115
7.1	PVD copper on quartz	116
7.2	High area copper substrates	121
7.3	CVD graphene suspensions	129
8	Overall discussion.....	139
9	Conclusions	145
10	Bibliography	147

11	Annex 1: Communications and publications.....	159
11.1	Communications	159
11.2	Publications	159
11.3	Publications in preparation	159
12	Annex 2: Sliding furnace parts list	161
13	Annex 3: Optimal methodologies.....	163
13.1	Copper electropolish	163
13.2	Graphene growth	164
13.3	Ferric Chloride transfer method.....	165
13.4	Bubbling transfer method	166

List of abbreviations

1D	One dimension
2D	Two dimensions
3D	Three dimensions
AFM	Atomic Force Microscope
APCVD	Atmospheric Pressure Chemical Vapor Deposition
CVD	Chemical Vapor Deposition
DF-TEM	Dark Field – Transmission Electron Microscope
EBS	Electron Backscatter Diffraction
GO	Graphene Oxide
J_{Me}	Methane flow
LPCVD	Low Pressure Chemical Vapor Deposition
MFC	Mass Flow Controller
PET	Polyethylene Terephthalate
P_{Me}	Partial pressure of methane
PMMA	Poly(methyl methacrylate)
R2R	Roll to Roll
rGO	Reduced Graphene Oxide
SDBS	Sodium dodecylbenzenesulfonate
SDS	Sodium dodecyl sulfate
STM	Scanning Tunneling Microscope
T	Temperature
TEM	Transmission Electron Microscope
THz-TDS	Terahertz Time Domain Spectroscopy

List of Tables

<i>Table 1-1 Mechanical properties of some common materials ⁶⁹</i>	30
<i>Table 1-2 Thermal conductivity of some common materials ⁷²</i>	31
<i>Table 1-3. Technology Readiness Level (TRL) for graphene ¹⁰⁶</i>	40
<i>Table 3-1. Acronym explanation</i>	51
<i>Table 3-2. Acronym explanation</i>	53
<i>Table 3-3. Reaction stages using the sliding furnace with typical gas flows used</i>	55
<i>Table 3-4. Electropolishing reactions for each electrode</i>	63
<i>Table 4-1. Description of samples used in this study</i>	77
<i>Table 4-2. Comparative results for all three graphenes obtained through ASTM and image analysis, showing average size and standard deviation for the latter. The number of grains used in the calculation is also shown. All sizes are expressed in μm.</i>	82
<i>Table 5-1. Summary of the gaps and temperatures used</i>	86
<i>Table 6-1. Samples used in this part of the study. Sample S_5 is sourced from our graphenes</i>	99
<i>Table 6-2: Conductivities for all three samples at 1 THz and 2.5 THz and compared with graphene conductivities obtained in a previous study</i>	105
<i>Table 6-3. Results for sample CNM-2</i>	112
<i>Table 7-1. Copper substrates used</i>	121
<i>Table 7-2. Combination of methane percentage and temperature used for each of the substrates. Growth time is set to 10 minutes</i>	122
<i>Table 7-3. Average grain size</i>	128
<i>Table 12-1. Standard ISO-KF parts for the CVD reactor</i>	161
<i>Table 12-2. Components of the sliding furnace structure</i>	162

List of Figures

Figure 1-1. Differences between diamond, left, and graphite.....	1
Figure 1-2. Scheme illustrating the possible evolution from graphene to fullerenes, nanotubes and graphite, from left to right ³	2
Figure 1-3. Number of graphene publications by year using SciFinder ⁷ data until 22 of December 2016. .	3
Figure 1-4. Carbon-carbon bonds in a graphene sheet.	4
Figure 1-5. Scanning tunneling microscopy (STM) of a single-crystal graphene grain on Cu. (b,c,d) represent magnifications marked on image (a). Structure is consistent on all 3 areas and although it is not marked on these images authors calculated separation between carbon atoms at 1.4Å ⁸	4
Figure 1-6. Types of graphene edges (a) armchair (b) Zigzag ⁹	5
Figure 1-7. Representation of graphene point defects: (a) single vacancy, (b) double vacancy, (c) adatom, (d) metal substitution ¹⁰	6
Figure 1-8. Representation of 1D defects in graphene as calculated by O.V. Yazyev ¹¹ . (a, b, c) represent dislocations while (d,e) represent Large-Angle Grain Boundaries.....	7
Figure 1-9. Representation of both approaches to graphene fabrication.	8
Figure 1-10. Micromechanical method: (a) Adhesive tape attached to a 3D graphite crystal so it peels of the top layers (b). This process is repeated until few layers are attached to the tape. Finally (c) the tape is pressed to the target substrate and (d) upon peeling of bottom layer is left on the substrate ¹²	8
Figure 1-11. Starting with a SiC wafer – left image – results on graphene after heating – right image –. In this case final graphene is bilayer with a buffer layer underneath showed with a dashed line ²¹	10
Figure 1-12. Graphene synthesized on copper. (a, b) SEM images on copper showing typical characteristics of this graphene. Clearly visible graphene on SiO ₂ coated Si wafer (c) and on top of glass (d) ²⁸	12
Figure 1-13. Effect of Temperature (T), methane flow (J_{Me}) and methane partial pressure (P_{Me}). Image on the right show how two combinations of these three factors influence graphene growth ²⁹	13
Figure 1-14. Left, optical images of graphene in its initial nucleation stages after transferring to SiO ₂ /Si wafer from copper substrate. Right, Nucleation clusters following copper grain boundaries and scratches ³¹	13
Figure 1-15. Rows show increasing H ₂ :CH ₄ ratios from top to bottom ³²	14
Figure 1-16. Right, SEM image of graphene nucleation on different copper orientations. Left and center, EBSD results that determine copper orientation ³³	14
Figure 1-17. Copper Vapor Pressure vs temperature ³⁴	15
Figure 1-18. Full copper enclosure for improving graphene growth ³⁶	16
Figure 1-19. Growth set-up to minimize loss of copper during graphene growth on silicon wafers ³⁷	17
Figure 1-20. Uniform graphene domains, left shows 2.3mm grain grown in 2012 ³⁸ , right centimeter scale domains ⁴¹	17

Figure 1-21. Simplified schema for a typical graphene transfer.....	18
Figure 1-22. Typical bubbling transfer set-up ⁴⁵	19
Figure 1-23. Samsung's roll-to-roll method. From left to right, tubular quartz CVD reactor, roll to roll transfer process and final transferred product ⁵	20
Figure 1-24. Sony's roll-to-roll process. Left shows the process: (a) continuous reactor with Joule effect heating, (b) continuous coating, (c) spray etching of copper layer, (d) final result. Right shows final result: (e) optical image after oxidation where red equals no graphene, (f) SEM image showing non-continuous graphene ⁶	21
Figure 1-25. Light transmittance of graphene and bilayer ⁴⁷	22
Figure 1-26. Graphene on top of silicon wafers coated with different thicknesses of SiO ₂ . (a) shows the optimal case off 300nm of SiO ₂ and white light, (b) same sample but irradiated with green light and (c) 200nm of SiO ₂ and white light ⁴⁸	22
Figure 1-27. Typical spectra for a monolayer graphene with the three peaks that define it.	23
Figure 1-28. Raman spectra from graphene to graphite ⁵²	24
Figure 1-29. Top left to right: STM ⁵⁴ image and TEM ⁵⁵ image of a graphene grain boundary. The colored image is the result of DF-TEM ⁵⁵ where each color represents a different grain orientation.	25
Figure 1-30. Copper/ graphene samples after oxidation using thermal and H ₂ O ₂ treatment. From left to right, fully covered, partially covered and bare copper samples ⁵⁸	26
Figure 1-31. YU method of permanganate assisted oxidation. (a,b) under-oxidized samples, (c) optimal oxidation with grain boundaries revealed as dotted lines and (d) over-oxidized sample ⁵⁹	26
Figure 1-32. (a) Schematics of Duong's method. Samples of graphene on copper (b) before oxidation, (c) after oxidation. (d) SEM and (e) AFM images of oxidized copper. Note the very thin dotted lines that represent grain boundaries and the dark spots that represent either graphene defects or copper foil impurities ⁵³	27
Figure 1-33. (a) Schematics for Cheng's method. Optical (b) and SEM (c) image of the same area after the oxidation process ⁶⁰	28
Figure 1-34. Using AFM technique in order to measure graphene's mechanical properties ⁶⁶	29
Figure 1-35. Set-up for thermal measurements on suspended graphenes ⁷⁰	30
Figure 1-36. Typical gold contacts for graphene. Build using lithography ⁷⁷	32
Figure 1-37. THz-TDS typical response for graphene. Left shows the temporal response in picoseconds and right, the frequency response after FFT.....	33
Figure 1-38. Schematics for Nonequilibrium Molecular Dynamics for simulating thermal transport in graphene ⁸⁸ , (b) shows the whole range of structural defects studied.....	35
Figure 1-39. Graphene tears crossing grain boundaries and folds observed by TEM ⁹²	36
Figure 1-40. Classification grid for the nomenclature of different graphene types. The axis represents the number of graphene layers, the carbon/oxygen (C/O) ratio and the average lateral dimensions ¹⁰⁵	37
Figure 1-41. Circuits printed on paper using graphene inks ¹¹²	42
Figure 1-42. Schematics of a Li-Ion rechargeable battery with an anode improved with graphene ¹¹⁶	43

Figure 1-43. Basic structure of a graphene barristor ¹¹⁹	44
Figure 1-44. Fully bendable and transparent working heart monitor (www.icfo.eu , 4/1/2017).....	44
Figure 1-45. Victor TK-9000 badminton racket with multi-layer graphene (www.victorsport.com , 4/1/2017).	46
Figure 1-46. Left, first HEAD skis with graphene ¹²⁵ . Right, Graphene XT racket ¹²⁶	47
Figure 1-47. Catlike graphene-containing products. Left, bike helmet. Right, bike shoes. Both have road and mountain bike variations ¹²⁸	47
Figure 1-48. Tires and rims containing graphene ¹²⁹	48
Figure 2-1. Scheme of the approach for the production of synthetic particulate monolayer graphene.	49
Figure 3-1. Fixed furnace reactor. Cooling fan was added as a first improvement to control final cooling stages.	51
Figure 3-2. Compression fittings as installed on the reactor.	52
Figure 3-3. Heat cycle of this reactor forcing the cooling using an additional fan, annealing and growth time can be tuned on demand.....	52
Figure 3-4. Final design with only one MFC and sliding heating element.	53
Figure 3-5. Critical components on sliding furnace structure. Top image shows completed structure complete with furnace and reactor. Bottom left shows a detail on the wheel units used and bottom right shows the calibrated 6mm rails.....	54
Figure 3-6. Grey line represents furnace temperature evolution while black line represents sample temperature. Rapid heating and cooling is caused by the furnace being slide to and away from the sample.	56
Figure 3-7. Copper being dissolved in FeCl ₃ . Image on the bottom right shows the PMMA/graphene layer on water after complete copper removal.....	57
Figure 3-8. Left growth for 30 minutes, right growth for 15 minutes.	58
Figure 3-9. Left growth for 15 minutes, right growth for 5 minutes using the fixed furnace with controlled cooling.	59
Figure 3-10. Left growth for 15 minutes, right growth for 5 minutes.	60
Figure 3-11. (a) to (f) images for 5, 10, 15, 20, 25 and 30 minutes respectively after oxidation using H ₂ O ₂ method. Scale bar in 20 μ m for all samples.....	61
Figure 3-12. Raman spectra for all 6 samples. It can be seen that at 5 minutes (a) no graphene can be found and for 10 minutes and more (b-f) monolayer graphene can clearly be observed. Reaction at 25 minutes (e) shows what appears to be multilayer graphene.	62
Figure 3-13. Electropolishing stages. (a) original copper foil, (b) 2 minutes, (c) 6 minutes and (d) 10 minutes. Scale bar in 100 μ m.	64
Figure 3-14. AFM images showing original rolling marks (left) and final electropolished substrate (right). Central SEM image present the copper sample just in the area that touches the liquid substrate, scale bar in 100 μ m.....	65
Figure 3-15. Cross-section of an electropolished copper foil.	65

Figure 3-16. Typical graphene wrinkles grown on electropolished copper.	65
Figure 3-17. Graphene on copper after 20 minutes of growth time. Left, optical image after H_2O_2 oxidation and right, SEM image.	66
Figure 3-18. Graphene on copper after 60 minutes of growth time. Left, optical image after H_2O_2 oxidation and right, SEM image.	67
Figure 3-19. Graphene on copper after 5 minutes of growth time. Left, optical image after H_2O_2 oxidation and right, SEM image.	67
Figure 3-20. SEM images of graphenes grown on electropolished copper during different times. (a-h) correspond to 0.5, 1, 3, 5, 10, 15, 20 and 30 minutes. Scale bar is 30 μm	69
Figure 3-21. Screening of various conditions. (a) 950°C and 30% of methane, (b) 950°C and 10% of methane, (c) 1050°C and 30% of methane, (d) 1050°C and 10% of methane.	70
Figure 4-1. Chronological order for the firsts attempts: (a) bare sample, (b) sample with TiO_2 30 μL drop, (c) after oxidation.	72
Figure 4-2. Graphene/copper sample before (a) and after (b) 120 minutes of photocatalytic oxidation using 0.1% of TiO_2 in water. Scale bar is 100 μm	72
Figure 4-3. SEM image of a Graphene/Copper sample after photocatalytic oxidation. Particles of TiO_2 can be clearly seen on the copper surface, bottom spectra confirm this observation.	73
Figure 4-4. Photocatalytic oxidation on Graphene/copper samples using different TiO_2 concentrations and different times. Scale bar is 10 μm	74
Figure 4-5. Small areas showing graphene grain boundaries. 0.1% TiO_2 and 120 minutes of oxidation is used. Scale bar is 20 μm	74
Figure 4-6. Schematic for the photocatalytic oxidation method.	75
Figure 4-7. Oxidation stages. 30 minutes shows under oxidized sample, 2h represents optimal oxidation with clearly visible graphene grain boundaries and 3h shows the result of over oxidation.	75
Figure 4-8. Evolution of a sample from original (top) to oxidation (bottom) after 2h of irradiation.	76
Figure 4-9. Raman spectra from all samples.	77
Figure 4-10. Both images are related to commercial graphene samples after photocatalytic oxidation. Image (a) is on top of original copper substrate – Sample 1 – as it can be seen that there are areas in which copper is already oxidized prior to treatment. Image (b) shows a similar graphene transferred to a clean and flat substrate – Sample 2 – presenting a much cleaner result. Concentrations of dark areas are due to the transfer process. The scale bar is 10 μm	78
Figure 4-11. Raman spectra of commercial graphene before – original – and after photocatalytic oxidation.	79
Figure 4-12. Results for graphenes made by our group. The rows from top to bottom show Samples 3, 4 and 5. Images (a), (b) and (c) represent SEM images from as-synthesized samples, while (d), (e) and (f) show optical images after photocatalytic oxidation. The scale bar is 10 μm	80
Figure 4-13. Raman spectroscopy mapping from Sample 5 with a 50x objective (both axes in microns). The dark blue spots represent bilayer or multilayer graphene islands; the rest is monolayer graphene.	80

Figure 4-14. AFM image of Sample 4 after photocatalytic oxidation. The profile on the right shows a large dip related to copper grain boundary and two smaller dips on either side that represent graphene boundaries after oxidation.	81
Figure 4-15. Representation of both grain size methods applied on sample 4 (1000x magnification). (a) Lines used for ASTM manual count and, (b) automatically recognized grain boundaries used for image analysis. The scale bar is 10 μm	81
Figure 4-16. Grain size distribution. Images represent distributions and adjusted Gaussian curve for (a) sample 3, (b) sample 4 and (c) sample 5. Image (d) represents the combination of the fitted Gaussian curves.	83
Figure 4-17. Q-Q plot representing sample quantile (grain size) vs. theoretical quantile (normal distribution). From left to right: samples 3, 4 and 5.	83
Figure 5-1. Cross-section of the reactor with applied restrictions.	85
Figure 5-2. CFD simulations of the three restrictions.	87
Figure 5-3: SEM images of graphene on copper using 10% methane and 10 minutes reaction time for different conditions of temperature and gas restriction. Scale bars are 5 μm for every image.	88
Figure 5-4. Graphene grain size measured for conditions with 10% methane and 10 minutes of growth time.	89
Figure 5-5: Raman spectroscopy data for graphene on SiO_2 in all growth regimes.	90
Figure 5-6: Raman spectroscopy mapping of the $I_{2D}:I_G$ ratio for graphene obtained at every condition. The scale bar is set at 5 μm . Color scale goes from 0 (blue) to 4 (red). Raman spectroscopy mapping for 950 $^\circ\text{C}$ "0 mm" gas flow restriction could not be obtained due to lack of optical resolution.	91
Figure 5-7. SEM images of graphene on copper using 30% methane and 10 minutes reaction time for different conditions of temperature and gas restriction. Scale bars are 5 μm for every image.	93
Figure 5-8. Graphene grain size measured for conditions with 30% methane and 10 minutes of growth time.	94
Figure 5-9: SEM images of graphene on copper at 1050 $^\circ\text{C}$ and 10, 40 and 60 minutes reaction time from left to right. Scale bar 5 μm	94
Figure 5-10: Graphene grain size measured for graphene for different reaction times at 1050 $^\circ\text{C}$ and "0 mm" gap.	95
Figure 6-1. Typical THz-TDS set-up. Red line represents incident laser and after split, blue represents probe laser and green pump laser ¹³⁸	98
Figure 6-2. Raman spectroscopy analysis of all the samples. Raman spectra (a) represents monolayer S_1 and S_3 , Raman spectra (c) represents monolayer S_5 while Raman spectra (b) represents bilayer S_2 and S_4	99
Figure 6-3. Typical time response for these samples.	100
Figure 6-4. transmittance to the THz radiation for all the samples.	100
Figure 6-5. Real part of the substrate refractive index.	101
Figure 6-6. Sheet conductivity.	101

Figure 6-7. THz attenuation.....	102
Figure 6-8: Raman spectra for all samples.	103
Figure 6-9: Grain size distributions. (a), (b) and (c) represent samples 1, 2 and 3 respectively with histograms of the real data and adjusted Gaussian curves. (d) is a comparison between the three Gaussian curves.....	104
Figure 6-10: Results for THz-TDS. (a) Untreated temporal response, (b) transmittance, (c) attenuation and (d) conductivity.....	104
Figure 6-11. Silicon wafers with germanium alignment marks.	106
Figure 6-12. Transferred samples. Left shows sample CNM-1 with the edge of the graphene covered area. Right shows sample CNM-2 with clearly separated graphene grains and marks the ones used for characterization.....	107
Figure 6-13. Raman spectroscopy mappings for 100x50 μm areas corresponding to CNM-1. 2D/G ratio color scale is shown next to the mapping image.....	107
Figure 6-14. AFM analysis of sample CNM-1.....	108
Figure 6-15. Contacts build on continuous monolayer graphene. Left shows groups of 4 contact pads with gaps between them of 5, 10, 25 and 50 μm . Right shows pairs of contact pads with separations of 5, 10, 25, 50 and 100 μm	109
Figure 6-16. Mean sheet resistance against distance for sample CNM-1.	110
Figure 6-17. Raman mapping of individual graphene grains of sample CNM-2.....	110
Figure 6-18. AFM analysis of an individual graphene grain in sample CNM-2.....	111
Figure 6-19. Contacts on sample CNM-2 across: (a) monolayer graphene, (b) monolayer graphene and across one grain boundary, (c) bilayer graphene.	112
Figure 7-1. Range of copper substrates used.	115
Figure 7-2. Original aspect of PVC coated quartz slides. Scale bar on micrographs is 100 μm	116
Figure 7-3. Profilometry analysis of the interphase between quartz and copper.....	117
Figure 7-4. AFM image of the PVD Copper surface and a corresponding profile for reference.....	117
Figure 7-5. Copper PCV on quartz after annealing at 950°C for 15 minutes. Scale bar on micrographs is 100 μm	118
Figure 7-6. Quartz slide after 15 minutes graphene growth. Scale bar on micrographs is 100 μm	119
Figure 7-7. SEM images of cross-sections of PVD copper on quartz. (a) Original copper layer, (b) and (c) after graphene growth. Scale bars are 10 μm for image (a) and 40 μm for images (b) and (c).....	120
Figure 7-8. Copper substrates used.	121
Figure 7-9. Graphene grown with 30% CH ₄ and 950°C.....	123
Figure 7-10. Graphene grown with 30% CH ₄ and 1050°C.....	124
Figure 7-11. Graphene grown with 10% CH ₄ and 950°C.....	125
Figure 7-12. Graphene grown with 10% CH ₄ and 1050°C.....	126
Figure 7-13. Foam surface: (a) original, (b) electropolished, (c) after thermal treatment.	127

<i>Figure 7-14. Sample on copper foil at 1050°C and 10% of methane. Left SEM image from before oxidation and right, optical image of the same sample after oxidation.</i>	<i>128</i>
<i>Figure 7-15. Falcon tube set-up for clean electrochemical graphene transfer directly onto solution.</i>	<i>130</i>
<i>Figure 7-16. Tyndall effect on graphene suspensions. (a) MiliQ® water, (b) Original NaOH solution, (c) blank and (d-f) graphene suspensions.</i>	<i>130</i>
<i>Figure 7-17. Copper wire before and after electrochemical transfer of graphene.</i>	<i>131</i>
<i>Figure 7-18. Filtered samples (a-b) using 0.25M NaOH as electrolyte.</i>	<i>132</i>
<i>Figure 7-19. Filtered samples (a-b) using 0.25M NaOH with 0.1 mM of SBDS as electrolyte.</i>	<i>133</i>
<i>Figure 7-20. Copper microparticles on top of filtered graphene flakes. Spectrums 1 and 3 on the right clearly show the copper nature of these particles.</i>	<i>134</i>
<i>Figure 7-21. Filtered GO and r-GO and their corresponding Raman spectra.</i>	<i>135</i>
<i>Figure 7-22. Raman spectra of a graphene flake deposited on SiO₂/Si wafer.</i>	<i>136</i>
<i>Figure 7-23. Graphene grown on copper wire using 10% methane, 1050°C and 30 sccm of gas flow. Left shows a 5 minute grown graphene and right a 10 minutes one.</i>	<i>136</i>
<i>Figure 7-24. SEM of filtered graphenes from Figure 7-23. Left shows 5 minute grown graphene and right a 10 minutes one.</i>	<i>137</i>
<i>Figure 8-1. Raman spectra for filtered graphene suspensions. (a) shows the spectra for synthetic graphene flakes while (b) presents commercial rGO flakes.</i>	<i>142</i>
<i>Figure 8-2. SEM image of a monolayer synthetic graphene flake on top of a Teflon® filter.</i>	<i>143</i>
<i>Figure 8-3. SEM image of a monolayer synthetic graphene flake on top of a Teflon® filter.</i>	<i>143</i>

1 Introduction

1.1 Brief history of Graphene

Carbon is a well-known chemical element that presents many different allotropes, due to its known sp , sp^2 and sp^3 hybridizations and the capacity to form σ and π bonds. Some of these carbon forms are present in nature and are widely used such as diamond and graphite. While diamond is formed by a mesh of highly organized carbon atoms with 3D interactions, graphite is composed by stacked thin sheets of carbon atoms (see Figure 1-1).

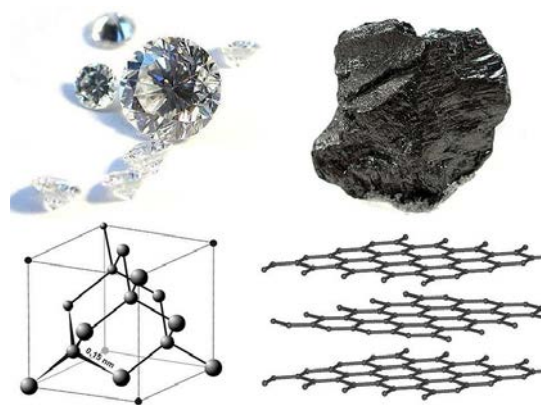


Figure 1-1. Differences between diamond, left, and graphite.

Studies related to the layered structure of graphite can be tracked as far back as 1859 when thermally reduced graphite oxide showed a highly lamellar structure. But it wasn't until 1916 when the structure of graphite was resolved by means of X-ray powder diffraction proving that it is composed of millions of one atom thick layers of carbon atoms. In 1947¹ the existence of these monolayers served as the basis for the theoretical calculation and understanding of graphite electronic properties. One year after – in 1948 – stacks of few graphite monolayers were observed in a Transmission Electron Microscope (TEM) confirming its existence and its completely symmetric hexagonal lattice. It was believed that the monolayer would be unstable at room temperature as it would crumple to form a 3D structure but it didn't stop several efforts to obtain it. Chemical Vapor Deposition (CVD) and exfoliation methods were improved to produce thin graphite on Nickel (1970's) and stacks around 50 layers thick (1990's). During 1994 IUPAC decides to include graphene as an official way to refer to the one atom thick carbon layer.

It was not until 2004 when Konstantin Novoselov and Andre Geim ² managed to finally isolate the graphene monolayer by repeatedly peeling bulk graphite with an adhesive tape. The method is known as micromechanical cleavage or Scotch tape method, for the brand of adhesive tape used. Graphene crystallites were then transferred to silicon wafers coated with nanometric layers of silicon dioxide and the first properties and characteristics of this material were reported. Geim and Novoselov then described graphene as "the mother of all graphitic forms"³ (see Figure 1-2). This purely two-dimensional material can be: (i) bent to form spheres called fullerenes (referred to as 0D), (ii) folded to form tubes of nanometer dimension called carbon nanotubes (referred to as 1D); (iii) stacked to what is known as graphite (referred to as 3D). The boundary between this 2D material and its 3D counterpart is usually established at 100 layer stack but for graphene it is reduced to 10^4 . Amazingly, it has been possible to obtain graphene strips – or nanoribbons – by cutting and unfolding carbon nanotubes.

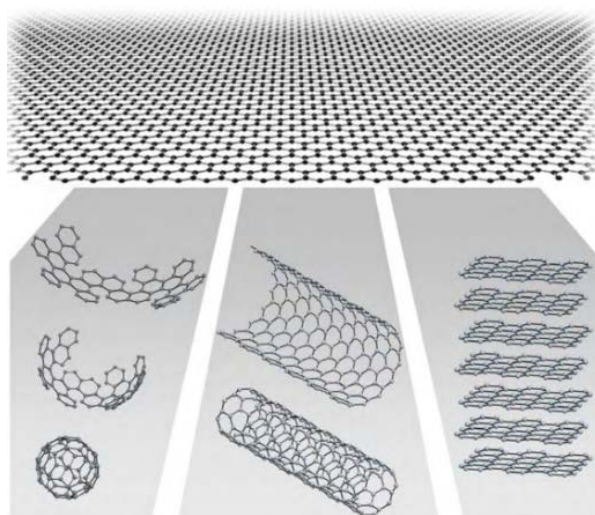


Figure 1-2. Scheme illustrating the possible evolution from graphene to fullerenes, nanotubes and graphite, from left to right ³.

From the beginning, graphene showed incredible properties being the first purely 2D material ever isolated and produced, flexible, transparent, arguably the best electrical and thermal conductor ever discovered and many times stronger than steel. Those first studies with graphene showed that, amazingly, it is stable at room temperature and can be manipulated with relative ease which translates in many potential applications for this material. All these discoveries translated in Geim and Novoselov receiving the Nobel Prize in physics in 2010 for their study "Electric Field Effect in Atomically Thin Carbon Films" ² and triggered the great hype for this material.

Synthetic graphene was successfully produced on nickel and copper foils using modified CVD methods just 5 years after its discovery, on 2009. The interest on these processes is based on the capabilities of producing large areas of monolayer control its quality and attempt to produce tailor made graphene for specific applications. On this subject Samsung ⁵ and Sony ⁶ target transparent and flexible screens and managed to produce 30in in diagonal and 100m long graphene sheets respectively. Although promising on its results there are many challenges to overcome, especially the amount of graphene that can be produced per batch. By 2016 there are a handful of companies that produce and sell CVD graphene – mostly to research centers and universities – being one of the most notable Graphenea, a San Sebastian based company that was funded in 2010.

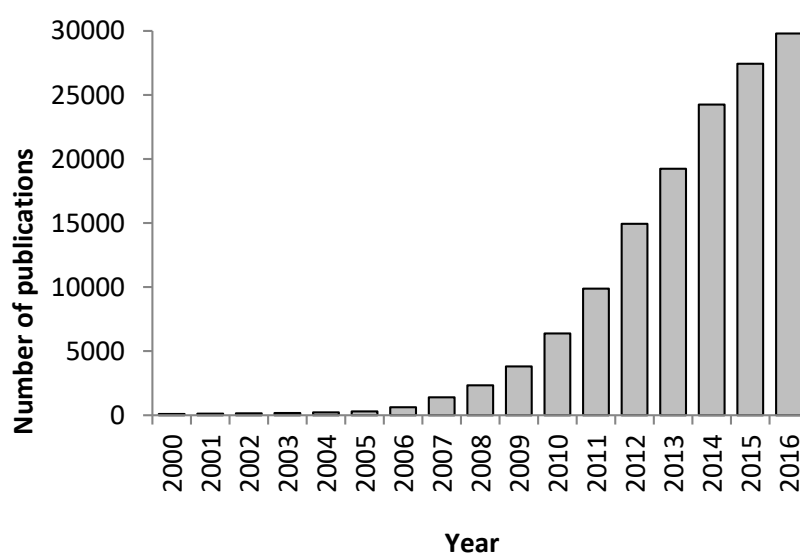


Figure 1-3. Number of graphene publications by year using SciFinder ⁷ data until 22 of December 2016.

1.2 Structure

Graphene is an allotrope of carbon with 2-dimensional properties. Its carbon atoms are arranged on one atom thick sheets following a honeycomb-like, completely symmetrical structure build out of regular hexagons. All carbon atoms in this lattice are sp^2 hybridized which means that three of four valence electrons are σ bonded in plane while one π -bond that is oriented out of plane (see Figure 1-4). As a result, each hexagon is approximately 0.32 nm across and carbon atoms are separated by 0.14 nm⁸ as Figure 1-5 shows.

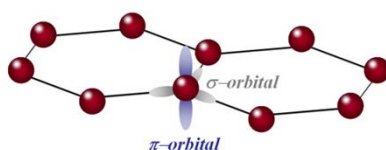


Figure 1-4. Carbon-carbon bonds in a graphene sheet.

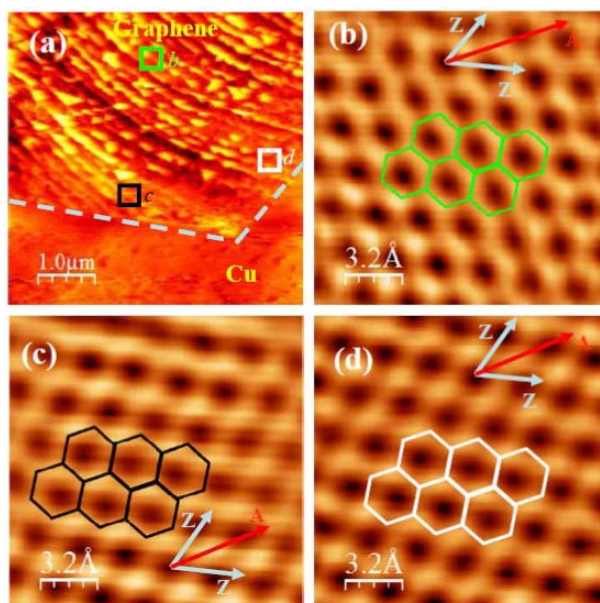


Figure 1-5. Scanning tunneling microscopy (STM) of a single-crystal graphene grain on Cu. (b,c,d) represent magnifications marked on image (a). Structure is consistent on all 3 areas and although it is not marked on these images authors calculated separation between carbon atoms at 1.4 \AA ⁸.

Due to this uniform hexagonal structure edges of monolayers are of particular interest. Firstly, those edges can be depassivated or passivated with hydrogen atoms. Secondly, depending on atom arrangement it can be differentiated between armchair or zigzag configuration, see Figure 1-6. Both factors deeply affect its properties and reactivity due to the amount of atoms that are accessible from outside the monolayer.

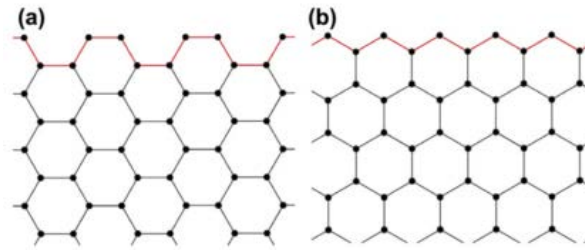


Figure 1-6. Types of graphene edges (a) armchair (b) Zigzag ⁹.

1.2.1 Defects

As Banhart *et al.*¹⁰ say:

“It is the second law of thermodynamics that dictates the presence of a certain amount of disorder in crystalline materials. But it is also due to the imperfection of material production processes that impurities and defects are always present in crystals”.

Graphene is no exception and even in its natural form will present defects that are accentuated when it is synthetically produced. A particular characteristic of graphene is its ability to partially reconstruct its lattice using non-hexagonal rings to attempt to maintain atomic symmetry and, to some extent, lattice integrity.

Being a purely 2D material means that some of the typical defects of 3D materials do not apply so the main defects present in graphene can be grouped in point defects and linear – or 1D – defects. Point defects consist in a punctual inconsistency in the hexagonal lattice in which there is one extra atom or one is missing, the most common are:

- **Single vacancy:** only one atom is missing and usually a ring of 9 and another of 5 atoms are formed.
- **Multiple vacancies:** several neighboring atoms are removed from the lattice and it can translate into holes that the lattice cannot close. One particular case is the double vacancy that translates into arrangements of rings of 5 and 7 atoms.

- **Adatoms:** consist on the addition of an extra atom on the third dimension – *out of plane* – and is usually located on a bridge position between two carbon atoms from the lattice translating on some deformation and loss of symmetry. If the adatom is a carbon atom this can translate into some sp^3 hybridization greatly distorting hexagonal lattice. If the adatom is a non-carbon atom it can be bonded by Van der Waals forces or covalent bonds. One particular property of adatoms is that they can move along the uniform graphene lattice and can also be trapped by other point defects. Adatoms can be exploited by controlling its amount and placement to tune graphene's chemical properties.
- **Substitutional impurities:** some carbon atoms are replaced by foreign atoms, usually boron or nitrogen which results in what is called doped graphene. This process translates into graphene with heavily radically different properties.

Figure 1-7 shows representations for these defects. There are some interesting things to be pointed, while vacancies break symmetry and leave holes do not disrupt the 2D nature of graphene but, on the other hand, adatoms and substitutions distort planarity but for some cases hexagonal symmetry is not broken.

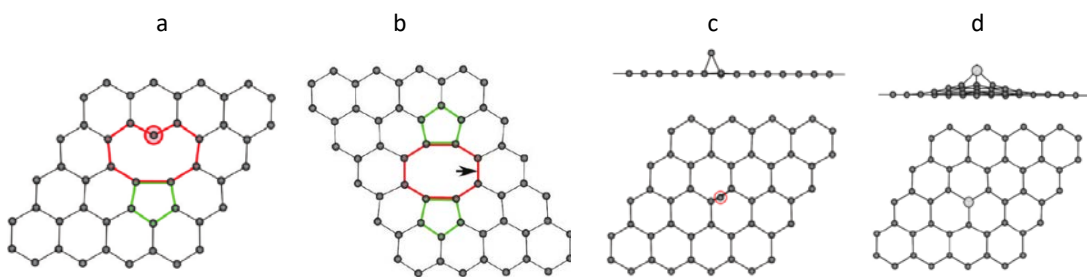


Figure 1-7. Representation of graphene point defects: (a) single vacancy, (b) double vacancy, (c) adatom, (d) metal substitution ¹⁰.

Graphene can also present one dimension defects that expand its area of effect along a line. Most noticeably:

- **Dislocation defects:** these mainly originate on areas with multiple vacancies aligned and the lattice is reconstructed.
- **Grain boundaries:** it's a particular case of dislocation. Especially on CVD processes graphene grows as a polycrystalline material and when these crystals – or grains – merge lines of non-hexagons are formed due to small alignment differences between grains.
- **Edge defect:** basically originate when graphene edges are damaged by introducing or removing carbon atoms and non-hexagonal rings are formed.

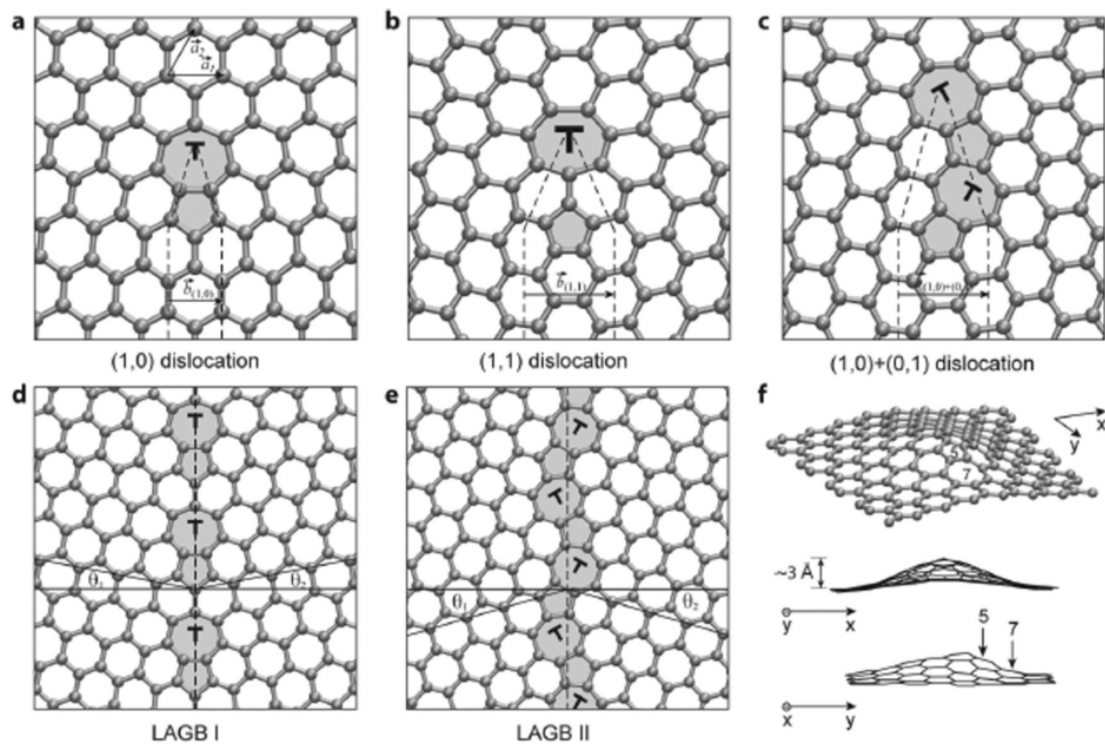


Figure 1-8. Representation of 1D defects in graphene as calculated by O.V. Yazyev¹¹. (a, b, c) represent dislocations while (d,e) represent Large-Angle Grain Boundaries.

It is well known that defects are not completely stationary and can migrate inside the crystal. While some of them – like vacancies – have extremely low mobility others – such as adatoms – present very high mobility across an unperturbed graphene lattice.

1.3 Fabrication methods

As opposed to fullerenes and carbon nanotubes, graphene have been showing an unprecedented ease in its fabrication. All methods can be grouped into two approaches: (i) **Top Down** as it starts from natural carbon sources such as graphite to obtain the monolayer and (ii) **Bottom Up** as it starts from carbonaceous precursors to synthetically form graphene, see Figure 1-9 for a visual representation. Both routes successfully obtain monolayer graphene but present some interesting differences, Top Down will be discussed before as contains the first method ever used.

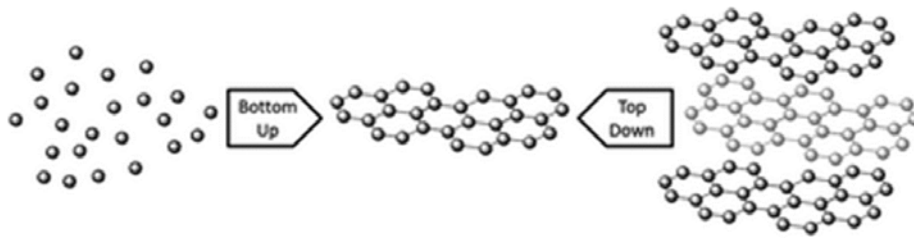


Figure 1-9. Representation of both approaches to graphene fabrication.

1.3.1 Top down approach

Micromechanical cleavage or “Scotch tape method”¹² was the method successfully used by Geim and Novoselov for isolating the first graphene crystallite and it is based on repeatedly sticking and peeling a piece of adhesive tape to a chunk of graphite effectively reducing the amount of layers until few layers and monolayers are obtained. Finally, these graphene crystallites can be transferred to almost any substrate by simply sticking them to the substrate and peeling adhesive tape. This method provides the best quality graphene with almost no defects induced to it if Highly Ordered Pyrolytic Graphite (HOPG) is used as a starting material.

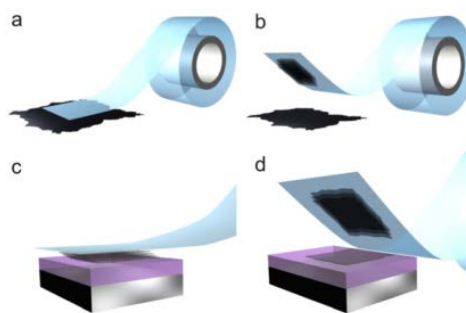


Figure 1-10. Micromechanical method: (a) Adhesive tape attached to a 3D graphite crystal so it peels of the top layers (b). This process is repeated until few layers are attached to the tape. Finally (c) the tape is pressed to the target substrate and (d) upon peeling of bottom layer is left on the substrate¹².

Quickly became clear that mechanically exfoliating graphite it is not a viable option to produce graphene in large quantities as it is extremely time consuming so batch processes using solvents and energy – such as ultrasonication – were adapted to graphene. Direct exfoliation of graphite into graphene suspensions proves to be difficult as it requires a lot of energy in form of ultrasonication and usually results in suspensions with less than a 5% of monolayer graphene^{13,14} and highly damaged graphene flakes. Alternatively, some methods use electrochemical processes to carefully separate the graphene layers¹⁵ that prove to be scalable and cost effective but induce some oxidation in the carbon lattice. Graphene suspensions in water are not very stable and require some sort of surfactant¹⁶ although recently it has been demonstrated that graphene can be suspended in degassed water¹⁷.

To reduce the amount of energy needed and increase the output, routes through graphite oxide and graphene oxide (GO) are being exploited. As a first step, graphite is subjected to highly oxidizing conditions that forces the formation of GO and drastically reduces the adhesion between layers, being the Hummer's method¹⁸ the most used and well known procedure. Afterwards, and after mild energy application, GO layers are separated in a controlled fashion, which can lead to almost 100% monolayer. The drawback is that GO is an insulating material and has almost no uses so it must be reduced back to graphene^{19,20} – reduced graphene oxide (rGO) – which presents the same structure of graphene but littered with defects. rGO is prone to agglomerate back to 3D structures, which effectively limits monolayer content of these suspensions to less than a 10%.

All the bulk methods produce large quantities of exfoliated material with almost no control over the size nor the number of layers of exfoliated platelets, which results in suspensions of multilayer graphene or thin graphite. Despite all these issues it represents the preferred method for mass producing graphene as it is very cost effective.

1.3.2 Bottom up approach

This approach is also known as chemical growth and graphene is formed from precursors that contain carbon while removing excess atoms. The goal is to produce high quality graphene over large areas effectively overcoming limitations associated to exfoliation.

A typical case is segregation from silicon carbide (SiC) where wafers of this material are heated to around 700°C under hydrogen atmosphere²¹ with the goal to sublime surface silicon leaving layers of carbon. When it cools down carbon layers crystalize into graphene layers. Although this process can be tuned to produce high quality monolayer graphene it results into this material being stuck into remaining SiC wafer and separating both is almost impossible. As a result, this process is not that used nowadays as most applications require this graphene to be transferred to other substrates.

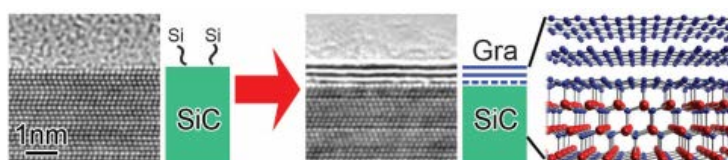


Figure 1-11. Starting with a SiC wafer – left image – results on graphene after heating – right image –. In this case final graphene is bilayer with a buffer layer underneath showed with a dashed line²¹.

Another approach that seems viable for production of graphene of very small size is the Molecular Approach. Here, precursors made of aromatic compounds are chemically combined to form larger polycyclic aromatic molecules and finally, graphene²². These approaches allow to produce small graphene discs with as much as 220 carbon atoms or nanoribbons (3nm x 12nm) with precisely controlled edge configuration. Although this approach allows to produce graphene with precisely located dopants to fine tune its properties it is clearly not very efficient in producing large volume of graphene.

1.3.2.1 Chemical Vapor Deposition (CVD)

From all Bottom-up approaches, CVD is the most widespread. CVD has been used for production of thin films and coatings but it wasn't until 2009 when Queen et al.²³ and Borysiak et al.²⁴ used nickel and copper foil, respectively, to successfully produce monolayer graphene. Both methods used a tubular quartz reactor able to withstand the temperatures in excess of 900°C and work under vacuum. Those two original methods showed that metal substrate plays a crucial role on the reaction as nickel can dissolve carbon to certain extent and form carbides, making it difficult to tune reaction conditions for the fabrication of monolayer graphene as it facilitates multilayer production. On the other hand, copper does not form carbides nor dissolves carbon in its lattice, under the conditions usually used²⁵, so graphene growth is stopped at one or two layers.

There is not much consensus on the precise mechanism followed by graphene growth on copper. It is assumed that the very low carbon solubility on copper limits this growth to a surface-adsorption process²⁶. Thus, methane is adsorbed onto the surface of the copper and then thermally splits into CH_x radicals and even C which recombine to form graphene. Some calculation based studies²⁷ suggest that copper not only limits reaction to its surface but also has the capability of rapidly generating large quantities of CH radicals, making it very effective at producing graphene.

Figure 1-12 shows a typical result for monolayer graphene on copper as obtained in the Ruoff group²⁸. Image (b) shows typical characteristics of these material under SEM: darker spots and steps are typical of graphene growth. The first appear as a result of multilayer graphene areas while the latter are formed during the cooling stage as copper and graphene shrink at different rates²⁸.

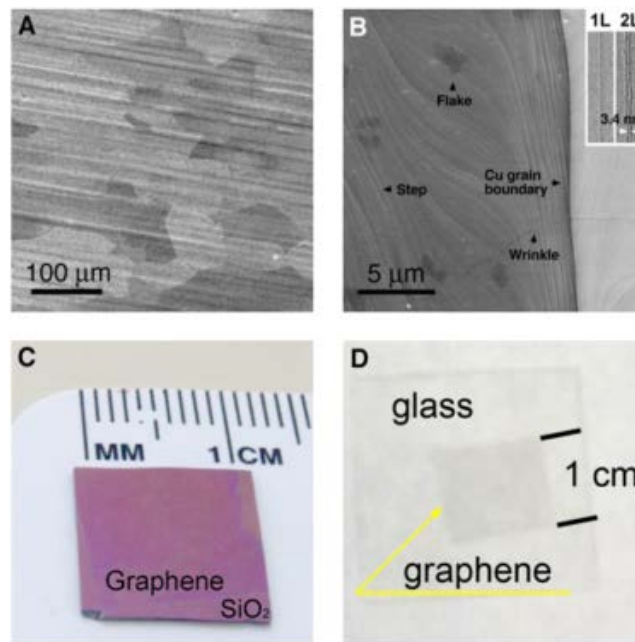


Figure 1-12. Graphene synthesized on copper. (a, b) SEM images on copper showing typical characteristics of this graphene. Clearly visible graphene on SiO₂ coated Si wafer (c) and on top of glass (d) ²⁸.

It is said that CVD graphene presents a lower quality than natural pristine graphene for several reasons. These processes follow a two-stage growth process comprised of a nucleation phase followed by a growth stage that progresses until neighboring grains collide and merge into a continuous layer. As a result, these layers are polycrystalline and because each grain presents some misalignment with its neighbors and when they fuse into a single layer line defects – or grain boundaries – are formed.

Many factors affect nucleation and growth of graphene such as temperature, gas flow, concentration of precursor, copper morphology, crystallographic orientation, and evaporation of growth metallic substrate. Li et al.²⁹ studied the first three factors and tried to establish an optimal recipe for large graphene grain fabrication. Increasing temperature yields lower nucleation densities and faster grain growth while lowering gas flow and concentration greatly hinders nucleation and growth. As Figure 1-13 shows the authors propose a two-step reaction process to maximize graphene grain size. Nucleation must be performed at high temperature with low concentration of precursor and low gas flow to minimize the amount of precursor available to form nuclei. Growth, on the other hand, must be performed at high temperature with more content of precursor and higher gas flows to maximize growth and negate the appearance of new nuclei.

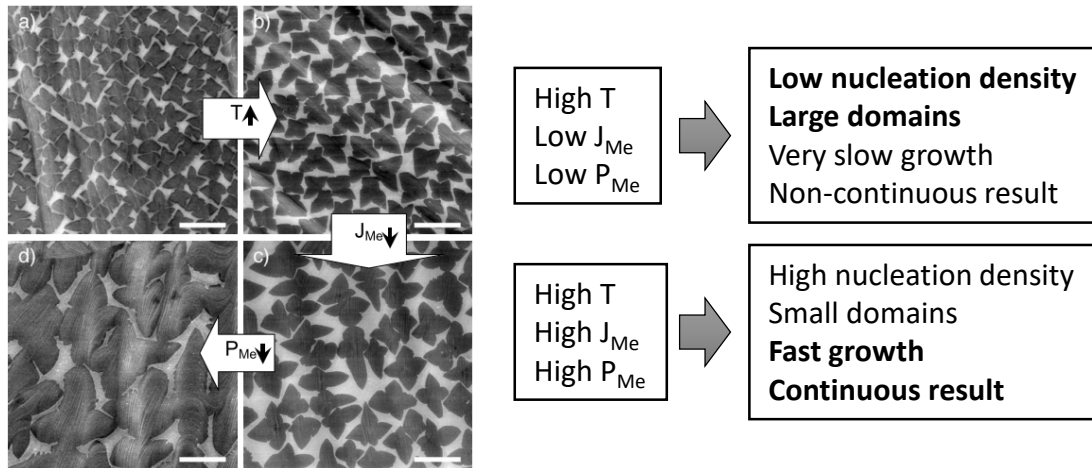


Figure 1-13. Effect of Temperature (T), methane flow (J_{Me}) and methane partial pressure (P_{Me}). Image on the right show how two combinations of these three factors influence graphene growth ²⁹.

All CVD processes to grow graphene on copper use some content of hydrogen mixed with the precursor for various reasons. At first, hydrogen is used to chemically reduce copper oxide from the copper surface and, during graphene growth, it is known to “purify” the final product. Graphene growth is governed by equilibrium between the deposition of new atoms to formed nuclei and etching of defective C-C links³⁰. The content of Hydrogen in combination with temperature, pressure and concentration of precursor can dictate the quality and morphology of formed graphene and, even, if it is possible to obtain a continuous layer.

There are more factors that dictate the quality of CVD graphene. Han et al.³¹ studied influences of copper morphology for the formation of nucleation seeds during initial CVD stages. They showed that the number of nucleation seeds and graphene domain sizes (growth rate) were strongly dependent on copper roughness. Polished copper improves its performance reducing nucleation densities and improves graphene uniformity, as shown in Figure 1-14. The authors also show that superficial defects, or carefully introduced defects such as scratches, act as nucleation clusters.

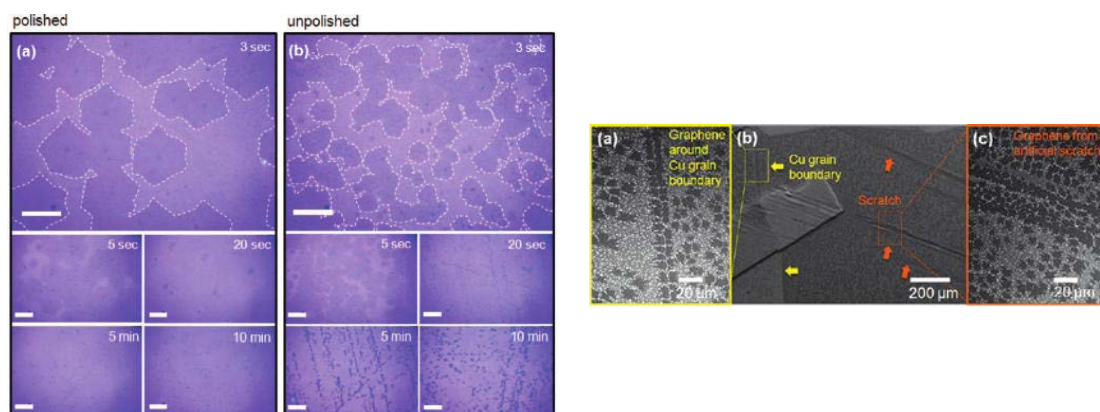


Figure 1-14. Left, optical images of graphene in its initial nucleation stages after transferring to SiO_2/Si wafer from copper substrate. Right, Nucleation clusters following copper grain boundaries and scratches ³¹.

Copper foils are also polycrystalline and graphene does not nucleate nor grow equally on all grains with different crystallographic orientations. Jacobberger et al.³² studied the effect of Cu grain orientation on graphene nucleation by producing mono-orientated copper layers by means of epitaxial growth. They tested three different copper orientations with multiple ratios of $H_2:CH_4$ to prove that in low pressure CVD (LPCVD) graphene tends to nucleate in a dendritic fashion that are symmetrical and regular on top of Cu (100) and became more irregular on Cu (110) and Cu (111). Figure 1-15 shows the dendritic nature of graphene just after nucleation and that increasing $H_2:CH_4$ ratio completely suppresses this dendritic effect and leads to smoother islands. A part from influencing the shape of graphene nucleation copper orientation also has an effect on nucleation density as can be seen in Figure 1-16³³ and it is clear that Cu(111) presents a much higher concentration of nuclei than the rest.

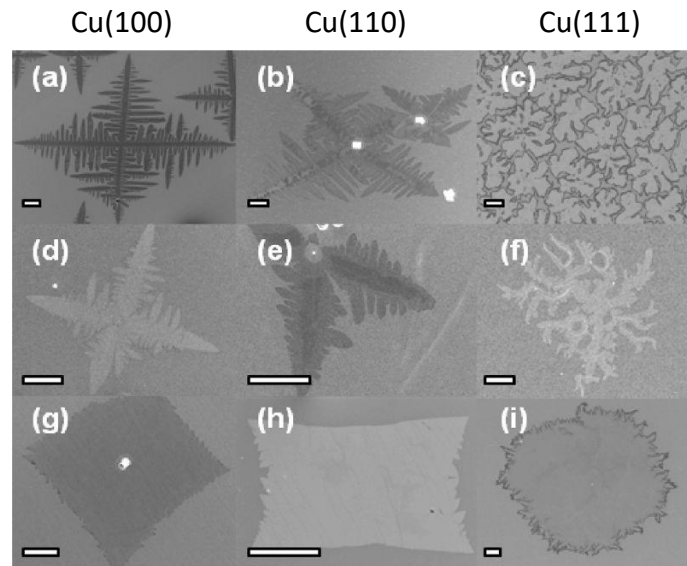


Figure 1-15. Rows show increasing $H_2:CH_4$ ratios from top to bottom³².

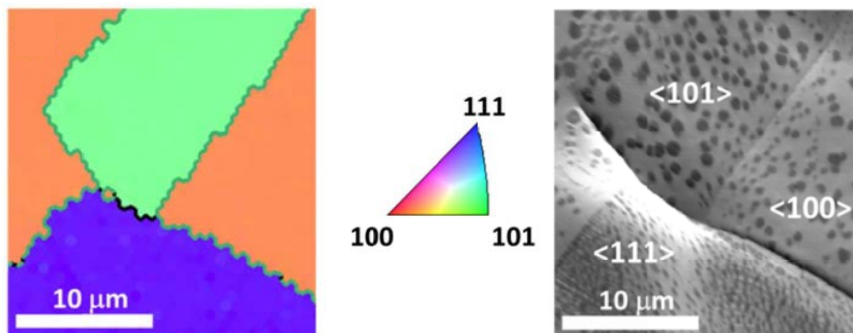


Figure 1-16. Right, SEM image of graphene nucleation on different copper orientations. Left and center, EBSD results that determine copper orientation³³.

Finally, and because CVD processes for graphene are usually performed at temperatures in excess of 950°C and under vacuum, copper is being evaporated. Figure 1-17 presents copper vapor pressure for the typical temperatures for CVD graphene growth ³⁴ and because typical pressures for these processes range from 10^{-3} mbar to 10 mbar it is clear that some copper will be evaporated.

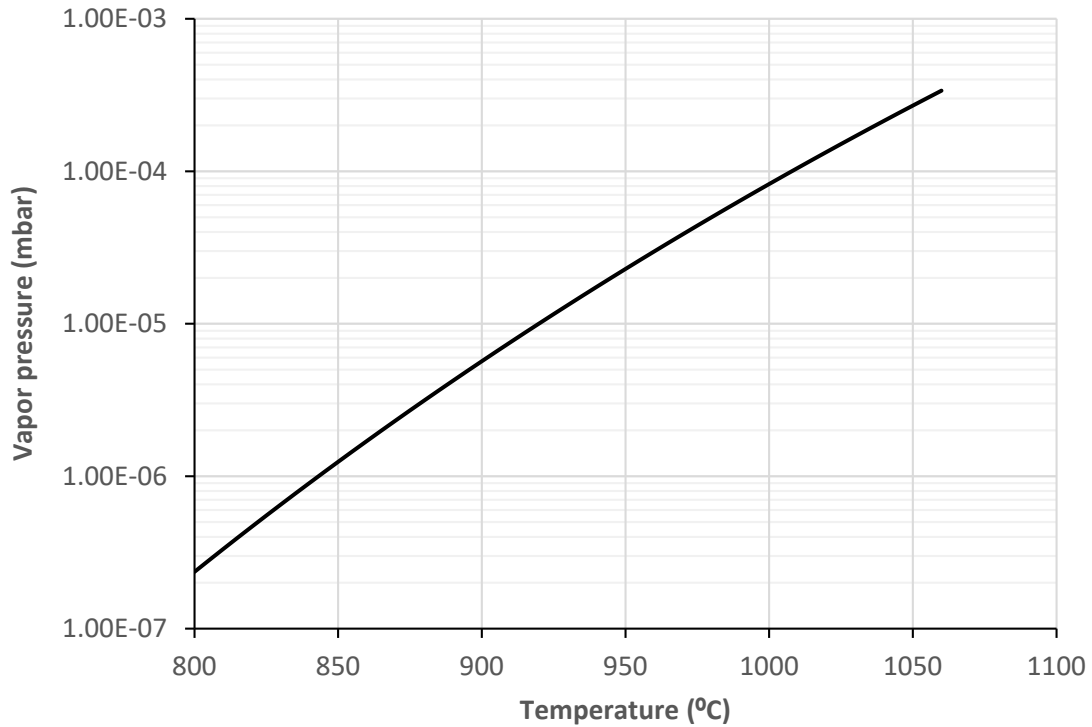


Figure 1-17. Copper Vapor Pressure vs temperature ³⁴.

This evaporation phenomenon is desired during the initial annealing stage in which copper evaporation helps to flatten its surface along with copper oxide reduction and copper recrystallization. During the growth of graphene, this evaporation is known to negatively affect the process. Vlassioug et al. ³³ determined that copper sublimation in LPCVD significantly limits graphene nucleation and suggested it must be minimized or avoided to obtain the best results. Atmospheric pressure CVD (APCVD) appears as the simplest solution to limit copper evaporation but presents a great deal of issues, mainly the difficulty of ensuring an oxygen free environment and having to work with hydrogen and methane within potential explosive conditions. Moreover, these APCVD are limited by the formation of a gas-phase boundary layer that difficult the deposition of carbon atoms on the metallic substrate ³⁵.

Other options inside LPCVD imply some restraint on copper evaporation and mainly imply introducing the sample inside some sort of restriction or enclosure. The simplest and most extended, resorts to folding copper to form an “inside face” and an “outside face”. The outer face evaporates while the inside one it is not clear if it does not evaporate or evaporates and redeposits but results in smoother copper and produces much more homogenous graphene growth. To achieve this effect some groups bend copper foil into a tub shape, but the extreme interpretation is a full copper enclosure developed by the Ruoff group ³⁶, see Figure 1-18. This enclosure not only limits copper evaporation but reduces methane accessibility, which is believed to help improve graphene quality by slowing nucleation and growth. The drawback of these enclosures is that these are not recyclable and must be remade after few reactions if not after each experiment. Also, reaction times tend to extent to many hours, sometimes, in excess of 6 hours.

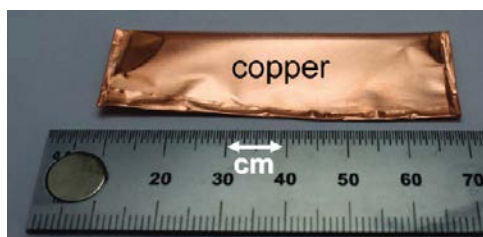


Figure 1-18. Full copper enclosure for improving graphene growth ³⁶.

When working with copper thin films, to grow graphene on whole Silicon wafers coated with thin layers of copper from 0.5 to 1.5 μm this evaporation must be avoided. Most processes rely on APCVD ³⁷ although some attempts have been made in introducing a second silicon wafer close to the copper surface to create an area with high concentration of evaporated copper. Although, copper evaporation is not completely avoided is greatly limited, which allows to use LPCVD with thin films of copper. Figure 1-19 shows a proposed set-up to minimize copper loss, note that both silicon wafers are coated with nanometric layers of silicon oxide that act as a barrier between silicon and copper and avoid the formation of alloys.

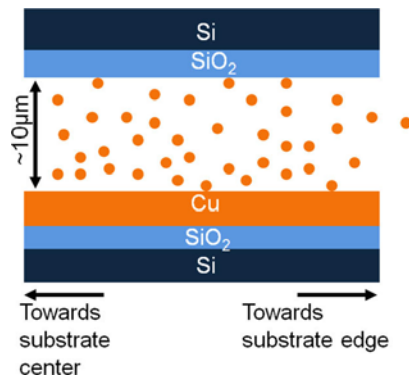


Figure 1-19. Growth set-up to minimize loss of copper during graphene growth on silicon wafers ³⁷.

Several groups are trying to obtain graphene monocrystals as big as possible. By 2012 the largest synthesized single layer graphene area with no defects was 2.3mm ³⁸, see Figure 1-20 left, and several methods for growing on the millimeter scale have been developed. All these methods ³⁹ share very long growing times with low concentrations of methane to ensure low nucleation and slow and homogeneous growth. To further enhance the odds of obtaining monocrystals all these methods use ultra-smooth copper surfaces and even liquid copper ⁴⁰ to reduce even more the nucleation density. If these methodology is taken to the extreme and controlling even the oxygen content inside the reactor, centimeter scale monocrystals can be obtained as Hao *et al.* ⁴¹ reported on 2013, Figure 1-20 right.



Figure 1-20. Uniform graphene domains, left shows 2.3mm grain grown in 2012 ³⁸, right centimeter scale domains ⁴¹.

1.3.2.2 Transfer

All CVD processes on copper or any other metal substrate result in graphene tightly attached to a conductive metal substrate that must be removed in order to fully utilize graphene's properties. These transfer processes are difficult and are prone to damage graphene.

There are two main variants of these methods: dry and wet transfer methods. Dry transfer^{42,43} relies on sticking a polymeric tape that is attached to graphene applying pressure. Polymer/graphene is mechanically peeled from the growth substrate, pressed to the new substrate and, finally polymer is separated from graphene by heating it. These dry approaches are prone to heavily damage graphene in the stage of mechanical release of graphene and the release of the polymer.

Wet transfer methods attempt to overcome the limitations of dry methods by chemically separating copper from graphene. Figure 1-21 shows a simplified representation of the common steps for wet transfer methods.

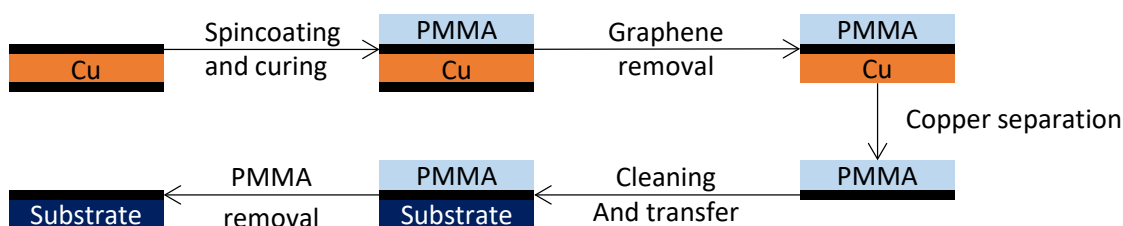
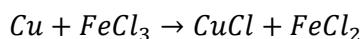
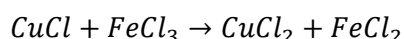


Figure 1-21. Simplified schema for a typical graphene transfer.

The most widespread wet method is based on chemically dissolving copper with a 55% solution of FeCl_3 in water. This solution easily dissolves copper following Reaction 1 and 2, Figure 3-7, but it is not acid enough to affect graphene. This method requires a careful and thorough cleaning of the samples to completely remove residues of ferric chloride and copper chloride. The several steps involved in isolating graphene translate into a method that is tricky and prone to damage graphene during handling. Having said this, applying it carefully allows for transfers with close to no defects induced.

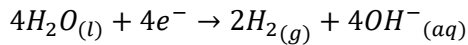


Reaction 1

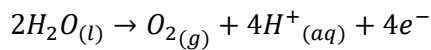


Reaction 2

A wet variant aimed to reuse the substrate has also been developed ^{44,45}. The only difference is that metallic substrate and graphene are separated via electrochemical processes. These use a platinum anode and place the sample of copper/metal on the cathode and use NaOH in water as electrolyte. Applying 5V of DC current triggers water splitting with Reactions 3 and 4 happening on the cathode and the anode respectively, according to De la Rosa et al. ⁴⁵. The hydrogen gas is formed in between copper and graphene inducing its release. Metallic substrate can be recovered, cleaned, and reused for graphene growth.



Reaction 4



Reaction 5

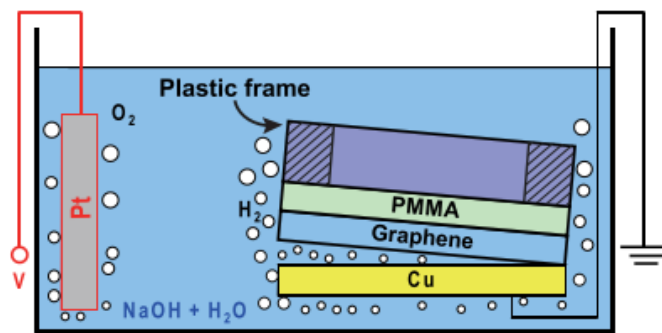


Figure 1-22. Typical bubbling transfer set-up ⁴⁵.

To summarize the wet transfer processes, may proceed as follows:

1. **Spincoating of PMMA:** To support graphene when the metallic substrate is removed.
2. **(not always) Removal of unwanted graphene:** Graphene grows on both sides of the metallic substrate so the unwanted side is removed using and Oxygen plasma or 22% HNO₃.
3. **Copper removal:** FeCl₃ dissolution or bubbling transfer.
4. **Cleaning and transfer:** PMMA/graphene is thoroughly cleaned using water to fully remove FeCl₃ or NaOH residues. After cleaning, it is placed on the final substrate and left to dry.
5. **PMMA relaxation:** the whole sample is heated at 160°C to allow PMMA to soften and release tensions and flatten onto the substrate.
6. **PMMA removal:** PMMA is usually dissolved using acetone or acetic acid if a slower removal is desired.

1.3.2.3 Large scale CVD

To approach CVD production of graphene to the industrial market it is necessary to scale up its production. Several options have appeared using silicon wafers covered with thin films of copper to increase the surface available for graphene growth. Aixtron ⁴⁶ sells commercial machines of plasma enhanced CVD aimed at producing graphene on top of Si wafer up to 4 inches (200 mm) in diameter. These machines are limited by the size of commercially available Si wafers and are not cost effective as these wafers are expensive. To solve this issue, roll-to-roll is being adapted to graphene production.

Roll-to-roll (R2R) is a family of manufacturing techniques involving continuous processing of a flexible substrate as it is transferred between two moving rolls of material. It has been mainly used for applying coatings or printing in a continuous or semi-continuous fashion.

These R2R processes are being adapted for graphene. The first approach was made by Samsung ⁵ and it is based on growing monolayer graphene over large copper sheets inside a tubular reactor and later use a roll-to-roll style process to dry transfer graphene. Figure 1-23 show this transfer process that is based on a transfer release tape that adheres to graphene using pressure and releases it using heat and, as a result, it yields graphene with lots of defects.

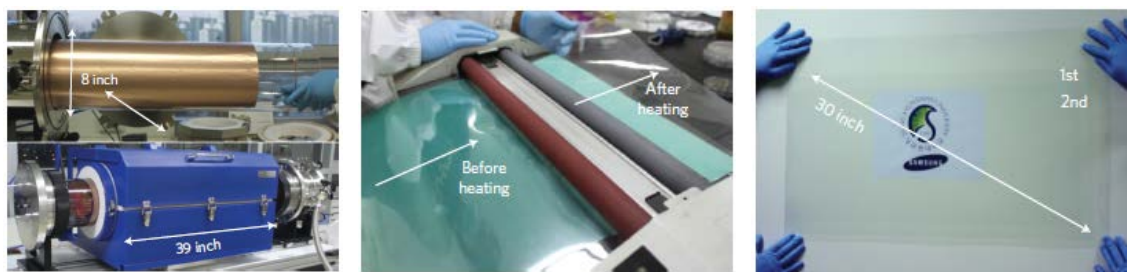


Figure 1-23. Samsung's roll-to-roll method. From left to right, tubular quartz CVD reactor, roll to roll transfer process and final transferred product ⁵.

On the other hand, Sony ⁶ uses roll-to-roll across the whole process, including growth, and managed to obtain 100 m of graphene. As Figure 1-24 shows, this process uses a continuous reactor and uses Joule effect to heat up only a small portion of the copper strip by flowing high current through it. Once graphene is synthesized the roll is extracted from the vacuum chamber that acts as a reactor and is placed into another roll-to-roll set-up that transfers graphene from the copper substrate onto the final PET strip. Although the authors claim they have produced 100m worth of graphene, optical and SEM images prove that this product is comprised of non-continuous graphene with its domains clearly separated.

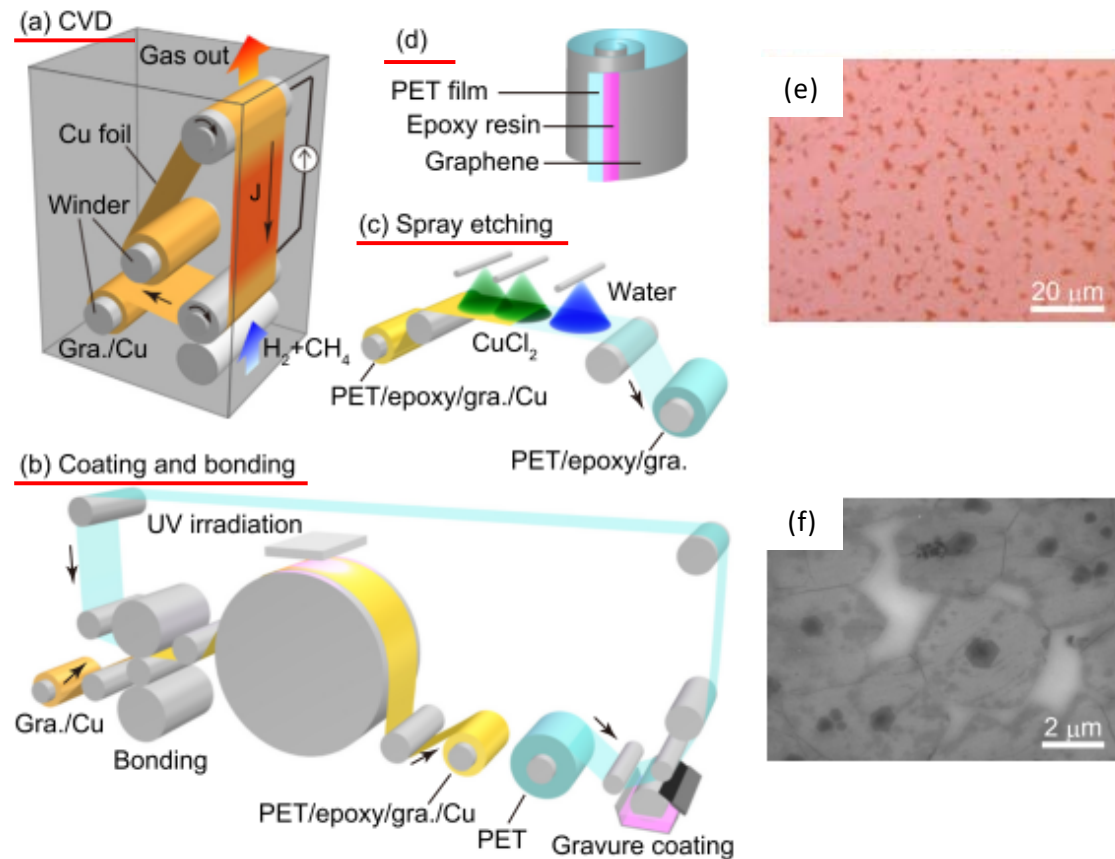


Figure 1-24. Sony's roll-to-roll process. Left shows the process: (a) continuous reactor with Joule effect heating, (b) continuous coating, (c) spray etching of copper layer, (d) final result. Right shows final result: (e) optical image after oxidation where red equals no graphene, (f) SEM image showing non-continuous graphene ⁶.

1.4 Structural and morphological characterization

Graphene only refers to the monolayer of carbon atoms although it appears that is well accepted to refer to few layer stacks as:

- **1 layer:** monolayer graphene
- **2 layer:** bilayer graphene
- **3 layer:** tri-layer graphene
- **Less than 10 layers:** few layer graphene or, simply, multi-layer graphene

This can lead to misconceptions and it is of paramount importance to precisely determine the layer count on each graphene sample. Also, as we already mentioned synthetic methods tend to produce polycrystalline layers of graphene that need a more in-depth characterization, mainly the size of the grains. At the moment this PhD is being written, it appears that the sole parameter that marks graphene quality is mostly the number of layers and little to none attention is given to grain size.

1.4.1 Number of layers

Number of layers can be observed optically if graphene is transferred on top of carefully selected substrates. Firstly, obtaining free-standing graphene or placing it on top of a very flat and homogeneous substrate allows to “see” graphene due to the 2.3% of light each layer absorbs⁴⁷, as shown on Figure 1-25.

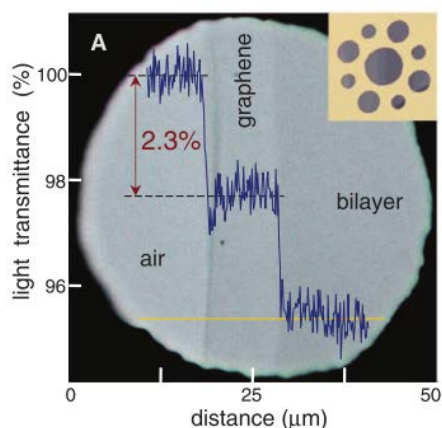


Figure 1-25. Light transmittance of graphene and bilayer⁴⁷.

This can prove to be difficult unless an optimal substrate is used since 2.3% of light is really a low value. It can be solved by transferring graphene onto silicon wafers coated with nanometric layers of silicon dioxide (SiO_2) in which graphene is clearly visible due to increased contrast with the purple background⁴⁸. Moreover, with the appropriate conditions it is possible to visually distinguish the number of layers as it gets progressively more contrasted, or darker. Although, visual methods are a viable option they rely on contrast between the background and graphene or between graphene layers, a more robust method is needed to unequivocally identify the number of layers.

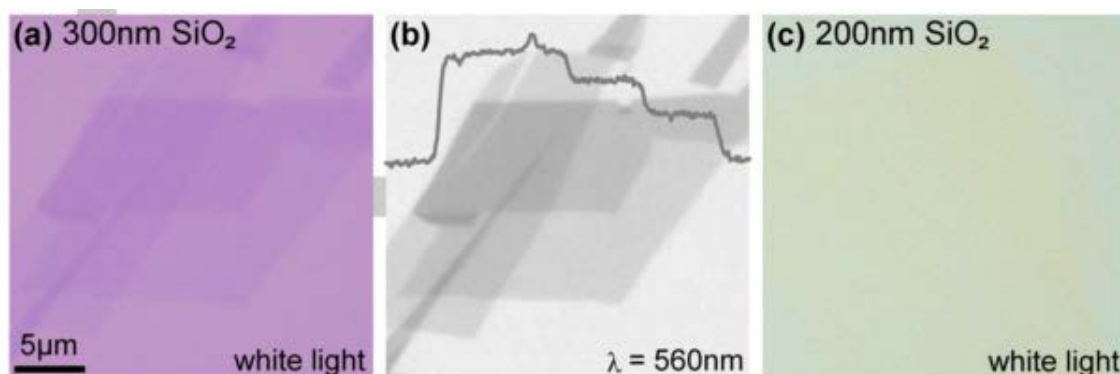


Figure 1-26. Graphene on top of silicon wafers coated with different thicknesses of SiO_2 . (a) shows the optimal case off 300nm of SiO_2 and white light, (b) same sample but irradiated with green light and (c) 200nm of SiO_2 and white light⁴⁸.

The solution was found in Raman spectroscopy. This technique is used to observe vibrational, rotational and other low-frequency modes from the atoms of a material structure⁴⁹. To achieve this effect, Raman spectroscopy irradiates the sample with single frequency radiation, monochromatic light, and detects the small part of radiation that scatters. This scattered light has a slightly different frequency than the incident beam because during the scattering process it is interacting with molecular vibrations and rotations.

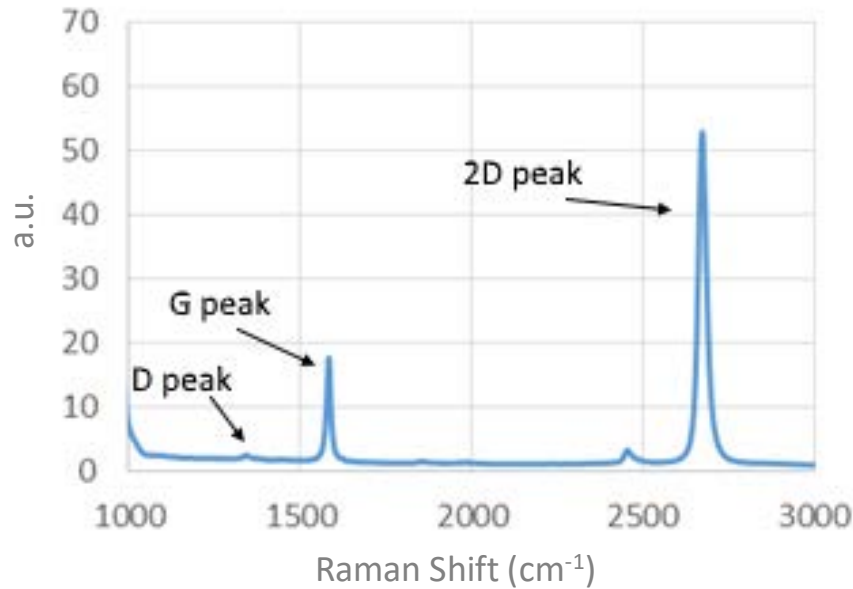


Figure 1-27. Typical spectra for a monolayer graphene with the three peaks that define it.

Raman spectroscopy is extremely useful for characterizing carbon allotropes. For the specific case of Graphene presents a very clean spectrum with only three possible peaks: peak D (1320 cm⁻¹), peak G (1620 cm⁻¹) and 2D (2690 cm⁻¹)^{50,51}. A typical monolayer graphene spectrum presents only a G and a 2D peaks that are sharp and symmetric and with a relation of intensities I_{2D}/I_G larger than 2. The appearance of a small D peak is directly related to the defects present inside the graphene lattice. Figure 1-28 shows a comparison on the spectra from monolayer graphene to graphite where it is clear Raman spectroscopy can unequivocally differentiate the number of layers from a graphene sample.

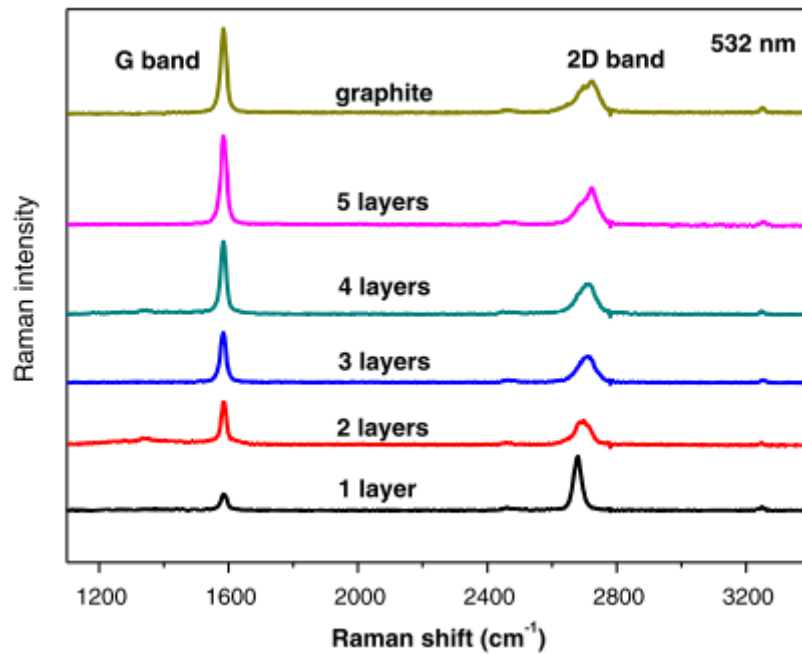


Figure 1-28. Raman spectra from graphene to graphite ⁵².

It must be noted that some combinations of substrate and laser wavelength, incident radiation, are not suitable for identifying graphene as large amounts of fluorescence can be observed and may obscure the graphene signal. An optimal, and preferred, combination is graphene transferred to SiO₂ coated Si wafers and 532 nm green laser excitation.

1.4.2 Grain size

Grain size is presenting more challenges than the number of layers because direct grain size measurement is not possible due to the nanoscale nature of grain boundaries ⁵³. There are two main options to study and measure grain size, either by using techniques capable of atomic resolution or by making grain boundaries observable with traditional microscopy.

Atomic resolution methods rely on directly observe graphene's atomic structure and locate defects and grain boundaries. STM ⁵⁴, TEM ⁵⁵ and DF-TEM ⁵⁶ are techniques able to reach atomic resolution and allow for the detection of structural defects and grain boundaries, see Figure 1-29 for an example of these techniques. All these share the same limitations; samples have to be transferred from the growth substrate to an ultra-smooth substrate for STM on TEM grids. These transfer processes are prone to damage graphene. Moreover, observation areas are limited to few nanometers or microns, which avoids the possibility of statistically studying grain size.

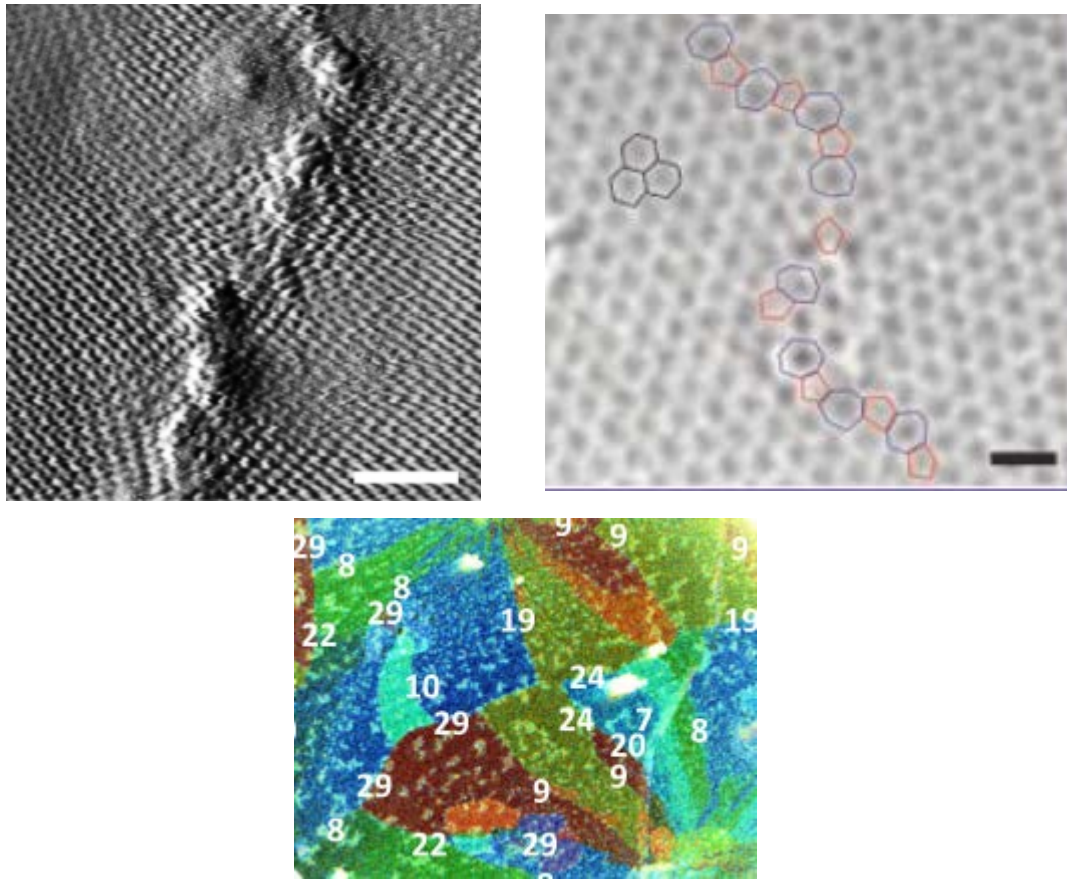


Figure 1-29. Top left to right: STM ⁵⁴ image and TEM ⁵⁵ image of a graphene grain boundary. The colored image is the result of DF-TEM ⁵⁵ where each color represents a different grain orientation.

In order to enhance the detection of grain boundaries, Nemes-Incze et al. proposed a method in which graphene is transferred to atomically flat mica and thermally oxidized in air ⁵⁷. Then, defects and grain boundaries can be observed using AFM, which greatly limits the detection area to a few micrometers. Using several AFM mappings of different areas of the same samples, the authors were able to generate a histogram of the characteristic grain size. Up to this point, all techniques are limited to small analysis areas, which translates to grain sizes well under 1 micrometer.

To improve on these, other methods are being developed that use selective oxidation of copper through graphene defects or uncovered areas and subsequent observation under an optical microscope. Jia *et al.* ⁵⁸ described a method in which copper is oxidized combining a thermal treatment with a chemical oxidation step using H₂O₂. This process induces a quick oxidation of the copper substrate and the presence of graphene protects it from oxidizing. As a result, exposed copper turns into a red-oxide color while graphene covered areas remain in the original copper color and are clearly contrasted for optical observations, see Figure 1-30. This method is very effective at revealing the presence of graphene after a CVD synthesis on copper but not capable of making its microstructure visible.

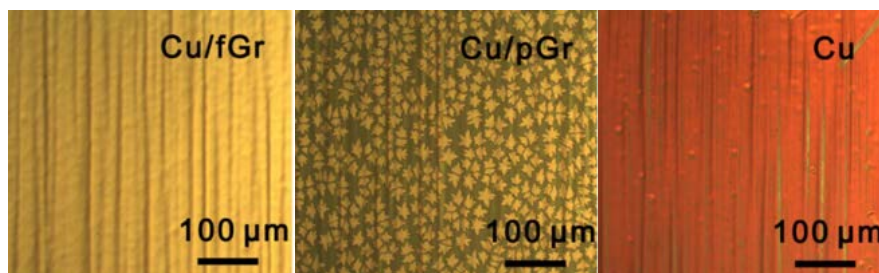


Figure 1-30. Copper/ graphene samples after oxidation using thermal and H_2O_2 treatment. From left to right, fully covered, partially covered and bare copper samples ⁵⁸.

Similarly, Yu *et al.* ⁵⁹ combines exposition to basic permanganate solutions followed by controlled heating in air. Precise heating times allow grain boundaries to be revealed as agglomerations of dark copper oxide spots, see in Figure 1-31. It appears that permanganate solution permeated through defects in the graphene lattice and remains there after cleaning. Following heating triggers the oxidation of copper in contact of permanganate. This method presents several issues, firstly, grain boundaries are not revealed as solid lines which greatly hinders the possibility of quantifying grain size. Furthermore, graphene is damaged along the grain boundaries during the process as the permanganate is also able to oxidize the C-C bonds of graphene.

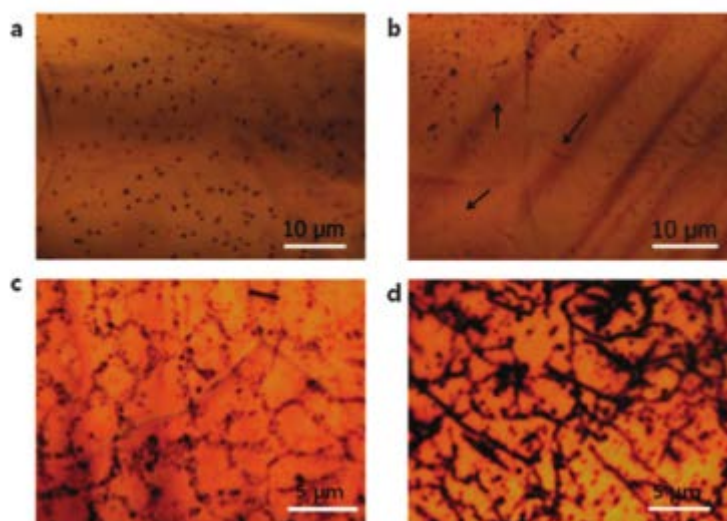


Figure 1-31. YU method of permanganate assisted oxidation. (a,b) under-oxidized samples, (c) optimal oxidation with grain boundaries revealed as dotted lines and (d) over-oxidized sample ⁵⁹.

In attempts to achieve more controlled oxidation that yield better defined grain boundaries, Duong et al.⁵³ presented a photo-oxidation process using humidity controlled ambient and UV light. This method is aimed at revealing the structural defects of graphene, especially grain boundaries. The authors show that it is a radical based reaction and generated O^* and OH^* radicals diffuse through graphene defects and oxidize the underlying copper, forming darker copper oxide. As a result, grain boundaries and defects are revealed as thin dotted lines as it can be seen in Figure 1-32. The samples also present abnormal concentrations of black areas that were attributed to copper foil impurities or graphene defects, although results are not conclusive about this. The authors provide an average grain area for the samples of the paper, although boundaries are difficult to observe due to the mentioned back spots that partially obstruct grain boundary identification. However, there is no explanation on how these grains are counted nor any statistics derived from the measurements.

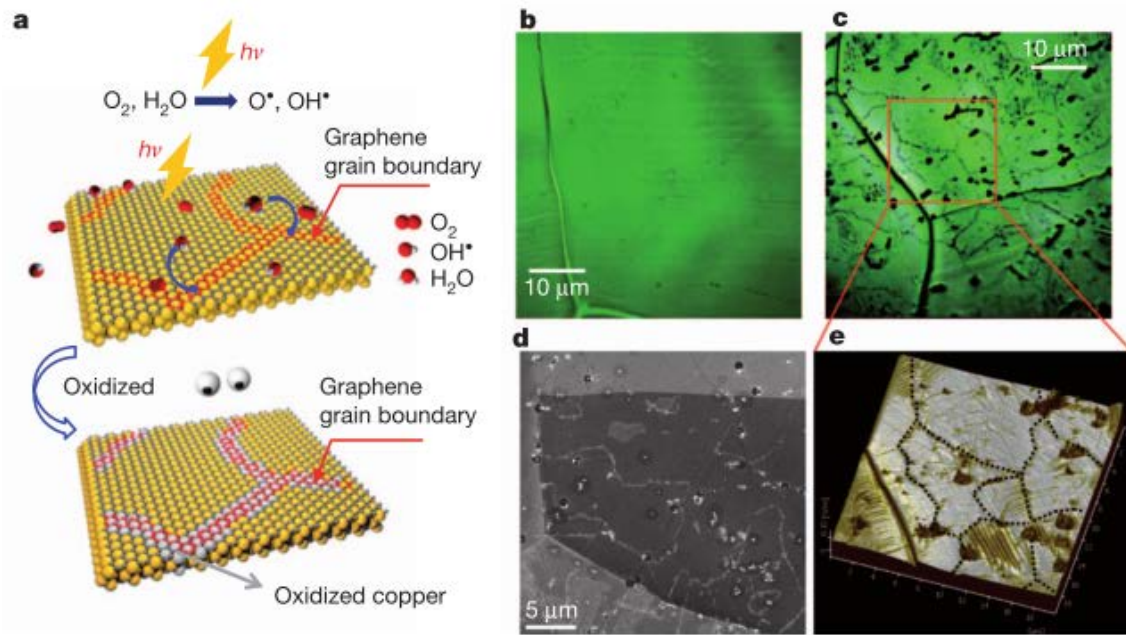


Figure 1-32. (a) Schematics of Duong's method. Samples of graphene on copper (b) before oxidation, (c) after oxidation. (d) SEM and (e) AFM images of oxidized copper. Note the very thin dotted lines that represent grain boundaries and the dark spots that represent either graphene defects or copper foil impurities⁵³.

The idea of characterizing graphene via optical microscopy has continued to be developed and more recently, Cheng *et al.*⁶⁰ presented a combination of UV exposure followed thermal oxidation in air. The process allows to differentiate the number of graphene layers from a CVD sample directly under an optical microscope. This is possible because copper oxidation is triggered at the edges of graphene and progresses inwards finding an increasing resistance with the number of layers. The authors also show that the process strongly damages graphene as the intensity of the D peak of the samples drastically increases after being subjected to the oxidation process.

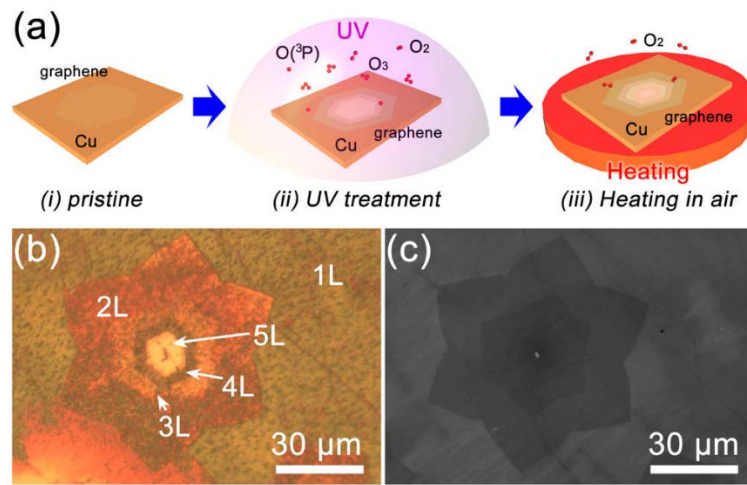


Figure 1-33. (a) Schematics for Cheng's method. Optical (b) and SEM (c) image of the same area after the oxidation process⁶⁰.

Summarizing, all the explained methods succeed in revealing the presence of graphene but only few of them manage to effectively expose grain boundaries. From these, the ones that require AFM or TEM are bounded to complex transfer techniques that can potentially damage graphene. Also, they are limited to the small observation areas characteristic of atomic-resolution techniques. The “easier” techniques that aim at using optical microscopy succeed on effectively revealing the presence of graphene covered areas and the number of layers. On the other hand, though, grain boundaries are revealed in such a fashion that are observable optically but are difficult to quantify in order to obtain statistical grain sizes for CVD graphenes.

As graphene is slowly approaching its industrialization it will be critical to extend quality control beyond the number of layers and, for now, no reliable method exists for precisely measuring the grain size of CVD grown graphene.

1.5 Properties

Fuhrer *et al.*⁶¹ pointed that the exponential growth of graphene research is fueled exclusively by its properties. As mentioned before, graphene is the first of the purely 2D materials that was successfully isolated and has many unique electrical, optical, mechanical properties and its potential applications, which make it one of the most studied materials in the past ten years⁶².

Due to its structure and being one atom thick graphene is highly transparent as it absorbs only 2.3%⁴⁷ of the light. Remarkably, it is impermeable to liquids and most gases⁶³. Also, the theoretical specific surface area of individual graphene sheets, $2630 \text{ m}^2\cdot\text{g}^{-1}$ ⁶⁴, is more than double that of the finely divided activated carbon used in water purification⁶⁵. But graphene is not limited to this and has been proven to present extreme properties that greatly exceeds present materials.

1.5.1 Mechanical properties

To measure graphene's mechanical properties free standing graphene is prepared by depositing the pristine layer on top of a silicon wafer with precisely made holes. Then this graphene is loaded with an AFM tip, see Figure 1-34, to experimentally obtain graphene's characteristics. It was found that it shows non-linear elastic behavior and brittle fracture⁶⁶.

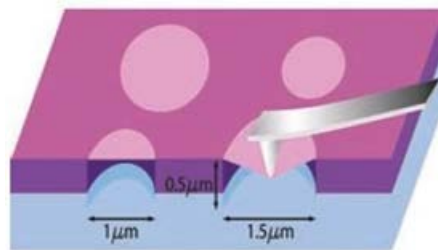


Figure 1-34. Using AFM technique in order to measure graphene's mechanical properties⁶⁶.

Huang *et al.*⁶⁷ indicate the breaking strength is $42 \text{ N}\cdot\text{m}^{-1}$ and the Young's modulus is 1.0 TPa, indicating it is one of the strongest materials ever measured, see Table 1-1. The breaking strength may not seem that big but taking in account an effective thickness of 0.335 nm it correlates to an intrinsic breaking strength of 130 GPa⁶⁸. Interestingly, this intrinsic breaking strength occurs at the point of brittle fracture of the graphene layer.

Table 1-1 Mechanical properties of some common materials ⁶⁹.

Material	Ultimate Tensile Strength (GPa)	Young's modulus (GPa)
PTFE	0.01 - 0.04	0.5
Titanium	1.04	105 - 120
Copper	0.21	110 - 130
Silicon	7	150
Steel	0.5 - 1.1	190 - 210
Tungsten	1.51	400 - 410
Diamond	2.8	1050 - 1200
Graphene	130	1000

1.5.2 Thermal properties

Another key aspect of graphene is its thermal conductivity. These properties are measured using an Optothermal Raman technique in which suspended graphene is placed between two heat sinks and is heated with the focused laser of a micro-Raman spectrometer ⁷⁰. In most cases the heat sinks are connected to thermocouples to obtain direct readings of heat flow.

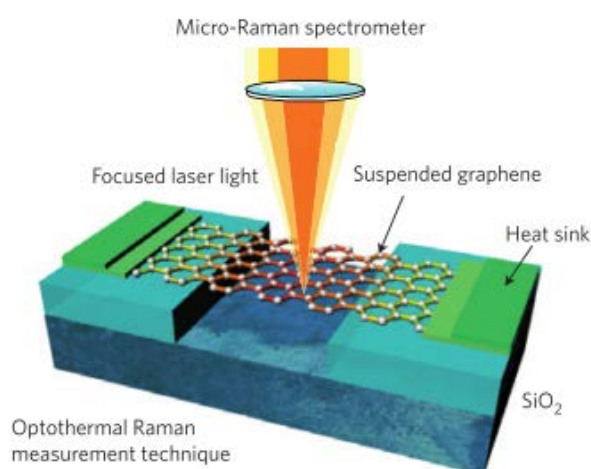


Figure 1-35. Set-up for thermal measurements on suspended graphenes ⁷⁰.

Measurements on graphene vary a lot. Both exfoliated and CVD suspended graphenes have been measured with a maximum thermal conductivity of 5000 W/m*K, which is 20 times more than copper, see Table 1-2, and even higher than diamond ⁷¹. Working with supported graphene has the undesired effect of the substrate which can effectively lower the reading to less than 600 W/m*K depending on the nature of the substrate ⁷⁰. Its thermal expansion coefficient is measured around $-6 \times 10^{-6}/K$, which is 5 to 10 times larger than that in ordinary graphite and can be explained by the lack of integration with other graphene layers.

Table 1-2 Thermal conductivity of some common materials ⁷².

Material	Thermal conductivity (W·m⁻¹·K⁻¹)
Carbon	1.7
Steel	43
Aluminum	205
Copper	401
Silver	429
Gold	310
Graphene	5000

1.5.3 Electrical properties

Probably the properties that gave graphene its notoriety are its ground breaking electric and electronic properties. As most of graphene's properties, these are strongly affected by the nature of the substrate where graphene lies. To exploit graphene's properties, an insulating substrate is usually needed and this is why CVD graphene must be transferred from its metallic growth substrate onto some sort of insulating material.

Four-point probe ⁷³ or van der Pauw ⁷⁴ method, and Hall effect measurements ⁷⁵ have applied to measure the characteristics of the graphene-like materials using direct tools. The Four-point probe and the van der Pauw methods measure only the conductivity or resistivity, while the Hall Effect measurement method measures the carrier density and the carrier mobility.

The four-point probe use a series of metallic contacts, usually gold, build using lithography techniques that allow probes to contact graphene, see Figure 1-36. The minimum size of these contacts is limited by lithography resolution to about 0.1 μm and require leads and contact pads to allow external probes to make proper contact. The resistance of these metallic leads can be easily calculated but the contact between graphene and the metal used is a major limiting factor. These interphases between metal and graphene generate temperature gradients of as much as 500 K ⁷⁶, which goes against thermal management in electronic devices. Also, these methods require earlier calculation and specific assumption of the sample size, shape and thickness to calculate the final results. Moreover, the four-point probe measures only direct current (DC) value.

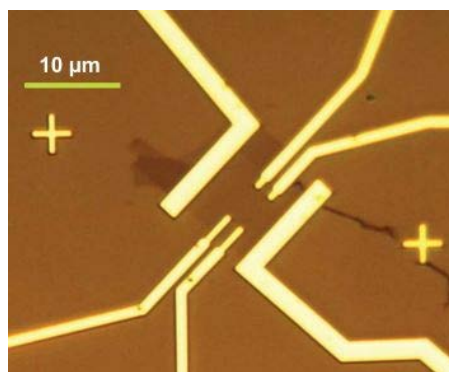


Figure 1-36. Typical gold contacts for graphene. Build using lithography ⁷⁷.

Graphene's presents exceptional electronic properties that can be partially explained by the fact that 3 of the 4 outer-shell electrons of carbon are connected to 3 other carbon atoms on the two-dimensional plane. The fourth electron is freely available in the third dimension, which forms a continuous π orbital across the whole graphene layer for electronic conduction. The most interesting fact of graphene is that it behaves as a zero band-gap semiconductor, which means that the valence band and conduction band meet originating the Dirac point. In this particular point electrons and holes behave as fermions with zero effective mass, also known as Dirac fermions.

Due to its massless nature, Dirac fermions can originate ballistic transport as those can travel some distance without scattering. For graphene it has been measured from the sub-micron range^{78–80} up to 28 μm ⁸¹. This gives rise to electrical mobility from 200,000 $\text{cm}^2\text{V}^{-1}\text{s}^{-1}$ to 40,000 $\text{cm}^2\text{V}^{-1}\text{s}^{-1}$ (depending on the substrate on which it is supported), more than an order of magnitude higher than some Si-based transistors⁸². Not only that, but it can sustain current densities of $5 \times 10^8 \text{ A/cm}^2$, or about 1 μA per atomic row of carbon⁸³. Finally, electrical conductivity can be quantified at a maximum of 10^8 S/m , which is about two orders of magnitude higher than silver.

1.6 Optoelectronic properties

As an alternative to these physical contact methods, optoelectronic methods based on far infrared techniques and THz-TDS are being developed to characterize graphene in a contact-less fashion. These techniques rely on the extremely short relaxation times, in the range of femtoseconds (10^{-15} s) to picoseconds (10^{-12} s), of graphene after it is excited by an incident radiation⁸⁴. Figure 1-37 shows a typical THz-TDS graphene measurement with a relaxation of picoseconds and the corresponding frequency response calculated through Fourier transforms.

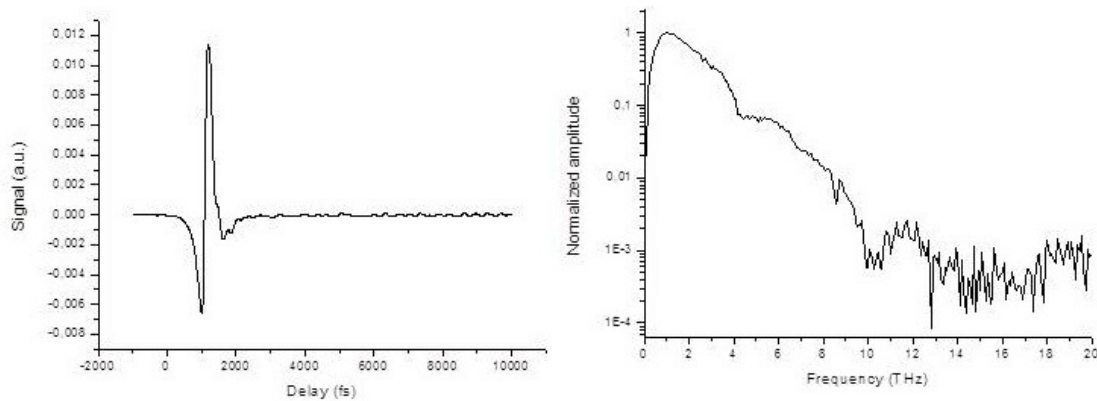


Figure 1-37. THz-TDS typical response for graphene. Left shows the temporal response in picoseconds and right, the frequency response after FFT.

Especially for THz-TDS, the effect of metallic contacts is completely removed as these are not needed and many materials that are opaque to visible and infrared light are transparent to THz radiation⁸⁵. Interestingly, studies on both exfoliated graphene and CVD graphene proved that it follows a Drude-type conductivity model⁸⁶ and moreover, THz conductivity is directly comparable with DC conductivity⁸⁷. For CVD graphene, these agreement is biased as DC measurements produce larger values for sheet resistance (about 30%) as the effect of grain boundaries and small voids in the graphene layers present larger effects on DC measurements than in THz-TDS.

Another advantage of THz-TDS is its ability to study local free carrier dynamics of graphene in contrast of global carrier dynamics in DC measurements. Also, THz-TDS can produce high-contrast imaging that enables studying graphene homogeneity and it is postulated as a possible quality control.

1.6.1 Influence of grain size

Many factors deeply affect graphene properties such as lattice defects or production method. But one of the least studied is the polycrystalline nature of synthetic graphene. It is known to have a negative effect on its properties when compared to natural pristine graphene, and increasing grain size (crystal domains) may lead to improve synthetic graphene's properties³⁹. Experimental studies are being held back by the difficulty related to precisely determining graphene grain size on real samples. For these reason, most works are simulation based.

Thermal properties of graphene are known to be hindered by the presence of grain boundaries and defects. Simulation studies show that grain boundaries will decrease thermal conductivity by a factor from 30 to 40% due to phonon scattering on these grain boundaries^{88–90}, see Figure 1-38 for typical schematic for these simulations. Few experimental experiments have been carried out on this subject, most noticeably, single grain boundaries have been studied, proving a decrease in thermal conductivity of only a 23%⁹¹.

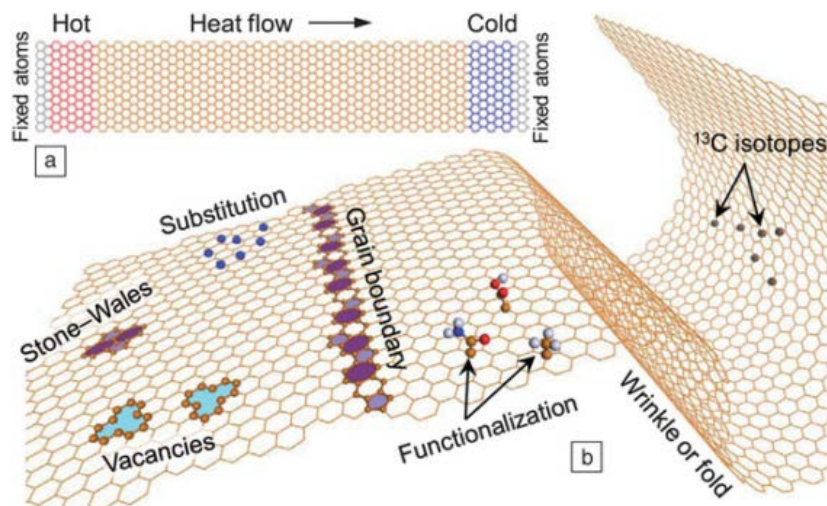


Figure 1-38. Schematics for Nonequilibrium Molecular Dynamics for simulating thermal transport in graphene ⁸⁸, (b) shows the whole range of structural defects studied.

Mechanical properties of graphene layers are another interesting subject. Although there is consensus on that polycrystallinity reduces mechanical strength of graphene it is not clear what role grain boundaries play. Studies on ripping graphene ⁹² showed that tears, or cracks, in graphene layers progress following zig-zag or armchair preferred directions and not random orientations. Experimental work showed that grain boundaries and folds do not stop the crack from progressing and barely deflects it, see Figure 1-39. This phenomenon can be explained either by the sp^2 hybridization of graphene that makes it behave as a brittle material ⁹³ or the succession of 5 and 7 atom rings on grain boundaries generate strain fields that cancel each other locally ⁹⁴. A particular case would be a succession of 5-8-5 atom rings, which will result in a concentration of stress forces and for a preferential point for fracture formation ⁹⁵. Some other studies report that grain boundaries will increase graphene resistance and make it as good, if not better, than natural pristine graphene ⁹⁶. It appears that this difference in behavior is related to the amount of angle mismatch between neighboring grains: low mismatch lowers strength up to a 59% while large mismatch retains up to 92% of the strength ⁹⁷.

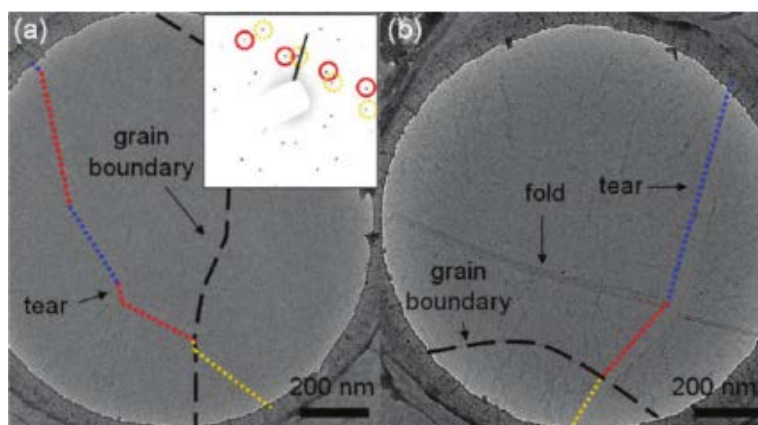


Figure 1-39. Graphene tears crossing grain boundaries and folds observed by TEM ⁹².

Overall strength of polycrystalline graphene related to grain size has only been studied by simulation. When taking into account the whole graphene surface, simulations yield erratic and, usually, contradictive results, note that these simulations use very small grain sizes under 15 nm. First of all, Kotakoski et al. ⁹⁸ showed that polycrystalline graphene is about 50% less resistant than natural graphene and there is no correlation between grain size and mechanical properties. On the other hand, some authors used simulation results to show both increase ^{99,100} and decrease ¹⁰¹ on mechanical properties with increasing grain size. It is clear than more studies are needed aiming at bigger grain sizes and, obviously, experimental data is needed.

Finally, electrical properties are also said to be reduced by grain boundaries and overall grain size but have not been extensively studied ^{8,102,103}. But these imperfections also allow for chemical functionalization and tailoring of electronic properties ¹⁰⁴, which makes CVD graphene very interesting.

1.7 Forms of graphene and applications

As we explained until now, although graphene relates only to the monolayer of carbon atoms, many forms appear on the bibliography. These forms go from the pure pristine monolayer graphene to multi-layer and graphene oxide. Obviously, all the forms present different structure, which affects its properties and the potential applications that are suitable for.

1.7.1 Forms of graphene

Graphene can be present in various forms as Figure 1-40 summarizes. True graphene is made of only one layer and maximum C/O content (0% of oxygen). From here, adding layers evolve to bi-layer, tri-layer, few-layer and multi-layer graphene until at more than 10 layers it is commonly considered graphite. On the other axis, decreasing the C/O ratio (increasing oxygen content) transforms graphene and graphite to the corresponding oxide form. Finally, modifying the lateral dimension goes from the nanometric to the micrometric version of graphene and graphite.

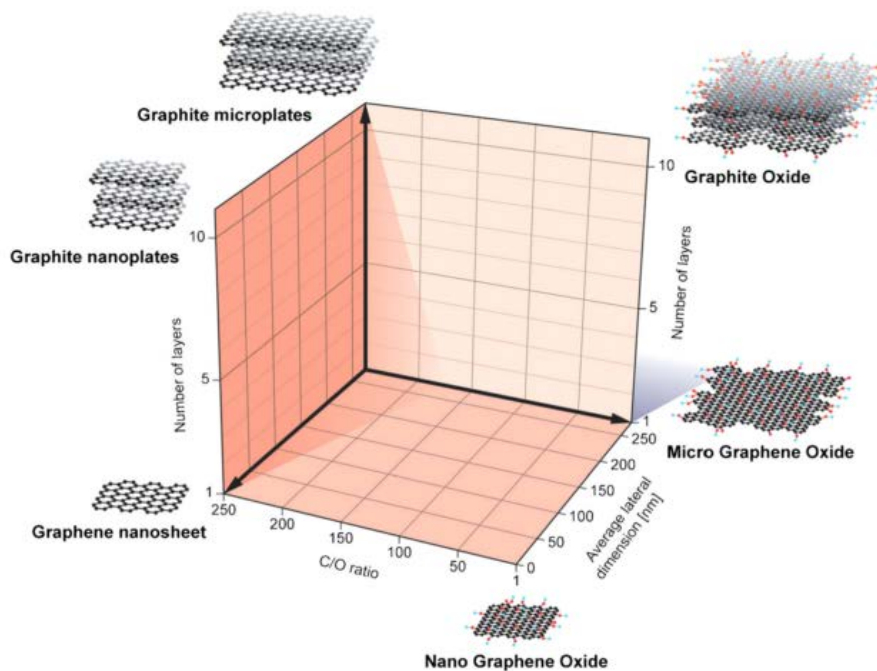


Figure 1-40. Classification grid for the nomenclature of different graphene types. The axis represents the number of graphene layers, the carbon/oxygen (C/O) ratio and the average lateral dimensions ¹⁰⁵.

Not all of these graphene forms are interesting nor useful. Among them, there are three that are of crucial importance:

- **Synthetic graphene (CVD graphene)**
- **Graphene Oxide (GO)**
- **Particulate graphene**

As explained before, CVD is a very effective way to produce graphene synthetically. All the products obtained through CVD are polycrystalline, which affect its properties. Having said this, CVD has the potential of fabricating large areas of graphene on copper as Samsung and Sony proved. It also has the potential of producing high quality graphene mono-crystals with properties like natural graphene. At this point in time (January 2017) though, both characteristics are impossible at the same time although it may seem feasible in a near future.

On the other end of the spectrum, GO is an intermediate for producing graphene suspensions as we explained before. The oxidation process allows to reduce the interaction between graphite layers thus reducing the energy needed to separate them. As a result, it is possible to obtain GO suspensions with close to 100% of monolayer content. The downside is that GO is mostly useless as it has properties opposed to graphene and is a good electrical insulator.

Particulate graphene is the result of reducing GO back to graphene and comprises both reduced graphene oxide (rGO) and graphene nano-platelets (GNP). The process of reduction effectively eliminates as much as 90% of oxygen content from the GO lattice but has the side effect of generating a lot of defects, which deeply affects its properties. Also, the resulting rGO suspensions tend to spontaneously aggregate into multilayered structures. Everything considered, the final product is a suspension or a powder with little content of monolayer graphene and very variable layer count for each grain and very variable properties.

Ideal graphene suspensions would be comprised of 100% monolayer graphene with controlled particle sizes and close to no defects on the lattice. In theory, it would be possible to produce CVD graphene with controlled grain size and directly release it from the growth substrate onto suspension. The addition of surfactants would increase the stability of monolayer graphene suspensions.

1.7.2 Potential applications

These multiple graphene forms and the multiple properties associated to these allow graphene to be suitable for multiple potential applications. A recent study¹⁰⁶ summarizes all applications in relation to its Technology Readiness Level (TRL), which reflects its development stage. Table 1-3 resumes this study. As it can be seen, there are a lot of potential applications and some are already reaching commercialization.

There are several common characteristics between all these applications. All the applications above TRL “Field tested” use exfoliated graphene coming from natural graphite and most of them aim at improving existing technologies. For example, all the additives and composites aim at improving the performance of existing materials and batteries. On the other hand, applications that use CVD graphene are limited by the availability of these and have not reached TRL’s past lab testing with the exception of Photodetectors, as these have already been demonstrated by ICFO several times.

Table 1-3. Technology Readiness Level (TRL) for graphene ¹⁰⁶.

Research		APPLIED R&D		DEMONSTRATION			COMMERCIAL	
Basic concept	Tech concept	Proof of concept	Lab tested	Field tested	Basic prototype	Final prototype	Fully tested	In operation
TRL-1	TRL-2	TRL-3	TRL-4	TRL-5	TRL-6	TRL-7	TRL-8	TRL-9
					Photodetectors		Oilfield chemicals	
					Thermal management	Water filtration membranes		
					Cement additives		Electron microscopy sample supports	
		Optical switches			Adhesives			
		Field effect transistors			Biosensors			
					Lubricants		Polymer composites	
		Medical device coatings			Flame retardants		Conductive inks	
		MRI contrasts agents			Paints and coatings		Conductive additives for displays	
		Stress strain actuators			Barriers and impermeable films		Humidity sensors	
					Anti-corrosion coatings	Inks & 3D printed materials		
					Thermal barrier		EMI shielding	Sporting goods
			Antibacterial		Supercapacitor additives		Antistatic coatings	Tires
					Anti-icing coatings		Battery additives	

From all the applications there are some that are of special importance and will be discussed individually.

1.7.2.1 Additives

It is worth noticing that most of graphene derivatives added to improve current materials, use exfoliated materials with very low content of monolayer graphene. It is safe to say that it has a similar effect as carbon black, or thin graphite, but amplified with the reduction of thickness.

When graphene is used as nano-filler into polymers it shows amazing increases in mechanical properties. Some authors show that by adding only 0.1% of graphene platelets it is possible to improve the Young modulus of an epoxy resin by as much as 31%¹⁰⁷. In some extreme cases adding 0.5% of graphene could translate into doubling the mechanical properties of some polymers¹⁰⁸. Increasing this content over 1% it is said to have no noticeable impact on the mechanical properties but to start to influence thermal properties and electrical conductivity¹⁰⁸.

Graphene is said to be a very effective lubricant or lubricant additive on oils^{109,110}. From all the studies it appears that multilayer graphene works the same way as graphite reducing friction by the low adhesion between layers while monolayer graphene provides marginal improvements. One a particular study¹⁰⁹ concludes that CVD graphene grown on nickel (multi-layer) is much better than CVD graphene grown on copper (monolayer), which has little or no effect.

It has been suggested that graphene-containing paints could greatly reduce deterioration of ships and cars through rust. The same technique could also be applied to brick and stone weatherproof houses or even to food packaging to stop the transfer of water and oxygen molecules, which causes food to go off.

1.7.2.2 Conductive inks

Electronic inks are mixtures of a functional material, stabilizers and rheology modifiers, and they must be print easily on appropriate substrates to produce devices with high charge-carrier mobility and long lifetime¹¹¹. Conventional conductive inks use either graphite or silver and, especially the latter, has lots of issues related with silver oxidation.

Graphene has the potential to fulfil most requirements to be used in conducting inks thanks to its high carrier mobility, mechanical robustness, environmental stability and potential for low-cost production, especially when produced by liquid-phase exfoliation in readily printable liquids such as water and organic solvents, resulting in a stable ink with good rheological properties for printing and coating ¹¹². Graphene has the potential of improving current inks due to its superlative electric conductivity and thermal and chemical stability.



Figure 1-41. Circuits printed on paper using graphene inks¹¹².

1.7.2.3 Anticorrosion and impermeable coatings

Graphene's impermeability to all gases, liquids, and salts ¹¹³ makes it an excellent candidate as anticorrosion coating, which may act as an effective barrier to water, oxygen and other corrosive materials. In addition, it has been reported that its excellent electrical conductivity provides an alternative path for electrons, so they are dispersed stopping any anodic corrosion potentially originated at the metal/coating interface ¹¹⁴. This type of corrosion is very critical for metals protected with insulating coatings.

1.7.2.4 Energy storage

Because of its extremely high surface area, excellent thermal conductivity and high mechanical strength, graphene may be used to improve various electrochemical energy storage devices.

In the field of batteries, conventional battery electrode materials can be significantly improved when enhanced with graphene, making them lighter, durable and suitable for high capacity energy storage, as well as shorten charging times ¹¹⁵. Some authors point that the addition of graphene on the formulation of Li-Ion batteries, see Figure 1-42, allow to double the specific capacity and dramatically increase the life cycles of the batteries.

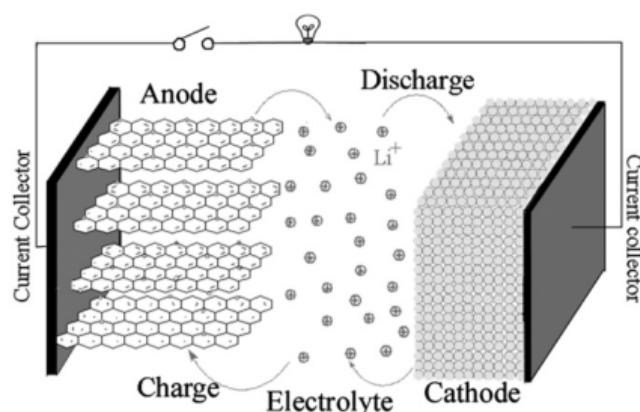


Figure 1-42. Schematics of a Li-Ion rechargeable battery with an anode improved with graphene ¹¹⁶.

But probably the most promising application of graphene in this field is its use in supercapacitors or ultracapacitors. These have the potential of charging as a capacitor and discharging as a battery while having extremely high energy capacities, as much as 85Wh/kg ¹¹⁷. Although this energy capacity is comparable with the best Ni metal hydride battery these supercapacitors have much shorter charge and discharge cycles and do not show signs of charge loss after thousands of cycles. Furthermore, ultracapacitors build entirely with graphene and flexible materials will allow to manufacture truly flexible energy storage devices ¹¹⁸, which can solve many applications needs and open many possibilities.

1.7.2.5 Electronics

Although these are not mentioned on Table 1-3, this represents one of the most interesting subjects for graphene and one of the niches for CVD graphene. Graphene has the potential of boosting transistor frequencies to the THz by improving the current technology or introducing new approaches such as the barristor ¹¹⁹, see Figure 1-43. All these have the big issue of having to overcome the lack of band gap in graphene through careful doping of graphene or physical construction of the device.

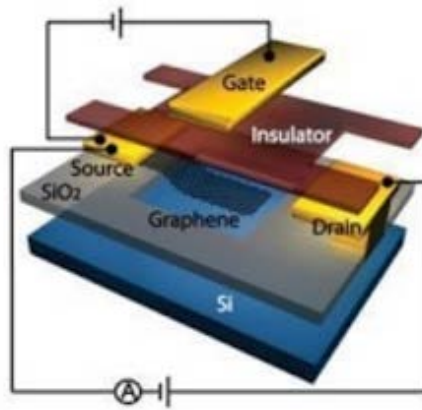


Figure 1-43. Basic structure of a graphene barristor¹¹⁹.

For conventional electronics, graphene has also the advantage of dissipating heat more efficiently ¹²⁰ and having a much higher limit temperature than current silicon-based electronics. This means that, despite the issues, building of transistors graphene has the potential of being able to greatly improve electronics.

Finally, graphene has the potential of enabling the manufacture of truly flexible and transparent electronics. Transparent conductors solely rely on ITO (Indium Tin Oxide) but it is very expensive, with limited availability, and fairly brittle. Flexible electronics, on the other hand rely on printable inks and conductive polymers that are usually black and have limited electrical conductivity. Monolayer CVD graphene has the potential of solving these issues having excellent electrical conductivity, great transparency and the smallest bending radius among all flexible transparent conductors characterized so far ¹²¹. Moreover, some prototypes are already being tested, as these fully bendable and transparent heart sensor, see Figure 1-44, developed by ICFO and showed at the 2016 Mobile World Congress in Barcelona.

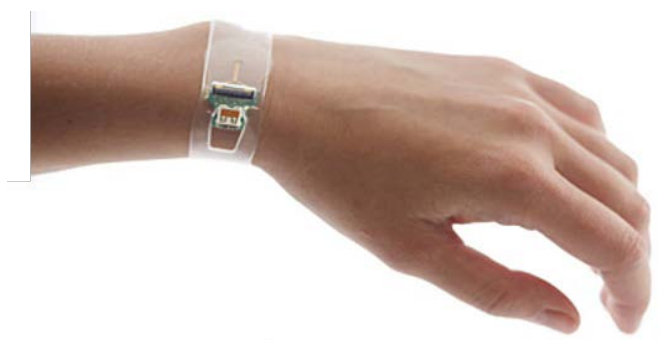


Figure 1-44. Fully bendable and transparent working heart monitor (www.icfo.eu, 4/1/2017).

1.7.3 Products on the market

From Table 1-3 it is clear that some graphene applications have already reached a market stage. Before checking of the most relevant it must be said that all of these products use graphene that comes from exfoliated graphite, with the exception of Electron microscope sample supports, and contains only a very small percentage of true monolayer graphene. Moreover, the marketing on most of these products usually makes it very difficult to determine both the quantity and quality of the used graphene. In most cases there is virtually no technical information about graphene's role in the properties and the scientific base is not clear. Commercial information collected here is updated as of January 4, 2017.

Electron microscope sample supports, especially for TEM, take advantage of the ultra-high conductivity of graphene to improve the performance of these sample holders and enable high resolution imaging. Besides this, due to the nature of graphene and the manufacturing techniques used, full coverage of the holders is ensured unlike for other conventional techniques. Companies specialized on TEM supplies like TED PELLA¹²² sell sample holders covered with graphene from 1 to 8 layers of graphene. Although there is little information on how these are produced, it is suspected that they are actually produced using CVD and wet transferred to the supports.

Graphene Nanochem¹²³ sells a whole range of products related to oilfield chemicals containing graphene that goes from drilling fluids to lubricants and, also, graphene conductive inks. Although they claim massive improvements on the properties due to the addition of graphene there is no reference to the quality of the graphene nor the number of layers, only that it comes from exfoliation.

There are other products that supposedly contain graphene, like the one produced by Graphenstone¹²⁴ (not included on Table 1-3). This Sevilla based company produces construction related products that contain graphene and range from mortar to paint. It is claimed that these products have 200% more strength, 20% more flexibility, up to 1000x electrical conductivity and increases in thermal conductivity. There is no information on the origin of the graphene, nor its nature and neither on the graphene content, as they only state "contains graphene".

On the sporting goods market there are several brands that opt for graphene on their product line. Starting with probably the products with a most honest and realistic marketing, Victor has a series of badminton rackets on the market with graphene. The Thruster K series use multi-layer graphene as a nano-charge to increase the stiffness of the racket shaft and decrease its weight. Figure 1-45 shows the TK-9000 a racket with multi-layer graphene in the construction of its shaft.



Figure 1-45. Victor TK-9000 badminton racket with multi-layer graphene (www.victorsport.com, 4/1/2017).

HEAD is also using graphene in some of its products, see Figure 1-46. On one hand, it has a fast-expanding range of skis¹²⁵ containing graphene in key areas of its core where they claim it helps control the rigidity and balance of the ski. Again, there is no information on the source, type and quality and quantity of graphene used. On the other hand, the first product that claimed to contain graphene was the Graphene XT tennis racket¹²⁶ that used it to construct a lighter thinner frame. A recent study on this racket¹²⁷, concludes that there is graphene in the area where the head of the racket meets the handle. This graphene though, is present in a form they call graphite nanoplatelets, which might refer to large stacks of graphene layers or thin graphite which is far from monolayer graphene and could translate into no graphene present on a graphene racket.



Figure 1-46. Left, first HEAD skis with graphene¹²⁵. Right, Graphene XT racket¹²⁶.

Continuing with the sporting goods, Catlike¹²⁸ uses graphene in a whole range of bike bike-related products to achieve lighter products with the same, if not better, performance. They state the use of graphene nano-fibers inside the polymer structure but there is no more information on the quantity used nor the quality of it.



Figure 1-47. Catlike graphene-containing products. Left, bike helmet. Right, bike shoes. Both have road and mountain bike variations¹²⁸.

Finally, Vittoria¹²⁹ uses graphene on a whole range of bike tires and rims, see Figure 1-48. Rims benefit from having a much higher lateral stiffness, increased strength in the spoke-hole area and the potential to produce lighter tires. On the tires they claim it helps increase durability. The graphene used is “Pristine graphene” called G+ from Directa Plus¹³⁰. This company produces graphene by means of Plasma Super Expansion in, which graphite is expanded and exfoliated to produce “accordion like structures” with a thickness of few nanometers in the best case. As the thickness of a graphene monolayer is less than 1 nm it is safe to say these exfoliated products are far away from pristine graphene and are made of thin flakes of graphite.



Figure 1-48. Tires and rims containing graphene¹²⁹.

2 Objectives

As explained above, graphene is a fast growing and promising market although production is presently still limited. Graphene sales can be narrowed to: (i) lab scale production of CVD layers and (ii) production of exfoliated graphite at the pilot plant or at small industrial scale. The first, represents the production of monolayer graphene on silicon wafers with sizes up to 4 inches in diameter. The later, has the potential of truly mass-producing graphene but with low quality, low content of monolayer, high density of lattice defects and, in many cases, considerably high oxygen content (in excess of 10%). Taking this scenario into account, the idea of producing high quality synthetic particulate monolayer graphene of controllable particle size becomes highly interesting. We made this idea the main objective of this thesis, following the scheme shown in Figure 2-1.

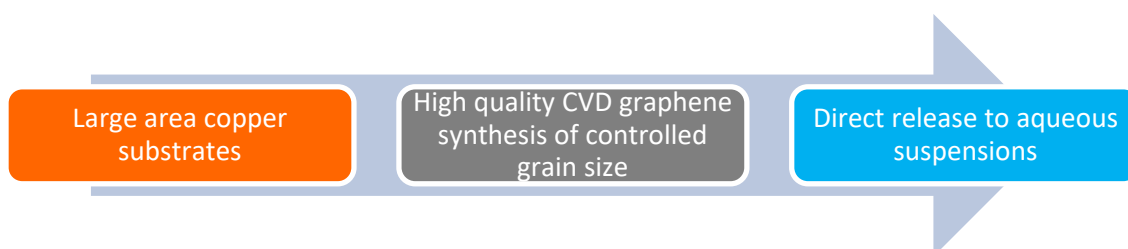


Figure 2-1. Scheme of the approach for the production of synthetic particulate monolayer graphene.

To achieve this objective, it is required to develop the following partial objectives:

- **Develop and build a CVD reactor for graphene synthesis.** Taking advantage of the knowledge of our research group in CVD deposition of ceramic layers a new reactor will be developed. This reactor must be capable of working with temperatures in excess of 950°C, low pressure and have multiple gas inlets.
- **Investigate a method to measure graphene grain size.** Since graphene of a controlled grain size is wanted it is necessary to precisely measure it. For this reason, a new method has to be developed with the requirements of being easier and more efficient than the ones described on the bibliography.
- **Explore ways to synthesize graphene with controlled grain size.** It is expected that grain size of graphene will be connected to the particle size of graphene platelets in suspension. For this reason, it is also an objective of this thesis to develop a strategy to control graphene growth in CVD processes. Gas flow restrictions will be applied as a tool to accomplish this.

- **Grow graphene on high surface area copper substrates.** To increase productivity, it would be needed to introduce more reactive copper surface inside the reactor. Thus, various high area solid copper substrates will be tested.
- **Achieve CVD graphene suspensions.** These suspensions must be produced by direct transfer from the copper substrate to the aqueous media by means of electrochemical (bubbling) transfer. The experimental conditions for these processes will be studied as well as ways to determine the presence of synthetic graphene flakes on these suspensions.

3 Monolayer graphene synthesis

The first step was to achieve the production of monolayer graphene on copper using CVD. For this purpose, a new reactor had to be build.

3.1 Reactor design

For this thesis, the reactor had to be developed and build from the ground up. At the end, several iterations have been made in order to improve the quality of the final graphene quality.

3.1.1 Fixed furnace

The first iteration was a simple tubular CVD reactor with a fixed furnace. Figure 3-1 shows an engineering scheme of this set-up. Its main features are 3 different gas intakes each one of them with a dedicated mass flow controller (MKS 1179A) and a single outlet equipped with a rotary vane pump and a pressure sensor. Pressure inside the reactor is set by the combination of pump and gas inlet. The reactor chamber is build out of 25mm outer diameter quartz tube and heated using a concentrically tubular furnace.

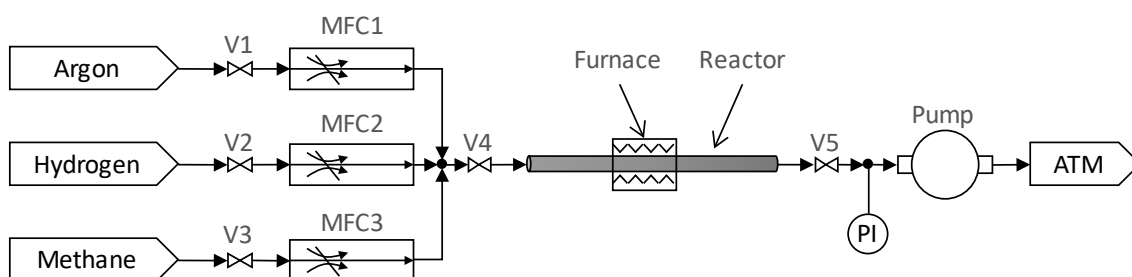


Figure 3-1. Fixed furnace reactor. Cooling fan was added as a first improvement to control final cooling stages.

Table 3-1. Acronym explanation.

Acronym	Meaning
V1, V2, V3, V4	Ball valves
V5	Seat valve
MFC1, MFC2, MFC3	Mass flow controllers
PI	Pressure indicator
ATM	Atmospheric exit

Apart from the quartz tube, all other pieces are made of stainless steel and two different standards have been used. From the gas inlet to valve V4 all is build using standard Swagelok 6mm components. After valve V4 everything was adapted to standard KF components from Pfeiffer. Annex 2 presents all KF pieces used. It is worth noticing that tube compression fittings are required to adapt fragile quartz components to steel – see Figure 3-2 – and the flexible corrugated hose may absorb pump vibrations. The combination of these two components prevent the quartz tube shattering during operation.

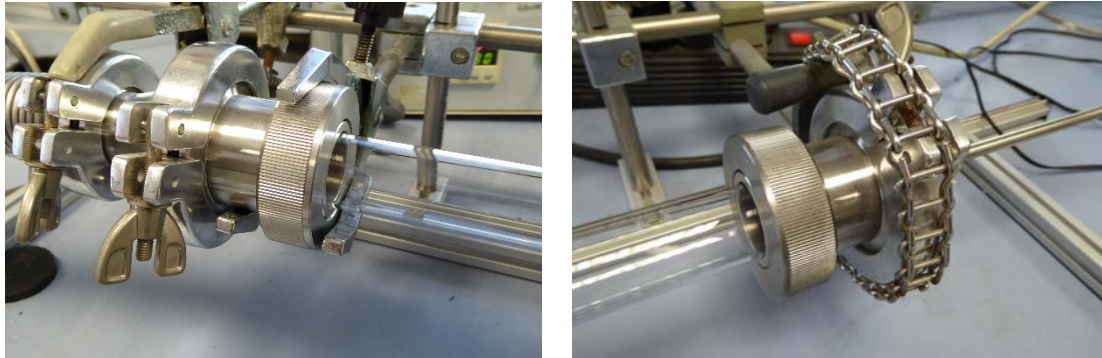


Figure 3-2. Compression fittings as installed on the reactor.

This reactor design allows for easy operation but leaves samples subjected to the complete heat cycle of the reactor meaning it is subjected to heating and cooling times in excess of 40 minutes, as seen in Figure 3-3. Cooling can be improved by removing part of the insulation and adding a fan to force fresh air into the furnace.

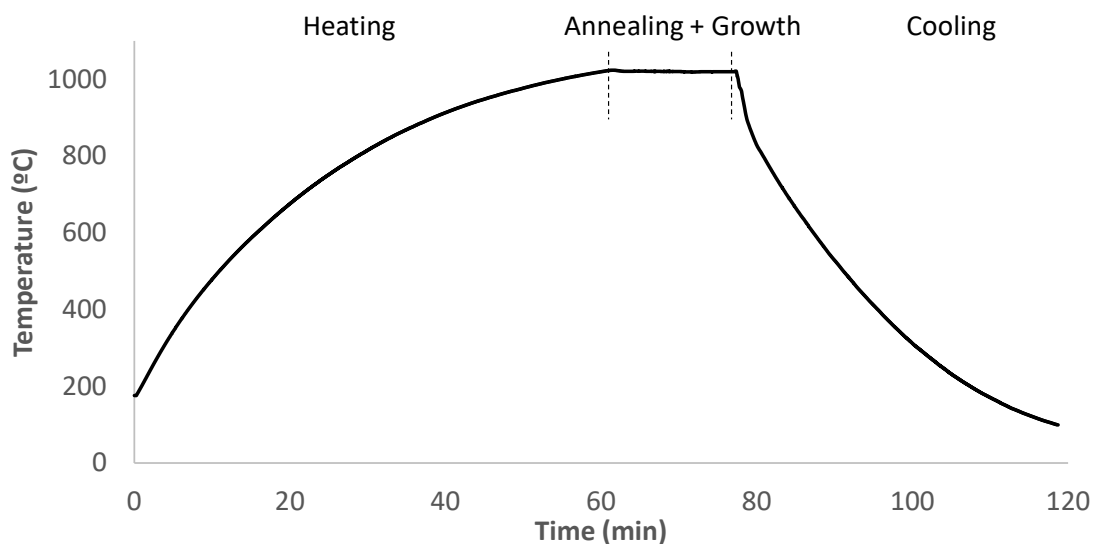


Figure 3-3. Heat cycle of this reactor forcing the cooling using an additional fan, annealing and growth time can be tuned on demand.

3.1.2 Sliding furnace

To have more control on the heat cycles that samples receive a sliding furnace reactor was developed. Figure 3-4 shows the engineering diagram for this new reactor. It should be noted that most of the setup remains unchanged except for two of the gas inlets. In this case, inlet gas is selected prior to the only mass flow controller. The rest of components are the same as in the previous fixed furnace setup.

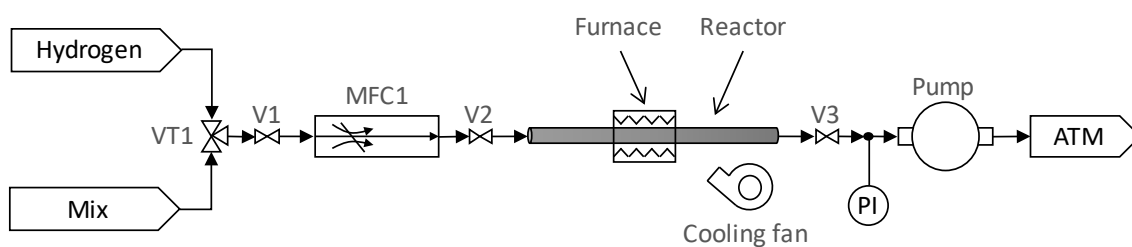


Figure 3-4. Final design with only one MFC and sliding heating element.

Table 3-2. Acronym explanation.

Acronym	Meaning
V1, V2	Ball valves
V3	Seat valve
VT1	Three-way valve
MFC1	Mass flow controller
PI	Pressure indicator
ATM	Atmospheric exit

The whole furnace is encased inside a custom-made structure that allows it to slide along 1.5 m rails. Figure 3-5 shows this structure and its critical components. The reactor lays on four wheels, two of which are fixed and the other two are adjustable allowing to correct misalignment issues during assembly. As mentioned before quartz wool insulation is added to seal the ends of the heating element, see Figure 3-5. There is an additional insulation on top of the reactor that serves, basically, to hide the electrical contacts and avoid accidental short circuits.

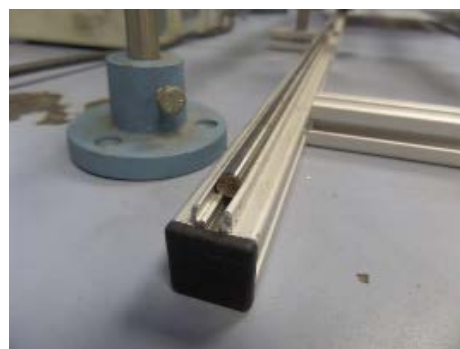


Figure 3-5. Critical components on sliding furnace structure. Top image shows completed structure complete with furnace and reactor. Bottom left shows a detail on the wheel units used and bottom right shows the calibrated 6mm rails.

This whole set-up allows for a much more precise control over the reaction steps. As can be seen on Table 3-3, each reaction cycle is split into three different phases. Firstly, the reactor is allowed to heat up away from the sample. Then, the heated reactor is moved to cover the sample and heat it up to trigger the start of the annealing and growth stages. Finally, the reactor is moved away from the sample and cooled using a fan. Although the sample cools really quickly, gas flow inside the reactor is maintained until the cooling cycle is entirely completed.

Table 3-3. Reaction stages using the sliding furnace with typical gas flows used.

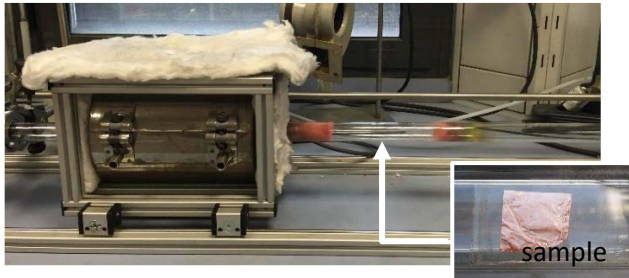

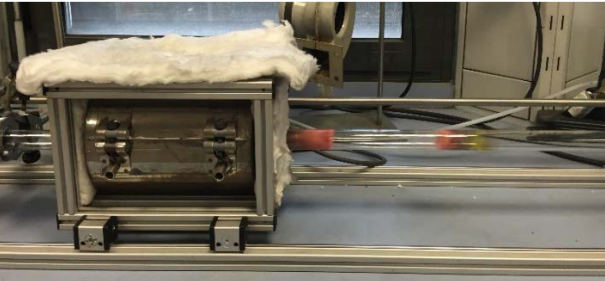
State of the reaction	Position of the reactor	Duration	Gaseous flow	Pressure
BEFORE (heating)		40-55 min	After 30 minutes: 30 sccm H ₂	0.7 mbar
DURING		Annealing: 15 min Reaction: 10 min	Annealing: 30 sccm H ₂ Reaction: 88 sccm CH ₄ +H ₂	Annealing: 0.7 mbar Reaction: 2.5-2.6 mbar
AFTER (cooling)		55-65 min	88 sccm CH ₄ +H ₂ Below 500°C: 30 sccm H ₂ Below 200°C: OFF	0.7 mbar

Figure 3-6 shows a typical temperature profile for this set-up. Note that the reactor profile is almost identical to the previous set-up but with a very small dip in temperature when the reactor is moved over the sample. From that moment, internal temperature follows a much sharper profile and usually heats up in 3 to 4 minutes and cools down to less than 500°C in approximately 30s.

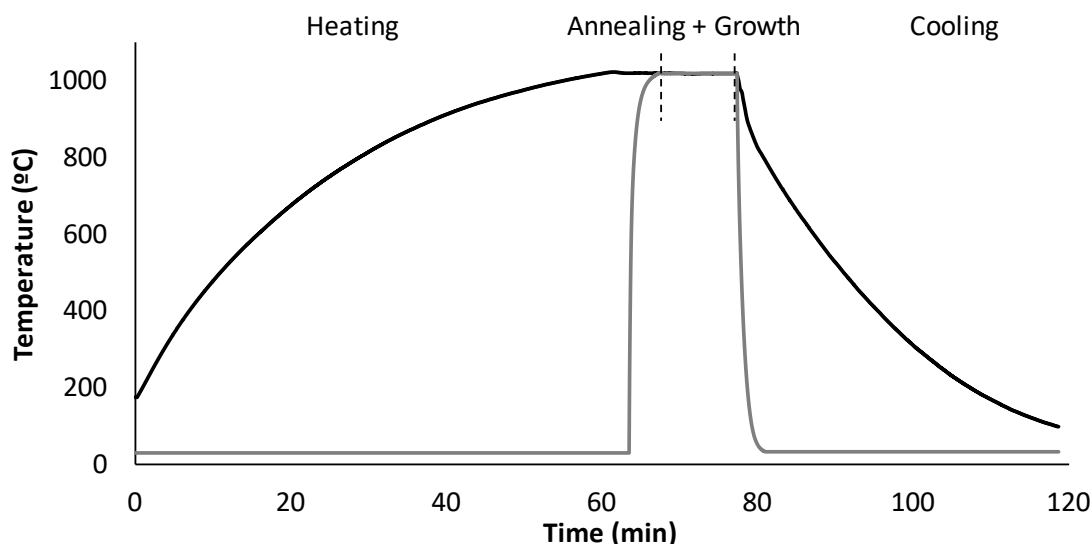


Figure 3-6. Grey line represents furnace temperature evolution while black line represents sample temperature. Rapid heating and cooling is caused by the furnace being slide to and away from the sample.

3.2 Graphene transfer

In this thesis, all the samples of graphene on copper foil are transferred using a wet transfer technique using FeCl_3 to etch copper away. As explained before (see section 1.3.2.2), samples are spin coated with 5% PMMA on toluene. This procedure produces a very thin layer of PMMA that after annealing at 175°C for 3 minutes, to increase the adhesion, acts as scaffolding for the graphene when the copper is removed. Prior to etch, the graphene present on the unwanted side of the copper foil must be removed by floating it on HNO_3 34% in water for a maximum of 3 minutes or until bubbles appear under the sample. This indicates that HNO_3 has effectively removed graphene and is starting to etch copper away.

The PMMA/Graphene/copper samples are then floated on top of a 50% FeCl_3 solution, which is capable of etching copper without damaging the remaining graphene. The whole process length varies depending on the thickness of the copper foil but, as a rule of thumb, samples must be kept on the FeCl_3 solution until no visible copper can be seen and 30 minutes more to ensure all copper is dissolved. Figure 3-7 shows the whole process for one representative sample with copper being dissolved by FeCl_3 and the sample with no copper remaining on the final clean water rinse bath.

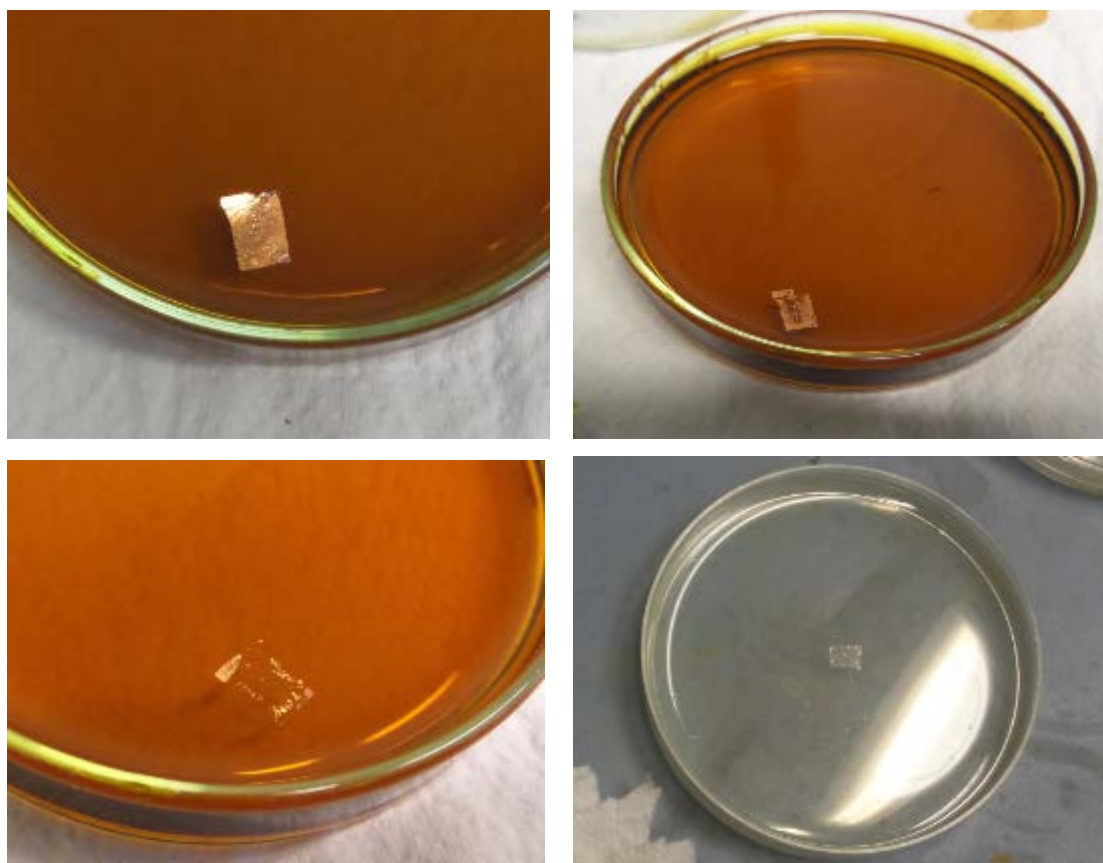


Figure 3-7. Copper being dissolved in FeCl_3 . Image on the bottom right shows the PMMA/graphene layer on water after complete copper removal.

3.3 Monolayer growth

The first objective for this thesis was to simply achieve production of monolayer graphene. A fixed reactor mimics a classical CVD furnace and allows for easy operation. The first conditions were established using bibliographical data as follows:

- **Temperature for annealing and growth:** 950°C
- **Annealing time:** 15 minutes
- **Annealing gas:** 30sccm H₂
- **Growth time:** variable
- **Growth gas:** 15 sccm H₂ + 30 sccm CH₄
- **Cooling gas:** 15 sccm H₂
- Transfer to silicon wafers.

Annealing under hydrogen serves to remove unwanted surface copper oxides and trigger copper recrystallization. Also, due to the high temperatures and vacuum conditions copper is also being evaporated, which further helps to remove unwanted impurities and flatten its surface.

Growing graphene using these conditions with times from 30 seconds to 60 minutes did not yield reproducible results. For long growth times, 30 minutes and longer, Raman spectroscopy showed the typical spectra for carbon thin films with broad intense D and G peaks and almost nonexistent 2D peak. On the other hand, growth at 15 minutes produced monolayer graphene on the first attempt with sharp and intense G and 2D peaks with a I_{2D}/I_G of approximately of 2 but with a moderately intense D peak indicating the presence of a lot of defects. This monolayer graphene could not be reproduced. Figure 3-8 shows Raman spectra for graphene grown using the fixed reactor at 30 and 15 minutes.

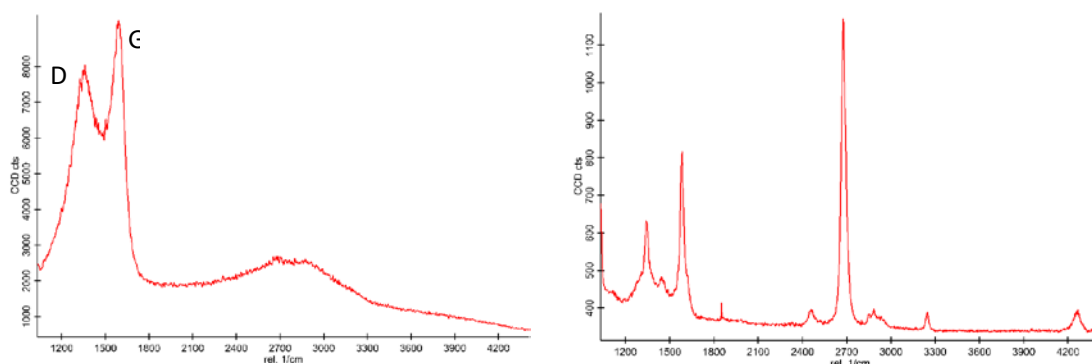


Figure 3-8. Left growth for 30 minutes, right growth for 15 minutes.

This first approach presented several issues that could be narrowed to the cooling stage. Firstly, reaction was stopped by switching off the methane flow and furnace at the same time. This

mean that the samples were subjected to high temperatures, close to the reaction temperature, for several minutes but only with hydrogen flow. Which means carbon can be etched away from the copper substrate while no new graphene could be formed. Secondly, cooling time was almost uncontrollable as relied onto small heat leaks through furnace insulation.

To try to avoid these issues the procedure was modified. The reaction end was marked by switching off the furnace while the methane flow was maintained until inside temperature decreased below 500°C. Also, to help maintain a more controlled cooling rate, insulation of furnace ends were removed at reaction end and a cooling fan was added. All these changes translated into a more controllable reactor and, for the first time, it was possible to obtain monolayer graphene consistently across multiple reaction times, see Figure 3-9. Raman spectroscopy analysis of multiple points of each sample showed that those were not uniform presenting areas of bilayer and many areas with no graphene at all. However, results were not repetitive across identical growth reactions.

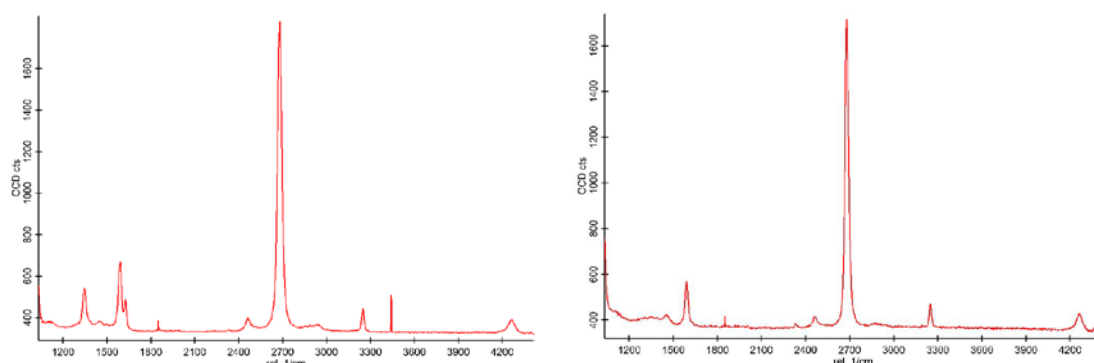


Figure 3-9. Left growth for 15 minutes, right growth for 5 minutes using the fixed furnace with controlled cooling.

In order to further control the cooling stage and minimize differences between reactions the sliding furnace was developed allowing precise reaction time control and extremely fast cooling times. This is expected to help obtain more consistent results between reaction batches. The drawback of this reactor set-up is the utilization of only one mass flow controller (MFC) instead of three, which greatly limits the flexibility of it in terms of inlet gases. To solve this limitation, several methane-hydrogen mixtures were ordered with methane contents ranging from 10% to 60%.

The first reactions using 30% methane for the growth stage proved to be very successful with consistent monolayer graphene fabrication (see Figure 3-10). Note the Raman spectra present sharp and symmetric G and 2D peaks with I_{2D}/I_G more than 3 and almost inexistent D peak, which all translates in high quality monolayer graphene. Moreover, samples proved to be homogeneous across the whole copper surface with Raman spectra being consistent on all analyzed areas.

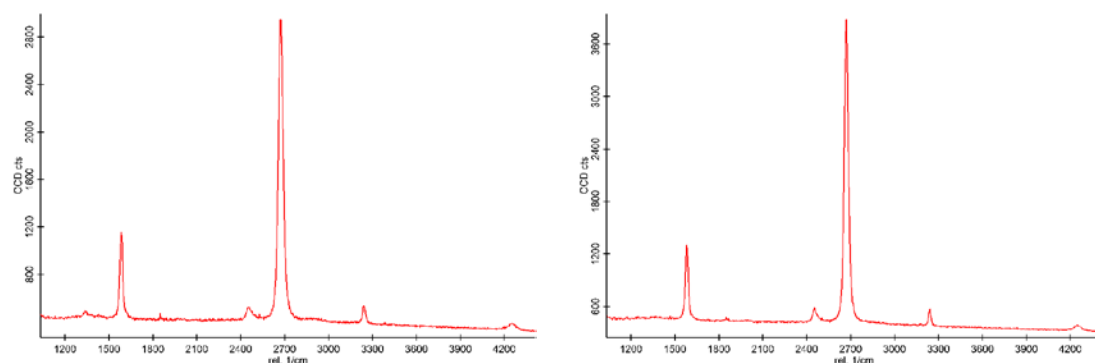


Figure 3-10. Left growth for 15 minutes, right growth for 5 minutes.

3.4 Determining conditions for monolayer graphene growth

With the ability of producing high quality monolayer graphene it was imperative to optimize its growth conditions and find ways to observe its structure. The easiest method to assess the continuity of the graphene layer was to oxidize uncovered copper ⁵⁸.

Growing graphene using the sliding furnace with a mixture of 30% methane and stopping the reaction at 5, 10, 15, 20, 25 and 30 minutes allowed for nucleation and growth stages to be observed (Figure 3-11). At 5 minutes, no graphene can be observed while for 10 minutes, and more, unoxidized areas can be observed, which unequivocally marks the presence of graphene. Increasing time from 5 to 20 minutes makes the production method evolve from no graphene to a continuous layer, where graphene protects all copper surface. Exceeding 20 minutes, graphene appears to not cover all the surface and it is possible that graphene etching by hydrogen is predominant over the deposition thus producing areas with no graphene, for long times over 25 minutes, graphene is clearly inhomogeneous and split into small pieces.

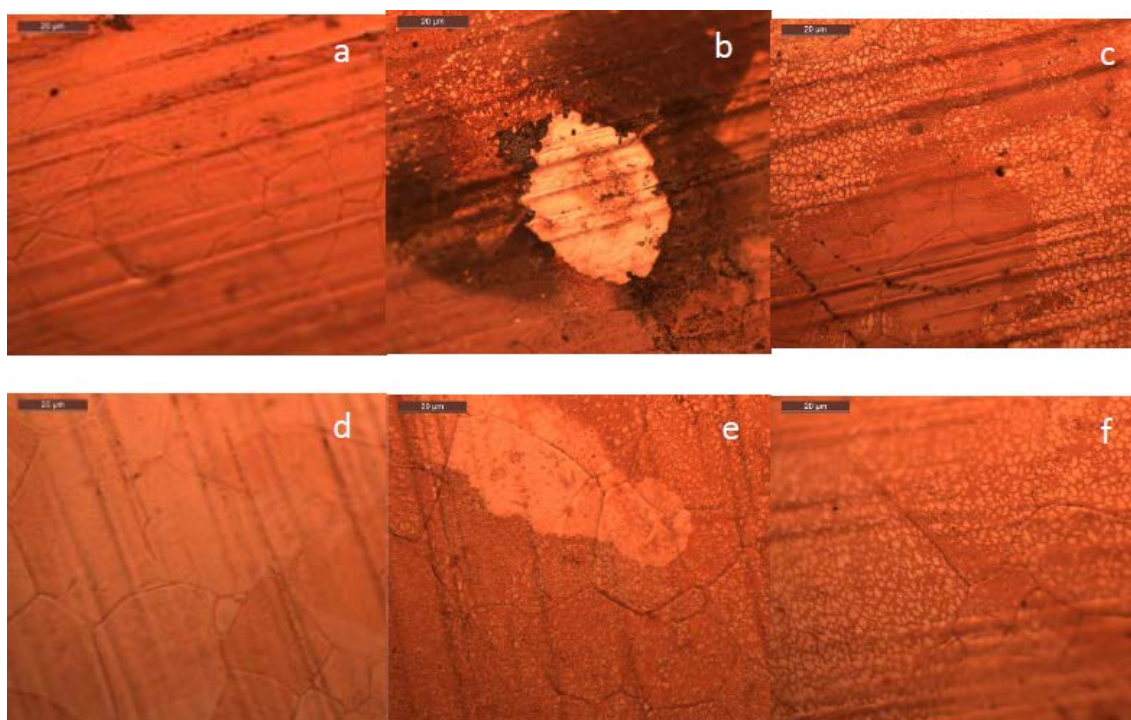


Figure 3-11. (a) to (f) images for 5, 10, 15, 20, 25 and 30 minutes respectively after oxidation using H₂O₂ method. Scale bar in 20 μm for all samples.

Raman spectroscopy analysis of these samples, Figure 3-12, confirms that no graphene is present at 5 minutes. It rapidly evolves to graphene for 10 and 15 minutes until it reaches high quality monolayer graphene at 20 minutes. From this point on it appears to evolve to bilayer graphene at 25 minutes and go back to monolayer for 30 minutes. From all the samples the only that presented a homogeneous graphene layer was 20 minutes of reaction time and it could be repeated consistently. Summarizing, using the sliding furnace reactor and untreated copper foil as a substrate the best growth time is 20 minutes.

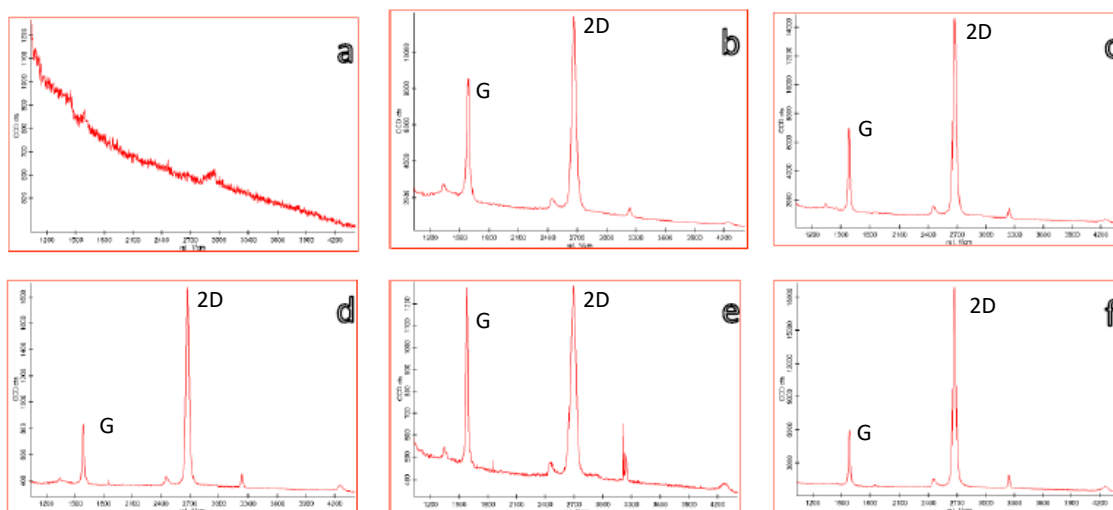


Figure 3-12. Raman spectra for all 6 samples. It can be seen that at 5 minutes (a) no graphene can be found and for 10 minutes and more (b-f) monolayer graphene can clearly be observed. Reaction at 25 minutes (e) shows what appears to be multilayer graphene.

While reaction times over 15 minutes yielded consistent and repeatable results, shorter times produced erratic nucleation and growth patterns that were difficult to reproduce between samples. It can be explained by the use of untreated copper foil as the growth substrate as it presents rolling marks typical of the production method used. As mentioned on the introduction, copper impurities and surface morphology plays a key role on the nucleation of graphene. And, improving copper surface roughness¹³¹ can yield much better graphene quality and control over its nucleation and growth. To achieve a better copper surface several methods can be used. Authors point that simply annealing for longer times is sufficient for this purpose but electropolishing is much more desired as it produces much more controlled and repeatable results.

3.4.1 Electropolishing

Electropolishing or electrochemical polishing is aimed at surface polishing metallic surfaces without the necessity of abrasives, which can lead into much smoother surfaces. Voltage must be precisely controlled as only a small range of voltages produces the required effect: if the voltage is too low it will produce pitting and if it is too high will translate into generation of gases, i.e. water splitting. Electrolyte must produce soluble salts with the electropolished material to avoid passivation and uneven polishing. Also, high viscosity is desired to facilitate the achievement of smooth surfaces. Copper electropolish is widely studied and easiest methods use phosphoric acid 55% in water as electrolyte, copper plate as a cathode, sample as the anode and apply 2V of DC current to trigger the reactions of Table 3-4. Time is dependent on the initial sample roughness.

Table 3-4. Electropolishing reactions for each electrode.

Electrode	Reactions	
Anode	$Cu \rightarrow Cu^{2+} + 2e^{-}$	Reaction 5
	$Cu^{2+} + 2OH^{-} \rightarrow Cu(OH)_2$	Reaction 6
Cathode	$2H^{+} + 2e^{-} \rightarrow H_2$	Reaction 7

For our case, initial copper foil presents rolling marks that are visible almost with the naked eye and cover the whole surface of the sample. To determine the optimal time of electropolishing, several different times were used until no visible rolling marks could be observed. Figure 3-13 shows the evolution of this process from an untreated foil until no visible marks remain at 10 minutes. As a side effect, copper grains become visible in SEM.

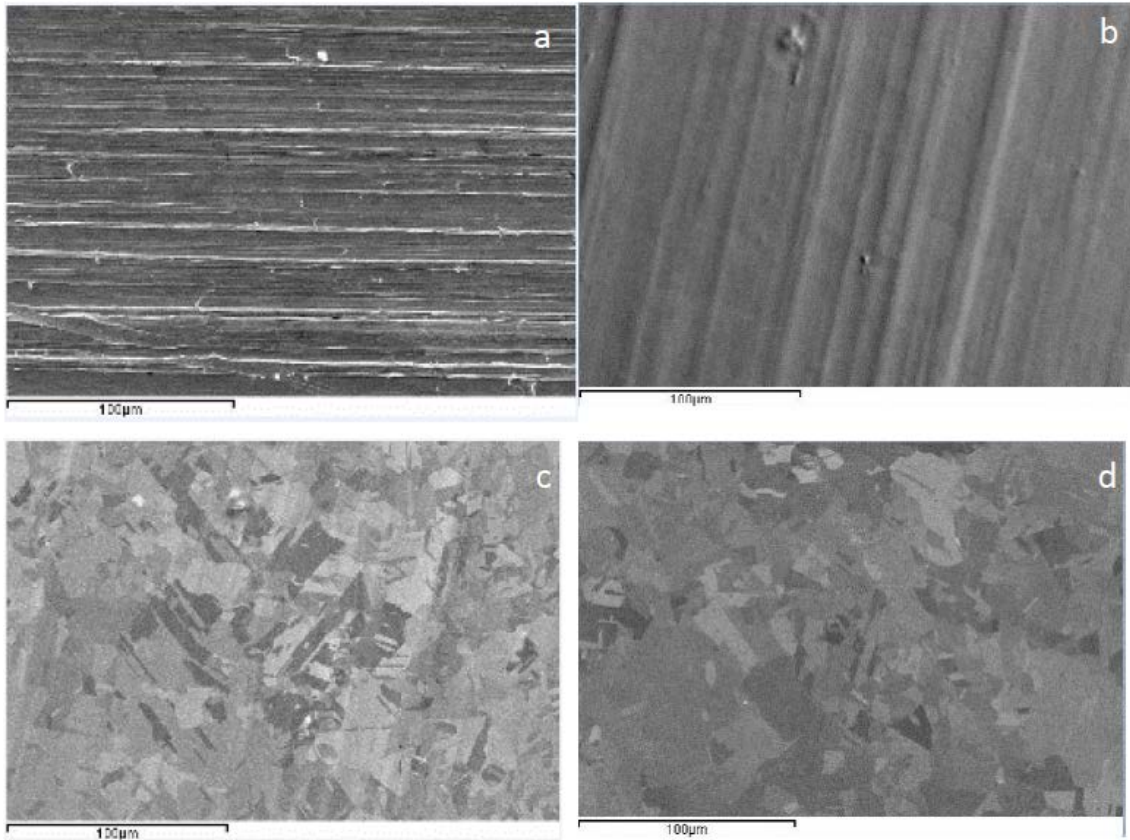


Figure 3-13. Electropolishing stages. (a) original copper foil, (b) 2 minutes, (c) 6 minutes and (d) 10 minutes. Scale bar in 100 μm .

Settling in 10 minutes to electropolish allows to completely remove rolling marks as SEM and AFM shows, see Figure 3-13 and Figure 3-14. Original marks present a height of approximately 100 μm each, which means the surface is very rough and irregular. After electropolishing, surface is virtually flat with a S_a on 10 nm measured through AFM. Also, observing a SEM image of just the area that touches the surface of the liquid electrolyte it became clear that a lot of the metal is etched away. Figure 3-15 shows a cross-section of the same sample and it can be measured that the electropolishing reduces the thickness of the copper foil to approximately half of the original, roughly down to 10 μm .

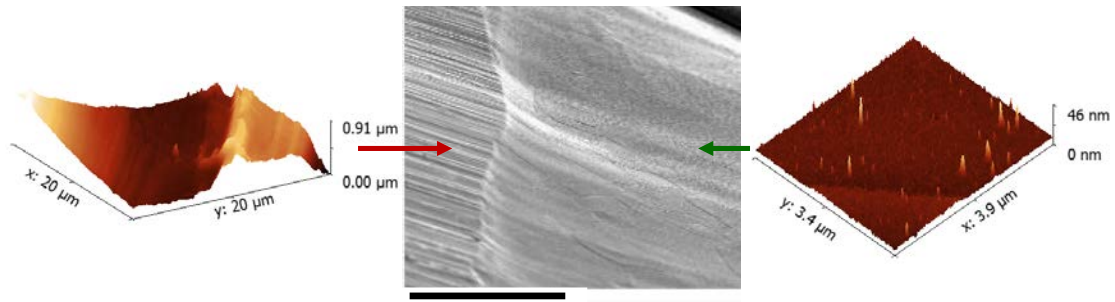


Figure 3-14. AFM images showing original rolling marks (left) and final electropolished substrate (right). Central SEM image presents the copper sample just in the area that touches the liquid substrate, scale bar in 100 μm

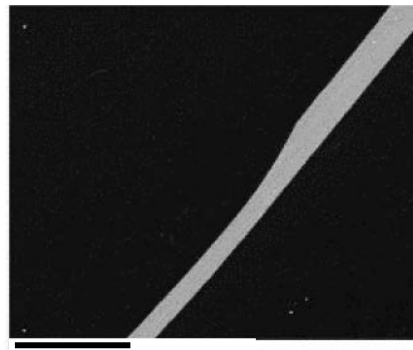


Figure 3-15. Cross-section of an electropolished copper foil.

Surface roughness hasn't been taken as a statistical value and has not been thoroughly studied for several reasons. Original roughness is due to linear, and parallel, rolling marks and superficial copper defects that are almost completely removed during electropolish. But, more importantly, the superficial roughness is further modified during the annealing and growth stages and the presence of graphene wrinkles impedes the precise analysis of its final roughness, see Figure 3-16.

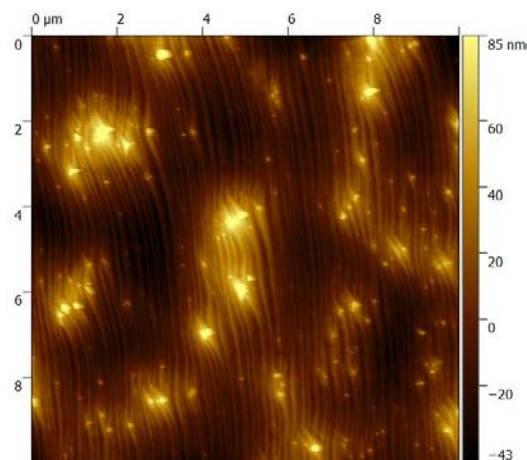


Figure 3-16. Typical graphene wrinkles grown on electropolished copper.

3.4.2 Growth on electropolished copper

Electropolishing greatly reduces surface roughness and removes almost all impurities present on the copper foil so it is expected to reduce the nucleation of graphene and somewhat extend the growing times required for forming a continuous layer. Polishing also makes graphene on copper clearly visible on SEM enabling the possibility of quality control after each growth reaction.

With the knowledge acquired on working with copper foil, the first graphene on electropolished copper foil was performed at 950°C with a mixture of 30% methane in hydrogen for 30 minutes. Figure 3-17 shows the result for this sample, it can be observed that H_2O_2 oxidation on copper shows what appears to be grain boundaries of the polycrystalline graphene. SEM on the other hand, reveals the presence of individual nuclei that have not totally coalesced into a full continuous graphene layer. More importantly, this sample is homogeneous across the whole copper surface.

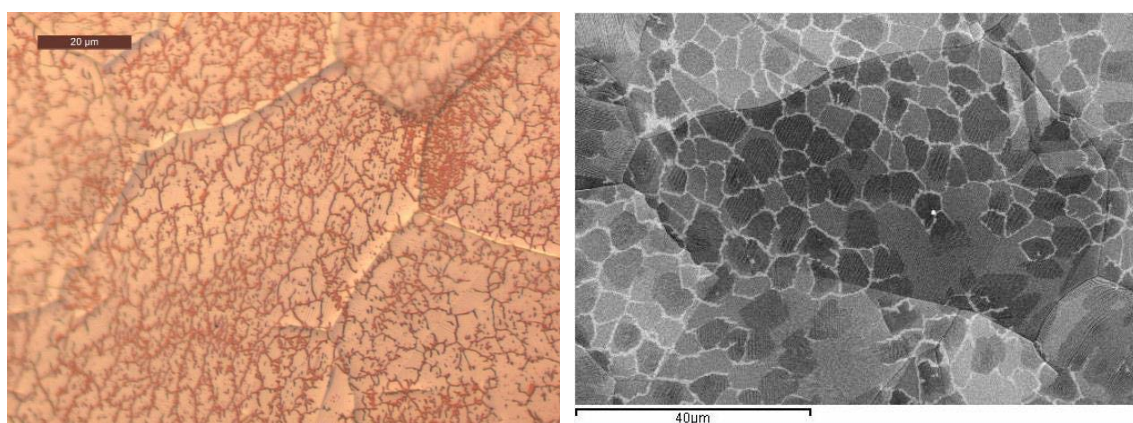


Figure 3-17. Graphene on copper after 20 minutes of growth time. Left, optical image after H_2O_2 oxidation and right, SEM image.

Increasing the time to 60 minutes allows to produce a continuous layer of monolayer graphene across the whole copper sample. As it can be seen in Figure 3-18, H_2O_2 oxidation only shows that copper is not affected, which means there are no gaps on the graphene layer. Moreover, SEM confirms this observation. For the first time, it is possible to observe (lower right corner of SEM image) the typical graphene wrinkles that form on the cooling stage due to the very different expansion coefficients of copper and graphene.

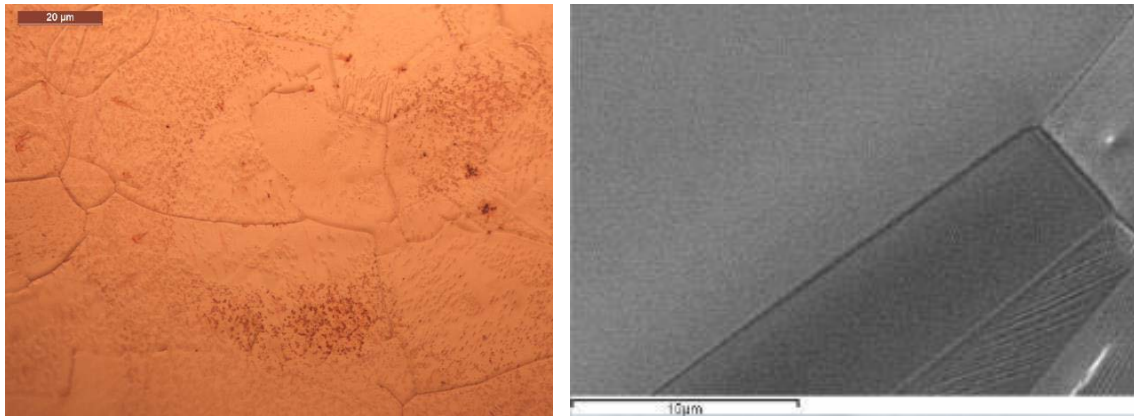


Figure 3-18. Graphene on copper after 60 minutes of growth time. Left, optical image after H_2O_2 oxidation and right, SEM image.

On the other hand, moving to the other end of the spectrum, performing a short growth reaction confirms that nucleation is extremely hindered by the lack of active points on the smooth copper surface. Figure 3-19 shows H_2O_2 oxidation and SEM images for a 5 minutes reaction, both are consistent and show individual nuclei on the firsts stages of growth with the typical dendritic forms. Note that these geometries are dependent on copper orientation³² and pressure and hydrogen content on the reaction gases³⁰.

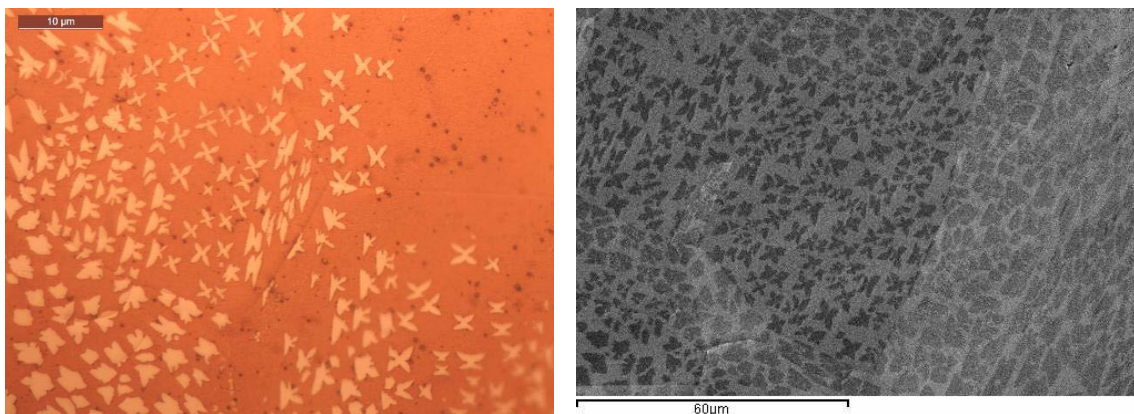


Figure 3-19. Graphene on copper after 5 minutes of growth time. Left, optical image after H_2O_2 oxidation and right, SEM image.

Figure 3-20 shows growth on electropolished copper foil using 30% methane in hydrogen and growth temperature of 950°C with increasing times. These experiments reveal interesting behaviors on graphene nucleation and growth. 30 seconds growth reveals sparse graphene nuclei that apparently have not started to grow. For subsequent increases of time show an increase in the number of nuclei until at 3 minutes there is no free copper left to generate more nuclei. From this point on these nuclei start to grow until they merge into a continuous layer. The different shapes of the nuclei observed at 0.5, 1 and 3 minutes can be attributed to different copper grain orientations and slight variations on overall pressure inside the reactor, which has been widely studied on the bibliography. For the growth conditions used (950°C and 30% of methane during the reaction) nucleation is very fast and produces a very high nucleation density, which hinders the growth stage and the possibility of obtaining large graphene grains. Note that for 5 minutes and longer grain grow to cover all available copper but do not completely merge, until times around 60 minutes as seen before. It is known that during graphene growth, its formation competes with etching of improperly attached carbon atoms by the hydrogen atmosphere inside the reactor, which can explain why under these conditions it is difficult to obtain homogeneous graphene layers. Interestingly, for times over 5 minutes, bilayer spots begin to appear and can clearly be seen as darker spots in SEM images.

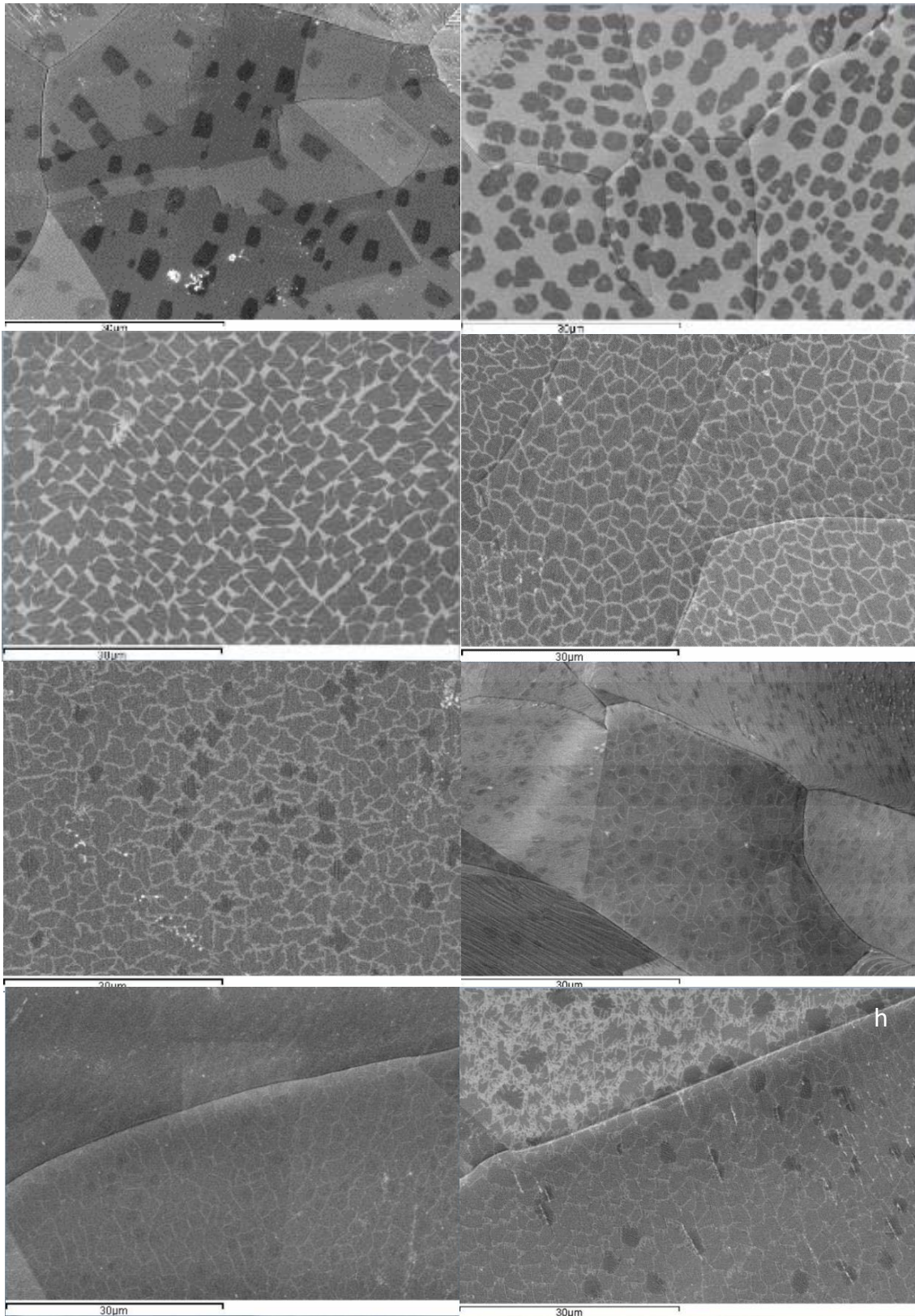


Figure 3-20. SEM images of graphenes grown on electropolished copper during different times. (a-h) correspond to 0.5, 1, 3, 5, 10, 15, 20 and 30 minutes. Scale bar is 30 μm

There are several options to hinder graphene nucleation and obtain larger grains. Most of these options rely on increasing reaction temperature, decrease the amount of methane inside the reactor and, even, enclose copper sample inside enclosures effectively impeding its access to methane. Because full copper enclosures are difficult, or impossible, to scale up to industrial production, the efforts were centered on different temperatures and methane content. Figure 3-21 shows a comparison between samples grown at 10 minutes under 950 to 1050 °C and 10 to 30% of methane. For 950°C decreasing the amount of methane translates into larger grains and, apparently, less growth because there is more space left in between each grain. Growing at 1050°C produces continuous layers already at only 10 minutes of growth with no visible separation between grains. Decreasing the percentage of methane produces also a continuous layer with lower bilayer content, compare the amount of dark spots between Figure 3-21-c and Figure 3-21-d.

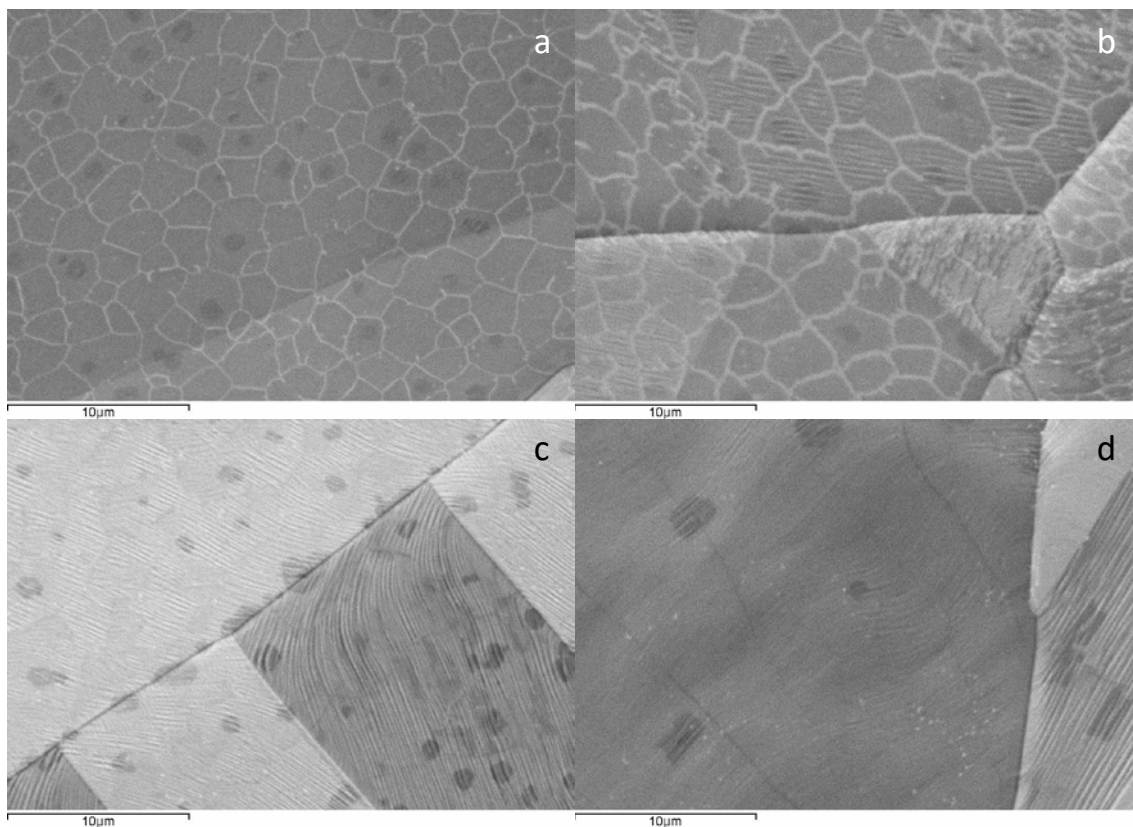


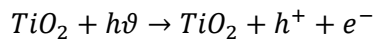
Figure 3-21. Screening of various conditions. (a) 950°C and 30% of methane, (b) 950°C and 10% of methane, (c) 1050°C and 30% of methane, (d) 1050°C and 10% of methane.

4 Graphene grain size

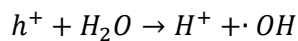
Adjusting the growth conditions serves to successfully and repetitively produce continuous monolayer graphene but, also, implies that SEM is not useful any more to differentiate graphene grain size between different samples of graphene on copper. As mentioned on the introduction, STM and TEM can observe grain boundaries at atomic resolution but are limited to very small areas and require complex transfer and sample preparation processes. On the other hand, methods like Duong's⁵³ manage to analyze larger areas by oxidizing copper through graphene defects and utilizing common optical microscopy. Trying to apply Duong's method proved to be unsuccessful as humidity could not be maintained and no visible oxidation could be observed. Thus, a new more robust method had to be developed following the photo-oxidation approach.

4.1 Photocatalytic oxidation of copper: preliminary results

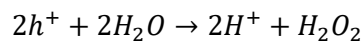
TiO₂ is a well-known photo-catalyzer able to split water when irradiated with UV light following reactions 8 to 10. Reactions 9 and 10 represent the two possible outputs of the photo-catalytic reaction producing either hydroxyl radicals or hydrogen peroxide. As Duong *et al.*⁵³ mention on their study, these are the species capable of oxidizing copper through graphene and TiO₂ maximizes the production of these. In theory, this modification can potentially provide a brand-new method for successfully revealing graphene grain boundaries more effectively.



Reaction 8



Reaction 9



Reaction 10

The firsts attempts were made by simply placing drops of TiO₂ (AEROXIDE® P25) water suspensions directly on top of copper samples and irradiating for a certain time from 10 to 120 minutes. The atmosphere was kept saturated with water to prevent evaporation. Figure 4-1 shows the complete process for these samples, these were attached to a SEM support using graphite tape and a 30 µL drop of TiO₂ water suspension is placed on top of it. After photocatalytic oxidation, the drops are rinsed off. This set-up is meant to allow both optical and SEM characterization. As it can be seen in Figure 4-1 (c), representative for all samples, it appears that samples are properly oxidized.

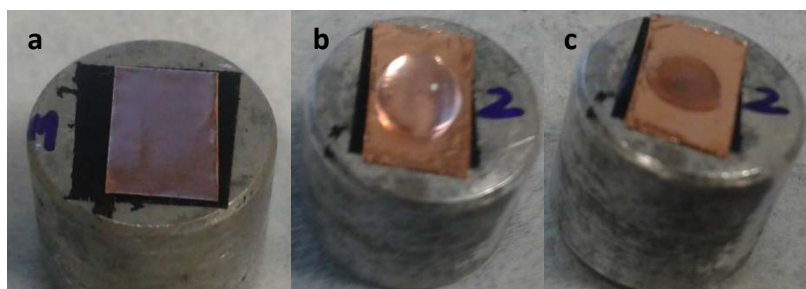


Figure 4-1. Chronological order for the firsts attempts: (a) bare sample, (b) sample with TiO₂ 30μL drop, (c) after oxidation.

Figure 4-2 shows samples before and after oxidation. Before show the typical rolling marks of copper and after photocatalytic oxidation it shows many dark spots, which might indicate a successful oxidation although it also appears that has some “3D effect”, which does seem coherent with the generation of copper oxides at the surface of copper surface through graphene.

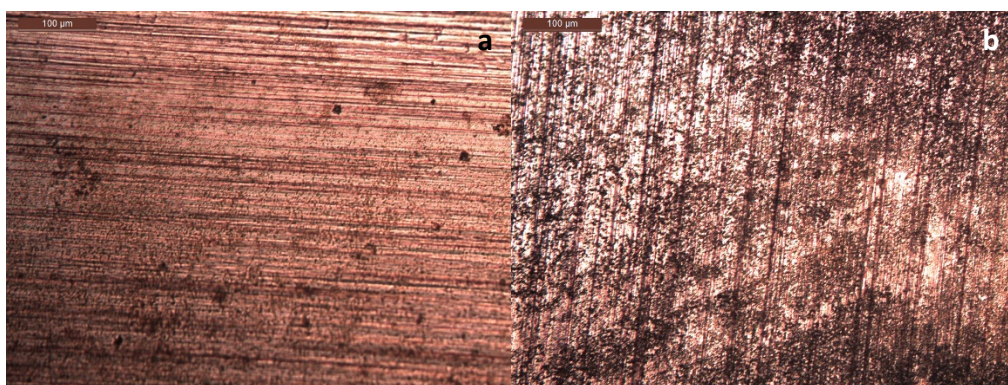


Figure 4-2. Graphene/copper sample before (a) and after (b) 120 minutes of photocatalytic oxidation using 0.1% of TiO₂ in water. Scale bar is 100 μm.

Although it seems consistent, this oxidation appears to be too high for what it was expected and as SEM confirms, see Figure 4-3, lots of TiO₂ particles deposited to the surface of the sample during the oxidation process due to the lack of agitation of the samples. Working with droplets of TiO₂ suspensions makes it very difficult to properly agitate samples and maintain TiO₂ particles properly suspended during the whole process. As an alternative, it is possible to properly remove the deposited particles using ultrasounds to assess the extent of the photocatalytic oxidation process. As a side effect of this deposition, clusters of TiO₂ particles can obscure the copper surface stopping the oxidation at some spots of it.

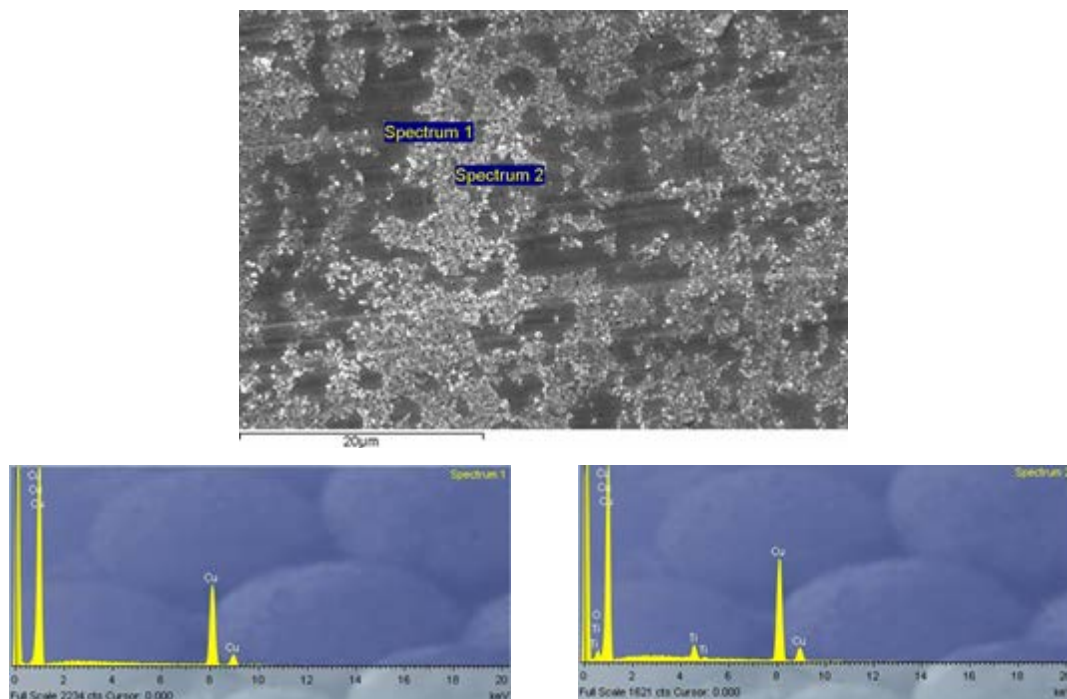


Figure 4-3. SEM image of a Graphene/Copper sample after photocatalytic oxidation. Particles of TiO_2 can be clearly seen on the copper surface, bottom spectra confirm this observation.

Figure 4-4 shows multiple oxidations using different concentrations of TiO_2 and different times after cleaning deposited TiO_2 particles. The first observation to be made is that extending the time from 2h to 4h does not produce any significant improvement to the oxidation. On the other hand, TiO_2 concentration plays a crucial role on the amount of oxidation achieved. Lower concentrations produce inhomogeneous oxidation patterns and erratic results. 0.005% TiO_2 showed some homogeneous patterns at 2h while the 4h sample seems to show close to no oxidation, and this can be attributed to TiO_2 particles aggregating and precipitating. Also, due to the low concentration it is entirely possible that different samples behave differently. Going up to 0.05% TiO_2 it still produces erratic results although oxidation spots seem to cluster up into larger areas. Finally, 0.1% of TiO_2 , which correspond to the maximum concentration that produces translucent drops produces the most homogeneous oxidation of the three. Oxidized areas cluster to form dark areas over almost the whole image, which is desirable as it will enable graphene characterization over large areas.

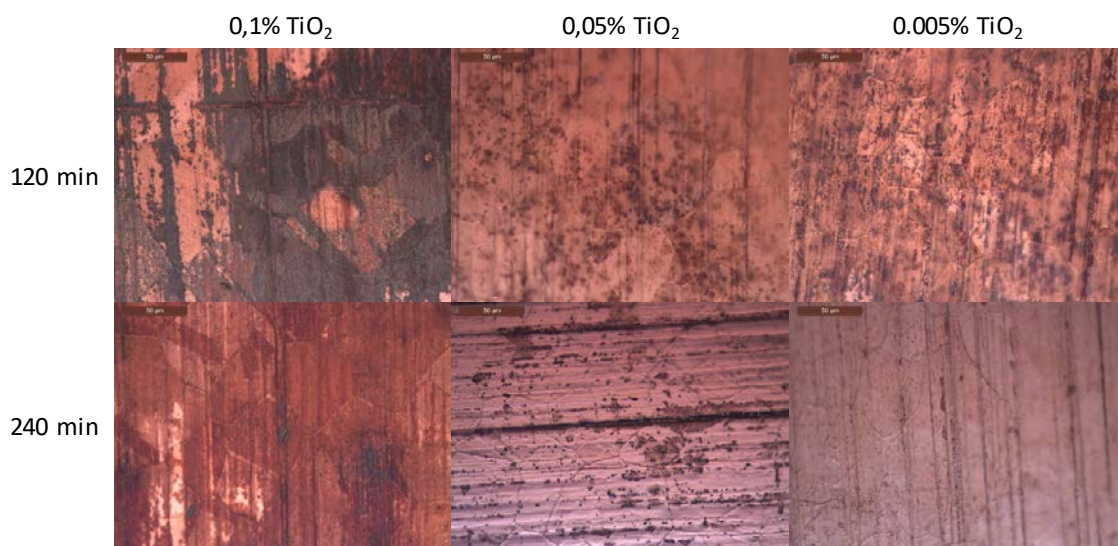


Figure 4-4. Photocatalytic oxidation on Graphene/copper samples using different TiO_2 concentrations and different times. Scale bar is 10 μm .

Although no graphene is present on Figure 4-4 these samples serve to determine the viability of the process. Performing this oxidation using 0.1% TiO_2 and 240 minutes with a graphene/copper sample it is possible to find small areas with properly revealed graphene grain boundaries. As Figure 4-5 shows inside the yellow circles, thin black lines can be observed that correspond to graphene grain boundaries. This result is consistent with Duong's observations.

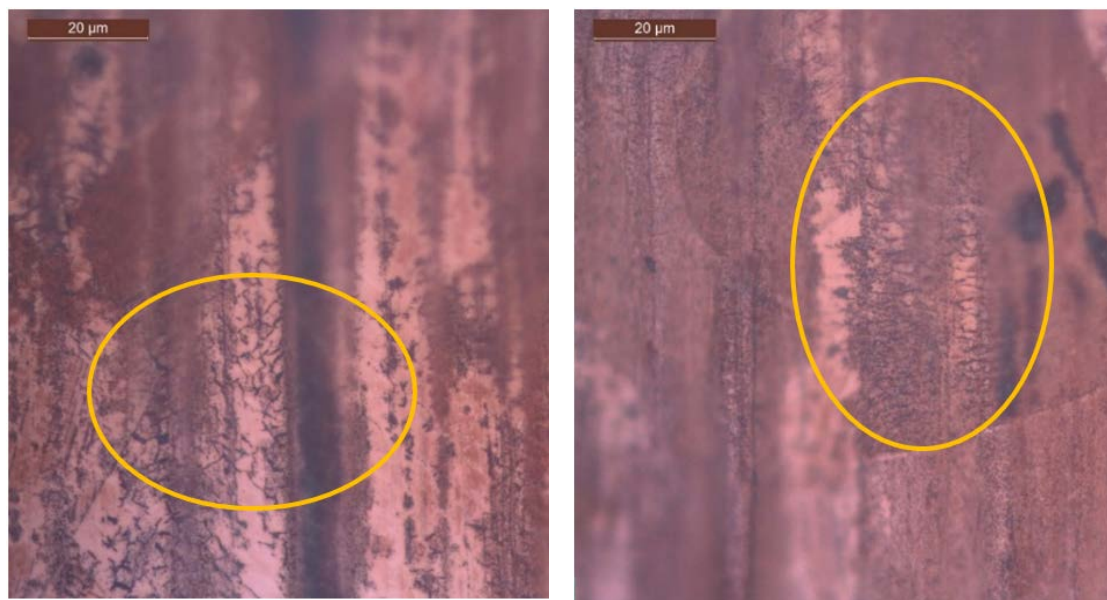


Figure 4-5. Small areas showing graphene grain boundaries. 0.1% TiO_2 and 120 minutes of oxidation is used. Scale bar is 20 μm .

4.2 Photocatalytic oxidation of copper: method development

Having established that the use of photocatalytic oxidation as a viable option to reveal grain boundaries using static TiO_2 suspension drops, it must be improved by continuously agitating samples to avoid TiO_2 precipitation. A viable option that might also simplify the application of the method is to entirely immerse the Graphene/copper samples into the 0.1% TiO_2 suspensions and continuously agitate the samples during UV irradiation using an orbital shaker to keep the catalyzer particles properly suspended. Figure 4-6 shows a schematic representation of this method.

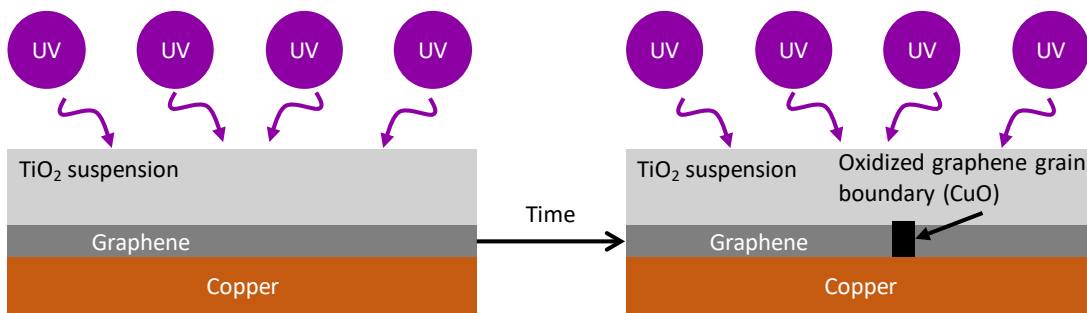


Figure 4-6. Schematic for the photocatalytic oxidation method.

Oxidation can be easily controlled by tuning the power of the irradiation lamps or adjusting the irradiation time. Because UV irradiation uses four 4W Philips fluorescent lamps with a wavelength of 254nm, power is left fixed at 16W. Having the particles suspended at all time meant that the process is much more efficient thus, the irradiation time had to be shortened. Time had to be adjusted and the optimal was found at 2h with clearly visible graphene grain boundaries as Figure 4-7 shows.

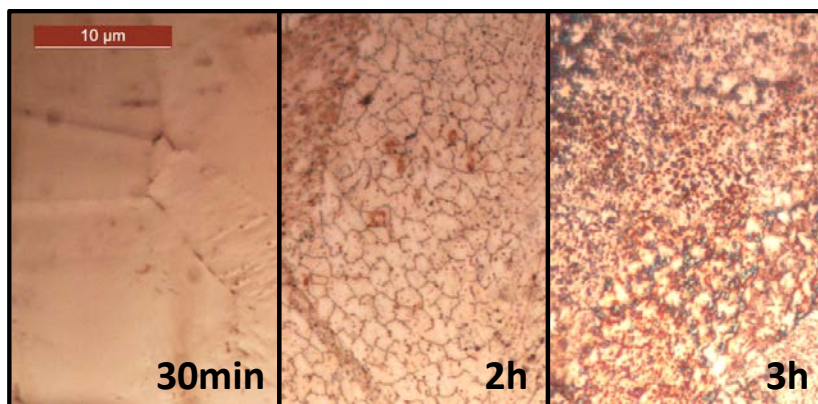


Figure 4-7. Oxidation stages. 30 minutes shows under oxidized sample, 2h represents optimal oxidation with clearly visible graphene grain boundaries and 3h shows the result of over oxidation.

Moreover, for a continuous sample where grain boundaries are invisible for both SEM and optical microscopy, this photocatalytic oxidation method allows to clearly reveal grain boundaries. Figure 4-8 shows how oxidized grain boundaries are observable as dark lines on optical microscopy and clear lines on SEM.

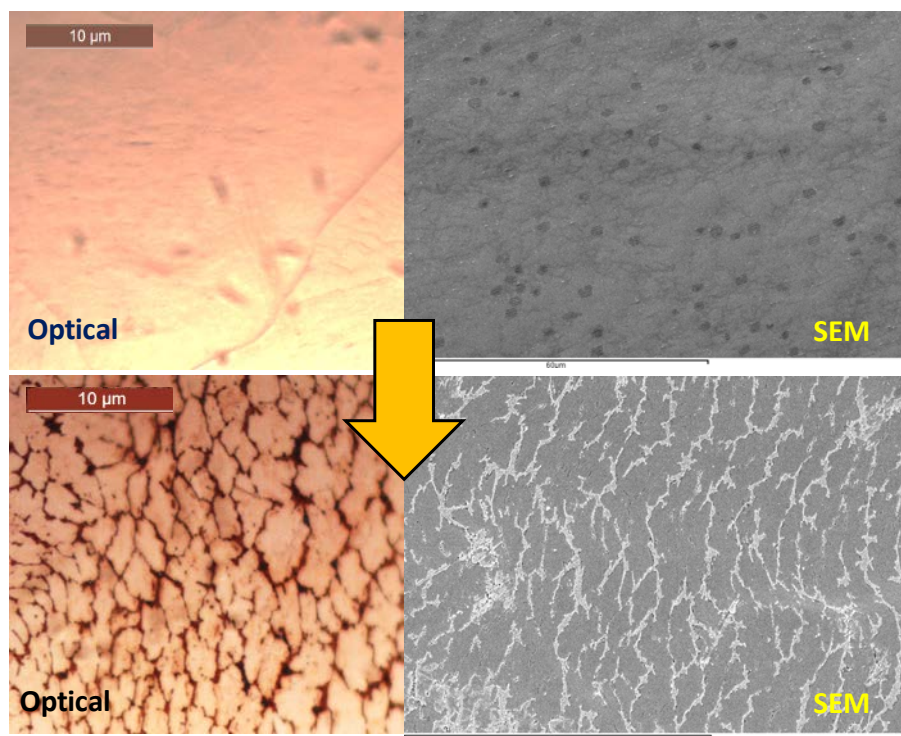


Figure 4-8. Evolution of a sample from original (top) to oxidation (bottom) after 2h of irradiation.

Table 4-1 summarizes the graphene samples used in this work. Samples 1 and 2 are commercially available graphene (monolayer graphene on Cu (60mm x 40mm), Graphenea S.L.) presenting full coverage of copper growth substrate. The rest are grown using the reactor developed in this thesis and share some characteristics: all are grown on electropolished copper, annealing is carried out at growth temperature under 30sccm of hydrogen and growth is performed under a fixed mixture of 30:70 methane: hydrogen with a flow of 88sccm. Sample 3 is grown at 1000°C for 15 minutes, while Samples 4 and 5 are grown using gas flow restrictions at 1030 and 1050°C for 30 and 60 minutes, respectively. These restrictions are performed by resting a quartz slide directly on top of the sample.

Table 4-1. Description of samples used in this study.

Sample	Description
#1	Commercial directly on growth substrate
#2	Commercial transferred onto electropolished copper
#3	950°C, 15min
#4	1030°C, 30min, full enclosure
#5	1050°C, 60min, full enclosure

Figure 4-9 shows Raman spectra for all samples. All exhibit well-defined and symmetrical G and 2D peaks with a relation of intensities I_{2D}/I_G over 2 for each case, meaning all samples are mainly composed of monolayer graphene.

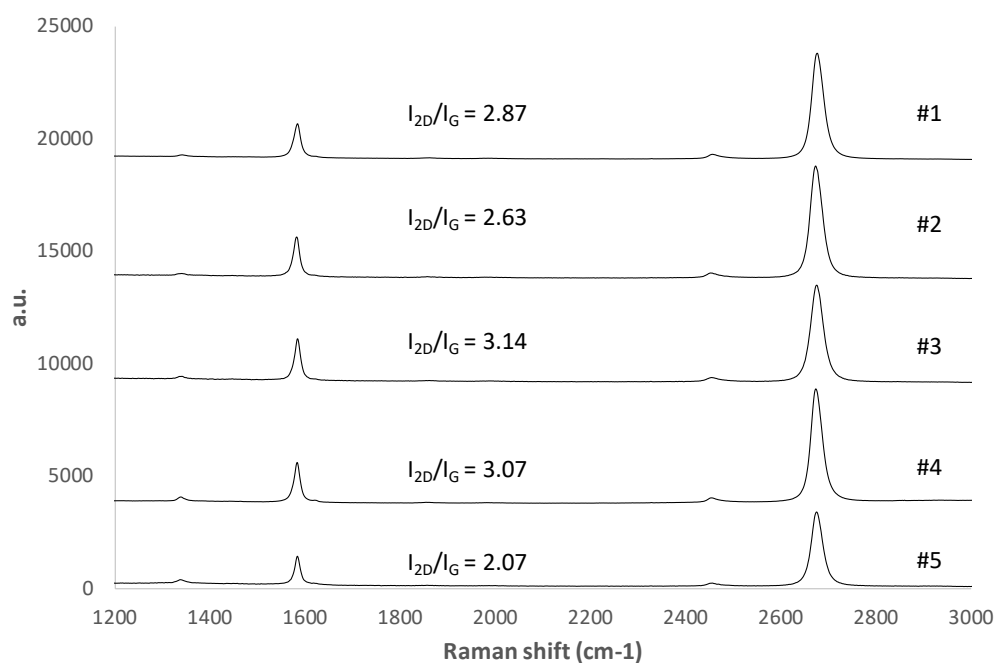


Figure 4-9. Raman spectra from all samples.

Using commercial graphene with known characteristics being a continuous monolayer with full coverage across the samples allowed us to validate the method. As mentioned before, the presence of graphene or its microstructure cannot be observed using optical microscopy directly on the growth substrate. After photocatalytic oxidation, graphene grain boundaries are revealed as thin dark lines. Sample 1 presents copper substrate with numerous imperfections, and it is not flat, which greatly hampers the observation of fine graphene structure under optical microscopy (see Figure 4-10-a). Transferring processes are not ideal due to their complexity, which can potentially damage graphene or induce local oxidation on the final substrate, especially when a wet method is used to transfer onto metallic substrates. Having said this, transferring another portion of the same commercial graphene onto a clean electropolished copper with an Sq (RMS) under 10nm – obtained through AFM measurements – dramatically improved the results obtained from photocatalytic oxidation (see Figure 4-10-b), making graphene grain boundaries visible through much larger areas. Thin dark lines correspond to graphene grain boundaries while larger oxidized areas occur during the water evaporation step of the wet transfer method used. These results confirm the viability of the method and its ability to perform over different substrates with different morphologies.

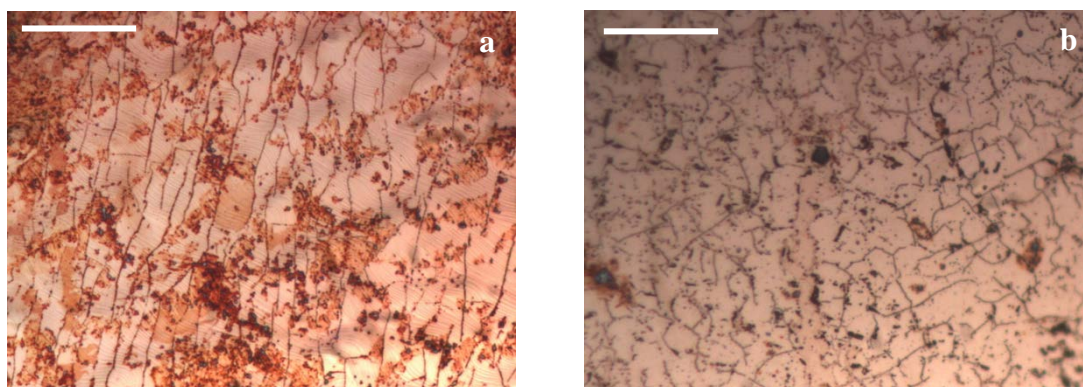


Figure 4-10. Both images are related to commercial graphene samples after photocatalytic oxidation. Image (a) is on top of original copper substrate – Sample 1 – as it can be seen that there are areas in which copper is already oxidized prior to treatment. Image (b) shows a similar graphene transferred to a clean and flat substrate – Sample 2 – presenting a much cleaner result. Concentrations of dark areas are due to the transfer process. The scale bar is 10 μ m.

Transferring both as-synthesized and oxidized – Sample 2 – commercial graphenes onto silicon wafers allows for the Raman spectroscopy study of these samples (see Figure 4-11). As expected, commercial graphene is monolayer with I_{2D}/I_G of 2.8, a sharp and symmetrical 2D peak and an almost inexistent D peak. After oxidation, however, I_{2D}/I_G decreased to 1.4 and D peak intensity almost doubled. As graphene cannot turn into a bilayer by itself, the difference in Raman spectra is related to lightly damaged graphene, and we expect that this damage is concentrated around grain boundaries. In 2013, Childres et al.¹³² exposed graphene to oxygen plasma pulses – a much more aggressive method sometimes used for graphene removal – achieving similar results with progressively decreasing I_{2D}/I_G and rapidly increasing D peak intensities for increasingly damaged graphene. Such observations confirm that our method moderately damages graphene.

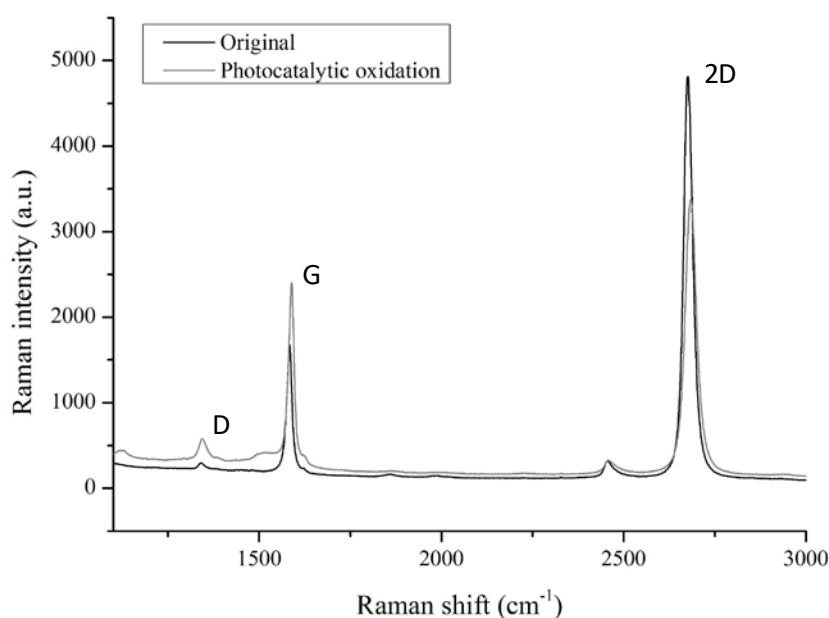


Figure 4-11. Raman spectra of commercial graphene before – original – and after photocatalytic oxidation.

The first column in Figure 4-12 shows SEM images of as-synthesized graphene on copper. As can be seen, Samples 3 to 5 show continuous graphene layers with barely visible grain boundaries. Sample 4 shows darker spots that resemble hexagons, which are bilayer graphene confirmed through Raman spectroscopy mapping (see Figure 4-13), as these spots present an I_{2D}/I_G of approximately 1. The second column in Figure 4-12 shows optical images after oxidation, and it can be observed that the graphene grain boundaries became much clearer. Optical images present these boundaries as dark lines corresponding to the darker copper oxide generated. Some discontinuities in grain boundaries can be observed in sample 5 (Figure 4-12-f), probably caused by the presence of local bilayer spots that would inhibit the oxidation of copper. This is consistent with the longer reaction time of sample 5, more prone to multilayer formation.

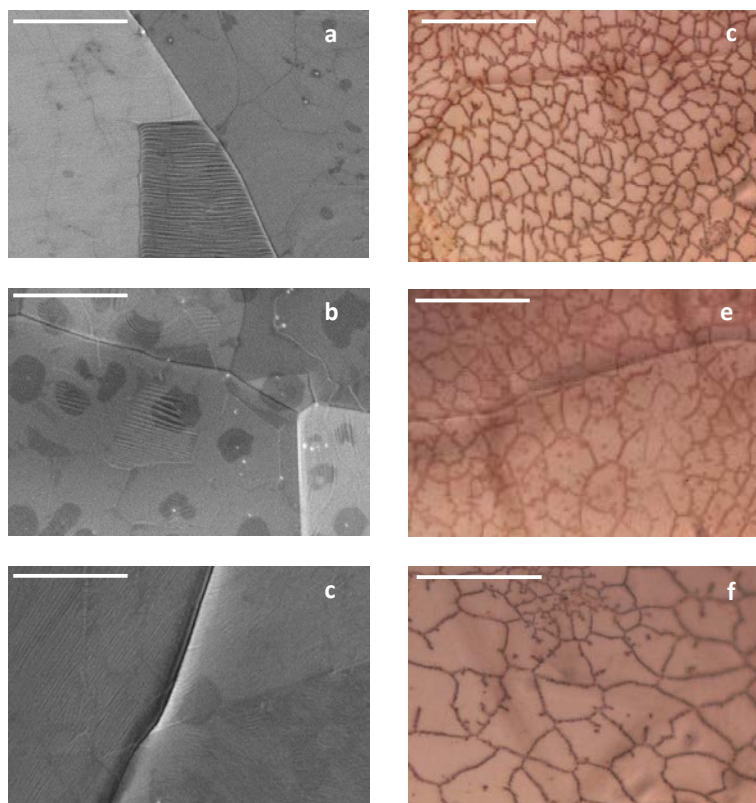


Figure 4-12. Results for graphenes made by our group. The rows from top to bottom show Samples 3, 4 and 5. Images (a), (b) and (c) represent SEM images from as-synthesized samples, while (d), (e) and (f) show optical images after photocatalytic oxidation. The scale bar is 10 μm .

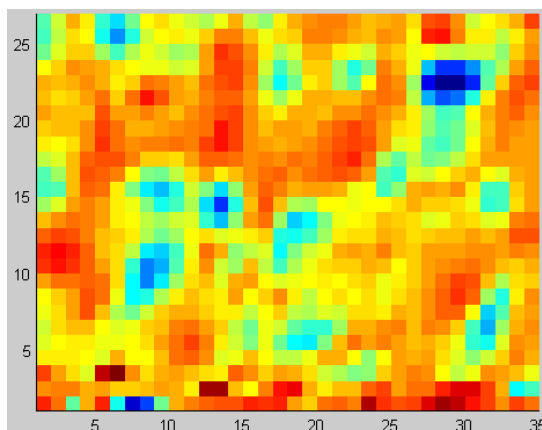


Figure 4-13. Raman spectroscopy mapping from Sample 5 with a 50x objective (both axes in microns). The dark blue spots represent bilayer or multilayer graphene islands; the rest is monolayer graphene.

AFM analysis of Sample 4 (see Figure 4-14) shows clearly revealed graphene grain boundaries against copper substrate, while the darker deeper line corresponds to a copper grain edge. These oxidized lines are expected to protrude from the surface, as copper oxide occupies more volume than copper metal. However, the ultrasonic cleaning required to fully remove TiO_2 particles causes copper oxide to spall off, leaving voids and craters behind.

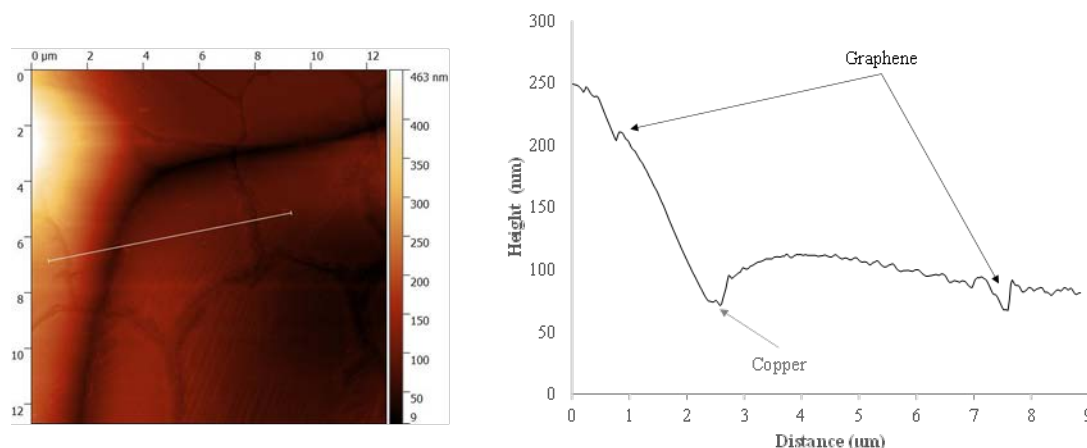


Figure 4-14. AFM image of Sample 4 after photocatalytic oxidation. The profile on the right shows a large dip related to copper grain boundary and two smaller dips on either side that represent graphene boundaries after oxidation.

Finally, we proceeded to analyse grain sizes from these samples using two different standardized methods. First, we applied ASTM 112-13¹³³ (see Figure 4-15-a), although this standard is originally intended for metallographic samples. This method is based on drawing two or more random lines and manually counting intersections with grain boundaries. We then performed an image analysis, using ImageJ freeware^{134,135} (see Figure 4-15-b), which allows for semi-automatic counting by recognizing grain boundaries. Finally, grain size was calculated as the diameter of equivalent circles of the same area.

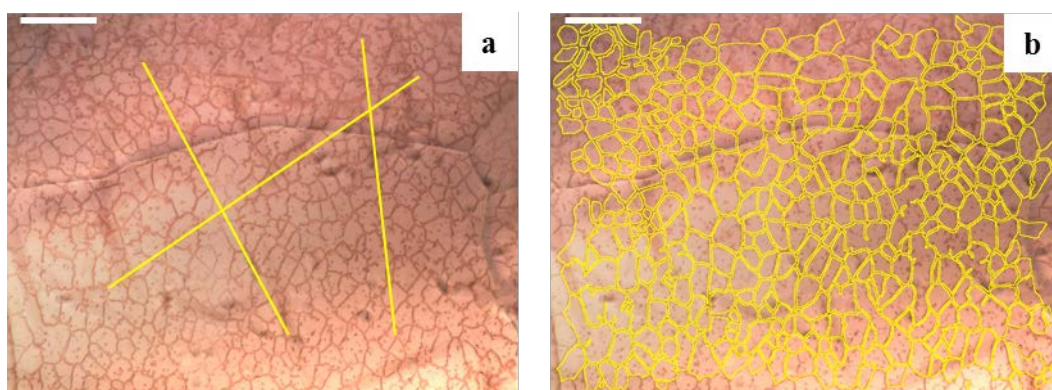


Figure 4-15. Representation of both grain size methods applied on sample 4 (1000x magnification). (a) Lines used for ASTM manual count and, (b) automatically recognized grain boundaries used for image analysis. The scale bar is 10 μm.

ASTM standard takes into account only those grains crossed by user drawn lines (in this case, three lines), while automatic methods consider virtually all grains in the image for statistics. Table 4-2 summarizes the results for Samples 3, 4 and 5. The grain size results are very similar for both methods, although they are slightly higher for image analysis. Sample 3 yields identical results for both methods while for samples 4 and 5 image analysis results in 7.7% and 5.1% bigger sizes respectively. Analysis of commercially available graphene samples could not be performed due to the excess of copper substrate imperfections.

Table 4-2. Comparative results for all three graphenes obtained through ASTM and image analysis, showing average size and standard deviation for the latter. The number of grains used in the calculation is also shown. All sizes are expressed in μm .

Sample	ASTM		Image analysis	
	size	number of grains	size	number of grains
#3	1.4	96	1.4 ± 0.5	1089
#4	2.4	39	2.6 ± 1.0	350
#5	3.7	32	3.9 ± 1.2	192

Although both methods provide a simple yet useful average grain size, image analysis also allows for more detailed statistics, yielding real graphene grain size distributions. Note that the number of grains used in the calculation is considerably higher in the case of image analysis, which allows for a statistical approach. Figure 4-16 shows grain size distribution for samples 3, 4 and 5; the bars represent frequency versus size, with increments of $0.2 \mu\text{m}$. In all cases, unimodal Gaussian curves can be fitted to histograms, and the larger crystals are more than five times the size of the smallest ones for each sample. Moreover, it is clear that, for bigger average grain sizes, these curves become flatter (lower number of grains), with slightly broader distributions (see increasing values of standard deviation in Table 4-2), which is common behavior for other materials such as metals.

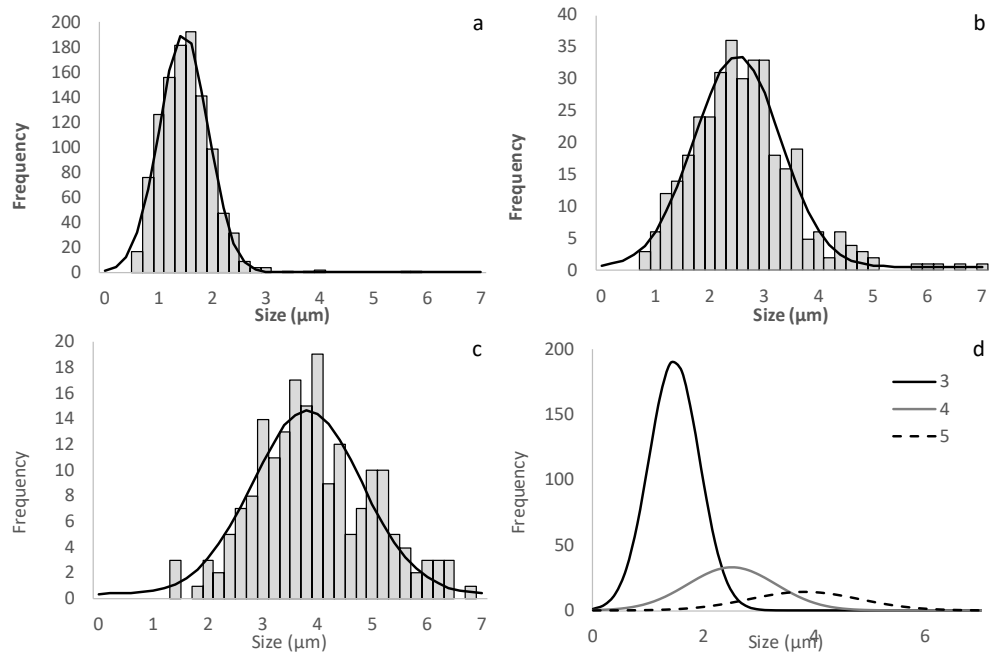


Figure 4-16. Grain size distribution. Images represent distributions and adjusted Gaussian curve for (a) sample 3, (b) sample 4 and (c) sample 5. Image (d) represents the combination of the fitted Gaussian curves.

Q-Q plots have been used to assess the quality of the fitting of real grain size data to Gaussian distributions. Figure 4-17 shows Q-Q plots for data between quantiles 10% and 90% for samples 3 to 5. In all cases grain size data are beyond doubt normally distributed, although samples 4 and 5 are slightly right skewed. As mentioned above, the latter could be explained by hidden grain boundaries under local bilayer graphene areas, which would cause image analysis to slightly overestimate sizes of some grains.

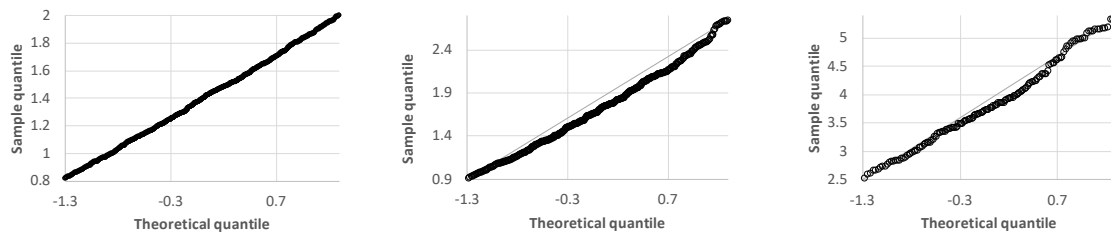


Figure 4-17. Q-Q plot representing sample quantile (grain size) vs. theoretical quantile (normal distribution). From left to right: samples 3, 4 and 5.

Overall, these results prove graphene grain size distributions can be measured using well-established and standardized methods from metallography. Ultimately, this can translate into a path to standardize the determination of graphene grain size distribution.

5 Grain size control

Until this point the solely quality control for our CVD graphene on copper was Raman spectroscopy to determine the presence of monolayer and the continuity using SEM. Having successfully developed the method for statistically analyzing grain sizes opens the possibility of assessing and trying to control grain size for CVD growth.

As we have already seen, changing the temperature and methane content of the graphene growth can have a deep impact on the final product. Higher temperatures decrease nucleation and increase growth rate while decreasing methane limits nucleation and growth. Many authors explain how to use copper enclosures to effectively suppress copper evaporation during graphene growth and improve its final quality. Because these enclosures are not reusable, must be prepared for each reaction and are difficult to scale up to industrial scale. A possible modification will be to “sandwich” the copper foil between two quartz slides to achieve a similar effect, authors used silicon wafers to suppress copper evaporation but have not studied its effects of graphene nucleation and growth ³⁷. This set-up though, opens the possibility of fine tuning the opening, or gap, between the two plates effectively restricting copper substrate access to methane slowing down graphene nucleation and growth. Figure 5-1 shows how a cross-section of the reactor with the quartz slides. Also, these gas flow restrictions are a first approach to a commercial CVD furnace growing graphene on lots of copper foils at the same time or, even, a fixed bed reactor full of copper particles.

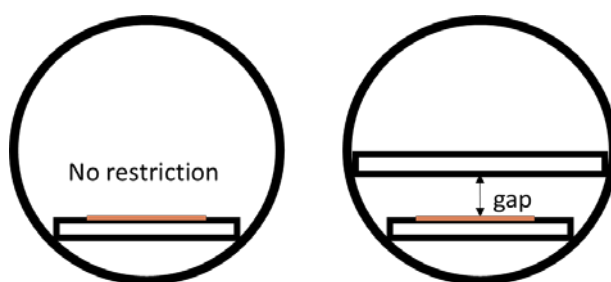


Figure 5-1. Cross-section of the reactor with applied restrictions.

To determine the effect of these restriction set-ups, graphene will be grown using 3 gaps between the plates at 3 temperatures each one. The gaps used are a standard set-up without the top quartz plate, a gap set to 0.5 mm and an extreme case with the top plate resting on the top of the copper foil thus, generating a gap of approximately 10 μm between the plates and “0 mm” where there is copper (it fills the gap). For the sake of reducing the number of variables, methane content during growth is fixed to 10% and the time at 10 minutes. By applying these restrictions, it is expected that nucleation is impeded and, thus, yielding graphene in the early stages of growth. Eventually, this can lead to non-continuous layers of graphene.

Table 5-1. Summary of the gaps and temperatures used.

Gap	Temperatures used
No restriction (only bottom plate)	950 $^{\circ}\text{C}$
0.5 mm	1000 $^{\circ}\text{C}$
“0 mm”	1050 $^{\circ}\text{C}$

Computational Fluid Dynamics simulations using SolidWorks® are performed for all three restrictions. These simulations are performed using the whole geometry of the tubular reactor, with an inlet of 88 sccm of 10% methane/hydrogen, an outlet set to 3×10^{-2} mbar. The walls of the reactor are set to ideal walls as the roughness is unknown but is expected to be very low as quartz is really smooth and the interaction between gases and solids is minimal. Although the absolute value of the gas flow might not be 100% accurate the important value is the decrease on the gas flow. As it can be observed on Figure 5-2 the “no restriction” configurations present a homogeneous gas flow across the whole section with a minimal velocity reduction when it meets the quartz plate. Due to the low roughness of all quartz surfaces, boundary layers are virtually inexistent. Creating a 0.5mm gap represent a reduction of gas velocity of about 40% while decreasing it to 10 μm it appears gas flow is completely stopped. There are two possible explanations to this, or the gap is too shallow for Solidworks® to actually calculate inside it (size of finite elements) or gas flow in these region is driven by diffusion, which is outside the ability of Solidworks®. In practice, these simulations confirm that the restrictions will affect the rate at how carbon atoms reach the surface of the copper catalyzer without the need of major modifications to the reactor.

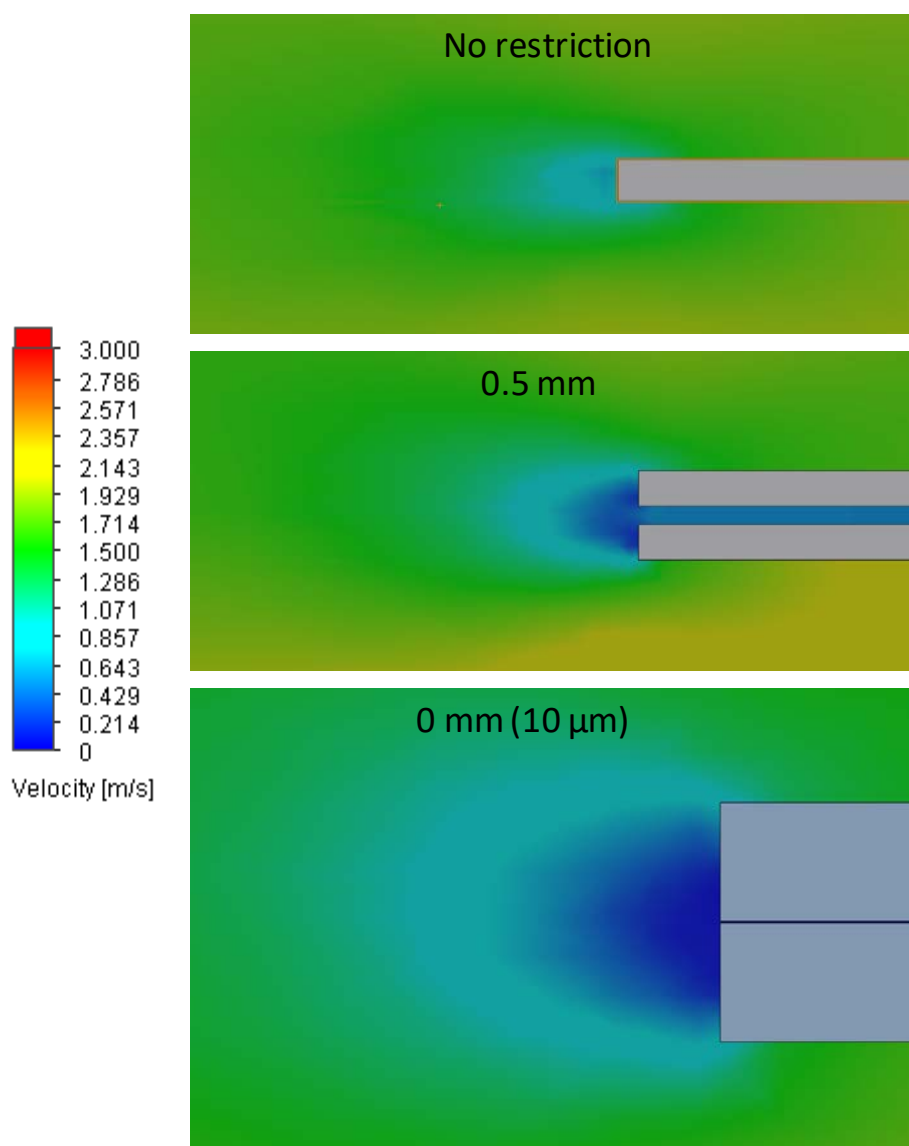


Figure 5-2. CFD simulations of the three restrictions.

Once graphene is grown samples are split into two pieces. The first is wet transferred (see recipe on Annex 3) onto Si wafers coated with 300 nm of silicon oxide to allow proper Raman spectroscopy analyses. The second piece is subjected to our photocatalytic oxidation method to measure its grain sizes.

SEM images of these reactions can be seen on Figure 5-3. Results clearly show that temperature limits graphene nucleation while boosting its growth rate. This is coherent with the bibliographic results as some authors indicate that higher temperatures decreases the life time of carbon atoms adsorbed to the copper surface, thus, decreasing the nucleation rate ¹³⁶. Past the nucleation stage, growth is limited by the mobility of carbon atoms at the surface, which is enhanced by higher temperatures ^{33,136}.

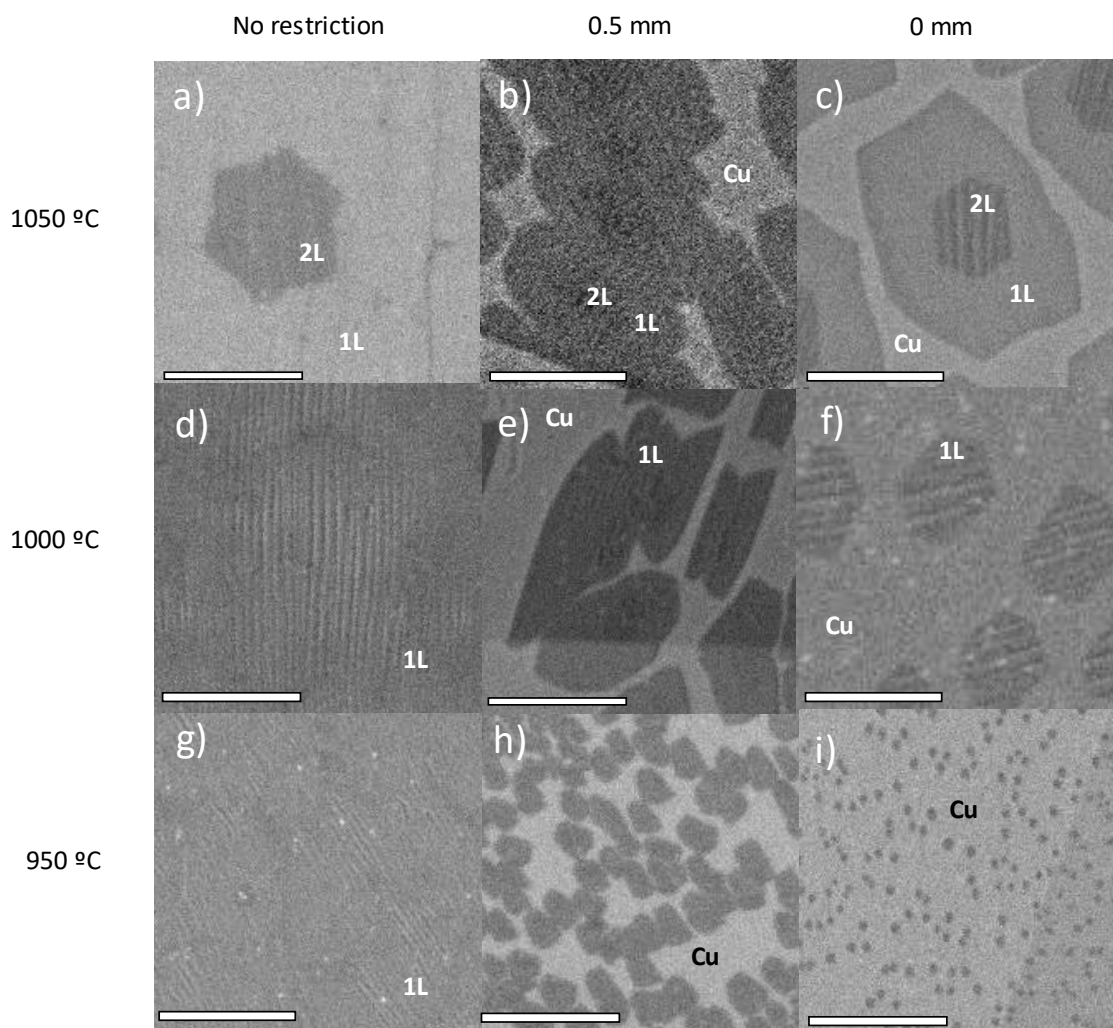


Figure 5-3: SEM images of graphene on copper using 10% methane and 10 minutes reaction time for different conditions of temperature and gas restriction. Scale bars are 5 μm for every image.

On the other axis, it can be observed that restrictions work as intended as the samples with free flow (“no restriction”) present continuous layers while the restricted ones show non-continuous graphene. These results are also coherent with the CFD simulations as reducing the gap seems to greatly impede methane accessibility to the copper substrate. Moreover, the “0 mm” gap generates an extreme situation with nucleation being very sparse.

As stated before and as Li *et al.* showed²⁹, lower temperatures translate into higher nucleation rates and slower growth while high temperatures have the reversed effect. This is amplified by applying these restrictions Figure 5-3-g shows a continuous graphene that rapidly translates into graphene nuclei in Figure 5-3-h. For the extreme situation of 950°C and “0 mm” gap, Figure 5-3-i, nucleation is much sparse and growth is reduced to a minimum, which means not much methane was present during the growth and confirms that these restrictions greatly impedes gas flow.

For the other extreme temperature, 1050°C, behavior is very similar although growth is much faster. Figure 5-3-a also presents a fully continuous layer but with islands of bilayer graphene. Figure 5-3-c shows clearly separated graphene nuclei but, this time, growth is fast enough to have generated already large grains that present the characteristic bilayer on its center. The middle temperature represents an intermediate situation between the other two.

Photocatalytic oxidation method allows to measure both non-continuous graphene and continuous graphene using the same equipment thus, eliminating variability. Figure 5-4 resumes the measurements obtained using this method. With no restriction, increasing temperature tends to produce larger graphene grains, being this consistent with reported results and our observations. The extreme restriction shows a steady increase on the size of graphene with temperature. Finally, the middle restriction shows a marginal increase from jumping from 1000°C to 1050°C.

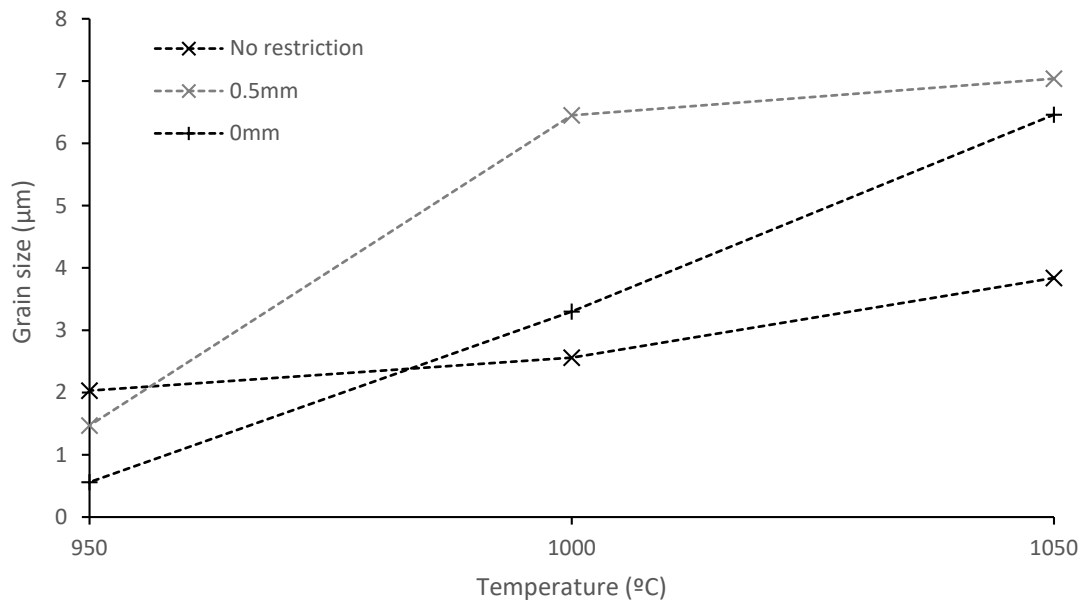


Figure 5-4. Graphene grain size measured for conditions with 10% methane and 10 minutes of growth time.

Although this comparison leads to conclude that 0.5mm restriction produces larger graphene grains it must be said that the 10 minutes of growth time is quite short and for some samples it is not sufficient. Looking at the images in Figure 5-3 it seems clear that the maximum restriction leaves nuclei much more separated, with more free copper to allow graphene growth. This might lead into maximum restriction producing larger grains at any temperature if samples are allowed enough time to grow.

For these samples both punctual Raman spectroscopy analysis and mapping are performed to fully characterize these samples. Punctual Raman spectra obtained for each sample is shown in Figure 5-5, revealing that the graphene obtained is monolayer with a I_{2D}/I_G ratio higher than 2³ and sharp and symmetrical peaks. The signal obtained around 1350 cm⁻¹ (D peak) is related to the defects present in graphene structure. Most of the samples show almost no D peaks except for 950°C with restrictions, where this peak is noticeable and correspond to the samples with smaller graphene nuclei. Raman spectra is being acquired taking into account graphene's edges due to the relatively large laser spot (approximately 1.5 μm) in comparison to the graphene nuclei.

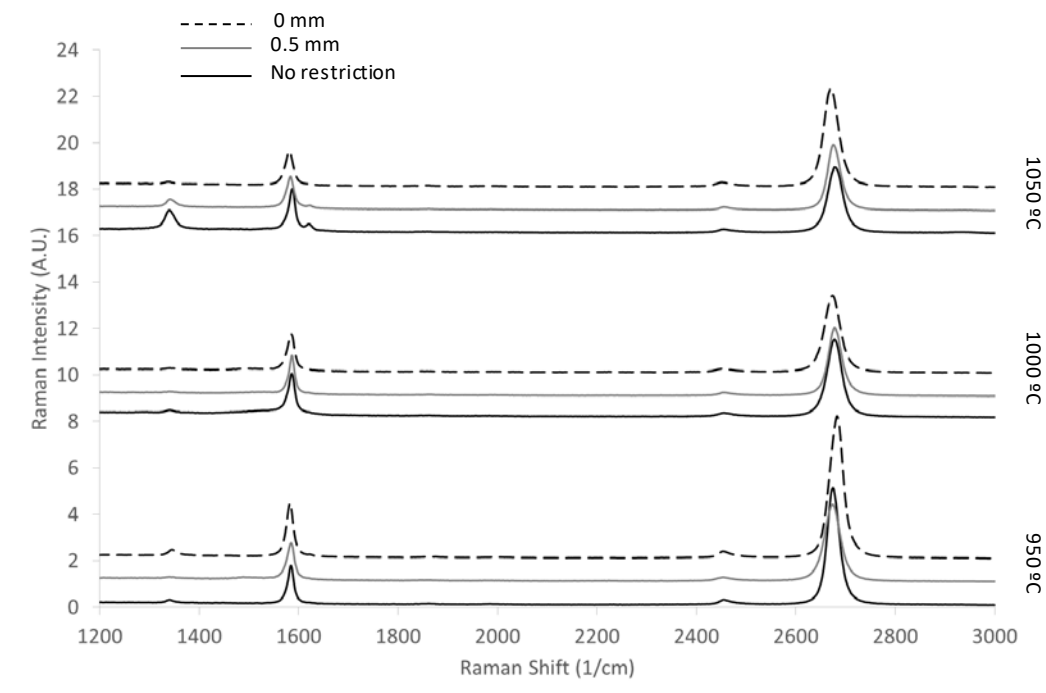


Figure 5-5: Raman spectroscopy data for graphene on SiO₂ in all growth regimes.

Although punctual Raman spectroscopy suggest these produced graphenes are purely monolayer, SEM images clearly show the presence of some bilayer zones. In order to fully characterize these samples and confirm the SEM observations, Raman spectroscopy mappings are performed using the same 532 nm green laser and a 1 μm resolution. Figure 5-6 shows mappings of the I_{2D}/I_G ratios for all the samples except for 950°C and maximum restriction, which has nuclei actually too small to produce a successful mapping. These Raman spectroscopy mappings are color coded with blue representing I_{2D}/I_G close to 1 and gradually increasing to green (about 2) and red (more than 3).

Figure 5-6 (b, c, e and f) present mappings of graphene grains that are isolated from the rest and although mapping suggests these have bilayer graphene on the center these appear to be surrounded also by bilayer graphene. These is due to the I_{2D}/I_G division, when there is graphene it is dividing actual Raman spectroscopy intensities but when there is no graphene the background noise of the equipment is being divided by itself producing an I_{2D}/I_G of 1. Although not shown here, this can easily be solved by looking at the I_{2D} or I_G maps and locating the areas with no G and 2D peaks to unequivocally pinpoint areas with no graphene.

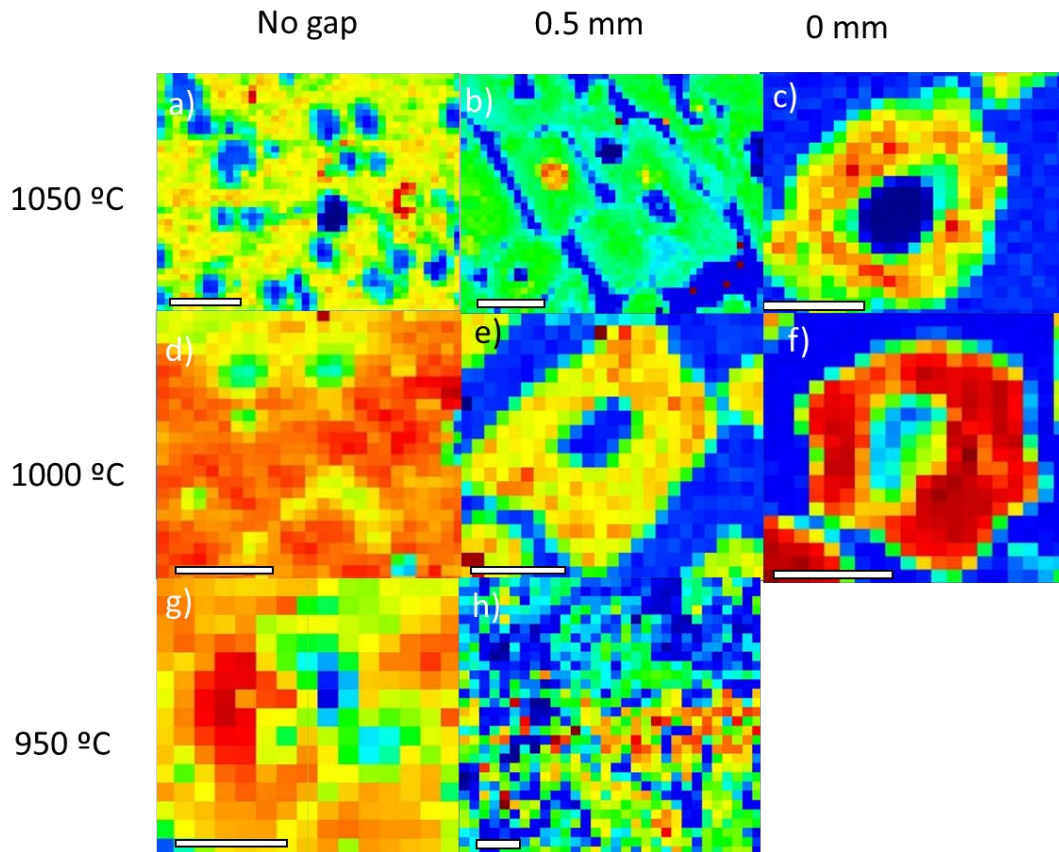


Figure 5-6: Raman spectroscopy mapping of the I_{2D}/I_G ratio for graphene obtained at every condition. The scale bar is set at 5 μm . Color scale goes from 0 (blue) to 4 (red). Raman spectroscopy mapping for 950 °C “0 mm” gas flow restriction could not be obtained due to lack of optical resolution.

In Figure 5-6-a, several multilayer spots can be observed, matching with the respective SEM image of the graphene obtained at 1050 °C and no gas flow restriction. In the continuous samples carried out at lower temperatures, lower percentage of multilayer graphene is observed, which is consistent with faster nucleation and slower growing. Graphene's grains obtained with gas flow restriction conditions shows the same pattern, having a multilayer in the center, matching with the darker zone observed in the SEM images. For 950 °C and the highest gas flow restriction, the graphene growth was too small, so no Raman spectroscopy mapping could be obtained.

Repeating the whole process but increasing methane concentration to 30% results are slightly different. Most noticeably, the increase on methane content translates into much faster growth rate and, somewhat higher nucleation rates. Samples grown at 950°C (Figure 5-7 g, h, and i) show much denser nucleation than before and reducing the restriction shows much faster growth. For the other two temperatures, the behavior is comparable as maximum restriction (Figure 5-7 c and f) nucleation is much denser and growth much faster than the same reactions performed at 10% of methane. Going to 0.5 mm restrictions (Figure 5-7 b and e) interestingly enables the production of 100% continuous monolayer graphene. Finally, graphene growth without restrictions (Figure 5-7-a, d and g) produces fully continuous graphene across the three temperatures.

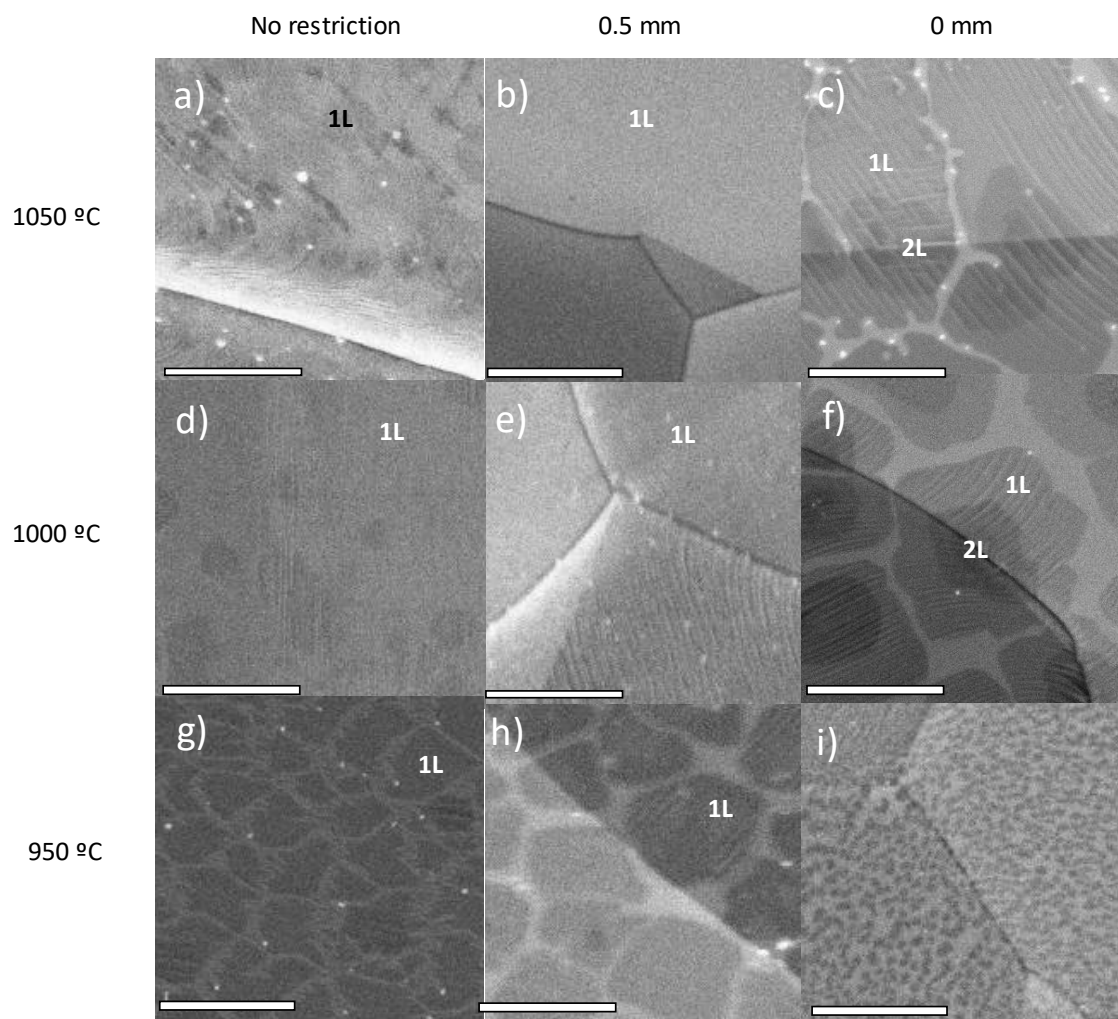


Figure 5-7. SEM images of graphene on copper using 30% methane and 10 minutes reaction time for different conditions of temperature and gas restriction. Scale bars are 5 μm for every image.

Figure 5-8 summarizes the results for the graphene grain sizes of Figure 5-7 after photocatalytic oxidation. Surprisingly, samples at 950°C not only follow a very similar pattern that before but grain sizes are also very similar. The restrictions however, exaggerate the behavior previously observed as more methane in the inlet gas means growth and nucleation are faster and the restrictions can have a greater effect than before. Specially for the samples with the maximum restriction nucleation is much sparse than for the others and plenty of exposed copper is left so graphene grains have room to grow. This is why samples with restrictions at 1050°C appear to be much smaller than the rest as these had not enough time to grow.

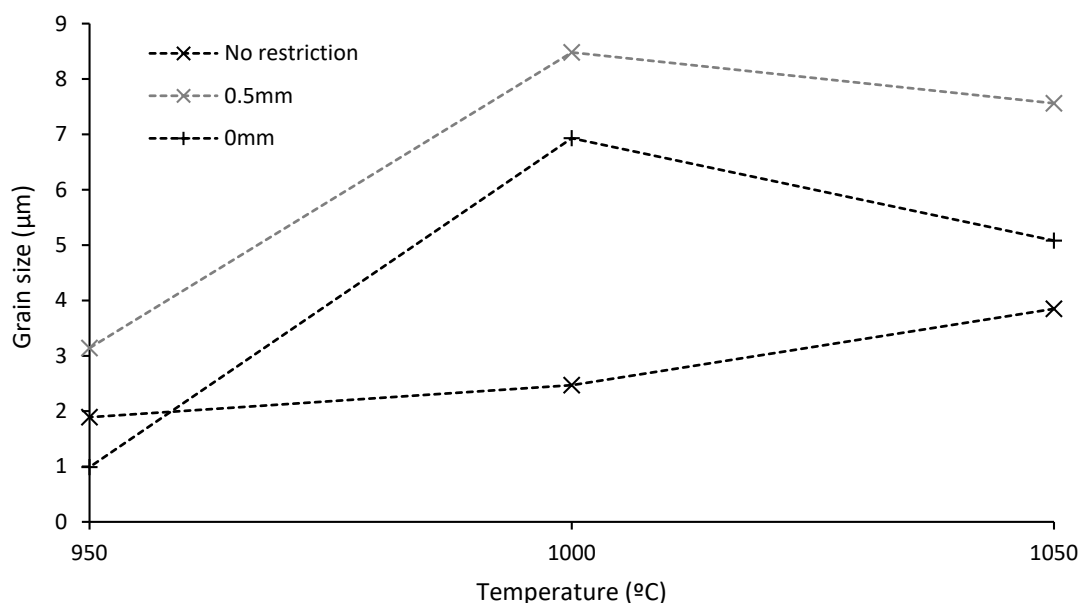


Figure 5-8. Graphene grain size measured for conditions with 30% methane and 10 minutes of growth time.

To check the possibility to obtain continuous layers with these restrictions, the conditions of 1050°C with the maximum restriction applied were selected and the time incrementally extended until a continuous layer was obtained. Figure 5-9 shows growth at 10, 40 and 60 minutes where a fully continuous graphene is obtained. Comparing the final time of one hour to just the 10 minutes required to obtain a continuous graphene without restrictions this further confirms gas flow restrictions grow by hindering methane access to the copper substrate and both nucleation and growth are slowed. An interesting feature is that both samples at 40 and 60 minutes are 100% monolayer, as determined by Raman spectroscopy, and show almost no islands of bilayer graphene.

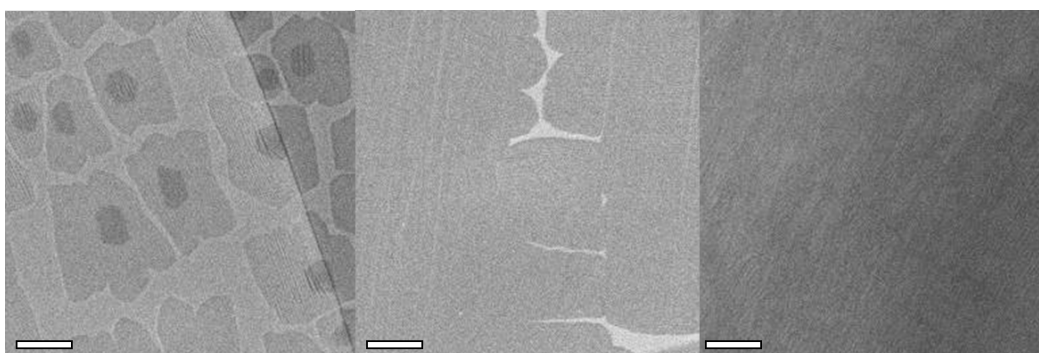


Figure 5-9: SEM images of graphene on copper at 1050 °C and 10, 40 and 60 minutes reaction time from left to right. Scale bar 5μ.

Applying the photocatalytic oxidation method makes possible to measure all three samples. Figure 5-10 show the average grain sizes and these sharply rise from 10 to 40 minutes as most of the copper is getting covered by graphene and some grains start to merge together. The increase from 40 to 60 minutes is much smaller as the remaining copper area is covered and full coalescence is achieved across the whole copper surface.

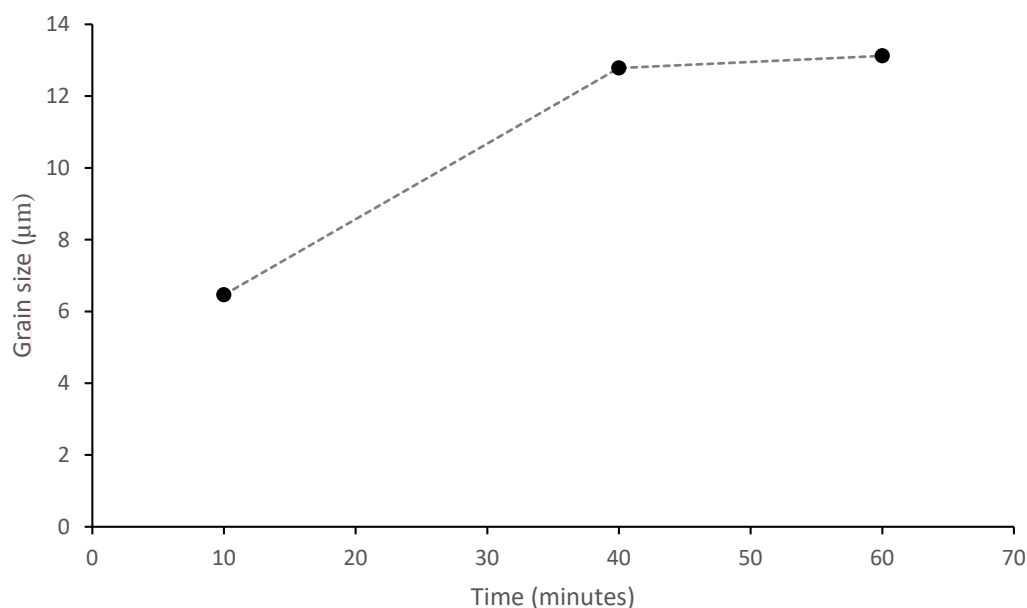


Figure 5-10: Graphene grain size measured for graphene for different reaction times at 1050 °C and “0 mm” gap.

Gas flow restrictions seem to be a viable way to alter the growth characteristics of graphene without having to apply major modifications to a graphene reactor. Also, being made of quartz allow these to be reused from sample to sample unlike copper enclosures describes by some authors.

6 Graphene characterization

Up to this point the solely characterization of graphene presented in this work was Raman spectroscopy, SEM and optical microscopy after photocatalytic oxidation. In order to compare with other graphenes it is imperative to determine its performance using some established techniques. Firstly, through a collaboration work with the Applied Physics Department at the Universitat Politècnica de Catalunya (UPC, Barcelona) it was possible to measure THz-TDS responses of our graphenes. Later, through another collaboration with Centro Nacional de Microelectrónica (CNM, Bellaterra), it was possible to physically measure electric graphene properties using a two-probe set-up after applying titanium-gold contacts through lithography.

6.1 Terahertz-time-domain-spectroscopy (THz-TDS)

THz-TDS is used to measure optoelectronic properties of materials and has the advantages of being 100% contactless and non-destructive. It has only one requirement, the substrate that holds the sample must be transparent to THz waves. These set-up uses a laser capable of emitting pulses with lengths on the range of femtoseconds (fs) or picoseconds (ps). These pulses are split into two known as the probe and the pump. The pump beam directly hits and pumps a radiofrequency emitting antenna that generates pulses in a range from 0.1 to 5 THz that are focused onto the graphene sample. These THz radiation crosses the sample interacting with it and are captured on an electro-optic THz detector. The pump pulse is delayed by a mobile mirror that varies the length of the laser path and insides on the same electro-optic THz detector to produce time-dependent transmission. The detector only gives an electrical signal when it is gated by the laser pulse. Thus, repeating the measurement at different probe delays allow to reconstruct the temporal response of the THz pulse after interacting with the sample ¹³⁷. A typical THz-TDS set-up can be seen in Figure 6-1.

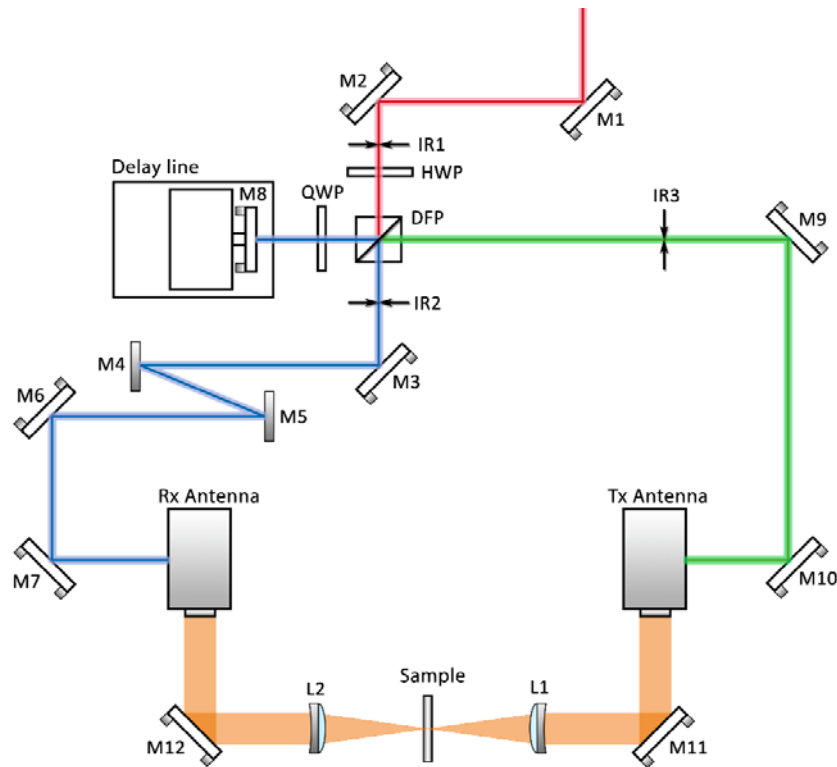


Figure 6-1. Typical THz-TDS set-up. Red line represents incident laser and after split, blue represents probe laser and green pump laser ¹³⁸.

The resulting temporal response can then be treated using Fourier Transforms (FFT) to obtain the frequency response and from here multiple parameters can be calculated such as the refractive index of the studied material, the transmittance, sheet conductivity, resistivity or attenuation on the THz range. This technique provides information that is individual and characteristic for each sample and material studied and it is said each material presents a unique signature (or pattern), which might allow to enable THz-TDS as an identification technique. Although it is not yet on this stage, it is emerging as a non-destructive and fast way of controlling the quality of materials ¹³⁹.

For the case of graphene, it has been demonstrated that THz-TDS measurements are a very viable way of characterizing it on top of substrates like polymers or quartz. Moreover, conductivities calculated using THz-TDS perfectly correlate with direct current conductivity measurements.

6.1.1 Comparison with other CVD graphenes and substrates

In this preliminary study, several CVD graphenes transferred to different substrates are studied by THz-TDS to compare the results. All samples are said to be grown using conventional CVD procedures on copper and then transferred to the desired substrate. There is no information on the growth process used for samples S_1 to S_4 as these are sourced from commercially available graphenes. But for sample S_5 it is grown on copper foil at 950°C during 25 minutes with 90 (88) sccm of 30% methane in hydrogen. These growth is preceded by the typical 15 minutes anneal at growth temperature under 30 sccm of hydrogen. As it is build using our in-house developed sliding furnace reactor, the sample is heated and cooled extremely fast.

Table 6-1. Samples used in this part of the study. Sample S_5 is sourced from our graphenes.

Sample	Substrate	Number of samples
S_1	PET	4
S_2	PEN	1
S_3	Silicon	4
S_4	Quartz	1
S_5	Quartz	1

Raman spectroscopy analysis of all 5 samples, Figure 6-2, shows that samples S_1 , S_3 and S_5 are monolayer with an I_{2D}/I_G well over 2 and sharp peaks. On the other hand, samples S_2 and S_4 are bilayer as the I_{2D}/I_G is just under 1.

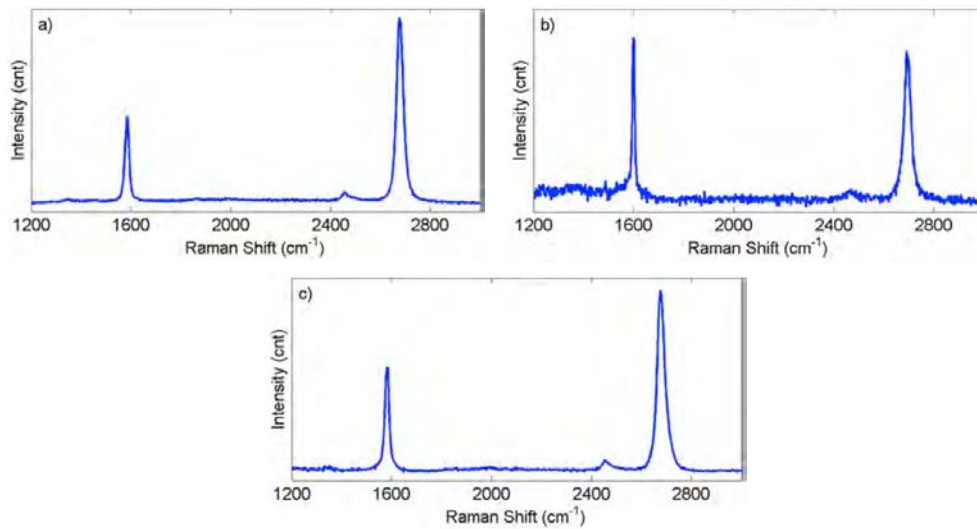


Figure 6-2. Raman spectroscopy analysis of all the samples. Raman spectra (a) represents monolayer S_1 and S_3 , Raman spectra (c) represents monolayer S_5 while Raman spectra (b) represents bilayer S_2 and S_4 .

The crude output of the THz-TDS apparatus is a temporal response that has the shape shown on Figure 6-3. To obtain the response of the graphene samples both substrate and graphene/substrate must be measured so subtract them and isolate graphene in each case. From here, FFT are applied to obtain the frequency response for each sample and enable further calculations.

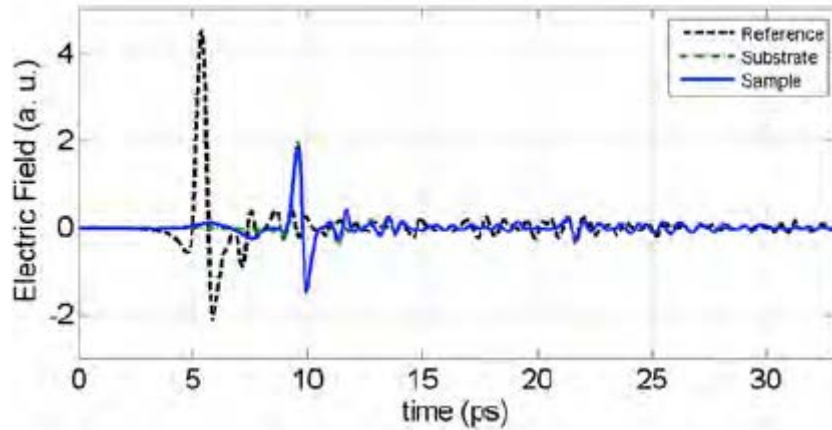


Figure 6-3. Typical time response for these samples.

The first parameter that can be calculated is the transmittance to the THz radiation, Figure 6-4, which has nothing in common with the optical transmittance. Monolayer graphene is expected to have a much higher transmittance than multilayer graphene. For these samples, bilayer samples present transmittances with very variable values in-between 60 and 80% while all monolayer graphenes are above 90%. Two of these stand out and are S_3 and S_5 that correspond to the two monolayer samples transferred to rigid substrates. The oscillations above 2 THz are typical of the THz-TDS apparatus if used under ambient conditions without controlling the humidity level nor temperature.

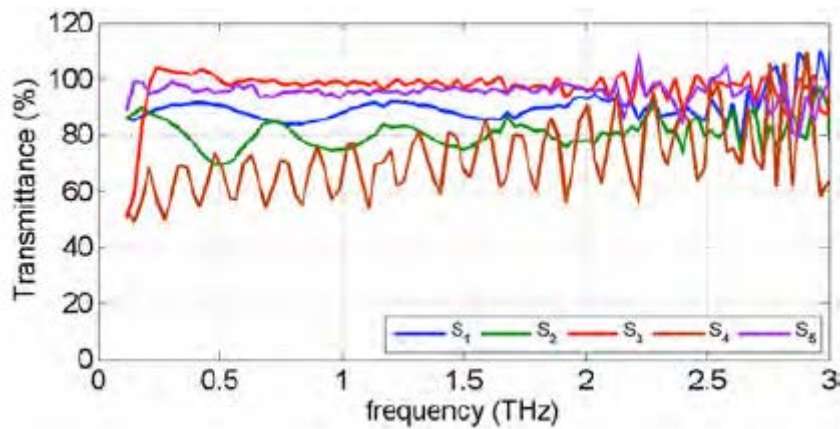


Figure 6-4. transmittance to the THz radiation for all the samples.

The next value to be calculated is related purely with the substrate and is its refractive index, Figure 6-5. Although there is not a lot to comment about these values, these are in line with what manufacturers and bibliography claim. Interestingly, though, the samples that provided a better transmittance, S_3 and S_5 , also have the refractive indexes with the much constant values of 2.2 and 1.9 respectively. The other three visually vary across the whole THz range.

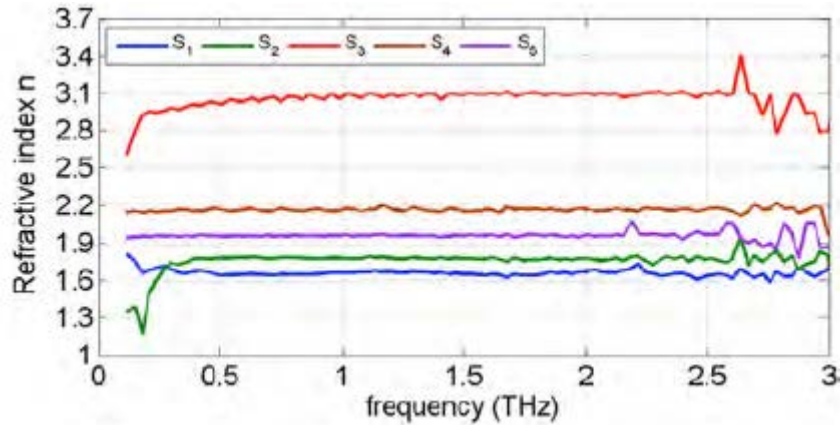


Figure 6-5. Real part of the substrate refractive index.

From here on, it is possible to calculate intrinsic graphene properties for these samples. Sheet conductivity, Figure 6-6, is compared with a minimum sheet conductivity of $60.85\mu S_{sq}$. All CVD graphene from S_1 to S_4 present conductivities that are 20 to 90 times the minimum value independently of the number of layers. Interestingly, though, sample S_5 presents a dual behavior. Below 1.2 THz it is clearly inferior to the other samples with only 2 to 10 times the minimum conductivity. Above 1.2 THz it goes on par with the rest achieving 20 to 90 times the minimum.

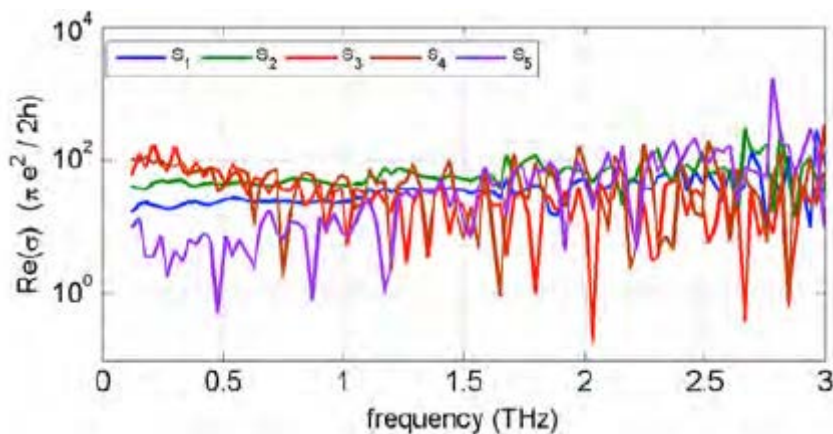


Figure 6-6. Sheet conductivity.

Finally, it is possible to extract the attenuation of these samples to the THz. It is expected that more thickness (more layers) will generate a greater attenuation. This is totally consistent with

our observations as samples S_2 and S_4 as they present an attenuation above 2 dB across the whole range of THz. The other monolayer samples present an attenuation of 1 dB or less being S_5 the one that provides the least attenuation consistently below 0.5 dB.

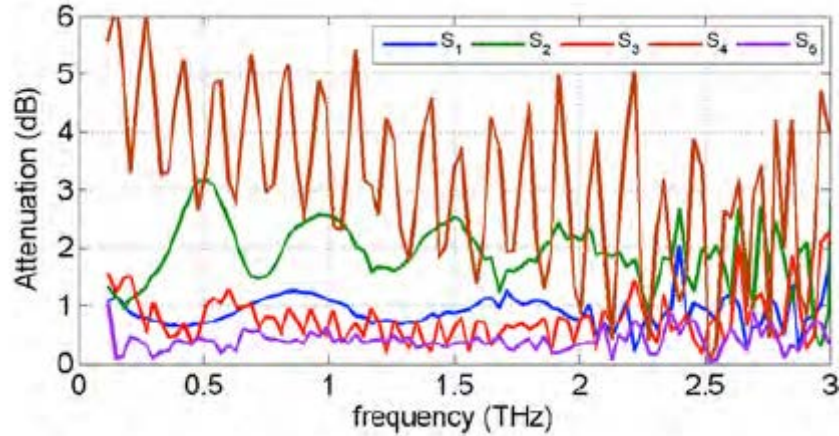


Figure 6-7. THz attenuation.

From this preliminary study it can be derived that samples synthesized at our lab at IQS are on par with renown commercial samples and that being purely monolayer puts them ahead in terms of shear attenuation.

6.1.2 Influence of grain size on THz conductivity

In the previous section 6.1.1 CVD graphenes over different substrates were compared using THz time domain spectroscopy (THz-TDS). It was shown that independently of the substrate all graphene performed better than ITO and that it can work on flexible substrates. Graphene, though, was only characterized using Raman spectroscopy. In this work, we further introduce grain size distribution information to assess THz conductivity measurements of CVD graphenes.

For this purpose, we have synthesized and analyzed three different continuous monolayer CVD samples to check the correlation between grain size and its THz response. Samples 1 and 2 are grown for 15 minutes at 950 and 1050°C respectively. Sample 3 is grown at 1050°C for 60 minutes inside a full enclosure, to promote grain growth vs. nucleation.

Raman spectroscopy, Figure 6-8, reveals that all three samples are mainly monolayer. Samples 1 and 2 are monolayer with I_{2D}/I_G ratio well over 2 and sharp peaks. Sample 3, however, presents a lower I_{2D}/I_G ratio, which might indicate has a higher content of bilayer or multilayer due to the longer growth time. This is confirmed through SEM imaging (not shown here)

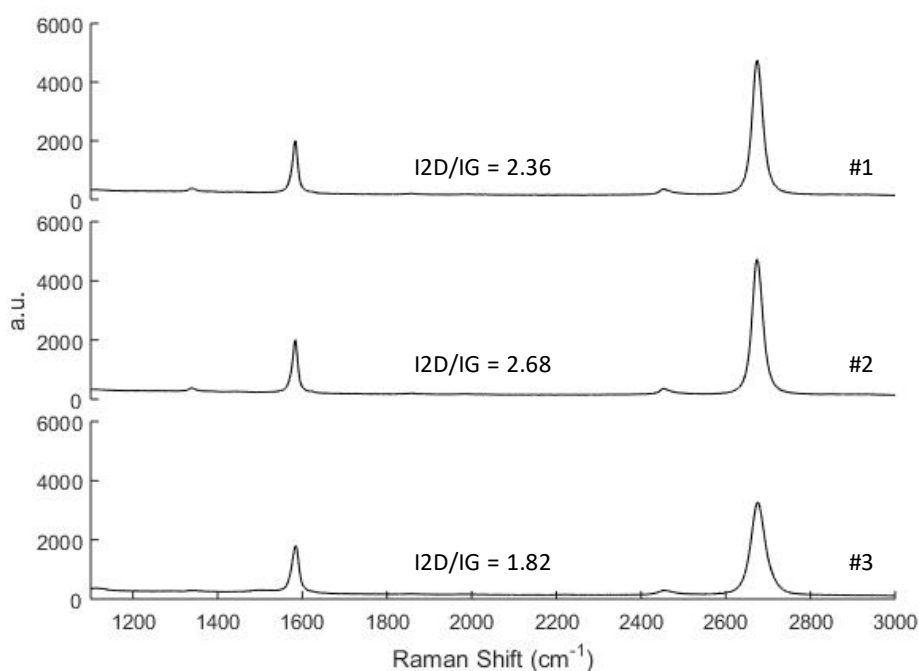


Figure 6-8: Raman spectra for all samples.

To characterize grain size, samples of graphene directly onto its copper growth substrate are subjected to a highly controlled photocatalytic oxidation using TiO_2 suspensions in water as catalyst and UV light during 2 hours, following the technique developed in this thesis. As a result, grain boundaries became clearly visible on optical microscopy as dark oxide lines contrasted against the copper background. These lines can be quantified through image analysis in order to obtain the area of each individual grain that can then be assimilated to a circle to obtain its grain size. With all individual sizes it is possible to build size distributions for each sample as seen in Figure 6-9. Samples 1, 2 and 3 present an average size of 1.6, 2 and 3.7 microns, respectively. As it is expected, larger grains present broader distributions with standard deviations of 0.7, 1.6 and 1.8 respectively for all three samples. Sample 2 grain size distribution is unexpectedly wide.

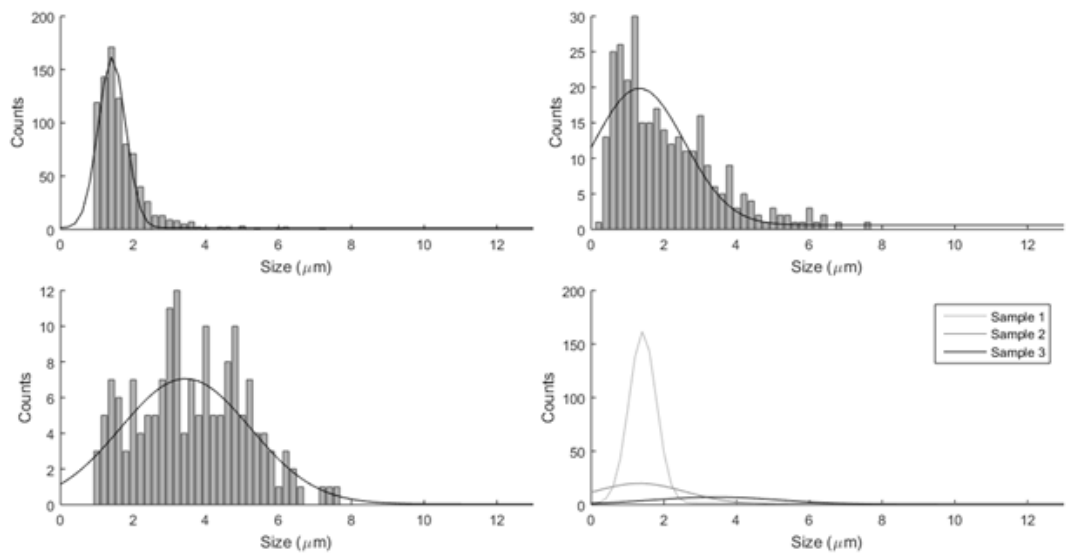


Figure 6-9: Grain size distributions. (a), (b) and (c) represent samples 1, 2 and 3 respectively with histograms of the real data and adjusted Gaussian curves. (d) is a comparison between the three Gaussian curves.

In order to characterize the optoelectronic response, a piece of each pristine sample was transferred to quartz slides through a wet transfer method using FeCl_3 to etch copper away. These are then characterized using THz-TDS for a range from 0.1 to 2 THz, results are shown in **Figure 6-10**. From the transmittance of bare substrate and the sample, we can determine a large set of optoelectronic properties. First, the refractive index of the substrate is calculated at a value of 2, which is coherent with bibliographical values¹⁴⁰. From here parameters such as attenuation, transmittance or sheet conductivity can be calculated for each sample.

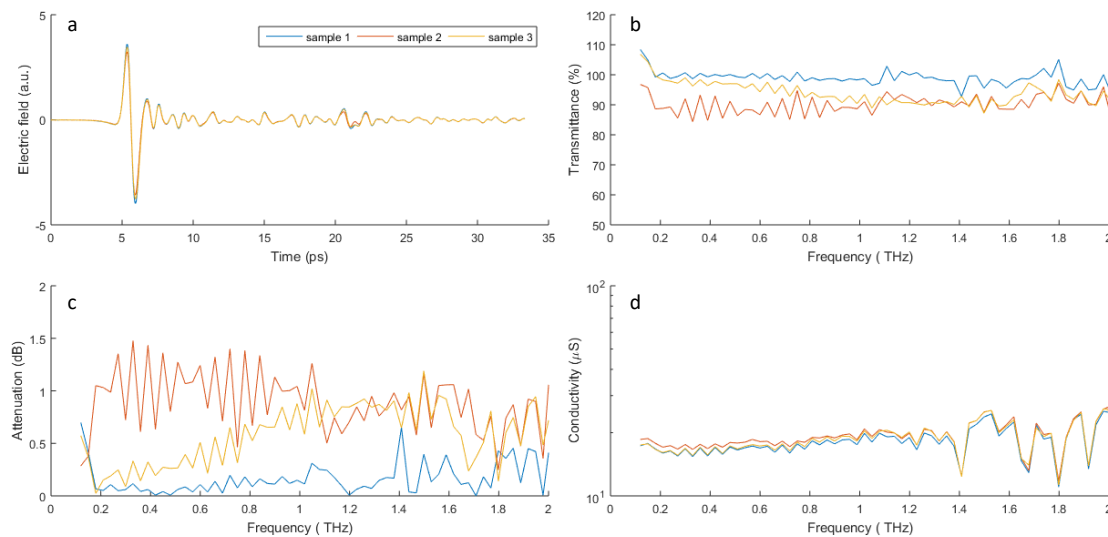


Figure 6-10: Results for THz-TDS. (a) Untreated temporal response, (b) transmittance, (c) attenuation and (d) conductivity.

Transmittance results (see figure 1b) show that sample 1 has a transmittance close to 100% and that sample 3 is the worst and most erratic, being Sample 2 positioned in the middle.

Attenuations follows a similar trend with sample 1 with minimal attenuation and the other 2 with larger values. From these results, we can summarize that sample 1 is the best of the three samples while sample 3 is the worst. Conductivity on the other hand, presents values for all three samples that are too close to call any difference between them. Although conductivities of these samples are on the lower side when compared with previous results reported in section 6.1.1, see Table 6-2, those are considered within the normal range for graphene conductivity as structure, production method and doping are known to affect its conductivity ¹⁴¹.

Table 6-2: Conductivities for all three samples at 1 THz and 2.5 THz and compared with graphene conductivities obtained in a previous study.

Sample	Conductivity at 1 THz (μS)	Conductivity at 2.5 THz (μS)
#1	18.37	27.43
#2	19.37	30.73
#3	19.03	26.46
Reported values	8.5 – 57.9	13.3 – 93.7

It is difficult to extract a clear correlation between grain size and THz-TDS results mainly since our production process requires long times that translate in slight less monolayer samples. The presence of local multilayer areas can explain why samples 2 and 3 present lower transmittance and higher attenuation. On the other hand, conductivity appears to not be affected by these local multilayer areas or results are compensated by the increase in properties due to larger grain size.

Although results are not conclusive and need to be extended with samples having radically smaller and larger grains, this study marks a new start for correlating CVD graphene properties to its grain structure. From what we can conclude, attenuation and transmittance are affected by graphene structure and grain size but overall conductivity is not really affected for this range of graphene grain sizes between 1.6 and 3.7 μm . Conductivity values range from 18.37 to 19.37 at 1THz and 26.46 to 30.73 at 2.5THz.

6.2 Physical electrical measurements

To physically measure electrical properties of graphene this must be transferred to an insulating substrate. In our case, graphene samples were transferred onto silicon oxide wafers coated with 300nm of SiO₂ that contain germanium alignment marks to easily locate graphene (see Figure 6-11). Transfer was performed at IQS following the optimal recipe describe in Annex 3 while all the contacts are prepared entirely inside CNM's clean room.

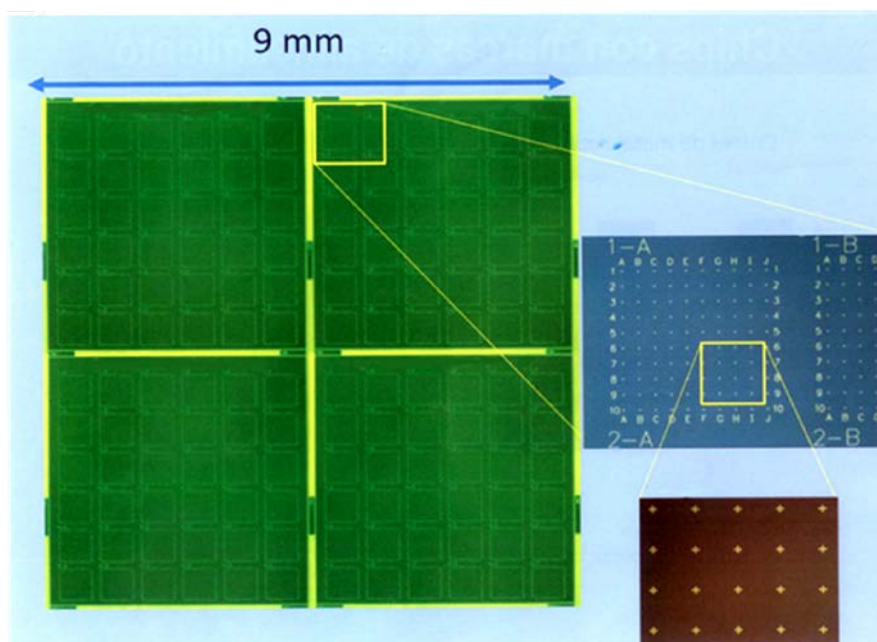


Figure 6-11. Silicon wafers with germanium alignment marks.

Two samples were transferred in order to be measured. The first (CNM-1) was composed of a continuous layer of monolayer graphene and was grown at 1050°C for 10 minutes using a maximum gas-flow restriction inside the reactor. The second (CNM-2) was composed of individual graphene flakes grown at 950°C for 10 minutes using, also, a maximum gas-flow restriction inside the reactor, “0 mm” of gap. Figure 6-12, shows the result of both transferred samples and optical microscopy confirms that sample CNM-1 is a continuous graphene layer while CNM-2 is a collection of individual graphene grains.

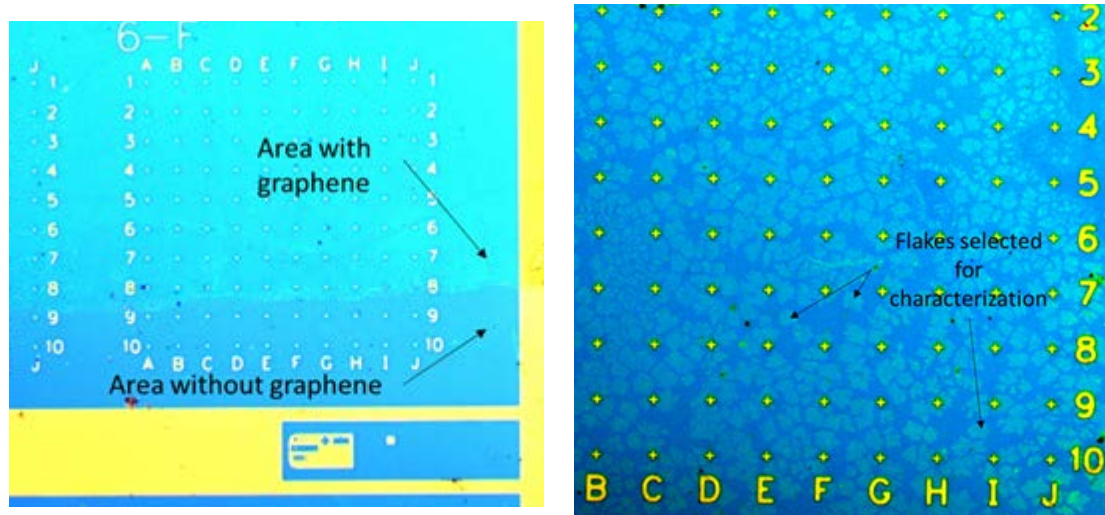


Figure 6-12. Transferred samples. Left shows sample CNM-1 with the edge of the graphene covered area. Right shows sample CNM-2 with clearly separated graphene grains and marks the ones used for characterization.

First sample CNM-1 is set to be analyzed and several preliminary steps are required to determine suitable areas for the process. Low resolution Raman spectroscopy mappings of $100 \times 50 \mu\text{m}$ with analysis every $2 \mu\text{m}$ allow to assess the homogeneity of the graphene. As it can be seen on Figure 6-12 all the areas of the sample CNM-1 present some minor spots of bilayer graphene, as expected for a CVD process, with an I_{2D}/I_G in the range of 1 while the majority of the surface presents an I_{2D}/I_G close to 5, which represents a clearly a monolayer graphene area.

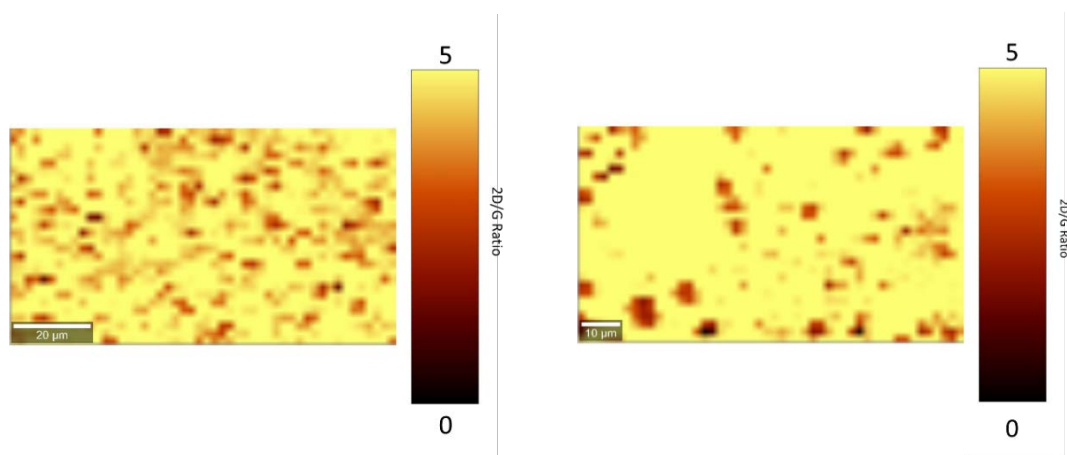


Figure 6-13. Raman spectroscopy mappings for $100 \times 50 \mu\text{m}$ areas corresponding to CNM-1. $2D/G$ ratio color scale is shown next to the mapping image.

After these Raman spectroscopy mappings, AFM was also performed to check the quality of the transfer and the amount of impurities left, mainly PMMA left-overs from the transfer and accumulated dust. All the areas of these sample CNM-1 were extremely clean with almost no impurities left and as flat as the silicon wafer substrate that holds graphene, see Figure 6-14.

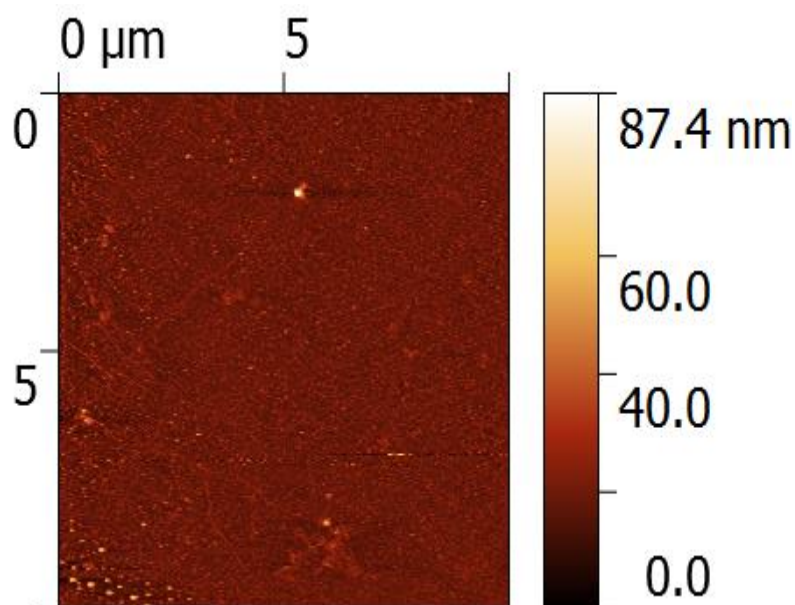


Figure 6-14. AFM analysis of sample CNM-1.

At this point, the contacts can be built on top of the sample. The process uses a sacrificial layer of PMMA that is patterned using lithography prior to depositing the metallic layer that forms the contact. After patterning and coating, the sacrificial layer is etched away removing the metal that is not directly attached to the sample thus, effectively leaving the contacts on the surface of the sample. The metal used for the contacts was a combination of 5 nm of Ti followed by 25 nm of Au, which seems to be an optimum combination to reduce the contact resistance between graphene and the metal and it also is the most common¹⁴². This lithographic process has a maximum resolution of 100 nm but the probe system (Semiautomatic Probe System Karl Suss PA 200 - Probe Station) requires contact pads of about 100x100 μm to ensure proper electrical conductivity. For the case of sample CNM-1 contact pads were directly built on top of the graphene layer at certain distances to allow measuring conductivity and determine sheet resistance against distance. Two zones of highly homogeneous and clean graphene were selected to build the contacts and analyze graphene. Figure 6-15 shows the arrangement of contact pads used with a range of separations from 5 to 100 μm, this set-up allows to maximize the areas of graphene available. Germanium marks allow the samples to be precisely positioned for lithography.

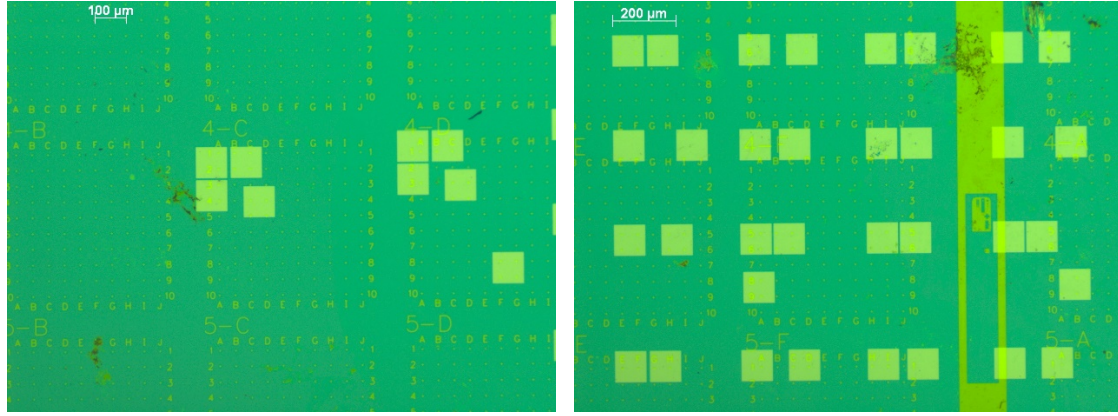


Figure 6-15. Contacts build on continuous monolayer graphene. Left shows groups of 4 contact pads with gaps between them of 5, 10, 25 and 50 μm . Right shows pairs of contact pads with separations of 5, 10, 25, 50 and 100 μm .

For measuring sheet conductivity, pairs of contact pads were contacted and a potential of 1 V was applied. Then, the current is measured and the resistance can be calculated by applying the Ohm's law. The resistance of the pads and the contact between metal and graphene can be estimated at a constant and subtracted from the calculated resistance to obtain the resistance attributed to the graphene. From this value, the sheet resistance can be calculated using equation 1 where R_s is the sheet resistance, R the resistance, W and L the width and length of the graphene area measured. For sample CNM-1, W is set to 100 μm , which is the width of the contacts and L is the distance between contact pads.

$$R_s = R * \frac{W}{L} \quad \text{Equation 1}$$

Mean sheet resistance of sample CNM-1 for the different distances is represented in Figure 6-16. Although all the values are inside the range accepted for graphene that can vary from 200 Ω/sq ¹⁴³ to 50,000 Ω/sq ¹⁴⁴ it should be constant across the whole range of distances. For the lower distances, specially 5 μm , the value of the sheet resistance is abnormally high when compared with the rest of points and can be attributed to a higher influence of the resistance between graphene and the metal contact pads. For distances over 20 μm , sheet resistance settles to around 1550 Ω/sq , which is an acceptable value for graphene and close to the values obtained for commercial graphene. Longer graphene paths, inevitably involve more graphene grain boundaries being crossed, but this doesn't seem to affect the sheet resistance as this is normalized by the graphene form factor.

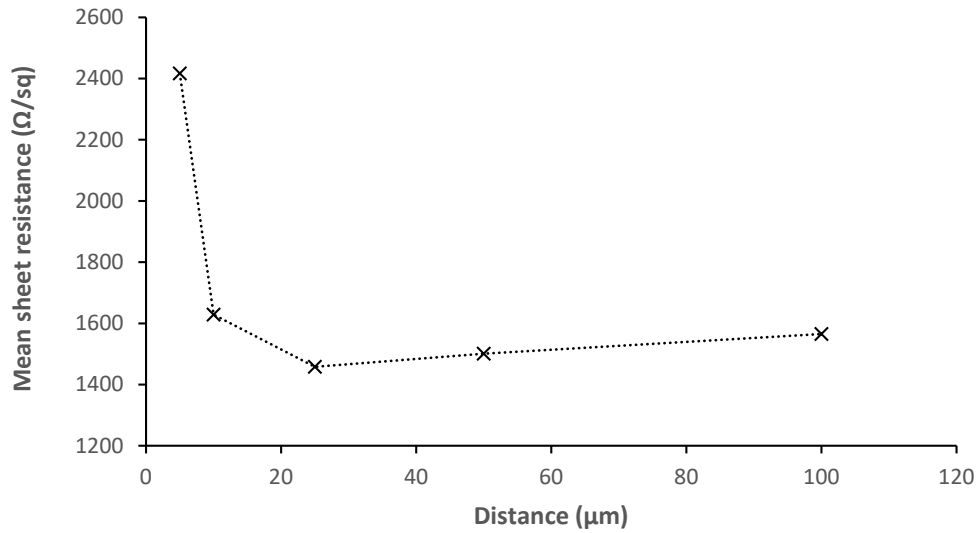


Figure 6-16. Mean sheet resistance against distance for sample CNM-1.

The whole process is repeated for sample CNM-2 to study individual grains and individual grain boundaries. Figure 6-17, shows Raman spectroscopy mapping representative of sample CNM-2 where each grain is fully monolayer graphene with a small spot of bilayer graphene in the center. As mentioned before, the presence of small bilayer areas on CVD graphene is almost unavoidable. The areas without graphene (black areas) show ratios close to 1 due to the division between two flat Raman spectra, the presence of signal noise generates the dots with abnormally high I_{2D}/I_G ratios, seen as bright dots where there is no graphene.

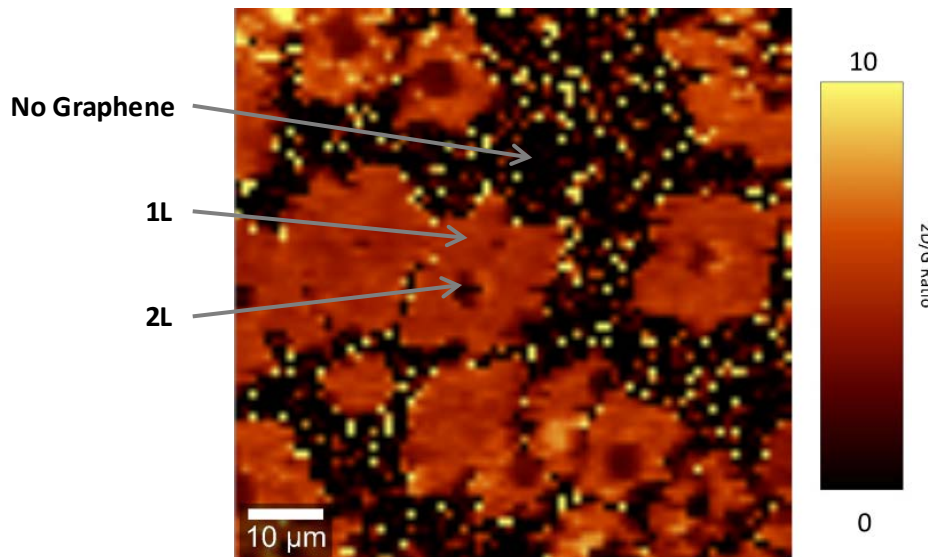


Figure 6-17. Raman mapping of individual graphene grains of sample CNM-2.

AFM analysis of these grains is much more interesting than for the continuous layer. As can be observed in Figure 6-18 these grains suffered from the transfer process and show some cracks and some residues of PMMA, which can be observed as “bumps” on the AFM analysis.

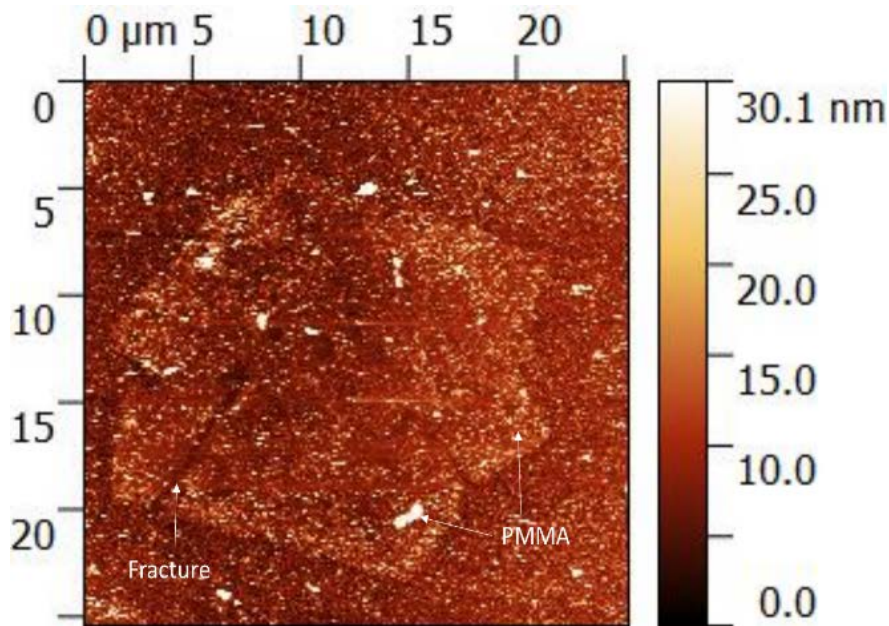


Figure 6-18. AFM analysis of an individual graphene grain in sample CNM-2.

The presence of fully monolayer grains, grains with small bilayer areas in the center and two grains forming one single monolayer opens the possibility of designing the contact patterns to analyze these scenarios. In sample CNM-2, contacts are more complex as the contact tips are only $1\ \mu\text{m}$ in width and leads must be extended to attach to the $100\times 100\ \mu\text{m}$ contact pads. These leads must avoid shorting with other leads by avoiding both direct contact with other metallic paths and contact through graphene crystals. This is partially why the grains in Figure 6-12 are chosen, as they are separated enough from their neighbors. With all these considerations, it was possible to build contacts with leads and its corresponding contact pads to enable measuring monolayer graphene grains, bilayer regions and monolayer areas crossing one single grain boundary, as can be observed on Figure 6-19.

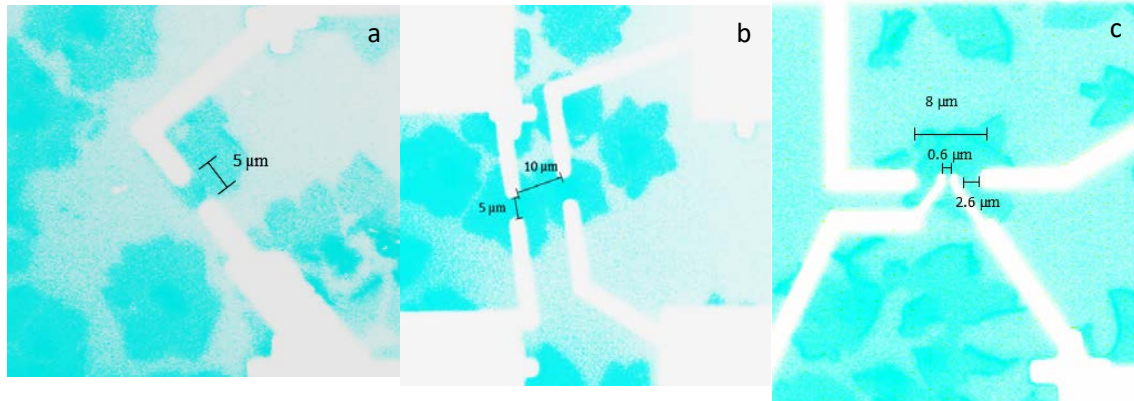


Figure 6-19. Contacts on sample CNM-2 across: (a) monolayer graphene, (b) monolayer graphene and across one grain boundary, (c) bilayer graphene.

This array of contacts allows to measure resistance and calculate sheet resistances for all these options, Table 6-3 summarizes this results. The grains on Figure 6-19 (b) were extremely clean with no presence of cracks and no PMMA left-overs, which allowed to measure high quality monolayer graphene resulting in the lowest sheet resistance in all our measurements and fits in the middle range of reported sheet resistances⁸. The grain in Figure 6-19 (a) corresponds to a monolayer grain with fractures and defects, as it can be observed in AFM in Figure 6-18, which translates into a larger sheet resistance although not as big as expected. This could be explained as the fractures do not go through the whole graphene crystal. Also, measuring across the single grain boundary gives a value of 1647 Ω/sq which is not that different from continuous graphene, see Figure 6-16, but this value is less than half the reported value in the literature⁸. These observations suggest each individual graphene grain is indeed a monocrystal composed of high quality graphene.

Table 6-3. Results for sample CNM-2.

Area measured (Figure 6-19)	Graphene nature	Distance	Mean sheet resistance (Ω/sq)
a	Monolayer	5	1140.15
b	Monolayer	5	958.21
b	Across the grain boundary	10	1647.39
c	Monolayer-bilayer- monolayer	8	1837.55
c	Bilayer	0.635	4735.07
c	Monolayer-bilayer	2.6	3370.64

Finally, measuring bilayer areas of Figure 6-19 (c) provides some unexpected results. Measuring from monolayer to monolayer regions across the bilayer area yields a sheet resistance comparable to a monolayer graphene with a single grain boundary as if the second layer has little to no effect. On the other hand, placing both contacts inside the bilayer zone or one on the monolayer and the other on the bilayer yields the higher resistances almost tripling the grain boundary measurement. Interestingly these measurements fit on the measurements performed for single grain boundaries in the bibliography⁸.

7 Synthetic graphene suspensions

Successfully producing monolayer graphene and developing means to characterize and partly control its grain size opens the possibility of attempting to produce new products. The main goal is to prove that it is possible to produce graphene suspensions directly from CVD graphene. To produce these synthetic graphene suspensions, first, CVD graphene is grown on copper and then transferred directly to suspension using an electrochemical method without applying any polymer support to the graphene. In principle, this will provide suspensions of monolayer graphene that will not be oxidized and much less damaged than bulk graphite exfoliation.

Graphene's thickness of only one atom means that 1 square meter only weights around 0.5 μg . Thus, attempting to produce CVD graphene suspensions would advise an increase in the area of graphene produced inside the reactor. This can be maximized by selecting a copper substrate with maximal area/volume ratio. Figure 7-1 shows the whole range of copper substrates used. As can be seen, this ranges from the standard copper foil to PVD copper coated quartz substrates.

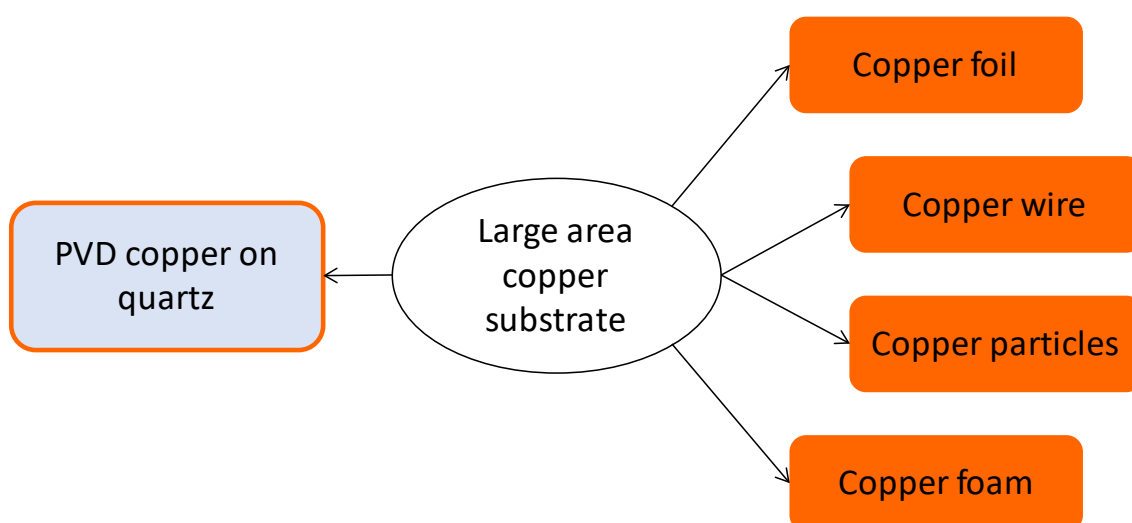


Figure 7-1. Range of copper substrates used.

7.1 PVD copper on quartz

As a first option to improve the surface area of copper inside the reactor, it was hypothesized the possibility of PVD coating quartz particles. Quartz is selected because it can have a smooth surface, it can easily handle graphene-growth temperatures and does not forms alloys with copper. For ease of handling, quartz slides were used to prove this concept.

Figure 7-2 shows a quartz slide coated copper using PVD. Because the slides were held using magnets these show rectangular uncovered areas at both ends. Moreover, the transition between uncovered and covered areas is not a sharp line but a graded transition as it can be seen in Figure 7-2.

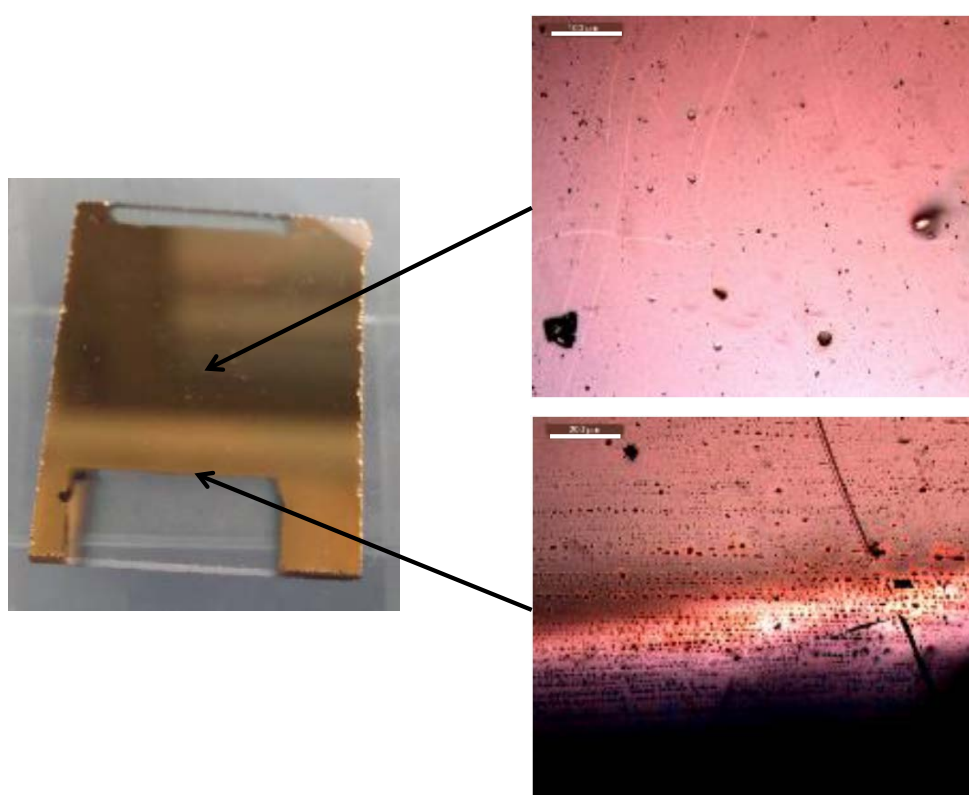


Figure 7-2. Original aspect of PVC coated quartz slides. Scale bar on micrographs is 100 μm .

Profilometry analysis for the first coating allows to further prove the transition between the bare quartz and the copper happens in around 100 μm and that the copper thickness is around 350 nm. These measurement is not 100% correct as the profilometer tip easily scratches the copper layer and can easily be measuring by defect. For the following samples, the PVD coating time was tripled so it is expected that the coating will be, at least, 1000 nm thick.

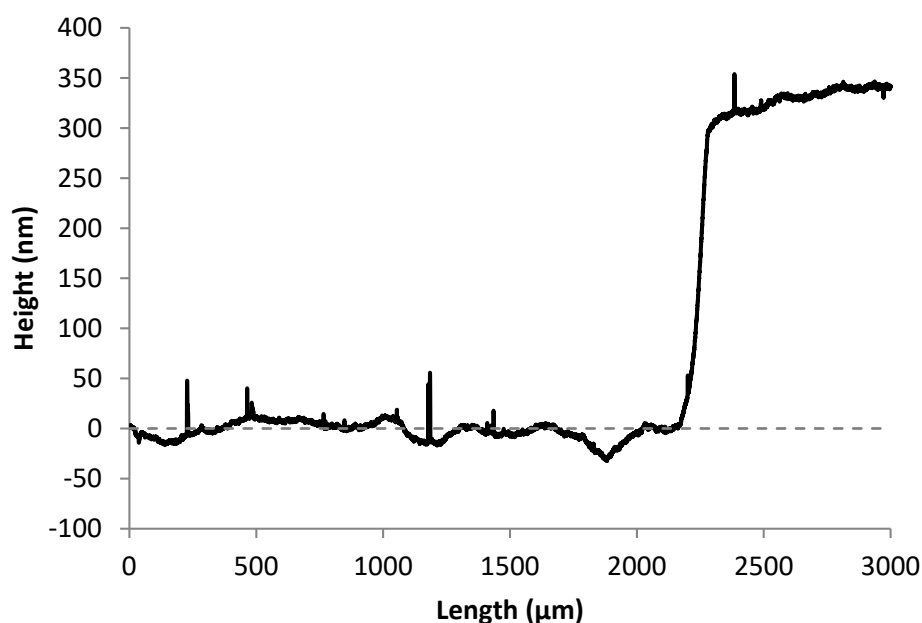


Figure 7-3. Profilometry analysis of the interphase between quartz and copper.

AFM analysis of the copper surface serve to observe its microstructure and determine its surface roughness. As seen in Figure 7-4, the copper layers show the typical geometry for a PVD layer with the columnar growth of the metal grains. Despite this appearance and dome holes being present (black spots) the surface roughness shows a Sa of just 5.0 nm and an Sq of 6.4 nm.

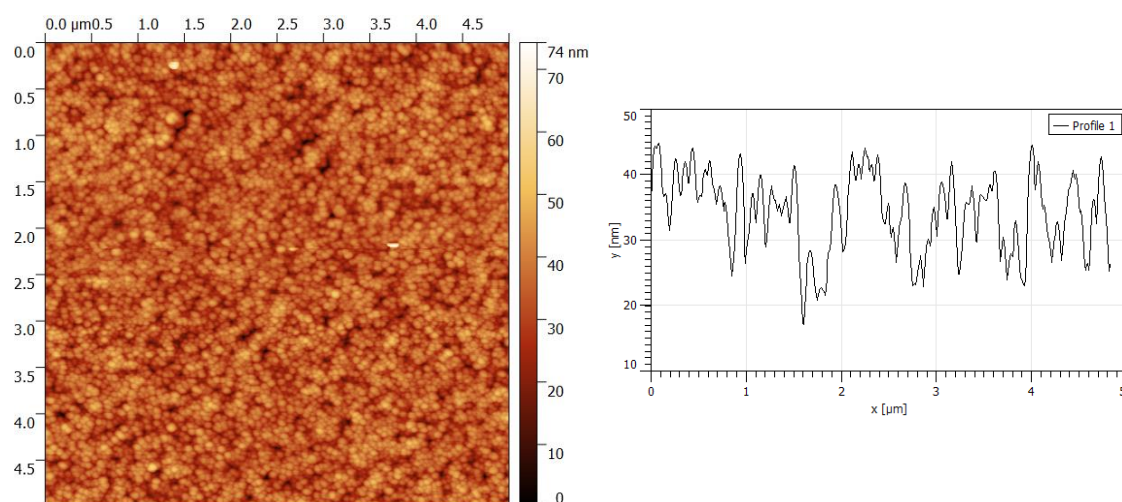


Figure 7-4. AFM image of the PVD Copper surface and a corresponding profile for reference.

As we showed during this thesis, copper evaporates due to the work temperatures and it is expected to represent a big issue for this approach. Only by subjecting these quartz slides to 950°C for 15 minutes under vacuum to mimic an annealing prior to graphene growth translates into major evaporation as the copper layer visually loses its gloss and turns almost transparent. Micrographs show that it not only evaporates but forms bubbles.

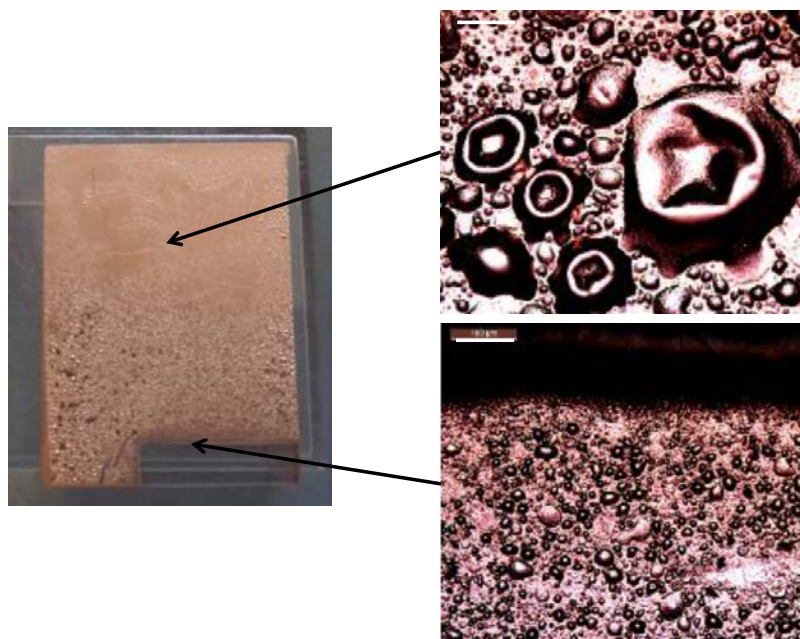


Figure 7-5. Copper PCV on quartz after annealing at 950°C for 15 minutes. Scale bar on micrographs is 100 μm .

Despite this results, it was decided to shorten the annealing stage to a minimum and carry on to attempt to grow graphene on these quartz slides. The process is set with an annealing of only the time the sample needs to reach 950°C (around 3 minutes) and then graphene is grown during 15 minutes under the standard 88 sccm of 30% methane mixture. As Figure 7-6 shows, it seems that the reaction with presence of methane limits copper evaporation as the PVD layer loses its gloss but does not turn visually transparent. The presence of bubbles is consistent with previous observations although these look flatter than before. It is perfectly possible that graphene has been successfully synthesized at this stage but it was impossible to isolate or detect by all the means used (optical after H_2O_2 oxidation, SEM and Raman spectroscopy).

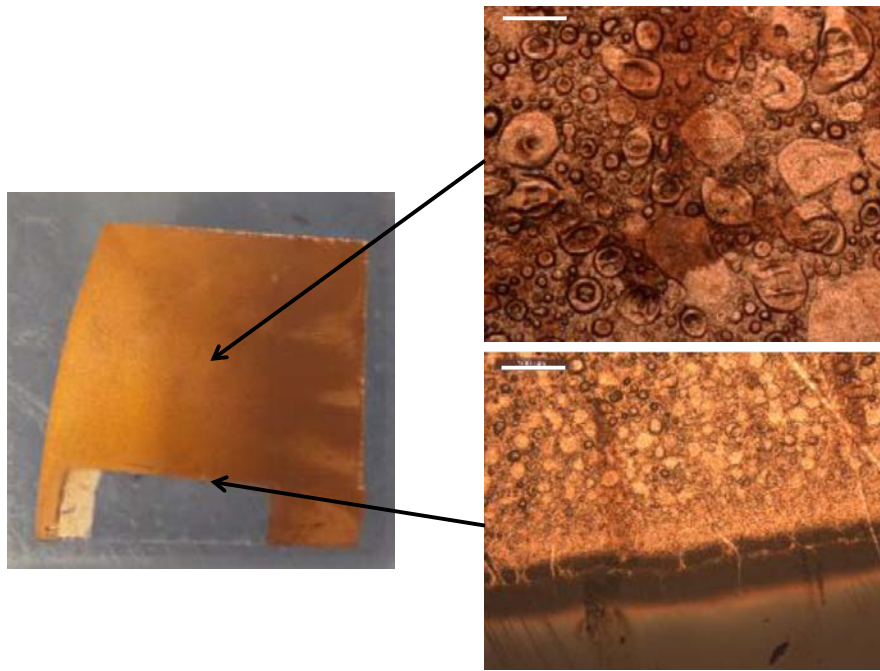


Figure 7-6. Quartz slide after 15 minutes graphene growth. Scale bar on micrographs is 100 μm .

In an attempt to determine the origin of the bubbles two samples were resin mounted to allow to cut and polish a cross-section and allow SEM measurements. Figure 7-7 shows these results and as it can be seen, the original copper layer is about 2.7 μm thick and has close to no imperfections apart from the typical columnar growth typical of the PVD processes. On the other hand, after graphene growth the layer has thinned out to about 1.5 μm , which means almost half of the copper thickness has been evaporated. Interestingly, the bubbles observed on optical microscopy are not empty but filled with copper, as confirmed through EDX directly inside the SEM. No further explanation has been found for these bubbles. Moreover, it was impossible to separate graphene from the copper layers.

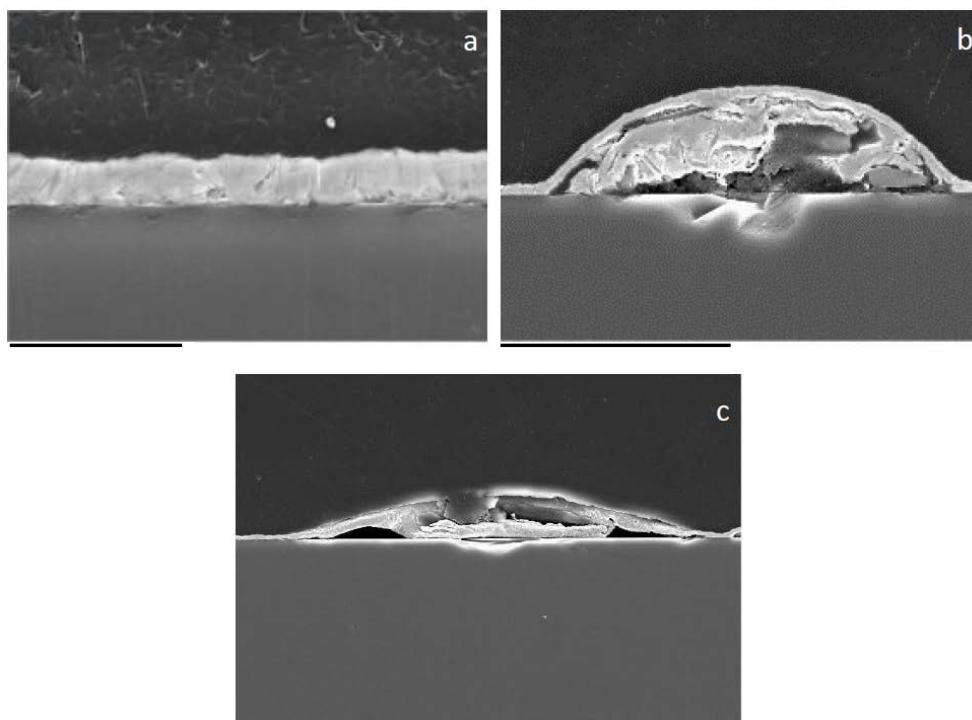


Figure 7-7. SEM images of cross-sections of PVD copper on quartz. (a) Original copper layer, (b) and (c) after graphene growth. Scale bars are 10 μm for image (a) and 40 μm for images (b) and (c).

With all these issues this route of PVD coating some ceramic substrate seems very interesting but it must solve the issues related to copper completely evaporating from some areas. More importantly, the bubbling effect must be avoided to be useful for graphene growth. Although it seems some companies like AIXTROM use PVD copper coated wafers to synthesize graphene the set-up and graphene growth conditions appear to be completely different than our reactor. Having considered all this, the PVD route is discarded in favor of solid copper substrates that will not present the problems of complete evaporation and bubbling.

7.2 High area copper substrates

The optimal substrate for maximum copper area would be spheres as small as possible. As these are not commercially available and working with copper nanoparticles does not seem viable the options of Table 7-1 have been studied. These have been selected for being commercially available products that are moderately affordable. Copper foil is the same that has been used for the rest of the thesis, while copper wire, particles and foam are added at this stage. Figure 7-8 shows pictures of all four substrates.

Table 7-1. Copper substrates used.

Substrate	Supplier	Additional information
Copper foil	Alfa Aesar	Thickness: 0.025 mm Purity: 99.8 %
Copper wire	Common electrical wire	Diameter: 0.3 mm Purity: >99.5 %
Copper particles	Pometon S.A.	Purity: >99.9 %
Copper foam	Nanoshel	Pore size: 1-2 mm Density: 850 g/m ² Purity: 99.9 %



Figure 7-8. Copper substrates used.

To check the viability of the substrates, each will be used to grow graphene under different conditions of temperature and methane content while keeping the time constant at 10 minutes. The results for each set of conditions will be compared against copper foil, as it is the benchmark for CVD graphene production. A total of 4 sets of conditions have been screened with temperatures of 950°C and 1050°C and methane content of 10% and 30%, Table 7-2 summarizes the experiments performed. Prior to graphene growth, all copper samples are thoroughly cleaned and electropolished (8 minutes for foil, wire, and foam and 15 for particles). Copper foil and foam are set flat on top of a quartz plate, while particles and wire are set directly on the quartz reactor tube. Particles are simply piled on the center of the tube and wire is set forming either a random skein or a neat coil with multiple wires minimizing the contact between each one, which makes no difference on the obtained graphene. The use of the conditions selected represent the extreme temperatures (lowest and highest) used and the two available methane/hydrogen mixtures and are designed to assess how the substrates perform in comparison with copper foil.

Table 7-2. Combination of methane percentage and temperature used for each of the substrates. Growth time is set to 10 minutes.

% of methane	TEMPERATURE
10%	950 °C
	1050 °C
30%	950 °C
	1050 °C

Starting with the first conditions used on this thesis – 950°C and 30% of methane – foil performs as expected, producing monolayer graphene grains that are not fully united into a continuous layer. Judging from the SEM images, copper particles perform almost identically than foil while copper wire forms a more homogeneous layer and foam performs radically different.

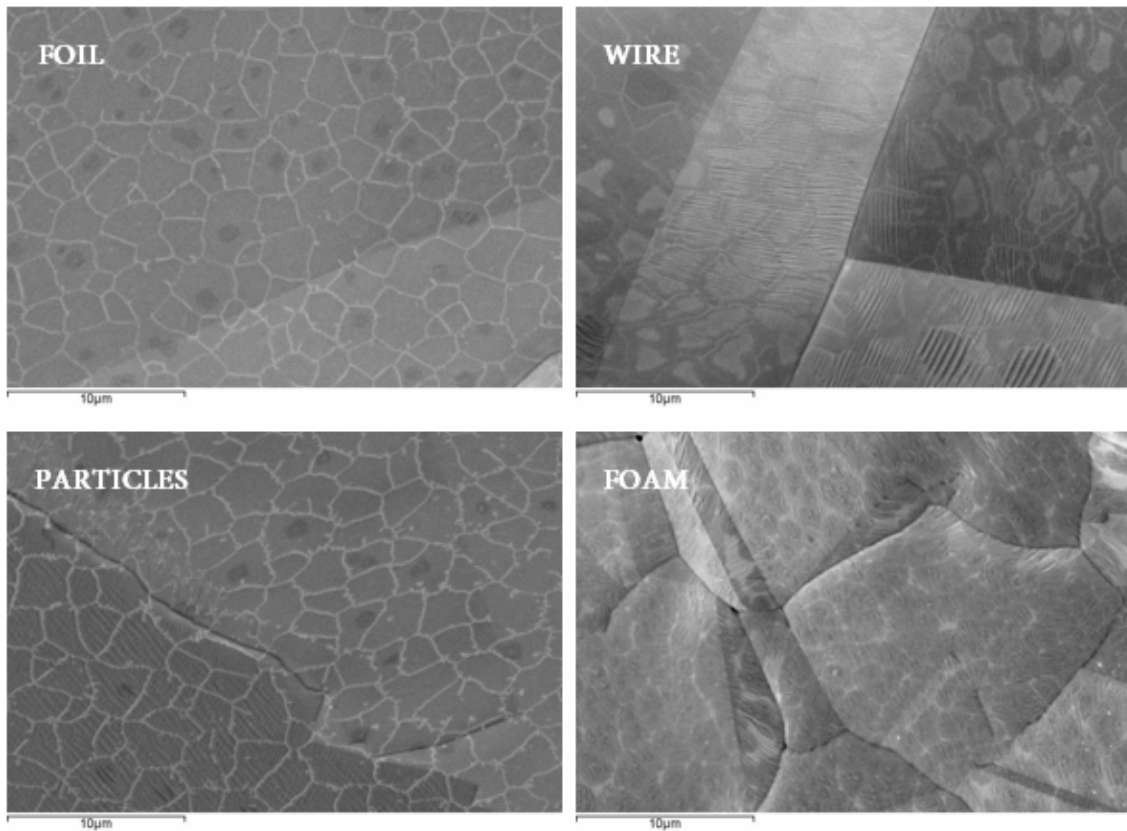


Figure 7-9. Graphene grown with 30% CH₄ and 950°C

As Figure 7-10 shows, increasing the temperature translates into homogenous monolayer graphenes for all the substrates, note the typical wrinkles for graphene growth. Foil and particles, again, perform very similarly producing continuous monolayer graphene with small islands of bilayer graphene. As before, wire seems to impede nucleation and growth, which also translates into a continuous layer of monolayer graphene but completely removes the formation of bilayer graphene. Foam appears to be viable to produce monolayer graphene but its surface is much rougher than the other three, which produces very variable graphene layers.

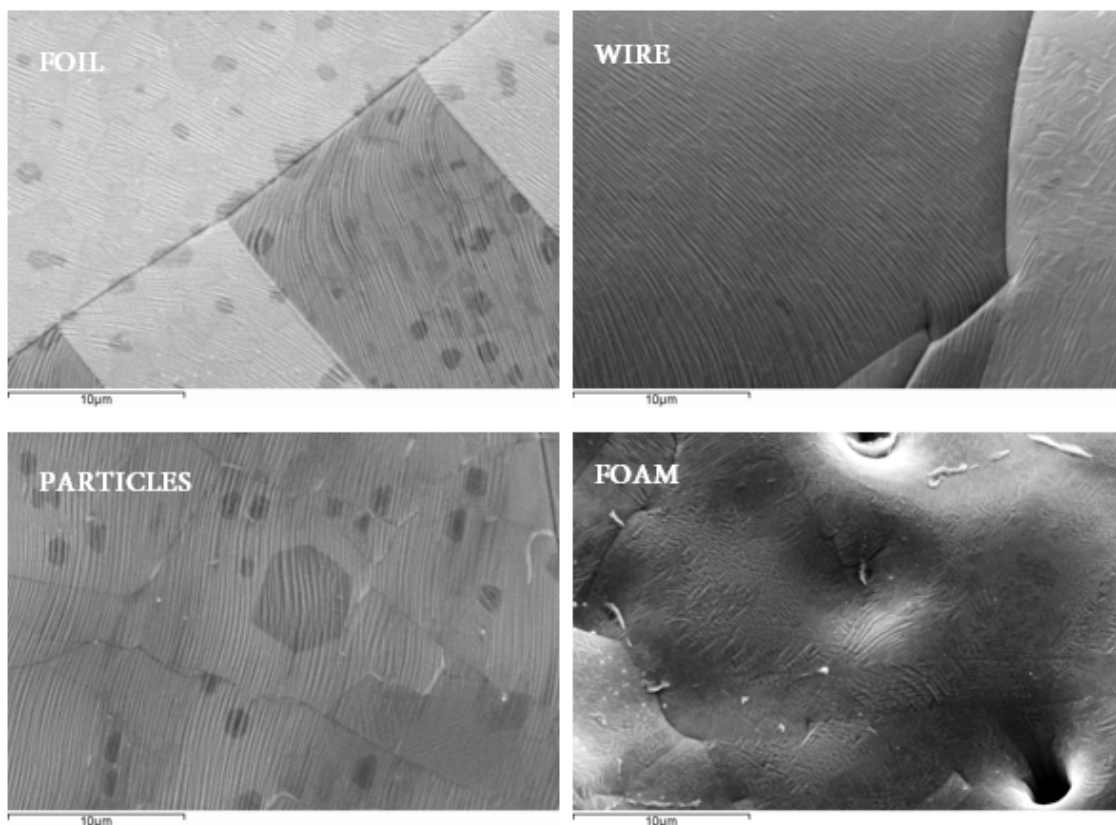


Figure 7-10. Graphene grown with 30% CH₄ and 1050°C

Decreasing methane percentage to 10% translates into producing graphene with larger grain sized for the same growth conditions as we established before. As expected, Figure 7-11 shows graphene grains much separated and visibly larger than those in Figure 7-9. Unexpectedly, at this methane concentration and temperature, wire performs almost the same as foil. Particles present a much lower growth than the rest and foam presents concentration of graphene nuclei with almost no growth as those are completely separated.

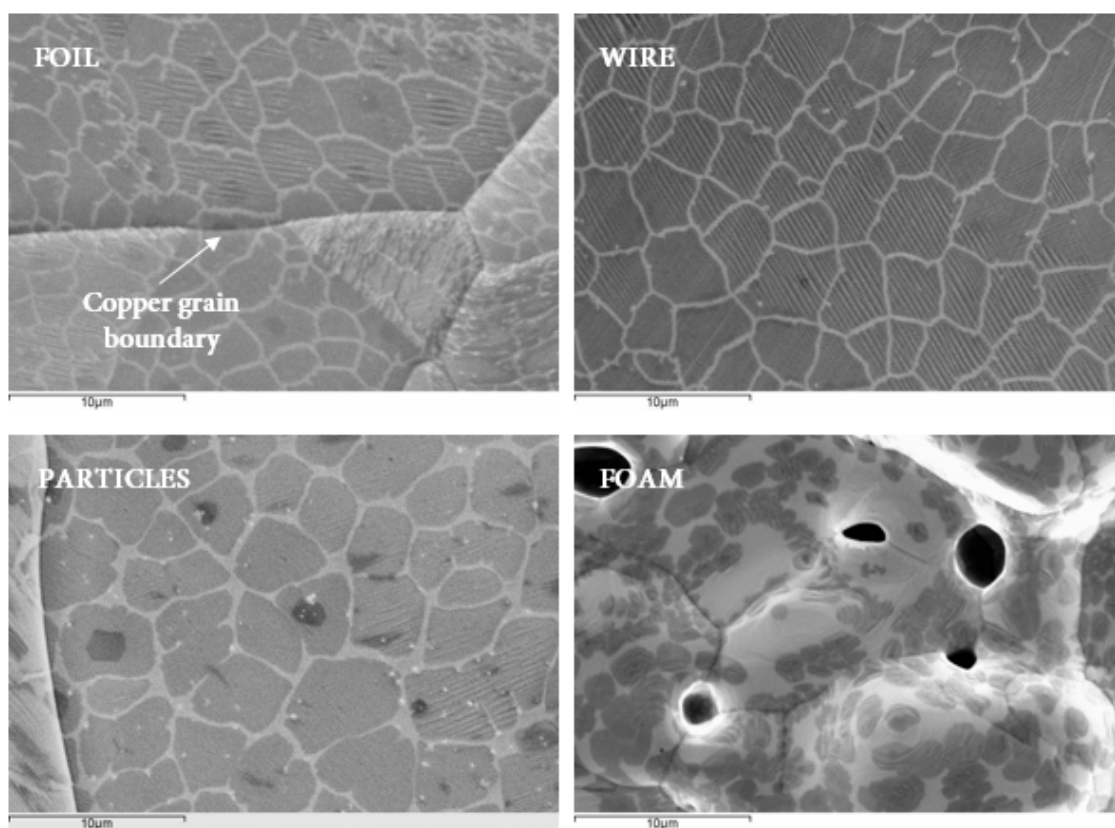


Figure 7-11. Graphene grown with 10% CH₄ and 950°C

Finally, Figure 7-12 presents the results for low methane content and high temperature. These conditions are expected to produce larger grains coupled with a complete coalescence between grains. Most interestingly, not only successfully produces continuous and homogeneous graphene layers it equalizes the behavior of all 4 substrates with no visible differences between those.

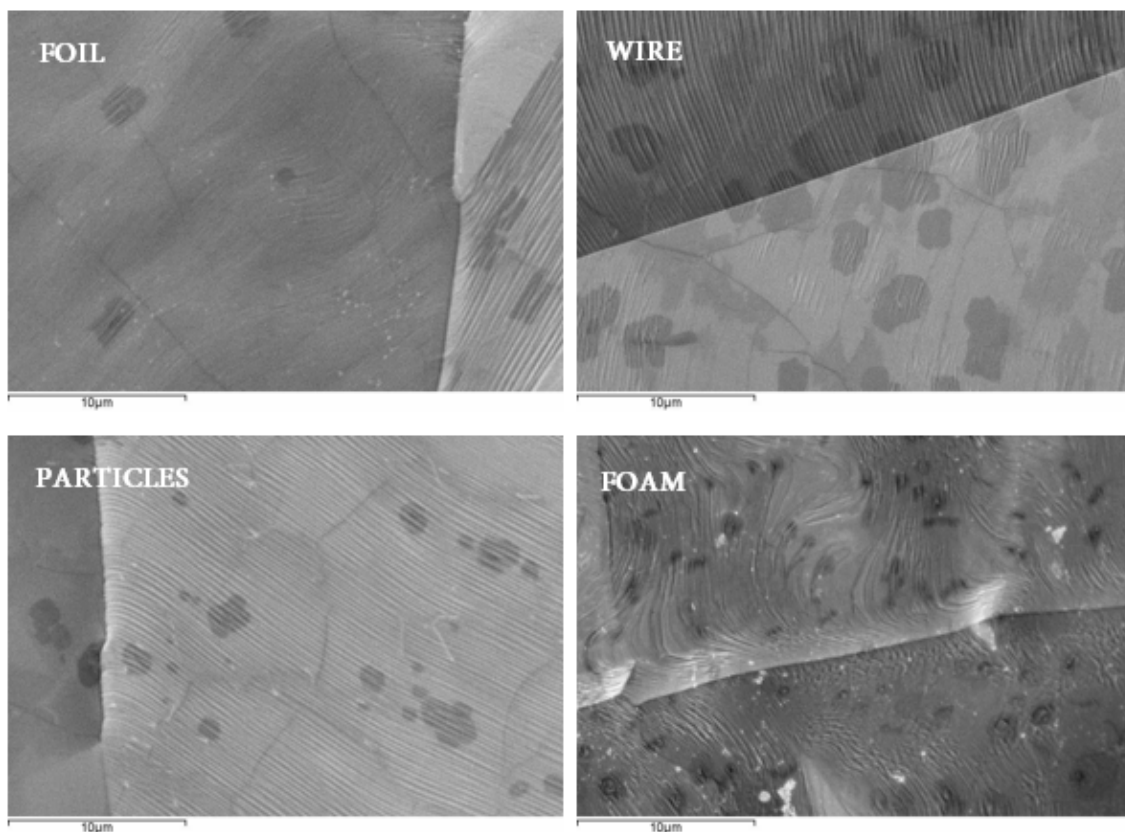


Figure 7-12. Graphene grown with 10% CH₄ and 1050°C

As expected, increasing temperature partially impedes nucleation and produces slightly larger graphene grains. It also promotes growth with allows to produce continuous graphene monolayers in the same amount of time. From the four substrates, foil is the most predictable and it was used as a control. Wire presents some minor differences with the foil that can be explained by the minimal difference in copper purity but it is also very predictable providing reproducible results. Particles perform very similarly to foam but are difficult to handle using a common tubular quartz reactor and piled particles tend to stick together due to the high reaction temperatures. Finally, foam produces very variable results that can be explained by the large amount of impurities and the very high roughness of its surface. Figure 7-13, shows the surface of these foams and as it can be seen the original surface is very rough presumably due to the production method used. Electropolishing vastly improves the surface appearance and roughness but it is still littered with holes and bumps that can affect graphene nucleation. and Simulating a graphene growth without adding methane to observe the effect of copper evaporation, shows that the surface improves a little more but still presents many holes. These can easily explain why foam results are very different from the other three substrates as copper impurities and surface roughness are known to induce graphene nucleation.

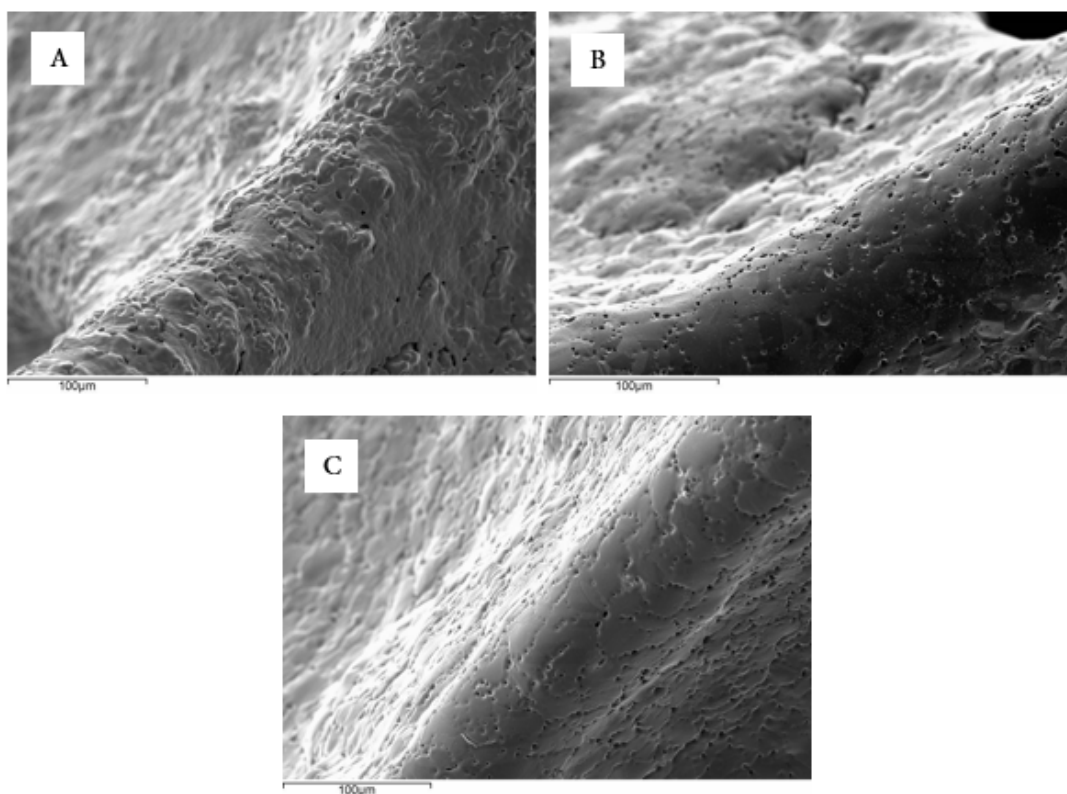


Figure 7-13. Foam surface: (a) original, (b) electropolished, (c) after thermal treatment.

It seems that increasing temperature and, specially, reducing methane content reduces nucleation and increases the size of graphene grains that can be obtained. Applying our photocatalytic oxidation method allows to measure grain sizes for all conditions and substrates except for foam at 950°C and 30% of methane and 1050°C and 10% of methane and wire. Wire could not be measured because its cylindrical geometry impedes the use of optical microscopy. Table 7-3 summarizes all graphene grain sizes and confirms what it was observed using SEM. Reducing methane content translates into almost doubling graphene grain sizes while increasing temperature does not appear to have much effect. This is interesting because going from 950°C to 1050°C does not consistently produce larger grains but produces continuous graphene.

Table 7-3. Average grain size

SUBSTRATE	Temperature	Avg. grain size	Avg. grain size
		(10% CH ₄)	(30% CH ₄)
FOIL	950°C	1.5 μm	1.2 μm
	1050°C	2.1 μm	1.1 μm
PARTICLES	950°C	2.6 μm	1.3 μm
	1050°C	2.1 μm	1.4 μm
FOAM	950°C	1.1 μm	----
	1050°C	----	0.8 μm

As we explained in section 4.2, the photocatalytic oxidation method allows to properly measure grain sizes even for samples with copper 100% covered by graphene. Figure 7-14 shows the before and after for the sample on copper foil at 1050°C and 10% of methane. As it can be observed, before oxidation, SEM does not show the graphene grain boundaries as the sample is 100% continuous. Interestingly, SEM can show small areas of bilayer graphene as islands with a darker shade of gray. After oxidation, though, graphene grain boundaries are clearly visible under optical microscopy, which enables grain sizes to be quantified.

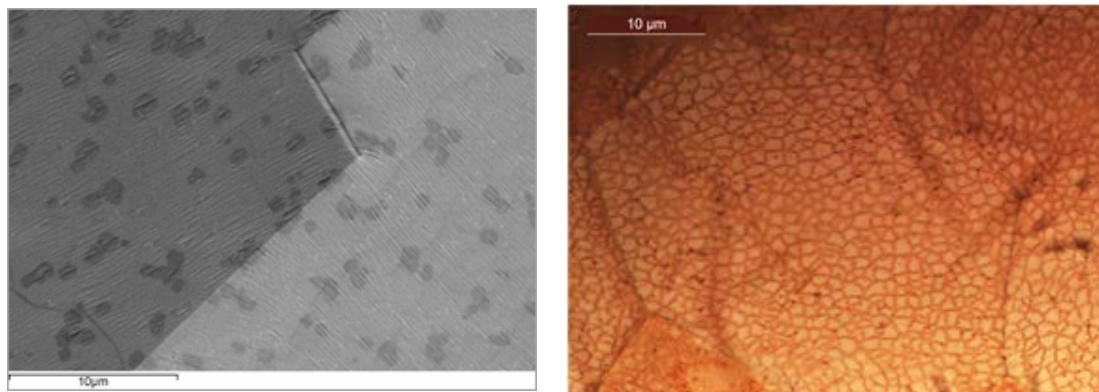


Figure 7-14. Sample on copper foil at 1050°C and 10% of methane. Left SEM image from before oxidation and right, optical image of the same sample after oxidation.

7.3 CVD graphene suspensions

Although for an industrial application, copper particles will be more suitable as the reactor can be easily packed forming a particle bed thus minimizing the empty space, these are a discrete substrate and it might be tricky to maintain electrical conductivity across all particles during graphene release. Copper wire is chosen over particles for several reasons, it is easy to acquire, has a good surface roughness, good purity, it is cheap and easy to handle as it can be formed into coils. Also, it allows to introduce long pieces of wire and increase available copper surface inside the reactor. Moreover, it naturally maintains electrical conductivity through the whole copper wire unlike the particles.

For these proofs of concept 1 meter of wire will be formed into tight coils that represent 9 cm² each one instead the 8 cm² of a typical copper foil sample (2x2 cm). Graphene will be grown by loading one coil into the reactor and using 10% of methane and 1050°C with the growth time set to 5 minutes. These coils serve several purposes as they allow to better pack copper inside reactor, are easier to handle, and also allow for a cleaner detach method. Figure 7-15 shows a schematic representation of the transfer setup. Everything is contained inside a 15 ml falcon tube to reduce to the minimum the amount of electrolyte solution to keep all the graphene/copper wire fully submerged, no more than 2 ml, and minimize outside contamination. To avoid accidental contacts between the platinum anode and the cathode sample a nylon tube is inserted concentrically between both. To ensure proper conductivity between electrodes, the tube has some holes to allow electrolyte movement. The electrolyte used is NaOH 0.25M in MiliQ® water, which gives a conductivity of 30 mS and transfer is achieved by applying 5V of DC current during 10 minutes.

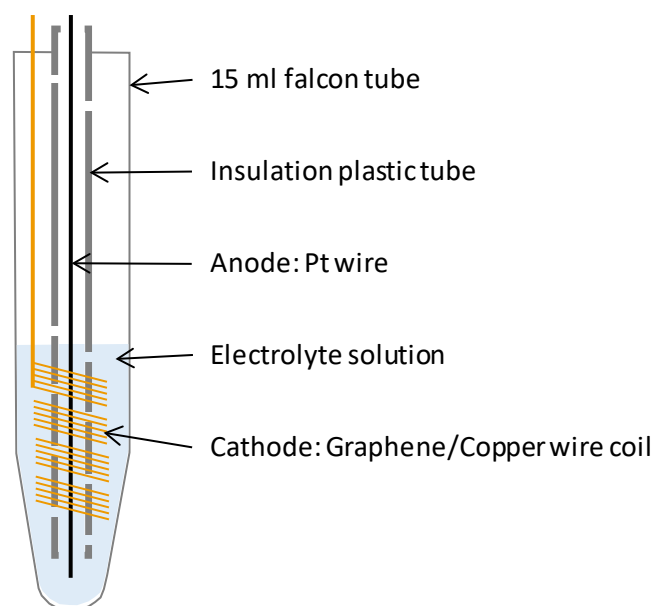


Figure 7-15. Falcon tube set-up for clean electrochemical graphene transfer directly onto solution.

Tyndall effect gives an indication on suspended solids as these disperse a laser beam (note that pure liquids or solutions do not disperse the laser beam). Figure 7-16 presents pictures for graphene suspensions obtained using the set-up in Figure 7-15. The first two images correspond to MiliQ® water (a) and electrolyte solution (b) and it is clear that those not give any Tyndall effect.

The third of the pictures (c) corresponds to a blank sample in, which a clean piece of copper is used to recreate the full process but without any graphene present. It is clear that some particles are present in the media as some Tyndall effect can be observed. At first it was believed that impurities on the electrodes caused this contamination but a much more plausible explanation is a small amount of copper by cavitation erosion. This phenomenon is derived from hydrogen bubbles generated on the surface of metals during electrolysis slowly eroding the electrode, which can explain the low intensity of the observed Tyndall effect.

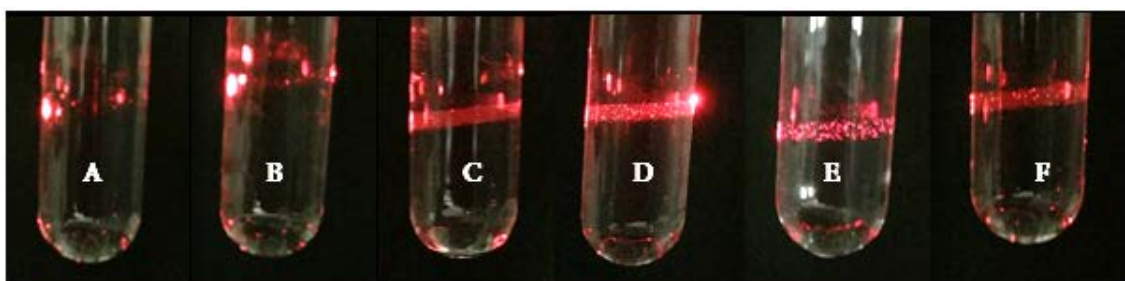


Figure 7-16. Tyndall effect on graphene suspensions. (a) MiliQ® water, (b) Original NaOH solution, (c) blank and (d-f) graphene suspensions.

For the latter 3 images (D-F) “something more” is suspended on the media as sparse bright spots are observed. These can only represent the graphene that separated from the copper coils. SEM further confirms both phenomenon, see Figure 7-17, as the typical graphene wrinkles and grain boundaries “disappear”. The removal of graphene leaves a homogeneous copper surface that presents the same shade of gray across the whole image. Also, small holes appeared along graphene’s grain boundaries, which corresponds with exposed copper and the starting points of the transfer process. More importantly, these holes confirm the presence of a mild cavitation corrosion during graphene release. The base concentration of 0.25M NaOH is taken directly from the bibliography⁴⁴ and produces a very vigorous hydrogen bubbling which can easily explain the mild erosion of copper but also can signify the release of graphene is merely a mechanical process as it is peeled away by the bubbles.

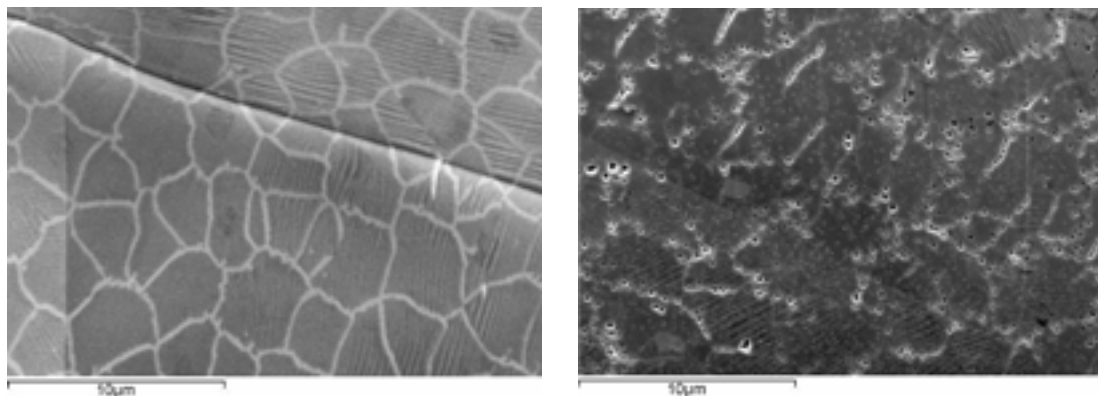


Figure 7-17. Copper wire before and after electrochemical transfer of graphene.

To confirm the presence of graphene it must be recovered from the suspension. The delicate part comes from the extremely low amount of graphene present. Surface wise, there is as much as 4.5 cm² per milliliter of suspension, which might indicate it will be easy to isolate. Weight wise, there is as little as 50 ng per milliliter, which means it will be a challenge to recover significant quantities of graphene from these suspensions.

To enhance the odds of recovering graphene from the suspensions these are vacuum filtered using 0.1 μm Teflon filters. In all cases, the full 2ml of suspension are filtered. This allows the electrolyte to be thoroughly washed leaving, hopefully, clean graphene on top of the filters. Figure 7-18 shows the results of filtering graphene suspensions obtained using 0.25M NaOH as electrolyte during the electrochemical release. Although some flakes are present on the filter it represents much less graphene than what is expected. The explanation is fairly simple, monolayer graphene flakes are very hydrophobic and do not form stable suspensions in water as they tend to aggregate to form multilayer stacks and precipitate over time. Raman spectra confirms that no monolayer graphene is present as it resembles the spectra of amorphous carbon.

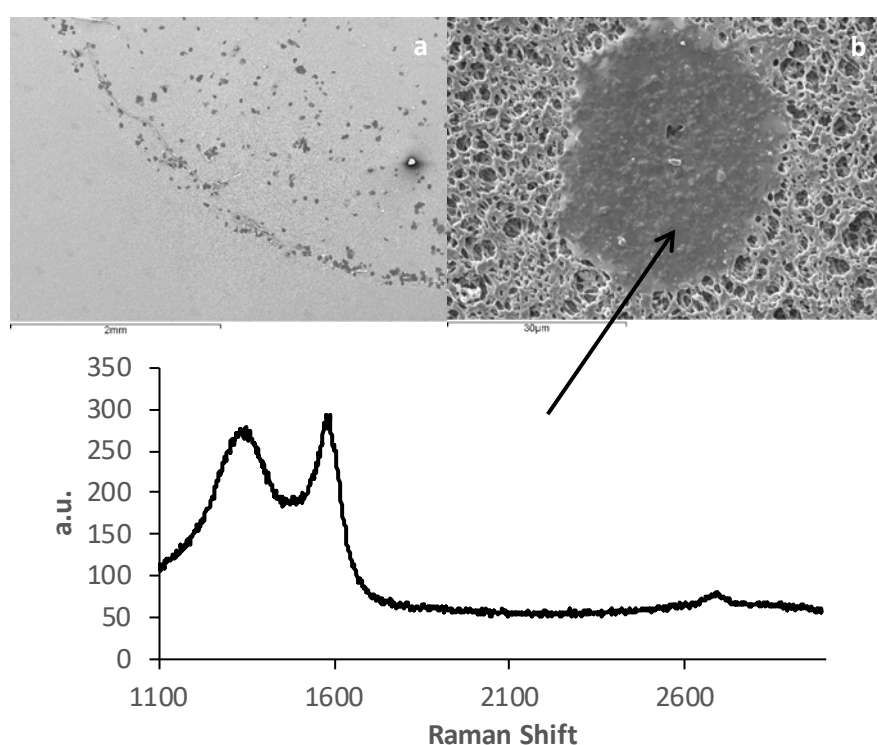


Figure 7-18. Filtered samples (a-b) using 0.25M NaOH as electrolyte.

Graphene suspensions in water are not very common and require some surfactant to stabilize graphene flakes to remain stable over time. The surfactants most used for these suspensions are sodium dodecyl sulfonate (SDS) and sodium dodecyl benzenesulfonate (SDBS). In our case, preparing new electrolyte with 0.25M NaOH and 0.1 mM SDBS allows to successfully transfer graphene to suspension from copper wires and obtain suspensions that do not aggregate as much as without surfactant. A noticeable side effect is that surfactant micelles do give an intense Tyndall effect, which renders this option totally ineffective at detecting graphene. On the other hand, filtering this suspension with SDBS allow for more graphene to be recovered, which could mean these are less aggregated or not aggregated at all, see Figure 7-19. Raman spectroscopy analysis in this case shows a graphene-like spectrum with sharp G and 2D peaks. It is not possible, though, to tell if this graphene is monolayer or bilayer as some fluorescence can be observed as a concave Raman spectroscopy baseline due to the influence of the Teflon® filter used.

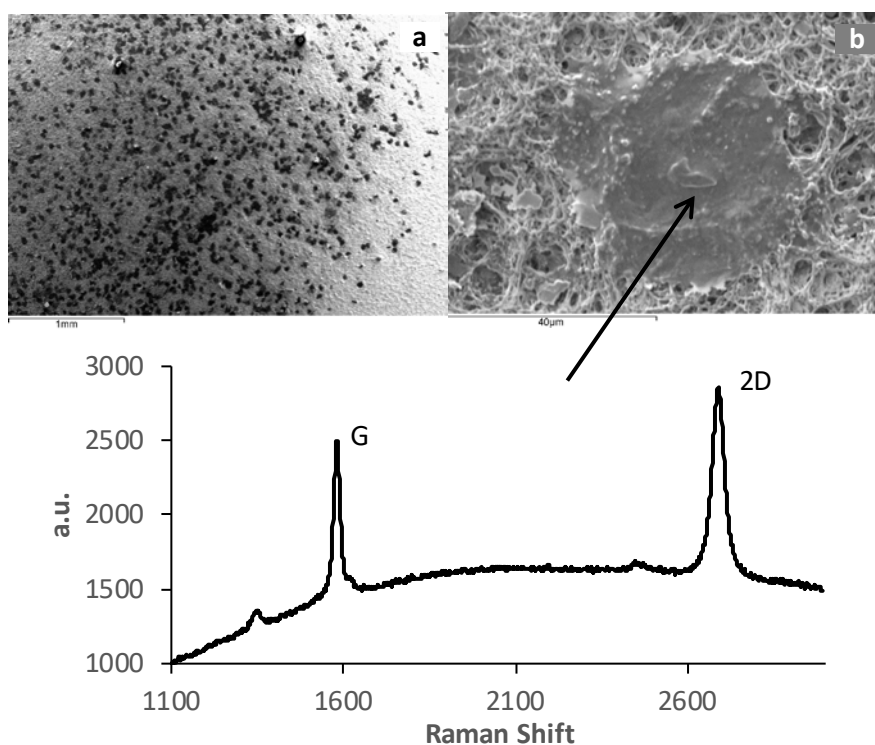


Figure 7-19. Filtered samples (a-b) using 0.25M NaOH with 0.1 mM of SBDS as electrolyte.

In both cases, the flakes observed at Figure 7-18 and Figure 7-19 are larger than the ones observed on top of the wire, Figure 7-17, by a factor of 6 to 8 times. There are two possible explanations for this: either graphene grains on Figure 7-17 are indeed connected forming a continuous layer and that bubbling transfer is vigorous enough to break the graphene layer or suspended graphene grains rapidly try to aggregate into larger structures.

Further SEM analysis on the filtered samples shows the presence of sub-micron copper particles, see Figure 7-20, which further confirms some erosion of the copper during the electrochemical release process. These particles are the same responsible of giving Tyndall effect with blank experiments using only copper, without graphene, as seen on Figure 7-16,

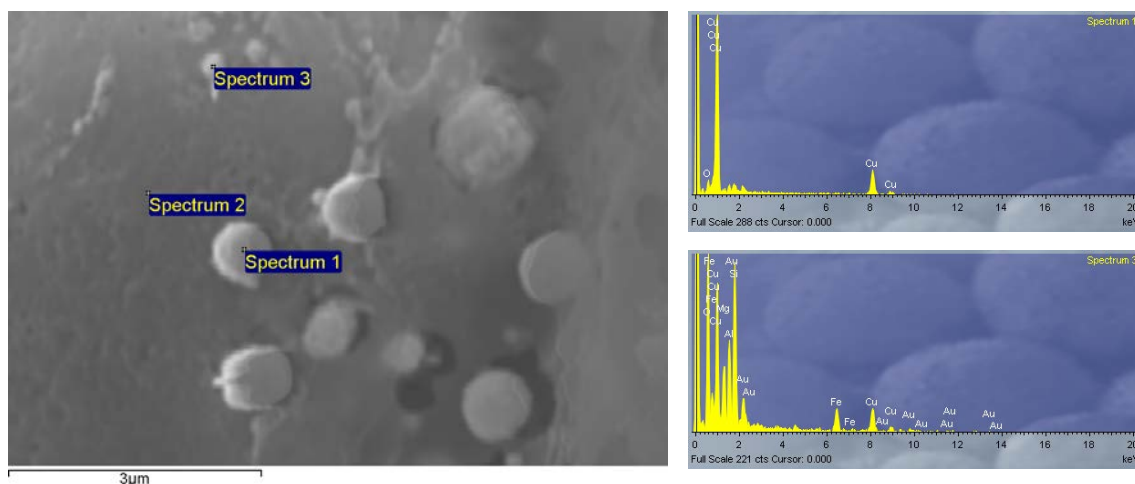


Figure 7-20. Copper microparticles on top of filtered graphene flakes. Spectrums 1 and 3 on the right clearly show the copper nature of these particles.

To establish a proper comparison with well-established graphenes, two commercial samples of graphene oxide and reduced GO (Graphenea, S.A.) are diluted to 100ng/mL, which is the range of concentration expected for our CVD graphene suspensions, and filtered the same way. It is expected that GO will present a radically different Raman spectroscopy response than graphene but it is also expected some monolayer graphene to be present on the rGO samples, according to the producer. Raman spectroscopy analysis on the filtered samples, Figure 7-21, show spectra that closely resemble amorphous carbon, which means that under the conditions these samples were produced, no monolayer graphene is present, not even for the commercial rGO. Furthermore, it appears to indicate that our procedure of producing CVD graphene suspensions directly on aqueous solution with presence of SDBS allows to stabilize monolayer graphene flakes and that these have a low tendency to aggregate.

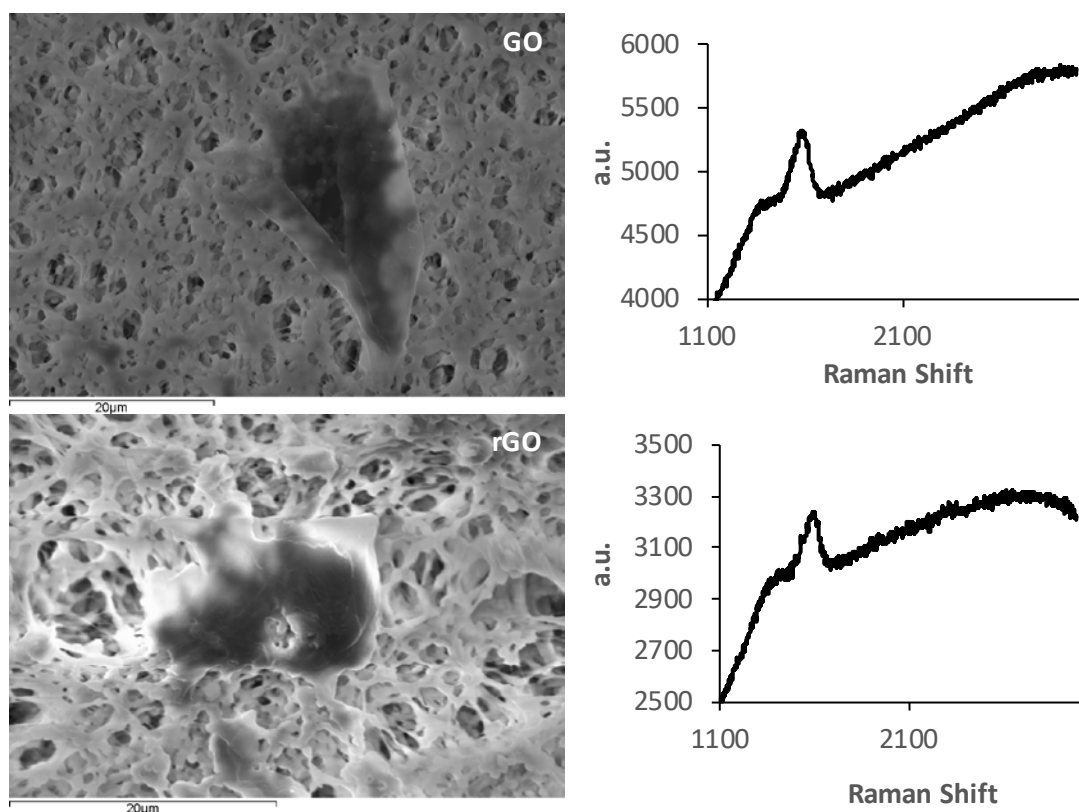


Figure 7-21. Filtered GO and r-GO and their corresponding Raman spectra.

Drying the graphene/SDBS/NaOH suspension on top on SiO₂ coated Si wafers would allow to optically locate the flakes and obtain much cleaner Raman spectra. Although this is possible it presents some issues related with the electrolyte. Because there are orders of magnitude more NaOH and SDBS than graphene these dry forming a solid white crust that must be removed. Statistically, some graphene flakes will be tightly bonded to the wafer while most of them will end up on top or mixed the NaOH/SDBS solid. After cleaning the solid residue only those graphene flakes that were contacting the wafer will remain, which greatly reduces the odds of actually finding a graphene flake. As seen in Figure 7-22, the process is entirely possible and some flakes can actually be found on the silicon wafers. Raman spectra is consistent with the ones obtained directly on the filters minus the fluorescence, which confirms minimal damage to the graphene with almost inexistent D peak. In this case, the ratio between 2D and G peaks seems to indicate this particular graphene flake is comprised of two layers, which means it might have folded in half or stacked with only one more flake.

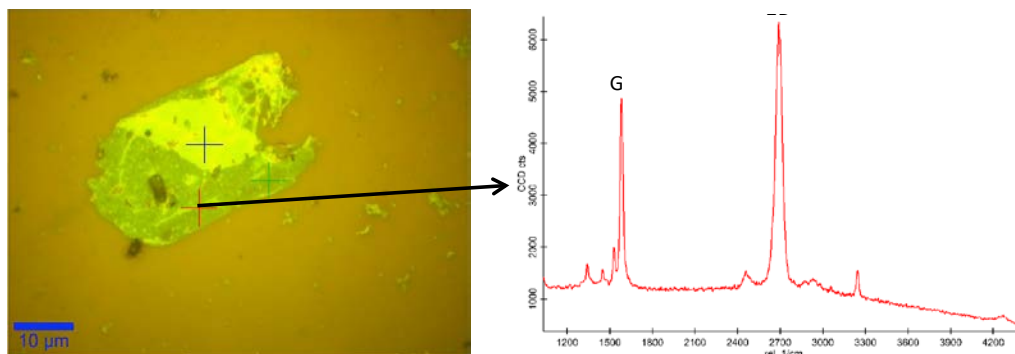


Figure 7-22. Raman spectra of a graphene flake deposited on SiO₂/Si wafer.

Up to this point, quasi-continuous graphene was being used for testing the process and abnormally large graphene flakes were being obtained, see Figure 7-17. This was a side effect of using copper wire which tends to favor nucleation when compared to copper foil thus producing smaller grains. By lowering the gas flow by a third, 30 sccm, overall pressure inside the reactor also decreased to about 0.7 mbar which served to limit both nucleation and growth. These conditions helped to obtain grains with an average size of 60 μm for a 5 minute growth and only 20 μm for a 10 minutes growth, see Figure 7-23. Although graphene crystals appear to be less dendritic and more homogeneous for the longer reaction these are clearly smaller which can be explained by “purification” effect of hydrogen that etched away defective areas of the formed graphene prior to deposition of new carbon.

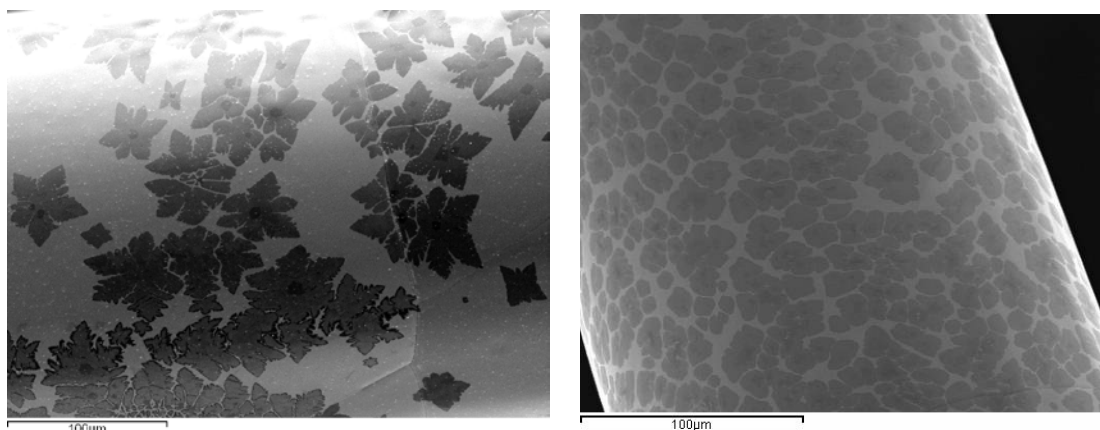


Figure 7-23. Graphene grown on copper wire using 10% methane, 1050°C and 30 sccm of gas flow. Left shows a 5 minute grown graphene and right a 10 minutes one.

Subjecting these two graphenes to the electrochemical detach method, Figure 7-24, individual graphene grains can be found. For the 5 minute reaction, the dendritic grains appear to have lost the points of the dendrites either because those broke during the release or they folded inwards when in suspension. Also, these appear to be thicker on the SEM image as the underlying filter is more obscured which might reinforce the idea that the points of the dendritic flakes folded and did not break. Despite this, the size of 40 μm is about 20 μm smaller than expected for Figure 7-23 but consistent with the loss of the points. On the other hand, the 10 minute reaction yielded more homogeneous grains and the release shows flakes that seem to be monolayer as these look almost transparent to SEM, revealing all the features of the filter beneath. For this case, the filtered flakes present roughly the same size than the original graphene, being around 20 μm each. This result is very promising as both filtrations present flake sizes in the same order of the original graphene which reinforces the thesis of allowing the production of suspensions with controlled particle sizes.

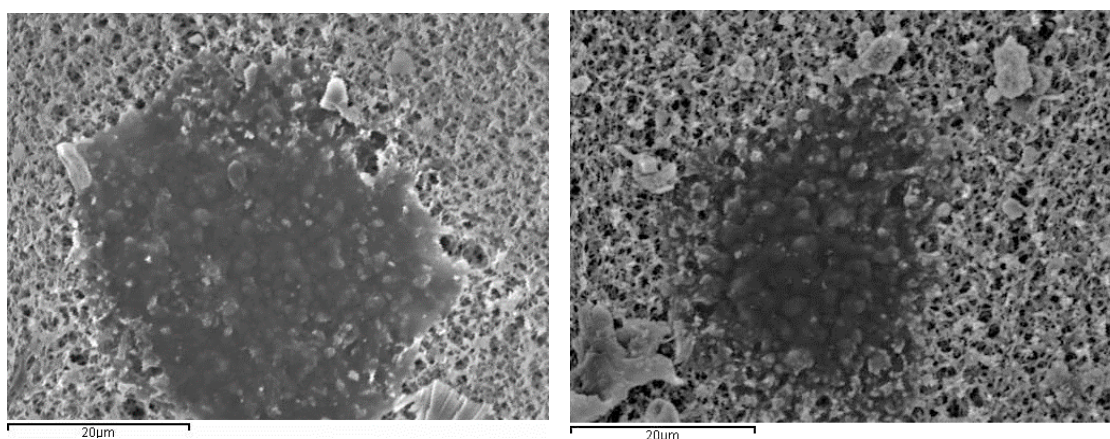


Figure 7-24. SEM of filtered graphenes from Figure 7-23. Left shows 5 minute grown graphene and right a 10 minutes one.

Present results suggest that this new strategy can fill the gap between exfoliated graphene from natural graphite and CVD graphene. By applying the know-how harnessed on this thesis it might be possible to fine tune graphene growth conditions to obtain graphene with controlled grain sizes and statistically measure it directly on the copper wires. This will, in theory, allow the production of CVD graphene suspensions with large contents of monolayer graphene with narrow particle size distributions. The whole process has been patented a Spanish patent under the title: “Procedimiento de fabricación de una suspensión de partículas de grafeno y suspensión correspondiente”.

8 Overall discussion

The widespread use of a material requires high-volume production through economically and technically viable processes. Graphene is not an exception and must jump from lab scale production to mass production. As we explained before, there are mainly two routes for producing graphene: (i) exfoliation of graphite and (ii) synthesis from gaseous carbon precursors.

Micro-mechanical exfoliation was the first method used and has the ability of producing graphene with the highest quality. However, it is very time consuming and not scalable at all. To solve these limitations, bulk exfoliations are being developed. Because exfoliation of graphite to graphene is difficult, the vast majority of processes subject graphite to extremely oxidizing conditions to produce graphite oxide, effectively reducing the adhesion between layers. At this point, mild sonication is then used to separate the layers producing graphene oxide (GO). It is important to highlight that GO has properties significantly different from graphene, e.g. it is not electrically conductive. GO can then be reduced to a sort of graphene (named rGO) through processes that remove part of the oxygen atoms (90% in the best-case scenario). In this particulate material, a lot of defects can be found and there is no control on the size of the platelets nor the amount of layers, which is rarely below 10. All this means that rGO is not truly graphene, although it can be considered a very low quality version of it. Finally, although GO and rGO paper sheets have been produced, there is no viable way of producing a continuous monolayer over large areas.

Synthetic methods are being studied to produce graphene with the aim of achieving monolayer graphene over large areas and quality closer to natural graphene. CVD represents the widest spread synthetic option and, as explained, uses catalytic metallic substrates (Ni, Cu, etc.) to promote the growth of graphene. The use of these substrates opens the possibility of producing various shapes and sizes of graphene while maintaining its monolayer nature but, also means it must be transferred to suitable substrates for each application. The two major limitations of graphene CVD synthesis are the growth and transfer processes. Graphene CVD very often presents a 3D superstructure, by the number of layers, and a 2D lattice structure composed of the uniform hexagonal lattice disrupted by the presence of defects and grain boundaries generated during the nucleation/growth synthesis mechanism.

Quality criteria are presently based only on the number of layers, but must be extended to include the amount of defects and grain size, as properties for synthetic graphenes vary with their 3D and 2D structures and, generally, are much inferior to the benchmark reference (natural manually exfoliated graphene). In this sense, properties of each commercially available graphene may be different and this must be taken into account for the application in mind.

In the first part of this thesis, a CVD reactor has been set-up and tuned-up for the synthesis of monolayer graphene using copper foil showing CVD is a simple and viable option for producing it. As it is usual for CVD systems, process was fine-tuned exploring different conditions of pressure, temperature, and gas composition. There are, though, some critical points that greatly influence the output such as copper annealing and, cooling stage which must be as fast as possible and be performed under the same gas atmosphere used during growth. The annealing stage prior to graphene growth is also extremely important as it serves several purposes: (i) recrystallizes copper, (ii) removes surface copper oxide contamination and, (iii) evaporates copper imperfections and flattens the surface, levelling grooves, scratches and rolling marks. As we showed, the original surface of commercial copper foil is very rough which generates lots of random nucleation spots for graphene and hinders the repeatability of the method. Electropolishing these copper foils prior to annealing and growth not only serves to drastically reduce surface roughness but also removes most of the surface contaminants and, in combination with the annealing, it also removes most of the preferred nucleation spots. Combination of all these effects translates into less nucleation, production of more uniform graphene and more repeatable graphene syntheses. An additional effect of the Electropolishing process is that graphene becomes visible under the SEM on top of copper foil without any additional treatment. Besides SEM, characterization through Raman spectroscopy serves to unequivocally determine the number of layers as graphene presents a very defined fingerprint. THz-TDS spectroscopy and physical electrical contacts served as quality control to compare our samples against the bibliography establishing these are comparable to commercial graphenes.

As we mentioned, one of the main features of CVD graphene is its polycrystalline nature and variable grain sizes. If grain size can be controlled in production of graphene this might enable fine tuning its properties. Continuous monolayer to discrete graphene grains are described in the literature, with grain sizes ranging from few nanometers to millimeters, being commercial graphenes most commonly around few microns. It is widely known that larger graphene grains are obtained by completely enclosing the substrate to limit, or avoid, the copper evaporation. Despite the fact, it is obvious that this restraint limits gas flow, little to no attention has been placed to systematically study the impact of these enclosures to graphene on nucleation and growth dynamics. In this thesis, we have explored the use of gas flow restrictions as a strategy to grow graphene with different grain sizes. Using two parallel quartz slides placed at different distances we showed graphene can be consistently synthesized with sizes ranging from 1 to 16 μm . In contrast, the bibliography reports grains up to the centimeter scale ⁴¹ but these are not common and do not form continuous layers. For continuous graphene few graphene grain sizes are reported and range from 250 nm ⁵⁶, 0.1 to 1 μm ⁵⁷, to 3 to 10 μm ⁵⁵. THz-TDS is a very viable option to perform contactless measures on graphene and might be a very viable option to characterize the differences between graphenes with different grain sizes. At the moment this thesis is written, only samples with graphene grain sizes ranging from 1.4 to 3.6 μm have been analysed proving that, inside this range, no major differences can be observed.

The singularity of graphenes 2D structure and the fact that it must be supported in all cases on a substrate, makes the measurement of grain size difficult. Presently, it is clear that there is not a standard procedure for this task. Most reported methods use oxidation of copper through graphene grain boundaries, followed by observation in an optical microscope. Oxidation is performed by different means, wet or dry. While wet chemistry and thermal treatments are simpler, oxygen plasma treatments show better results regarding image quality. In this thesis, we have developed a novel photocatalytic wet lab-bench method that yields sharp and crisp images that are clean enough to enable using ASTM standards or image analysis methods for grain size analysis. Latest publications on this subject still insist on the use of oxygen plasma ¹⁴⁵. From all the published papers on this subject only Nemes-Incze et al.⁵⁷ show a grain size distribution calculated from multiple atomic resolution AFM images with grains mostly below 400 nm. All the other papers on this subject^{53–56,58,59} present no real grain size distributions.

We have already pointed out the importance of particulate graphene for many applications, as it can be incorporated into other materials to form nanocomposites or used suspended in liquids. Evidences of this are the commercial products based on graphene platelets. In fact, nowadays, particulate graphene is being produced at a reasonably large scale and some products are already being sold. This particulate graphene comes in all cases from exfoliation of graphite and, as we established, it is not monolayer and contains oxygen due to the incomplete reduction from GO to rGO. For these reasons, particulate graphene must be improved while controlling both the number of layers and the size of the particles. In this thesis, we made the first steps towards the production of synthetic graphene suspensions by producing close to 100% monolayer CVD graphene and releasing it directly to aqueous suspensions. The results are very diluted suspensions that keep monolayer graphene in suspension thanks to the use of small quantities of surfactant (SDBS). After filtration, both Raman and SEM characterization allow to determine that our suspensions are far superior than commercial products. Raman spectroscopy of filtered synthetic graphene flakes detects monolayer graphene, while Raman spectra of commercial rGO resemble that of amorphous carbon, as it can be seen on Figure 8-1.

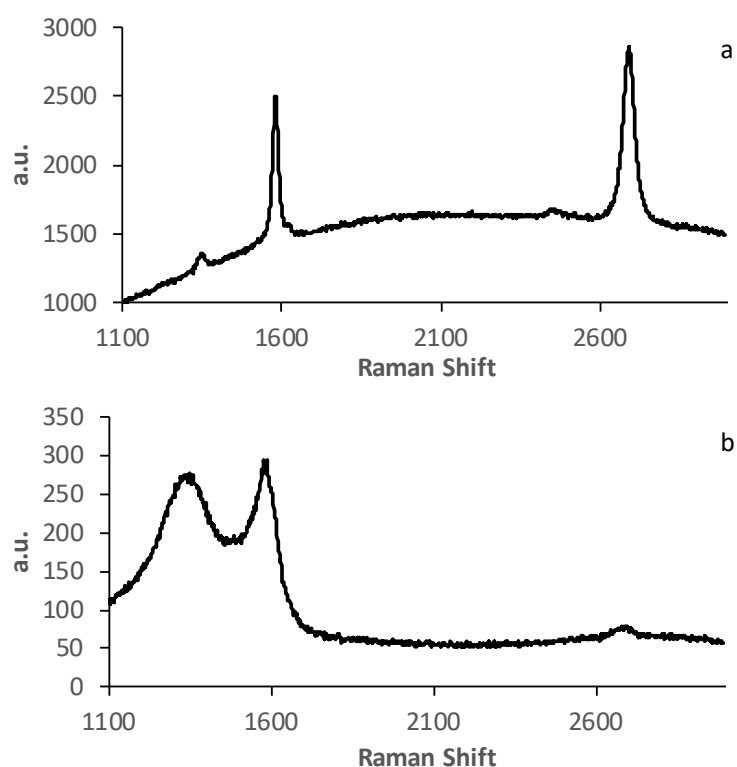


Figure 8-1. Raman spectra for filtered graphene suspensions. (a) shows the spectra for synthetic graphene flakes while (b) presents commercial rGO flakes.

Figure 8-2 and Figure 8-3 show SEM micrographs of filtered graphene suspensions of synthetic graphene and commercial rGO, respectively, using 10kV as accelerating voltage. Outstandingly, our synthetic graphene flakes are exceptionally transparent under SEM allowing to see the underlying filter, unlike commercial rGO flakes which are thick enough to completely hide the filter. Considering that fact that secondary electrons roughly penetrate from 1 to 10 nm (depending on accelerating voltage, atomic number of sample atoms, etc.), this images make evident the differences in thickness of both flakes. This point has been repeatedly confirmed in all filtered synthetic graphene and rGO suspensions. These SEM images are consistent with Raman analysis in confirming that filtered synthetic graphene suspensions are mainly monolayer, while rGO are not.

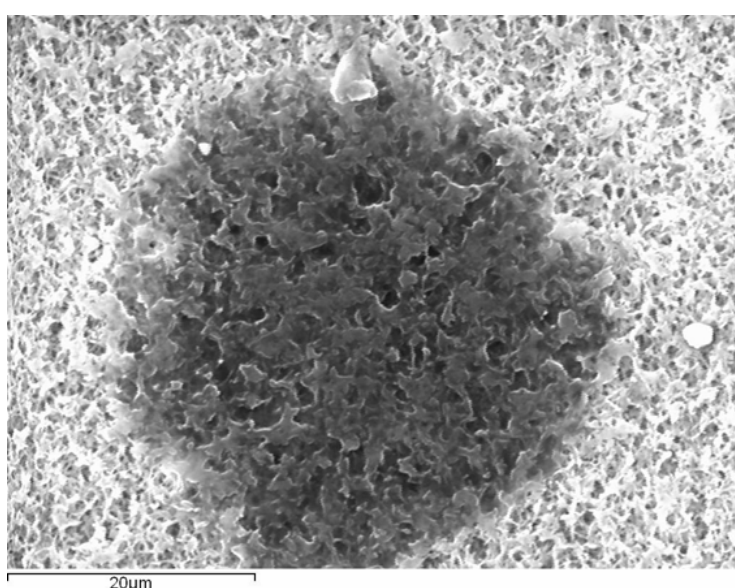


Figure 8-2. SEM image of a monolayer synthetic graphene flake on top of a Teflon® filter.

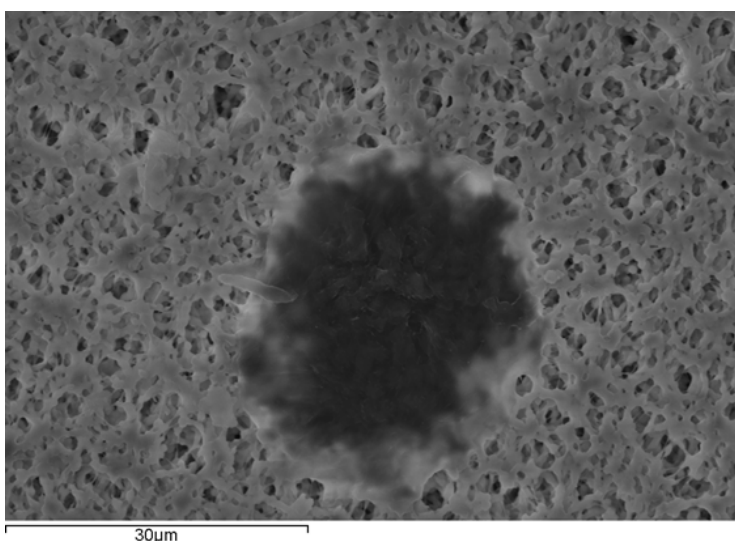


Figure 8-3. SEM image of a monolayer synthetic graphene flake on top of a Teflon® filter.

Present results suggest that suspensions of high quality monolayer graphene can be produced. Moreover, there are evidenced that forcing the production of individual graphene domains yields suspended grains with roughly the same size which might allow the fabrication of suspensions with very narrow and controlled particle sizes. Production could be as follows. First, graphene of custom grain size must be deposited on a high area copper substrate. For this purpose, copper wire meshes or packs of copper particles could be used. In both cases, reactive gases flow through the free space between copper wires or particles. This limits the gas flow and plays in favour of limiting nucleation and promote growth. This situation has been roughly modelled in this thesis by two parallel plates of quartz. After CVD synthesis, grain size analysis of graphene can be performed to check the size of future platelets. Thereafter, graphene is released electrochemically from copper straight to water suspension. Ideally, this step should leave copper unaffected, ready for the next CVD process. This idea of combining all the knowledge developed in this thesis to produce monolayer graphene with precisely controlled grain sizes must be confirmed. More work is needed to establish a direct link between particle size of graphene grains synthesized on copper and the size of graphene platelets found in suspension.

Moreover, although synthetic graphene suspensions have successfully been produced, some issues have to addressed, e.g. graphene concentration in suspension. Lab scale experiments with a copper area of 1.5 cm^2 yielded extremely diluted suspensions with concentrations between 50 and 100 ng/ml. At an industrial scale, it is expected that copper areas in excess of 0.15 m^2 would be needed for graphene concentration in the 0.1 mg/ml (typical concentration for commercial graphene suspensions). Following this idea, growth conditions have to be adjusted to allow more copper to be introduced at once inside the reactor or, even better, move to a semi-continuous set-up.

9 Conclusions

Monolayer graphene has been successfully produced by CVD. A quartz tubular reactor with fixed furnace allows to produce monolayer graphene albeit it is erratic due to the uncontrollable cooling stages. By means of developing a sliding furnace reactor, cooling can be precisely controlled allowing to cool down the sample from 1050°C to under 500°C in less than 30 seconds. This also allows to repeatedly produce monolayer graphene over a great range of reaction conditions. Electropolishing the copper foil prior to graphene growth highly reduces its surface roughness and impurities, effectively improving graphene synthesis. As an additional positive effect, it also makes graphene visible on SEM.

A novel benchtop method for revealing graphene grain boundaries has been successfully developed. TiO₂ photocatalytic oxidation directly on the graphene/copper samples produces dark lines of copper oxide along the graphene grain boundaries. These are clearly visible under optical microscopy and enable grain size analysis of large graphene areas by means of ASTM methods or image analysis. The latter enables measurement and characterization of individual graphene grains resulting in real statistical distributions of graphene grain size.

Combining the reactor developed in this work, the method for grain size analysis and gas flow restrictions inside the reactor, it has been possible to demonstrate light control on CVD graphene grain size during its growth. These restrictions effectively limit the amount of methane available on the surface of the copper catalyst at any time, thus decreasing nucleation and growth rates. Extreme restrictions, placing a quartz slide directly on top of the copper foil, allows to minimize nucleation and grain sizes radically increase. Lengthen growth time enables to obtain monolayer graphene even for the maximum flow restrictions and 1050°C, where nucleation and growth are greatly hindered resulting in grain sizes up to 16 µm.

Using both THz-TDS and a 2-probe system allowed to characterize some graphene samples. THz-TDS was performed in two stages. At first, it was established that CVD graphene grown using our sliding furnace reactor is as good as renowned commercial graphenes. At a second stage, three graphene samples with statistically measured average grain sizes of 1.6, 2 and 3.7 microns were measured and it was determined that, within this range, graphene grain size does not affect its THz response. Measurements using physical probes were aimed at determining the influence of graphene grain boundaries. By measuring a continuous layer across different length of graphene it was observed that for distances over 20 μm its sheet resistance settles to around 1500 Ω/sq which is an acceptable value for graphene. Further analysis of individual graphene grains allowed to measure high quality monolayer areas and a single grain boundary with abnormally low sheet resistivity.

Finally, it has been demonstrated the possibility of obtaining CVD graphene suspensions by means of direct electrochemical detachment from the copper growth substrate to aqueous suspension. The need of a high surface area copper substrate leads to attempt to produce graphene on PVD copper coated quartz, copper foil, wire, particles and foam. PVD copper is discarded due to extreme evaporation and bubbling of the copper layer and the issues related to releasing graphene from it. The four solid copper substrates were successful at producing monolayer graphene and wire is selected over the others for its ease of use being a continuous media and also by its low price and high availability. Electrochemically releasing graphene from copper wire to 0.25M NaOH solutions allow to use Tyndall Effect to determine the presence of graphene on the suspensions. These are not stable over time and tend to agglomerate. Adding SDBS allows to produce stable suspension that apparently do not aggregate. Filtering both allows Raman spectroscopy to be applied and determine the presence of graphene-like species on the suspensions with surfactant. Drying the suspension with SDBS on top of silicon wafers allows to optically locate some graphene flakes that present roughly the same Raman spectra as the filtered suspensions. All in all, and despite the low concentrations, around 50 ng/ml, it has been shown that high quality monolayer graphene suspensions directly from CVD graphene on copper.

The combination of the know-how developed on graphene grain size measurements, control of the graphene nucleation and growth and electrochemical release directly to suspension has the potential of enabling the production of CVD graphene suspensions with close to 100% on monolayer graphene and narrow particle size distributions.

10 Bibliography

1. Wallace, P. The band theory of graphite. *Phys. Rev.* **71**, 622–633 (1947).
2. Novoselov, K., Geim, A. & Morozov, S. Electric field effect in atomically thin carbon films. *Science* (80-.). **22**, 2–6 (2004).
3. Geim, a K. & Novoselov, K. S. The rise of graphene. *Nat. Mater.* **6**, 183–91 (2007).
4. Partoens, B. & Peeters, F. From graphene to graphite: Electronic structure around the K point. *Phys. Rev. B* **74**, 75404 (2006).
5. Bae, S. *et al.* Roll-to-roll production of 30-inch graphene films for transparent electrodes. *Nat. Nanotechnol.* **5**, 574–8 (2010).
6. Kobayashi, T. *et al.* Production of a 100-m-long high-quality graphene transparent conductive film by roll-to-roll chemical vapor deposition and transfer process. *Appl. Phys. Lett.* **102**, 23112 (2013).
7. <https://scifinder.cas.org>. 22/12/2016
8. Yu, Q. K. *et al.* Control and characterization of individual grains and grain boundaries in graphene grown by chemical vapour deposition. *Nat. Mater.* **10**, 443–9 (2011).
9. Warner, J. H. *Graphene*. (2013). doi:10.1093/oxfordhb/9780199585762.013.0001
10. Banhart, F., Kotakoski, J. & Krashennnikov, A. V. Structural defects in graphene. *ACS Nano* **5**, 26–41 (2011).
11. Yazyev, O. & Louie, S. Topological defects in graphene: Dislocations and grain boundaries. *Phys. Rev. B* **81**, 1–7 (2010).
12. Novoselov, K. S. & Castro Neto, A. H. Two-dimensional crystals-based heterostructures : materials with tailored properties. *Phys. Scr.* **14006**, 1–6 (2012).
13. Hernandez, Y. *et al.* High-yield production of graphene by liquid-phase exfoliation of graphite. *Nat. Nanotechnol.* **3**, 563–8 (2008).
14. Paton, K. R. *et al.* Scalable production of large quantities of defect-free few-layer graphene by shear exfoliation in liquids. *Nat. Mater.* **13**, 624–30 (2014).

15. Parvez, K. *et al.* Exfoliation of graphite into graphene in aqueous solutions of inorganic salts. *J. Am. Chem. Soc.* **136**, 6083–6091 (2014).
16. Lotya, M. *et al.* Liquid phase production of graphene by exfoliation of graphite in surfactant/water solutions. *J. Am. Chem. Soc.* **131**, 3611–20 (2009).
17. Bepete, G. *et al.* Surfactant-Free Single Layer Graphene in Water. *arXiv:1603.05421* (2016).
18. Hummers, W. S. & Offeman, R. E. Preparation of Graphitic Oxide. *J. Am. Chem. Soc.* **80**, 1339–1339 (1958).
19. Toh, S. Y., Loh, K. S., Kamarudin, S. K. & Daud, W. R. W. Graphene production via electrochemical reduction of graphene oxide: Synthesis and characterisation. *Chem. Eng. J.* **251**, 422–434 (2014).
20. Pei, S. & Cheng, H. M. The reduction of graphene oxide. *Carbon N. Y.* **50**, 3210–3228 (2012).
21. Norimatsu, W. & Kusunoki, M. Epitaxial graphene on SiC{0001}: advances and perspectives. *Phys. Chem. Chem. Phys.* **16**, 3501–11 (2014).
22. Soldano, C., Mahmood, A. & Dujardin, E. Production, properties and potential of graphene. *Carbon N. Y.* **48**, 2127–2150 (2010).
23. Reina, A. *et al.* Large area, few-layer graphene films on arbitrary substrates by chemical vapor deposition. *Nano Lett.* **9**, 30–5 (2009).
24. Borysiak, M. Graphene Synthesis by CVD on Copper Substrates. *Natl. Nanotechnol. Infrastruct. Netw.* 70–71 (2009).
25. C. Mattevi *et al.* A review of chemical vapour deposition of graphene on copper. *J. Mater. Chem.* **21**, 3324–3334 (2011).
26. Li, X., Cai, W., Colombo, L. & Ruoff, R. S. Evolution of graphene growth on Ni and Cu by carbon isotope labeling. *Nano Lett.* **9**, 4268–72 (2009).
27. Riikonen, S., Krashennnikov, A. V., Halonen, L. & Nieminen, R. M. The role of stable and mobile carbon adspecies in copper-promoted graphene growth. *J. Phys. Chem. C* **116**, 5802–5809 (2012).

28. Li, X. *et al.* Large-area synthesis of high-quality and uniform graphene films on copper foils. *Science* (80-.). **2009**, 1–12 (2009).
29. Li, X. *et al.* Graphene films with large domain size by a two-step chemical vapor deposition process. *Nano Lett.* **10**, 4328–34 (2010).
30. Vlassiuk, I. *et al.* Role of Hydrogen in Chemical Vapor Deposition Growth of Large Single-Crystal Graphene. *ACS Appl. Mater. Interfaces* **5**, 6069–6076 (2011).
31. Han, G. H. *et al.* Influence of copper morphology in forming nucleation seeds for graphene growth. *Nano Lett.* **11**, 4144–8 (2011).
32. Jacobberger, R. M. & Arnold, M. S. Graphene Growth Dynamics on Epitaxial Copper Thin Films. *Chem. Mater.* **25**, 871–877 (2013).
33. Vlassiuk, I. *et al.* Graphene nucleation density on copper: Fundamental role of background pressure. *J. Phys. Chem. C* **117**, 18919–18926 (2013).
34. Lide, D. R. CRC Handbook of Chemistry and Physics, 84th Edition, 2003-2004. *Handb. Chem. Phys.* **53**, 2616 (2003).
35. Bhaviripudi, S., Jia, X., Dresselhaus, M. S. & Kong, J. Role of kinetic factors in chemical vapor deposition synthesis of uniform large area graphene using copper catalyst. *Nano Lett.* **10**, 4128–4133 (2010).
36. Li, X. & Magnuson, C. Large-area graphene single crystals grown by low-pressure chemical vapor deposition of methane on copper. *J. Am. Chem. Soc.* **133**, 2816–2819 (2011).
37. Lee, Y. *et al.* Wafer-scale synthesis and transfer of graphene films. *Nano Lett.* **10**, 490–3 (2010).
38. Yan, Z. *et al.* Toward the Synthesis of Wafer-Scale Single-Crystal Graphene on Copper Foils. *ACS Nano* **6**, 9110–9117 (2012).
39. Yan, Z., Peng, Z. & Tour, J. M. Chemical vapor deposition of graphene single crystals. *Acc. Chem. Res.* **47**, 1327–37 (2014).
40. Geng, D. *et al.* Uniform hexagonal graphene flakes and films grown on liquid copper surface. *Proc. Natl. Acad. Sci. U. S. A.* **109**, 7992–6 (2012).

41. Hao, Y. *et al.* The role of surface oxygen in the growth of large single-crystal graphene on copper. *Science* (80-.). **342**, 720–723 (2013).
42. Lock, E. H. *et al.* High-quality uniform dry transfer of graphene to polymers. *Nano Lett.* **12**, 102–7 (2012).
43. Fecine, G. J. M. *et al.* Direct dry transfer of chemical vapor deposition graphene to polymeric substrates. *Carbon N. Y.* **83**, 224–231 (2015).
44. Gao, L. *et al.* Repeated growth and bubbling transfer of graphene with millimetre-size single-crystal grains using platinum. *Nat. Commun.* **3**, 699 (2012).
45. de la Rosa, C. J. L. *et al.* Frame assisted H₂O electrolysis induced H₂ bubbling transfer of large area graphene grown by chemical vapor deposition on Cu. *Appl. Phys. Lett.* **102**, 22101 (2013).
46. <http://www.aixtron.com/en/products/technologies/nanotechnology/>. 10/12/2016
47. Nair, R. R. *et al.* Fine Structure Constant Defines Visual Transperency of Graphene. *Science* (80-.). **320**, 2008 (2008).
48. Blake, P. & Hill, E. Making graphene visible. *Appl. Phys. ...* 13–15 (2007).
49. Smith, E. & Dent, G. *Modern Raman Spectroscopy: A Practical Approach. Modern Raman Spectroscopy - A Practical Approach* (2005). doi:10.1002/0470011831
50. Ferrari, a. C. *et al.* Raman Spectrum of Graphene and Graphene Layers. *Phys. Rev. Lett.* **97**, 1–4 (2006).
51. Ferrari, A., Meyer, J. & Scardaci, V. The Raman Fingerprint of Graphene. *arXiv Prepr. cond-mat/ ...* **1**, 1–5 (2008).
52. Liu, Y., Liu, Z., Lew, W. S. & Wang, Q. J. Temperature dependence of the electrical transport properties in few-layer graphene interconnects. *Nanoscale Res. Lett.* **8**, 335 (2013).
53. Duong, D. L. *et al.* Probing graphene grain boundaries with optical microscopy. *Nature* **490**, 235–9 (2012).

54. Koepke, J. C. *et al.* Atomic-scale evidence for potential barriers and strong carrier scattering at graphene grain boundaries: a scanning tunneling microscopy study. *ACS Nano* **7**, 75–86 (2013).
55. Kim, K., Lee, Z., Regan, W. & Kisielowski, C. Grain boundary mapping in polycrystalline graphene. *ACS Nano* **5**, 2142–2146 (2011).
56. Huang, P. Y. *et al.* Imaging Grains and Grain Boundaries in Single-Layer Graphene: An Atomic Patchwork Quilt. *Nature* **469**, 389–92 (2011).
57. Nemes-Incze, P. *et al.* Revealing the grain structure of graphene grown by chemical vapor deposition. *Appl. Phys. Lett.* **99**, 23104 (2011).
58. Jia, C., Jiang, J., Gan, L. & Guo, X. Direct optical characterization of graphene growth and domains on growth substrates. *Sci. Rep.* **2**, 707 (2012).
59. Yu, S. U. *et al.* Fast benchtop visualization of graphene grain boundaries using adhesive properties of defects. *Chem. Commun. (Camb)*. **49**, 5474–6 (2013).
60. Cheng, Y. *et al.* Direct Identification of Multilayer Graphene Stacks on Copper by Optical Microscopy. *Chem. Mater.* **28**, 2165–2171 (2016).
61. Fuhrer, M. S., Lau, C. N. & Macdonald, A. H. Graphene : Materially Better Carbon. **35**, 289–295 (2010).
62. Obeng, Y. & Srinivasan, P. Graphene: Is It the Future for Semiconductors? An Overview of the Material, Devices, and Applications. **184**, 2007–2012 (2011).
63. Miao, M., Nardelli, M. B., Wang, Q. & Liu, Y. First principles study of the permeability of graphene to hydrogen atoms. *Phys. Chem. Chem. Phys.* **15**, 16132–7 (2013).
64. Wang, X. & Shi, Y. Fabrication Techniques of Graphene Nanostructures. *Nanofabrication its Appl. Renew. Energy* 1–30 (2014). doi:10.1039/9781782623380-00001
65. Li, D. & Kaner, R. B. MATERIALS SCIENCE: Graphene-Based Materials. *Science (80-.)*. **320**, 1170–1171 (2008).
66. Ovid’ko, I. Mechanical Properties of Graphene. *Rev. Adv. Mater. Sci.* **34**, 1–11 (2013).
67. Huang, X. *et al.* Graphene-based materials: synthesis, characterization, properties, and applications. *Small* **7**, 1876–902 (2011).

68. Lee, C., Wei, X., Kysar, J. W. & Hone, J. Measurement of the elastic properties and intrinsic strength of monolayer graphene. *Science* **321**, 385–8 (2008).
69. Bunch, J. S. Mechanical and Electrical Properties of Graphene Sheets. (2008).
70. Balandin, A. A. Thermal properties of graphene and nanostructured carbon materials. *Nat. Mater.* **10**, 569 (2011).
71. Balandin, A. a *et al.* Superior thermal conductivity of single-layer graphene. *Nano Lett.* **8**, 902–7 (2008).
72. http://www.engineeringtoolbox.com/thermal-conductivity-d_429.html. 19/02/2015
73. Klarskov, M. B. *et al.* Fast and direct measurements of the electrical properties of graphene using micro four-point probes. *Nanotechnology* **22**, 445702 (2011).
74. Li, X. *et al.* Transfer of large-area graphene films for high-performance transparent conductive electrodes. *Nano Lett.* **9**, 4359–63 (2009).
75. Tedesco, J. L. L. *et al.* Hall effect mobility of epitaxial graphene grown on silicon carbide. *Appl. Phys. Lett.* **95**, 2–4 (2009).
76. Sundaram, R. S. *et al.* The graphene-gold interface and its implications for nanoelectronics. *Nano Lett.* **11**, 3833–3837 (2011).
77. <http://litographene.ifs.hr/Page.aspx?id=9>. 02/01/2017
78. Areshkin, D. a, Gunlycke, D. & White, C. T. Ballistic transport in graphene nanostrips in the presence of disorder: importance of edge effects. *Nano Lett.* **7**, 204–10 (2007).
79. Gunlycke, D., Lawler, H. & White, C. Room-temperature ballistic transport in narrow graphene strips. *Phys. Rev. B* **75**, 1–5 (2007).
80. Mayorov, A. S. A. *et al.* Micrometer-scale ballistic transport in encapsulated graphene at room temperature. *Nano Lett.* **11**, 2396–9 (2011).
81. Banszerus, L. *et al.* Ballistic Transport Exceeding 28 μm in CVD Grown Graphene. *Nano Lett.* **16**, 1387–1391 (2016).
82. Welser, J., Hoyt, J. L. & Gibbons, J. F. Electron mobility enhancement in strained-Si n-type\nmetal-oxide-semiconductor field-effect transistors. *IEEE Electron Device Lett.* **15**, 100–102 (1994).

83. Standley, B. *et al.* Graphene-based atomic-scale switches. *Nano Lett.* **8**, 3345–9 (2008).
84. Dawlaty, J. M., Shivaraman, S., Chandrashekhara, M., Rana, F. & Spencer, M. G. Measurement of ultrafast carrier dynamics in epitaxial graphene. *Appl. Phys. Lett.* **92**, (2008).
85. Tonouchi, M. Cutting-edge terahertz technology. *Nat. Photonics* **1**, 97–105 (2007).
86. Docherty, C. J. & Johnston, M. B. Terahertz properties of graphene. *J. Infrared, Millimeter, Terahertz Waves* **33**, 797–815 (2012).
87. Buron, J. D. *et al.* Electrically continuous graphene from single crystal copper verified by terahertz conductance spectroscopy and micro four-point probe. *Nano Lett.* **14**, 6348–6355 (2014).
88. Pop, E., Varshney, V. & Roy, A. K. a. K. Thermal properties of graphene: Fundamentals and applications. *MRS Bull.* **37**, 1273–1281 (2012).
89. Serov, A., Ong, Z. & Pop, E. Effect of grain boundaries on thermal transport in graphene. *Appl. Phys. Lett.* **102**, 33104 (2013).
90. Liu, H. K., Lin, Y. & Luo, S. N. Grain boundary energy and grain size dependences of thermal conductivity of polycrystalline graphene. *J. Phys. Chem. C* **118**, 24797–24802 (2014).
91. Hantehzadeh, R. Role of an Individual Grain Boundary in Thermal Transport across Single Crystalline CVD Graphene. (2014).
92. Kim, K. *et al.* Ripping graphene: preferred directions. *Nano Lett.* **12**, 293–7 (2012).
93. Dumitrica, T., Hua, M. & Yakobson, B. I. Symmetry-, time-, and temperature-dependent strength of carbon nanotubes. *Proc. Natl. Acad. Sci. U. S. A.* **103**, 6105–6109 (2006).
94. Yakobson, B. I. & Ding, F. Observational geology of graphene, at the nanoscale. *ACS Nano* **5**, 1569–74 (2011).
95. Wang, S., Yang, B., Yuan, J., Si, Y. & Chen, H. Large-Scale Molecular Simulations on the Mechanical Response and Failure Behavior of a defective Graphene: Cases of 5–8–5 Defects. *Sci. Rep.* **5**, 14957 (2015).

96. Lee, G.-H. *et al.* High-Strength Chemical-Vapor-Deposited Graphene and Grain Boundaries. *Science (80-.)*. **340**, 1073–1076 (2013).
97. Zhang, P. *et al.* Fracture toughness of graphene. *Nat. Commun.* **5**, 3782 (2014).
98. Kotakoski, J. & Meyer, J. C. Mechanical properties of polycrystalline graphene based on a realistic atomistic model. *Phys. Rev. B - Condens. Matter Mater. Phys.* **85**, 0–4 (2012).
99. Mortazavi, B. & Cuniberti, G. Atomistic modeling of mechanical properties of polycrystalline graphene. *Nanotechnology* **25**, 215704 (2014).
100. Chen, M. Q. *et al.* Effects of grain size, temperature and strain rate on the mechanical properties of polycrystalline graphene - A molecular dynamics study. *Carbon N. Y.* **85**, 135–146 (2015).
101. Song, Z., Artyukhov, V. I., Yakobson, B. I. & Xu, Z. Pseudo hall-petch strength reduction in polycrystalline graphene. *Nano Lett.* **13**, 1829–1833 (2013).
102. Tsen, a. W. *et al.* Tailoring Electrical Transport Across Grain Boundaries in Polycrystalline Graphene. *Science (80-.)*. **336**, 1143–1146 (2012).
103. Jauregui, L. A., Cao, H. L., Wu, W., Yu, Q. K. & Chen, Y. P. Electronic properties of grains and grain boundaries in graphene grown by chemical vapor deposition. *Solid State Commun.* **151**, 1100–1104 (2011).
104. Seifert, M. *et al.* Role of grain boundaries in tailoring electronic properties of polycrystalline graphene by chemical functionalization. *2D Mater.* **2**, 24008 (2015).
105. Wick, P. *et al.* Classification framework for graphene-based materials. *Angew. Chemie - Int. Ed.* **53**, 7714–7718 (2014).
106. Future Markets Inc.. *The Global Nanotechnology and Nanomaterials Market Opportunity Report*. (2016).
107. Rafiee, M. a *et al.* Enhanced Mechanical Properties of nanocomposites at Low Graphene Content. *ACS Nano* **3**, 3884–3890 (2009).
108. Kuilla, T. *et al.* Recent advances in graphene based polymer composites. *Prog. Polym. Sci.* **35**, 1350–1375 (2010).

109. Kim, K. S. *et al.* Chemical vapor deposition-grown graphene: The thinnest solid lubricant. *ACS Nano* **5**, 5107–5114 (2011).
110. Berman, D., Erdemir, A. & Sumant, A. V. Graphene: A new emerging lubricant. *Mater. Today* **17**, 31–42 (2014).
111. Ahn, J. *et al.* Things you could do with graphene. *Nat. Nanotechnol.* **9**, 737–737 (2014).
112. Torrisi, F. *et al.* Ink-Jet Printed Graphene Electronics. *ACS Nano* 1–12 (2011). doi:10.1021/nn2044609
113. Bunch, J. S. *et al.* Impermeable Atomic Membranes from Graphene Sheets. 3–7 (2008). doi:10.1021/nl801457b
114. Bohm, S. Graphene against corrosion. *Nat. Nanotechnol.* **9**, 741–742 (2014).
115. Graphene-info.
116. Liang, M. & Zhi, L. Graphene-based electrode materials for rechargeable lithium batteries. *J. Mater. Chem.* **19**, 5871 (2009).
117. Liu, C., Yu, Z., Neff, D., Zhamu, A. & Jang, B. Z. Graphene-Based Supercapacitor with an Ultrahigh Energy Density. *Nano Lett.* **10**, 4863–4868 (2010).
118. He, Y. *et al.* Freestanding three-dimensional graphene/MnO₂ composite networks as ultralight and flexible supercapacitor electrodes. *ACS Nano* **7**, 174–182 (2013).
119. Yang, H. *et al.* Graphene barristor, a triode device with a gate-controlled Schottky barrier. *Science* **336**, 1140–3 (2012).
120. Balandin, A. A. Graphene Heat Spreaders and Interconnects for Advanced Electronic Applications. 1–6 (2015).
121. Bae, S.-H. *et al.* Graphene-P (VDF-TrFE) multilayer film for flexible applications. *ACS Nano* **7**, 3130–3138 (2013).
122. https://www.tedpella.com/Support_Films_html/Graphene-TEM-Support-Film.htm#graphene_films. 04/01/2017
123. <http://www.graphenenanochem.com/business-segments/advanced-chemicals/oilfield-chemicals>. 04/04/2017

124. <http://www.graphenstone.com/productos.html>. 04/01/2017
125. <http://www.head.com/es/ski/technology/graphene/>. 04/01/2017
126. <http://www.head.com/es/racquetsports/technology/graphene-xt/>. 04/01/2017
127. Young, R. J. & Liu, M. The microstructure of a graphene-reinforced tennis racquet. *J. Mater. Sci.* **51**, 3861–3867 (2016).
128. <https://www.catlike.es/es/es/>. 04/01/2017
129. <https://www.vittoria.com/>. 04/01/2017
130. <http://www.directa-plus.com/Default.asp>. 04/01/2017
131. Polat, E. O. *et al.* Synthesis of Large Area Graphene for High Performance in Flexible Optoelectronic Devices. *Nat. Publ. Gr.* 1–10 (2015). doi:10.1038/srep16744
132. Childres, I., Jauregui, L., Park, W., Cao, H. & Chen, Y. in *New Developments in Photon and Materials Research* 1–20 (2013). doi:10.1016/B978-0-444-53175-9.00016-7
133. ASTM E112-13. Standard Test Methods for Determining Average Grain Size. *ASTM Int. West Conshohocken, PA* (2013).
134. Abràmoff, M. D., Magalhães, P. J. & Ram, S. J. Image processing with imageJ. *Biophotonics Int.* **11**, 36–41 (2004).
135. Schneider, C. a, Rasband, W. S. & Eliceiri, K. W. NIH Image to ImageJ: 25 years of image analysis. *Nat. Methods* **9**, 671–675 (2012).
136. Kim, H. *et al.* Activation energy paths for graphene nucleation and growth on Cu. *ACS Nano* **6**, 3614–3623 (2012).
137. Bakken, C. H. S. Terahertz Time-Domain Spectroscopy. *Master of Science in Electronics* (2012).
138. Ferguson, B. & Zhang, X.-C. Materials for terahertz science and technology. *Nat. Mater.* **1**, 26–33 (2002).
139. http://www.das-nano.es/index.php?option=com_content&view=article&id=18&Itemid=27. 05/01/2017

140. Naftaly, B. M. & Miles, R. E. Terahertz Time-Domain Spectroscopy for Material Characterization. *Proc. IEEE* **95**, 1658 (2007).
141. Hwang, H. Y. *et al.* Nonlinear THz conductivity dynamics in P-Type CVD-grown graphene. *J. Phys. Chem. B* **117**, 15819–15824 (2013).
142. Conwill, A. Contact Resistance of Graphene-Based Devices by TLM. *Technology* 88–89 (2010).
143. Krupka, J. & Strupinski, W. Measurements of the sheet resistance and conductivity of thin epitaxial graphene and SiC films. *Appl. Phys. Lett.* **96**, (2010).
144. Eda, G., Fanchini, G. & Chhowalla, M. Large-area ultrathin films of reduced graphene oxide as a transparent and flexible electronic material. *Nat. Nanotechnol.* **3**, 270–274 (2008).
145. Lee, J.-Y. *et al.* Direct observation of grain boundaries in chemical vapor deposited graphene. *Carbon N. Y.* **115**, 147–153 (2017).

11 Annex 1: Communications and publications

11.1 Communications

Poster: “Grain size analysis of CVD graphene based on the photocatalytic oxidation of copper.” at the GraphIn 2016, Barcelona, 2016.

Poster: “Nobel Photocatalytic Method to observe grain boundaries of large-area graphene on Copper by optical microscopy.” at the Trends in Nanotechnology International Conference (TNT2015), Toulouse, 2015.

Oral Communication: “Noves estratègies en el creixement del grafè” at the “Vuitena Trobada de Joves Investigadors dels Països Catalans”, Andorra la Vella, 2013.

11.2 Publications

Journal Article: Gabriel D., Sempere B., Colominas C., Ferrer-Anglada N.; “THz-conductivity of CVD graphene on different substrates”, *Physica Status Solidi (b)*, 252 (11), p. 2423-2428, 2015

Spanish Patent: Colominas C., Sempere B., “Procedimiento de fabricación de una suspensión de partículas de grafeno y suspensión correspondiente”, P 201631357, 2016

11.3 Publications in preparation

Journal Article: Sempere B., Herrero J., Bermúdez J., Agea B., Colominas C., “Statistically meaningful grain size analysis of CVD graphene based on the photocatalytic oxidation of copper.”, *Graphene Technology*, submitted.

Journal Article: Sempere B., Gabriel D., Ferrer-Anglada N., Colominas C.; “Correlation between graphene grain size and THz response”; in preparation.

Journal Article: Herrero J., Sempere B., Colominas C.; “Controlling graphene nucleation and growth through gas flow restrictions”; in preparation.

Journal Article: Sempere B., Baldi T., Colominas C.; “Synthetic graphene suspensions”; in preparation.

12 Annex 2: Sliding furnace parts list

Table 12-1. Standard ISO-KF parts for the CVD reactor.

Part name	Reference number	3D image
ISO-KF Centering Ring	122ZRG025	
ISO-KF Clamp for Elastomer Seal	120BSR025	
ISO-KF Conical Reducer	120RRK040-025-40	
ISO-KF Centering Ring	122ZRG040	
ISO-KF Clamp for Elastomer Seal	120BSR040	
Tube Compression Fittings ISO-KF	120XQV040-25	
ISO-KF Swagelok® Adapter	120ASW025-6	
ISO-KF Corrugated Hose, Flexible	120SWN025-1000	

Table 12-2. Components of the sliding furnace structure.

Part name	Reference number	3D image
Perfil 5 20x20, natural	0.0.370.03	
Kit unión estándar 5, cincado	0.0.370.08	
Unidad rodadura 5 D6 fija	0.0.390.15	
Unidad rodadura 5 D6 regulable	0.0.390.16	
Calibrado D6, brillante	0.0.356.01	
Perfil brida calibrado 5 D6, natural	0.0.390.02	

13 Annex 3: Optimal methodologies

13.1 Copper electropolish

The final process can be summarized as:

1. Clean copper piece
 - a. Water and ultrasound
 - b. Acetone
 - c. Isopropyl Alcohol
2. Connect electrodes
 - a. Anode: sample to be electropolished
 - b. Cathode: clean scrap piece of copper
3. Connect DC current at 2V
4. Stop after the desired time depending on the substrate:
 - a. Foil: 8 minutes
 - b. Foam:
 - c. Cable:
 - d. Particles: 20 minutes (agitate every 2 to 5 minutes)
5. Clean by submerging in DI water
6. Dry using acetone, isopropyl alcohol and compressed air

13.2 Graphene growth

- Vent gas lines and reactor for 5 minutes
- Insert sample and close reactor
- Vacuum to below 2×10^{-2} mbar
- **Heat furnace:**
 - Downstream from the sample
 - Keep hydrogen atmosphere to avoid copper oxidation
- **Annealing:**
 - Move furnace when at reaction temperature
 - Allow sample to reach reaction temperature (3 to 5 minutes)
 - Maintain hydrogen during the annealing
 - Typical time: 15 minutes
- **Growth:**
 - Change gas flow and swap to methane mixture
 - Maintain temperature and gas during growth
 - Typical time: 5 to 30 minutes
- **Reaction stop:**
 - Move furnace downstream of the sample
 - Switch fan on to assist in cooling
 - Maintain methane gas flow
 - Sample reaches safe temperatures (below 500°C) in around 30 to 60 seconds
- **Final steps:**
 - When sample temperature is under 500°C gas can be switched to hydrogen
 - Allow furnace to fully cool down
 - Stop gas flow and isolate MFC, close all valves.
 - Break vacuum and extract sample

13.3 Ferric Chloride transfer method

1. Spin coating of PMMA.
2. Curing of PMMA at 175°C on a hotplate for 3 minutes
3. Removal of unwanted graphene by floating the stack onto XXX% nitric acid
4. Removal of copper by floating the stack onto 55% FeCl₃ until no copper left
5. Cleaning of the PMMA/Graphene in two steps stack by transferring to gradually cleaner water.
6. Final clean in MilliQ® water for 2h
7. Transfer to its final substrate
8. Dry overnight
9. Relax PMMA layer by heating to 150°C on a hotplate for 2h
10. Dissolve PMMA in acetic acid for a maximum of 4h
11. Clean in DI water
12. Final clean in acetone

13.4 Bubbling transfer method

1. Spin coating of PMMA.
2. Curing of PMMA at 175°C on a hotplate for 3 minutes
3. Removal of unwanted graphene by floating the stack onto XXX% nitric acid
4. Removal of copper by electrochemical reaction:
 - a. Connect PMMA/Graphene/Copper stack onto the anode
 - b. Connect a Titanium counter electrode onto the cathode
 - c. Submerge it into NaOH 0.25M on water
 - d. Apply 2V until full detachment
5. Cleaning of the PMMA/Graphene in two steps stack by transferring to gradually cleaner water.
6. Final clean in MilliQ® water for 2h
7. Transfer to its final substrate
8. Dry overnight
9. Relax PMMA layer by heating to 150°C on a hotplate for 2h
10. Dissolve PMMA in acetic acid for 4h
11. Clean in DI water
12. Final clean in acetone